Dipl.-Ing. Georg Franz Baldauf-Sommerbauer, BSc

Reductive calcination of mineral iron carbonate and mineral magnesium carbonate

DISSERTATION

zur Erlangung des akademischen Grades

Doktor der technischen Wissenschaften

eingereicht an der

Technischen Universität Graz

Betreuer

Univ.-Prof. Dipl.-Ing. Dr.techn. Matthäus Siebenhofer

Institut für Chemische Verfahrenstechnik und Umwelttechnik

Fakultät für Technische Chemie, Verfahrenstechnik und Biotechnologie

Graz, April 2017

EIDESSTATTLICHE ERKLÄRUNG

Ich erkläre an Eides statt, dass ich die vorliegende Arbeit selbstständig verfasst, andere als die angegebenen Quellen/Hilfsmittel nicht benutzt, und die den benutzten Quellen wörtlich und inhaltlich entnommenen Stellen als solche kenntlich gemacht habe. Das in TUGRAZonline hochgeladene Textdokument ist mit der vorliegenden Dissertation identisch.

19.4.2017
Datum

Unterschrift

Dipl.-Ing. Georg Franz Baldauf-Sommerbauer, BSc.

Reductive calcination of mineral iron carbonate and mineral magnesium carbonate

Dissertation

First assessor

Univ.-Prof. Dipl.-Ing. Dr. techn. Matthäus Siebenhofer

Institute of Chemical Engineering and Environmental Technology

Graz University of Technology

Second assessor

Univ.-Prof. Dipl.-Ing. Dr. techn. Harald Raupenstrauch

Chair of Thermal Processing Technology

Montanuniversitaet Leoben

Copyright © 2017 Georg Baldauf-Sommerbauer

All rights reserved. No part of the material protected by this copyright notice may be reproduced or utilized in any form or by any means without written permission from the author.

Danksagung

Ich möchte Prof. Matthäus Siebenhofer für seine intensive Betreuung während der letzten drei Jahre danken. Er hat es mir ermöglicht, selbstständig und frei zu arbeiten, mit dem Wissen, dass ich jederzeit mit meinen Fragen und Anliegen zu ihm kommen kann. Dadurch war es mir möglich, eine Arbeit zu verfassen die großteils auf Publikationen basiert, die ihm Kernteam Baldauf-Sommerbauer/Lux/Siebenhofer entstanden sind, und doch meine Arbeit repräsentieren. Ass.Prof.in Susanne Lux möchte ich für die Mitbetreuung der Dissertation und vor allem für die Aufnahme in das Projektteam des Forschungsprojektes „Reduzierende Kalzinierung" danken. Sie hat mir dadurch ermöglicht mich mit diesem spannenden Forschungsthema intensiv auseinanderzusetzen und über die Anstellung als Universität-Projektassistent meine Tätigkeit finanziell vergütet zu bekommen. Ihre wertschätzende Haltung und die wissenschaftliche Zusammenarbeit auf Augenhöhe hat mir ein gewisses Maß an Selbstvertrauen geschenkt. Die finanzielle Förderung durch den Klima- und Energiefonds im Rahmen des Projekts „Reduzierende Kalzinierung" hat meine Dissertationsstelle möglich gemacht, vielen Dank dafür. Die Projektpartner VA Erzberg GmbH vertreten durch Dr. Alfred Stadtschnitzer und DI Armin Kogelbauer und voestalpine Stahl Linz GmbH vertreten durch Dr. Herbert Schmid haben durch die praxisnahe Beratung und Hilfestellung erfolgreich zum Abschluss dieses Projektes beigetragen. Prof. Harald Raupenstrauch möchte ich für die Zweitbegutachtung der Dissertationsschrift danken. Die Vielzahl an Experimenten und Analysen die zu dieser Dissertation beigetragen haben wären nicht ohne die Hilfe von Wolfgang Aniser, Bernhard Ottitsch, Astrid Loder, Georg Kaufmann, Alexander Kathrein, Patrick Krenn, Darren Kong und das ICVT-Team (H. Luttenberger, P. Letonja, T. Weiß, S. Brander, A. Toth u.a.) möglich gewesen.

Großer Dank gilt meinen Eltern Gertrude und Werner, die mir vieles erst ermöglicht haben, die mit mir durch Höhen und Tiefen gewandert sind und mir das Vertrauen geschenkt haben, dass ich etwas schaffen und erreichen kann. Der größte Dank gilt aber meiner Ehefrau Elisabeth. Sie ist meine treue Partnerin und mein Rückhalt, der mich fördert und fordert. Sie hat mir zwei wunderbare Töchter geschenkt, einen Gutteil der Betreuungsarbeit übernommen und dabei ihre eigenen wissenschaftlichen Pläne hintangestellt. Vielen Dank!

Abstract

Mitigation of carbon dioxide emissions is a predominant topic in current chemical engineering research. Direct process CO_2 emissions, as encountered in the beneficiation of mineral carbonates, have to be addressed by process optimization and/or carbon dioxide utilization approaches. Two alternatives to state-of-the-art beneficiation of mineral iron and magnesium carbonate are presented. As a first alternative, thermal decomposition of iron carbonate in nitrogen atmosphere is evaluated. Thermal decomposition of iron carbonate in nitrogen instead of state-of-the-art roasting omits hematite formation. As a consequence, less reducing agent is needed for pig iron production in the blast furnace, directly abating CO_2 emissions. As a second alternative, reductive calcination is introduced and applied as a means of carbon dioxide utilization during mineral carbonate beneficiation. Reductive calcination includes the thermal decomposition of carbonates in hydrogen atmosphere. Carbon monoxide and methane are formed in a single-stage process from mineral iron carbonate and magnesium carbonate. The yield of CO and CH_4 can be partially regulated via carbonate mineral, reaction temperature, and pressure. The solid state kinetics for the thermal decomposition of mineral iron carbonate in nitrogen and hydrogen was determined from linear heating rate thermogravimetric data. Based on design of experiments, the optimal conditions for high methane yield during single-stage reductive calcination of mineral iron carbonate were identified. A lump kinetics model for the reductive calcination of 5-10 mm mineral iron carbonate in the temperature range 375-415 °C at ambient pressure and 8 bar overpressure is presented. Additionally, a nickel-magnesium oxide catalyst for the gas-phase methanation of carbon dioxide was developed and investigated for its activity, stability, and reaction kinetics.

Kurzfassung

Die Einsparung von Kohlendioxidemissionen ist ein tonangebendes Thema in der aktuellen chemischen und verfahrenstechnischen Forschung. Direkte CO_2-Emissionen, wie sie bei der Aufbereitung von karbonatischen Mineralien auftreten, können durch Prozessoptimierung und/oder CO_2-Nutzungsansätze eingespart werden. In der vorliegenden Dissertationsschrift werden zwei Alternativen zur Aufbereitung von mineralischem Eisen- und Magnesiumkarbonat nach dem Stand der Technik präsentiert. Als erste Alternative wird die thermische Zersetzung von Eisenkarbonat in Stickstoffatmosphäre evaluiert. Durch thermische Zersetzung in Stickstoff wird die Bildung von Hämatit, dem Produkt der Röstung nach dem Stand der Technik, vermieden. Dadurch ist im Hochofenprozess zur Roheisenerzeugung weniger Reduktionsmittel, in diesem Fall Kohle, notwendig. Dies führt zu einer direkten Einsparung von CO_2-Emissionen. Als zweite Alternative wird die reduzierende Kalzinierung diskutiert. Nach einer allgemeinen Einführung des Konzepts wird die Anwendung der reduzierenden Kalzinierung als Möglichkeit der CO_2-Nutzung in der Aufbereitung von mineralischen Karbonaten evaluiert. Bei der reduzierenden Kalzinierung wird das Karbonat in Wasserstoffatmosphäre thermisch zersetzt. Kohlendioxid, Kohlenmonoxid und Methan werden in einem einstufigen Prozess aus mineralischem Eisen- und Magnesiumkarbonat gebildet. Die Ausbeute an CO und CH_4 kann in bestimmten Grenzen durch die Auswahl des Karbonats, der Reaktionstemperatur und des Reaktionsdrucks gesteuert werden. Die Feststoffkinetik der thermischen Zersetzung von mineralischem Eisenkarbonat in Stickstoff und Wasserstoff wurde anhand von thermogravimetrischen Messdaten bestimmt. Mit Hilfe statistischer Versuchsplanung konnte die Methanausbeute der einstufigen reduzierenden Kalzinierung von Eisenkarbonat optimiert werden. Die reduzierende Kalzinierung von mineralischem Eisenkarbonat der Kornklasse 5-10 mm konnte anhand eines vereinfachten Reaktionsmodells, das im Temperaturbereich 375-415 °C bei Umgebungsdruck und 8 bar Überdruck gültig ist, beschrieben werden. Zusätzlich wurde ein Nickel/Magnesiumoxid Katalysator für die heterogen-katalysierte Umsetzung von Wasserstoff und Kohlendioxid zu Methan entwickelt und charakterisiert.

Table of contents

1 Introduction

Industry is a major contributor to anthropogenic CO_2 emissions. Approximately one third of the total anthropogenic CO_2 emissions can be attributed to the industrial sector [1]. Due to the harmful effect on earth's climate [2], the reduction of CO_2 emissions is a global challenge. According to the 5th IPCC report [1], 2.1 Gt of CO_2 are directly emitted from the production of ferrous and non-ferrous metals. The calcination step (alternatively called thermal decomposition, Eq. 1) of metal carbonates is a considerable contributor to these CO_2 emissions.

$$MCO_3 \rightarrow MO + CO_2 \quad (1)$$

The production of magnesium oxide for refractory production accounts for nearly 7 Mt $year^{-1}$ of CO_2 emissions, with 0.41$year^{-1}$ Mt in Austria alone [3]. In China [4] and Austria [5] iron carbonate (= siderite) deposits provide to iron and steel production. In Austria, more than 2 Mt of iron ore with a proximate content of 70 wt.% iron carbonate is processed in iron and steel production [5]. During calcination of the ore in the sinter plant, 0.6 Mt $year^{-1}$ of CO_2 are liberated as direct process emissions. Indirect CO_2 emission from the industrial sector can be reduced by a transition of the energy and transport system from fossil to renewable resources. Direct process CO_2 emissions, however, can only be omitted by either (a) process optimization, (b) utilizing carbon dioxide (CDU) or (c) capturing and storing carbon dioxide (CCS) [6-18]. Chapter 2 and 3 focus on aspect (a), process optimization applied to mineral iron carbonate beneficiation. Chapters 4-7 reveal how the concept of reductive calcination, introduced in chapter 4, can be used as a means of (b) carbon dioxide utilization to mitigate carbon dioxide emission during mineral iron and magnesium carbonate processing.

The state-of-the-art for iron carbonate beneficiation in iron and steel production is blending of ores in the sinter plant prior to feeding it into the blast furnace. During sintering, iron carbonate is calcined in air (= roasting) and hematite Fe_2O_3 is formed by oxidation. In chapter 2, published in *Thermochimica Acta* [19], it is shown that calcination of iron carbonate in nitrogen leads to the formation of wuestite FeO and magnetite Fe_3O_4. Consequently, the specific iron content of the calcination product is raised compared to roasting and the amount of reducing agent for iron production from iron carbonate is decreased. This leads to a decrease of carbon dioxide emissions, since less coke is needed for chemical reduction of the oxidic feed in the blast furnace process. Two computational methods to determine the solid state kinetics from thermogravimetric measurements – an isoconversional and a multi-variate non-linear regression (MVNR) method – are applied and compared. It is shown that MVNR is the more robust method to determine the kinetics of the conversion of heterogeneous natural minerals. The carbon dioxide emissions during iron production from iron carbonate can be further decreased by direct reduction with hydrogen. In chapter 3, published in *Green Chemistry* [20], this process is described and the kinetics of iron carbonate reduction with hydrogen is determined by MVNR from thermogravimetric data. Furthermore, a dual-step process is

outlined that couples hydrogen reduction of iron carbonate and catalytic carbon dioxide hydrogenation to diminish inevitable CO_2 emissions from carbonate decomposition. The combination of carbon dioxide emission and the utilization step is investigated in chapter 4. The concept of 'reductive calcination' (see Eq. 2) is introduced and results from its application to iron carbonate beneficiation are presented. Depending on process temperature and pressure, it is possible to partially convert iron carbonate into carbon monoxide and/or methane in a single-stage process. Results from the reductive calcination of mineral magnesite (98 %wt. $MgCO_3$) are presented in chapter 5, published in *Chemical Engineering & Technology* [22]. Chapter 6, published in *Chemie-Ingenieur-Technik* [21], displays the results from the reductive calcination of the magnesite fraction of a mineral consisting of magnesite and dolomite in a 1:1 molar ratio.

$$(a+b)MCO_3 + \left[(a+b)\left(\frac{c}{2}+d\right)+b\right]H_2 \rightarrow$$

$$a\,MO + b\,M + (a+b)CH_cO_{2-d} + [b+d(a+b)]H_2O \qquad (2)$$

Due to the necessity of robust heterogeneous methanation catalysts for the gas valorization of the product gas from reductive calcination aiming at high methane yields, nickel/magnesium oxide catalysts were developed and characterized. Results of the catalytic methanation with Ni/MgO-catalysts are presented in chapter 7, which is intended for publication. Finally, the findings and some questions left for future research will be summarized at the end of the thesis.

References

[1] IPCC, Climate Change 2014 Synthesis Report, Geneva, 2014.

[2] United Nations Framework Convention on Climate Change FCCC/CP/2015/L.9, Adoption of the Paris Agreement, Paris, 2015.

[3] I. Szednyj, D. Brandhuber, Stand der Technik zur Kalk-, Gips und Magnesiaherstellung: Beschreibung von Anlagen in Österreich, 2007.

[4] D. Zhu, X. Zhou, J. Pan, Y. Luo, Direct reduction and beneficiation of a refractory siderite lump, Miner. Process. Extr. Metall. 123 (2014) 246–250. doi:10.1179/1743285514Y.0000000081.

[5] A. Boehm, M. Boehm, A. Kogelbauer, Neutrons for mineral processing - Thermo diffractometry to investigate mineral selective magnetizing flash roasting, Chemie Ing. Tech. 86 (2014) 883–890. doi:10.1002/cite.201400024.

[6] A.M. Appel, J.E. Bercaw, A.B. Bocarsly, H. Dobbek, D.L. Dubois, M. Dupuis, et al., Frontiers, opportunities, and challenges in biochemical and chemical catalysis of CO2 fixation, Chem. Rev. 113 (2013) 6621–6658. doi:10.1021/cr300463y.

[7] C. Song, Global challenges and strategies for control, conversion and utilization of CO2 for sustainable development involving energy, catalysis, adsorption and chemical processing, Catal. Today. 115 (2006) 2–32. doi:10.1016/j.cattod.2006.02.029.

[8] J. Qiao, Y. Liu, F. Hong, J. Zhang, A review of catalysts for the electroreduction of carbon dioxide to produce low-carbon fuels, 2014. doi:10.1039/c3cs60323g.

[9] M. Peters, B. Köhler, W. Kuckshinrichs, W. Leitner, P. Markewitz, T.E. Müller, Chemical technologies for exploiting and recycling carbon dioxide into the value chain, ChemSusChem. 4 (2011) 1216–1240. doi:10.1002/cssc.201000447.

[10] M. Mikkelsen, M. Jørgensen, F.C. Krebs, The Teraton Challenge. A review of fixation and transformation of carbon dioxide, Energy Environ. Sci. 3 (2010) 43–81. doi:10.1039/B912904A.

[11] M. Aresta, A. Dibenedetto, Utilisation of CO2 as a chemical feedstock: opportunities and challenges, Dalt. Trans. (2007) 2975–2992. doi:10.1039/b700658f.

[12] G. Centi, E.A. Quadrelli, S. Perathoner, Catalysis for CO2 conversion: a key technology for rapid introduction of renewable energy in the value chain of chemical industries, Energy Environ. Sci. 6 (2013) 1711–1731. doi:10.1039/C3EE00056G.

[13] D. Mattia, M.D. Jones, J.P. O'Byrne, O.G. Griffiths, R.E. Owen, E. Sackville, et al., Towards carbon-neutral CO2 conversion to hydrocarbons, ChemSusChem 8 (2015) 4064–4072. doi:10.1002/cssc.201500739.

[14] G. Centi, S. Perathoner, Opportunities and prospects in the chemical recycling of carbon dioxide to fuels, Catal. Today. 148 (2009) 191–205. doi:10.1016/j.cattod.2009.07.075.

[15] I. Dimitriou, P. García-Gutiérrez, R.H. Elder, R.M. Cuéllar-Franca, A. Azapagic, R.W.K. Allen, Carbon dioxide utilisation for production of transport fuels: process and economic analysis, Energy Environ. Sci. 8 (2015) 1775–1789. doi:10.1039/C4EE04117H.

[16] A. Otto, T. Grube, S. Schiebahn, D. Stolten, Closing the loop: captured CO2 as a feedstock in the chemical industry, Energy Environ. Sci. 8 (2015) 3283–3297. doi:10.1039/C5EE02591E.

[17] H. Arakawa, M. Aresta, J.N. Armor, M. a Barteau, E.J. Beckman, A T. Bell, et al., Catalysis research of relevance to carbon management: progress, challenges, and opportunities., Chem. Rev. 101 (2001) 953–96. doi:10.1021/cr000018s.

[18] N. MacDowell, N. Florin, A. Buchard, J. Hallett, A. Galindo, G. Jackson, et al., An overview of CO2 capture technologies, Energy Environ. Sci. 3 (2010) 1645. doi:10.1039/c004106h.

[19] G. Baldauf-Sommerbauer, S. Lux, J. Wagner, M. Siebenhofer, Determination of the kinetic triplet by an isoconversional and a regression method applied to the decomposition of mineral iron carbonate in nitrogen, Thermochim. Acta. 649 (2017) 1–12. doi:10.1016/j.tca.2017.01.001.

[20] G. Baldauf-Sommerbauer, S. Lux, M. Siebenhofer, Sustainable iron production from mineral iron carbonate and hydrogen, Green Chem. 18 (2016) 6255–6265. doi:10.1039/C6GC02160C.

[21] G. Baldauf-Sommerbauer, S. Lux, W. Aniser, M. Siebenhofer, Synthesis of carbon monoxide from hydrogen and magnesite/dolomite, Chemie Ing. Tech. 89 (2017) 172–179. doi:10.1002/cite.201600078.

[22] G. Baldauf-Sommerbauer, S. Lux, W. Aniser, M. Siebenhofer, Reductive calcination of mineral magnesite: hydrogenation of carbon dioxide without catalysts, Chem. Eng. Technol. 39 (2016) 2035–2041. doi:10.1002/ceat.201600094.

2 Determination of the kinetic triplet by an isoconversional and a regression method applied to the decomposition of mineral iron carbonate in nitrogen[1]

Abstract

The determination of a suitable combination of reaction model f(α), activation energy E_a, and pre-exponential factor A – the kinetic triplet – is a key issue in the modeling of solid state decomposition reactions. Two complementary methods for determination of the kinetic triplet were applied and compared: (1) an isoconversional method and (2) the multi-variate nonlinear regression method proposed by Opfermann (J. Therm. Anal. Calorim. 2000). The isoconversional method was based on the evaluation of master plots y(α) and z(α) and the activation energy according to the Friedman and Kissinger-Akahira-Sunose approach. The kinetic computations were performed for the determination of the kinetic triplet of the decomposition of mineral iron carbonate in nitrogen atmosphere. The industrial practice for mineral iron carbonate beneficiation is sintering in air to convert it into Fe_2O_3. Thermal decomposition of mineral iron carbonate in inert nitrogen atmosphere produces FeO and Fe_3O_4. Consequently, the specific iron content of the solid product is increased. This is economically and environmentally advantageous, as less reducing agent is needed for iron production from FeO and Fe_3O_4 compared to production from Fe_2O_3.

[1] This chapter is based on an article published by Elsevier and is reprinted under licence number 4038831184207 of Jan. 30, 2017:
G. Baldauf-Sommerbauer, S. Lux, J. Wagner, M. Siebenhofer, Determination of the kinetic triplet by an isoconversional and a regression method applied to the decomposition of mineral iron carbonate in nitrogen, Thermochim. Acta. 649 (2017) 1–12. doi:10.1016/j.tca.2017.01.001.

Greek symbols

α	-	Conversion (relative: 0-1)
α_M	-	Value of α at maximum of y(α)
α_P	-	Value of α at maximum of z(α)
β	°C min^{-1}	Heating rate
γ	-	Stoichometric parameter used in Eq. 15-17 that ranges from 5/3 (only Fe_3O_4 is formed) to 2 (only FeO is formed)
$\Delta_R G°$	-	Standard Gibbs reaction energy
$\Delta m_{max,rel}$	%	Maximum relative mass loss defined in Eq. 18
π	-	Approximation function for temperature integral
ρ,τ	-	Stoichiometric coefficients

Symbols

a,b,c,x	-	Stoichiometric coefficients
A	s^{-1}, min^{-1}	Pre-exponential factor
A_α	s^{-1}, min^{-1}	Pre-exponential factor determined with an isoconversional method
A_{der}	s^{-1}, min^{-1}	Pre-exponential factor determined with Eq. 11
A_{reg}	s^{-1}, min^{-1}	Pre-exponential factor determined with Eq. 10
E_a	kJ mol^{-1}	Arrhenius activation energy
E_α	kJ mol^{-1}	Isoconversional activation energy
$E_{\alpha,i}$	kJ mol^{-1}	Activation energy calculated with the Friedman (i = F) or KAS (i = KAS) approach
E_{iso}	kJ mol^{-1}	Mean activation energy determined with an isoconversional method
F	-	Value of the F-Test
f(α)	-	Reaction model
K_{cat}	-	Model parameter for the nth order autocatalysis reaction model CnB
m	-	Model parameter for Bna model
n	-	Reaction order
p	-	Factor used to determine the parameters n and m of the Bna model applying the isoconversional methodology
R	-	Regression coefficient
R_{gas}	kJ mol^{-1} K^{-1}	Ideal gas constant
t	min, s	Time
T	°C	Temperature
w_i	-	Mass fraction of element i according to ICP-OES analysis
wr_i	-	Weight ratio based on TG experiment (i=TG) or RIR (i=RIR)
y(α)	-	Master plot curve y as defined in Eq. 6
z(α)	-	Master plot curve z as defined in Eq. 7

Abbreviations

a.u.		Arbitrary units
An		N^{th}-order Avrami-Erofeev reaction model
AW	g mol^{-1}	Atomic weight
Bna		Extended Prout-Tompkins model, alternatively called truncated Sestak-Bergren model
CnB		n^{th}-order autocatalysis reaction model
CRTA		Constant rate thermal analysis
DSC		Differential scanning calorimetry
EDXS		Energy dispersive X-ray spectrometry
Fn		N^{th}-order reaction model

ICM200		Iron carbonate mineral, 100-200 µm fraction
ICP-OES		Inductively coupled plasma-optical emission spectroscopy
KAS		Kissinger-Akahira-Sunose
m.b.		Molar basis
MVNR		Multi-variate nonlinear regression
MW	g mol^{-1}	Molecular weight
RIR		Reference intensity ratio
SEM		Scanning electron microscopy
SEP200		Siderite enriched phase, 100-200 µm fraction
TG		Thermogravimetry, thermogravimetric
TGA		Thermogravimetric analysis
vol		Volume
wt.		Weight
XRD		X-ray diffraction

2.1 Introduction

Siderite minerals, containing varying amounts of $FeCO_3$, are used as raw materials in the metallurgic industry. For pig iron and steel production, it is beneficial to increase the iron content by thermal decomposition, often referred to as calcination. If calcination is performed in oxidizing atmosphere (=roasting, sintering, Eq. 1a), hematite Fe_2O_3 is the main product [1,2]. In nitrogen atmosphere, however, wuestite FeO and magnetite Fe_3O_4 are produced [1] according to Eq. 2a. The stability of wuestite possibly arises from magnesium and manganese substitutions often found in natural siderite minerals [1,3]. Thermal decomposition in nitrogen atmosphere provides two economic and environmental advantages over roasting in oxidizing atmosphere: Firstly, the specific iron content of the product is increased because of FeO formation. Secondly, less reducing agent is needed when magnetite or wuestite are processed compared to hematite, as exemplarily shown for reduction with H_2 in equations 1b and 2b.

$$FeCO_3 + 0.5O_2 \xrightarrow{Q,air} 0.5Fe_2O_3 + CO_2 \quad (1a)$$

$$0.5\ Fe_2O_3 + 1.5\ H_2 \rightarrow Fe + 1.5\ H_2O \quad (1b)$$

$$FeCO_3 \xrightarrow{Q,\ N_2} FeO_{1+x} + (1-x)CO_2 + x\ CO, \quad \max(x) = 0.33 \quad (2a)$$

$$FeO_{1+x} + (1+x)H_2 \rightarrow Fe + (1+x)H_2O \quad (2b)$$

A review of the thermodynamic properties and the general decomposition behavior of iron carbonate can be found in [4]. Decomposition pathways in oxidizing atmosphere have been investigated with Xinjiang siderite ore by thermogravimetric analysis (TGA), X-ray diffraction (XRD), and titration [5]. Mg-Mn-siderite with a composition of $(Fe_{0.30\text{-}0.95}Mg_xMn_y)CO_3$ was investigated using differential scanning calorimetry (DSC) and it was shown that the decomposition temperature decreases with increasing iron amount [6]. DSC was used to determine the enthalpy of decomposition of mineral siderite and ankerite $(Ca_a,Fe_b,Mg_c,Mn_d)(CO_3)_y$ in nitrogen and air [7.8]. The decomposition properties of mineral siderites found in tertiary Australian oil shales in retorting atmosphere were analyzed with TGA [9]. The temperature dependent ferromagnetic properties of products from mineral siderite decomposition has been reported in [10}.

The decomposition kinetics of different mineral siderites in air was investigated for isothermal [2] and non-isothermal conditions [2,11,12]. The kinetics of direct conversion of mineral carbonate with hydrogen into iron has recently been published [13]. Gotor et al. [14] applied a combinatorial thermogravimetry/constant rate thermal analysis (TG/CRTA) at a single heating rate of 0.52 °C min^{-1} (TG) and decomposition rate of $3*10^{-3}$ min^{-1} (CRTA) to elucidate the kinetics of the decomposition of synthetic $FeCO_3$ and natural Spanish siderite under vacuum conditions. The decomposition kinetics of mineral siderite for continuous nitrogen flow at ambient pressure has only been scarcely studied [15-18]. None of the studies [15-18] applied the recommendations of the International Confederation for Thermal Analysis and Calorimetry

(ICTAC) Kinetics Committee for collecting experimental data for kinetic computations [19,20], and the results are therefore not based on a solid foundation. The results reported in [16,17] can hardly be checked and validated, as they are available in Chinese language only.

In this paper the decomposition kinetics of mineral Mg-Mn-siderite in nitrogen atmosphere, determined with two complementary methods is reported. The first method is based on the isoconversional methodology [21]. The Friedman [22] and Kissinger-Akahira-Sunose [23 methods were used for the determination of the activation energy. Master plots [24] together with Málek's method [25] were used to evaluate the reaction model and the pre-exponential factor. The second method based on multi-variate nonlinear regression (MVNR) was proposed by Opfermann [26]. It is implemented in the software Netzsch Thermokinetics 3.1. Calculations were based on four experimental TGA data sets under constant heating rate conditions (0.8, 1.8, 5, 10 °C min^{-1}). A fifth data set (3 °C min^{-1}) was used to check the predictability achievable with the respective solution of the two calculation methods (MVNR, isoconversional) applied. Additionally, two different materials are compared: (1) the original iron carbonate bearing mineral; (2) a siderite enriched phase produced from the original mineral. Mineral reactants and products were comprehensively characterized, applying X-ray diffraction analysis (XRD), scanning electron microscopy coupled with energy-dispersive X-ray spectrometry (SEM/EDXS), inductively coupled plasma-optical emission spectroscopy (ICP-OES), and thermogravimetric analysis (TGA).

2.2 Materials and methods

2.2.1 Equipment and chemicals

A Netzsch Jupiter STA 449C thermobalance and alumina sample pans were used in all thermogravimetry (TG) experiments. Nitrogen was supplied by Air Liquide in 99.999 % quality. XRD spectra were recorded on an X'Pert Pro diffractometer manufactured by Panalytical (Co-Kα at 0.178901 nm) and analyzed with the HighScore Plus software using the Inorganic Crystal Structure Database. The semi-quantitative analysis of the XRD patterns was conducted using the reference intensity ratio (RIR). Elemental analysis of the solid mineral samples was performed by means of ICP-OES (Spectro Acros by Spectro Ametek) after dissolution of 200 mg of the solid samples in a 3:1 (vol) mixture of concentrated hydrochloric acid (C. Roth, p.a.) and concentrated nitric acid (J.T. Baker, p.a.). Images were taken with an acceleration voltage of 15kV at an Ultra 55 scanning electron microscope from ZEISS equipped with an Octane Silicon Drift Detector (SDD) for energy dispersive X-ray spectrometry (EDXS) from EDAX. The High Definition Angle selective Backscatter electron (HDAsB®) detector was used to distinguish between mineral phases.

The iron carbonate mineral (Erzberg, Austria) was supplied by VA Erzberg GmbH, grinded and sieved to 100-200 µm. This material will be referred to as ICM200 (**i**ron **c**arbonate **m**ineral, 100-**200** µm). To minimize the influence of the presence of ankerite and dolomite $(Ca,Mg)(CO_3)_2$ on

the kinetic analysis, a siderite enriched sample was prepared at the Institute of Mineral Processing (Montanuniversitaet Leoben, Austria). This material will be referred to as SEP200 (**s**iderite **e**nriched **p**hase, 100-200 µm). The preparation procedure consisted of grinding of ICM200, separation of the 100-200 µm fraction, sorting by density, and electromagnetic separation in the isodynamic field.

TG measurements described in section 3.2 were conducted with a sample mass of 2.00 ± 0.10 g and a TG sample holder at a linear heating rate of 3 °C min^{-1}. TG measurements for the preparation of the datasets suitable for kinetic analyses were conducted with a sample mass of 20 ± 2 mg. The total gas flow rate in all experiments was set to 100 cm^3 min^{-1}. The linear non-isothermal TG measurements for the computation of kinetic parameters were conducted in accordance with the recommendations of the ICTAC Kinetics Committee [19,20]. Four different linear heating rates were used: 0.8, 1.8, 5, and 10 °C min^{-1}. A temperature calibration with indium, tin, bismuth, zinc, and aluminum reference materials was executed before the experimental series was started. A blank measurement was recorded every time the experimental conditions were changed. Experimental runs were replicated. Conversion α was calculated from the mass loss. Kinetic calculations were based on the mean, blank value corrected data sets.

2.2.2 Theoretical background

All kinetic computations were performed on the experimental data sets recorded for the decomposition of the Mg-Mn-siderite $[Fe_{0.873}Mg_{0.073}Mn_{0.054}]CO_3$ present in ICM200 and SEP200. This was achieved by limiting the evaluated temperature range to 380-550 °C, as ankerite and dolomite decompose at temperatures beyond 550 °C (see Figure 2-1 and Figure 2-3). The aim of the kinetic analysis was to find a suitable approach for the rate law depicted in Eq. 3.

$$\frac{d\alpha}{dt} = \beta * \frac{d\alpha}{dT} = k(T) * f(\alpha) = A * e^{\frac{-E_a}{R_{gas}T}} * f(\alpha) \quad (3)$$

2.2.2.1 Isoconversional method for the determination of the kinetic triplet

The integral Kissinger-Akahira-Sunose [23] (KAS, Eq. 4) and the differential Friedman method [24] (Eq. 5) were used to calculate the run of the isoconversional activation energy E_α with increasing conversion.

$$\ln\left[\frac{\beta_i}{T_{\alpha,i}^2}\right] = const - \frac{E_\alpha}{R_{gas}T_{\alpha,i}} \quad (4)$$

$$\ln\left[\frac{d\alpha}{dt}\right]_{\alpha,i} = \ln(f(\alpha)A_\alpha) - \frac{E_\alpha}{R_{gas}T_{\alpha,i}} \quad (5)$$

The master plot functions y(α) and z(α) [24,25] were calculated according to Eq. 6 and 7. As the exponential term on the right hand side in Eq. 7 does not change the shape and maximum of the

curve, it can be neglected [27] and z(α) can be approximated by the product of the derivative and T_α^2. All master plots were normalized to a (0, 1) interval.

$$y(\alpha) = \left(\frac{d\alpha}{dt}\right)_\alpha * \exp\left(\frac{E_{iso}}{R_{gas}T_\alpha}\right) = Af(\alpha) \quad (6)$$

$$z(\alpha) = f(\alpha)g(\alpha) = \left(\frac{d\alpha}{dt}\right)_\alpha T_\alpha^2 * \exp\left(\frac{\pi\left(\frac{E_{iso}}{R_{gas}T_\alpha}\right)}{\beta T_\alpha}\right) \approx \left(\frac{d\alpha}{dt}\right)_\alpha T_\alpha^2 \quad (7)$$

The extended Prout-Tompkins model, alternatively called (truncated) Sestak-Bergren model, Bna (see Eq. 8) includes two model parameters: the reaction order n, and the model parameter m. It was shown [24] that physically meaningful values of m should be within zero and one.

$$\text{Bna: } f(\alpha) = \alpha^m(1-\alpha)^n \quad (8)$$

The parameters n and m for the Bna model can be calculated from the maximum of the y(α) curve α_M with Eq. 9. Eq. 10 was applied to calculate n, whereas the linearity of Eq. 10 only holds in the α-interval (0.20, 0.80). Eq. 10 can also be used to determine the pre-exponential factor [25]. Alternatively, the pre-exponential factor can be calculated with Eq. 11, whereas T_{max} is the temperature and α_{max} is the conversion at the maximum of the derivative of conversion with respect to temperature dα/dT [21]. Pre-exponential factors calculated with Eq. 10 will be referred to as A_{reg}, pre-exponential factors calculated with Eq. 11 will be referred to as A_{der}.

$$p = \frac{m}{n} = \frac{\alpha_M}{1-\alpha_M} \quad (9)$$

$$\ln\left[\frac{d\alpha}{dt}\exp\left(\frac{E_{iso}}{R_{gas}T_\alpha}\right)\right] = \ln A_{reg} + n * \ln\left(\alpha^p(1-\alpha)\right) \text{ for: } 0.20 \le \alpha \le 0.80 \quad (10)$$

$$A_{der} = \frac{-\beta * E_{iso}}{R_{gas}T_{max}^2 * \frac{df}{d\alpha}(\alpha_{max})} * \exp\left(\frac{E}{RT_{max}}\right) \quad (11)$$

2.2.2.2 Multivariate non-linear regression (MVNR) method for the determination of the kinetic triplet

The MVNR method proposed by Opfermann [26], and implemented in Thermokinetics 3.1, was applied for the determination of the kinetic triplet. Sixteen different reaction models, commonly applied to solid state kinetics, were considered (see section 3.2.2, Table 3-1). For the statistical analysis and comparison of the goodness of fit of reaction models, the regression coefficient R (Eq. 12) and the F-test (Eq. 13) were computed.

$$R = \sqrt{1 - \frac{\sum_{i=1}^{h}\sum_{j=1}^{v}\left(y_{ij} - y_{calc,ij}\right)^2}{\sum_{i=1}^{h}\left(\sum_{j=1}^{v} y_{ij}^2 - \frac{\left(\sum_{j=1}^{v} y_{ij}\right)^2}{v}\right)}} \quad (12)$$

$$F(d_A, d_B) = \frac{\sum_{i=1}^{h}\sum_{j=1}^{v} d_A^{-1}(y_{ij} - y_{calc,ij}(model\ A))^2}{\sum_{i=1}^{h}\sum_{j=1}^{v} d_B^{-1}(y_{ij} - y_{calc,ij}(model\ B))^2} \quad (13)$$

2.3 Results and discussion

2.3.1 Thermodynamic stability of reaction products

The temperature dependency of the standard Gibbs reaction energy $\Delta_R G°$ for relevant reactions is depicted in Figure 2-1. At isothermal conditions $\Delta_R G°$ decreases in the order: $CaCO_3$ > $MgCO_3$ > $MnCO_3$ > $FeCO_3$. The formation of FeO and Fe_3O_4 is favored over the formation of Fe_2O_3 during decomposition of iron carbonate in nitrogen. Therefore, the maximum formal oxygen content of the iron oxide on the right-hand-side of Eq.2a is 1.33.

2.3.2 Characterization of the feed mineral samples

The main element found in ICM200 is, as expected, iron at a level of 33.5 %wt. Furthermore, calcium, magnesium, and manganese are present as carbonate forming elements (see Table 2-1). Qualitative and semi-quantitative analysis of the XRD pattern (Fig. 2 and Tab. 2) revealed that iron is present in the form of siderite $FeCO_3$ and ankerite, a mixed carbonate of the elements calcium, iron, magnesium and manganese $(Ca_a,Fe_b,Mg_c,Mn_d)(CO_3)_y$. Calcium and magnesium are also present in the form of dolomite $(Ca,Mg)(CO_3)_2$. Silicon is present in the form of quartz SiO_2. Aluminum and the remaining silicon are present as the potassium aluminosilicate muscovite $KAl_2(AlSi_3O_{10})(OH)_2$. The XRD pattern (Figure 2-2) and semi-quantitative analysis are based on the reference intensity ratio (RIR) (see Table 2–2) of SEP200. They confirm the enrichment of siderite and the separation of other phases present.

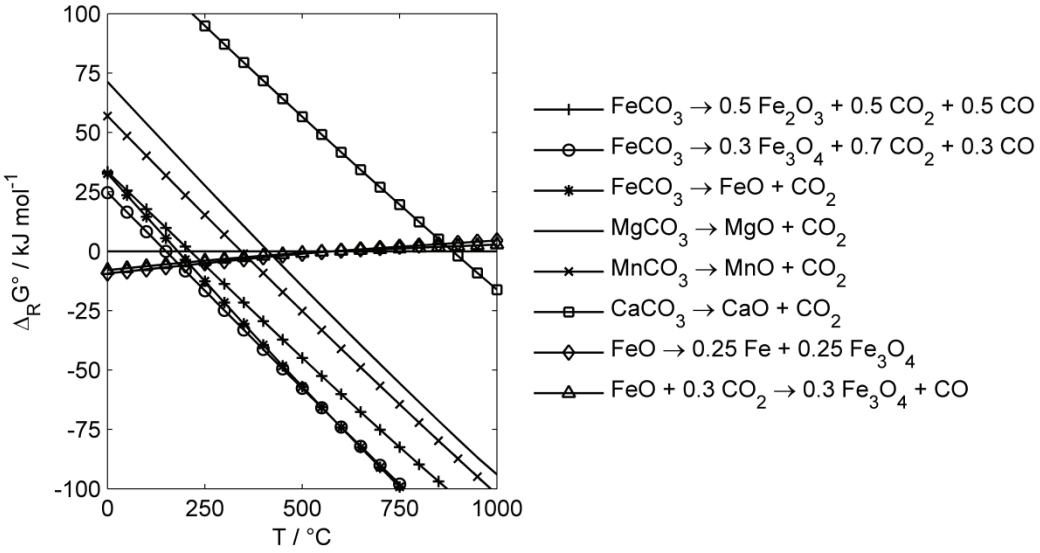

Figure 2-1: Standard Gibbs free reaction energy $\Delta_R G°$ at 1.013 bar total pressure [28].

Table 2-1: Elemental composition of the mineral samples determined by ICP-OES. The metal to iron ratio M:Fe was calculated on a molar basis (m.b.).

	ICM200		SEP200	
	%wt.	M:Fe, m.b.	%wt.	M:Fe, m.b.
Fe	33.5	1.00	39.9	1.00
Ca	4.1	0.17	0.9	0.03
Mg	2.4	0.16	2.0	0.12
Mn	2.0	0.06	2.4	0.06
Si	2.5	0.15	1.0	0.05
Al	0.3	0.02	0.4	0.02

As can be seen in Table 2-1, the metal to iron ratio M:Fe (calculated on a molar basis) decreases for calcium and magnesium from ICM200 to SEP200, but remains constant for manganese. According to the XRD results (Table 2–2), only traces of ankerite are present in SEP200. Under the assumption that magnesium and calcium are present as dolomite, the remaining magnesium and manganese most possibly substitute iron in the siderite lattice. Thus, the mineral enriched in SEP200 could be considered as a Mg-Mn-siderite with the nominal chemical composition $[Fe_{0.873}Mg_{0.073}Mn_{0.054}]CO_3$. This composition is in good agreement with the semi-quantitative result of the XRD analysis calculated from the RIR (Table 2–2 for comparison).

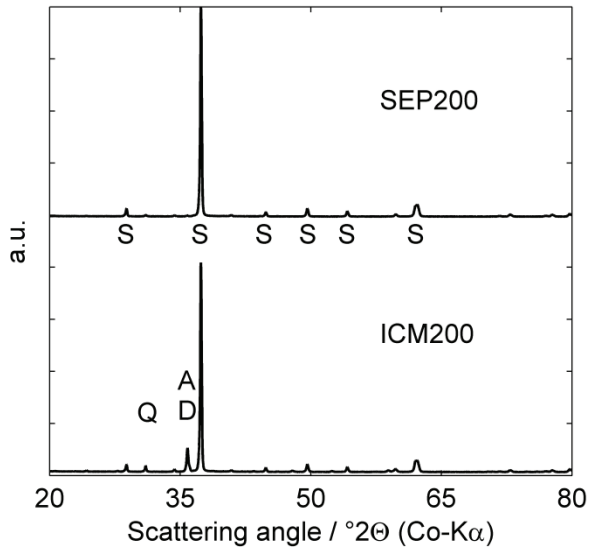

Figure 2-2: XRD of ICM200 and the 100-200 µm, SEP200. Compounds marked (position of marker symbol in the abscissa direction is valid for all spectra): siderite S, quartz Q, ankerite A, dolomite D. The signal at approximately 37 ° is characteristic for dolomite and ankerite and decreases substantially, confirming the enrichment of the siderite phase in SEP200.

Table 2-2: Phases detected (column 1) and semi-quantitative analysis (columns 2 and 3) using the reference intensity ratio of the XRD signal. The data in column 4 were calculated from the elemental analysis with ICP-OES of SEP200 and a siderite composition of $[Fe_{0.873}Mg_{0.073}Mn_{0.054}]CO_3$.

Compound	ICM200 %wt.^{RIR}	SEP200 %wt.^{RIR}	SEP200 %wt.^{ICP}
Siderite	66	94	93
Dolomite	20	3	4
Ankerite	10	1	0
Quartz	3	1	2
Muscovite	1	1	2

2.3.3 Characterization of the solid reaction products

The general decomposition behavior of ICM200 and SEP200 in inert nitrogen atmosphere was investigated by recording a TG curve at a heating rate of 3 °C min^{-1} (see Figure 2-3). The TG-curve of SEP200 shows a distinct single step due to the decomposition of siderite, followed by a negligible mass loss due to the decomposition of traces of dolomite. The TG-curve of ICM200 shows three consecutive steps of decomposition due to the different carbonates present in the sample. The ratio of the three consecutive mass loss steps amounts to 1:0.09:0.17. Up to approximately 500 °C the TG-curves for SEP200 and ICM200 overlap and the inflection point for the first mass loss of both materials is in the same range. Consequently, the first mass loss for both materials can be attributed to the decomposition of the Mg-Mn-siderite present. The second and the third mass loss for ICM200 partially overlap and can be attributed to the decomposition of ankerite and dolomite.

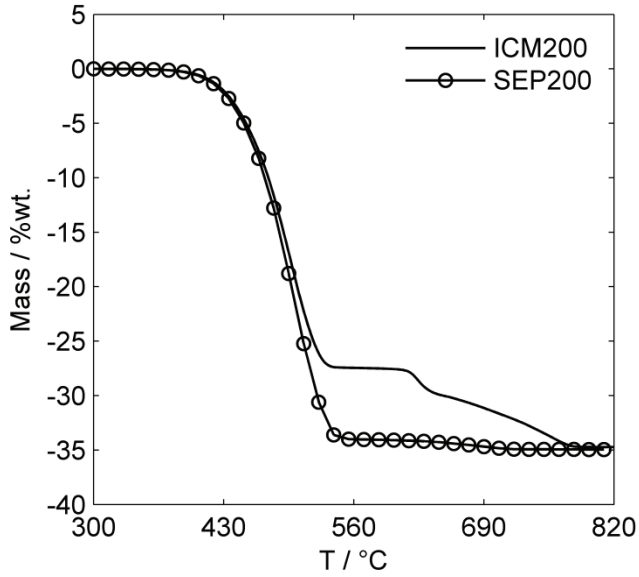

Figure 2-3: TG-curve of ICM200 and SEP200 in 100 %vol. nitrogen atmosphere. Sample mass = 2.00 ± 0.10 g, heating rate 3 °C min^{-1}, 100 cm^{3}min^{-1} N_2 flow, and atmospheric pressure.

Table 2-3: Elemental composition of the products of the decomposition of ICM200 and SEP200 in nitrogen determined via ICP-OES.

	ICM200, N_2 %wt.	SEP200, N_2 %wt.
Fe	52.6	62.2
Ca	6.15	1.62
Mg	3.72	3.13
Mn	3.23	3.60
Si	3.65	1.87
Al	0.76	0.65

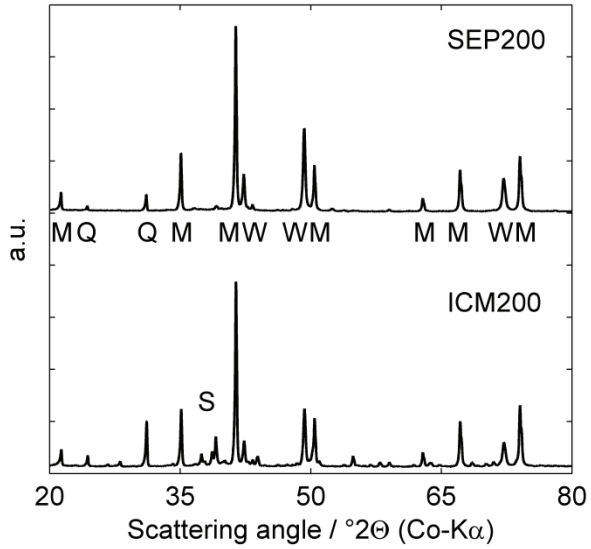

Figure 2-4: XRD pattern of products of the decomposition of ICM200 and SEP200 in nitrogen. Compounds marked (position of marker symbol in the abscissa direction is valid for all spectra): Magnetite Fe_3O_4: M, quartz SiO_2: Q, wuestite FeO: W, srebrodolskite $Ca_2Fe_2O_5$: B.

The metal content of ICM200 and SEP200 increases after decomposition (see Table 2-3). The major products of the decomposition of ICM200 and SEP200 in nitrogen according to the XRD analysis (see Figure 2-4) refer to magnetite Fe_3O_4 and wuestite FeO. As expected from the thermodynamic calculations (see Figure 2-1) hematite was not formed. The mass based ratio of FeO:Fe_3O_4 calculated from the RIR equals 0.64 for the decomposition product of SEP200 and 0.76 for the decomposition product of ICM200. There are no XRD signals for elemental iron. Consequently, the formation of magnetite cannot be explained by the decomposition of wuestite according to Eq. 14.

$$4\ FeO \rightarrow Fe + Fe_3O_4 \qquad (14)$$

A comparison of the XRD pattern of the products of the thermal decomposition of ICM200 and SEP200 (Figure 2-4) shows that a mixed calcium iron oxide with the diffraction pattern of srebrodoloskite $Ca_2Fe_2O_5$ is only present when ICM200 is decomposed. Ankerite is present in ICM200 but only in traces in SEP200.

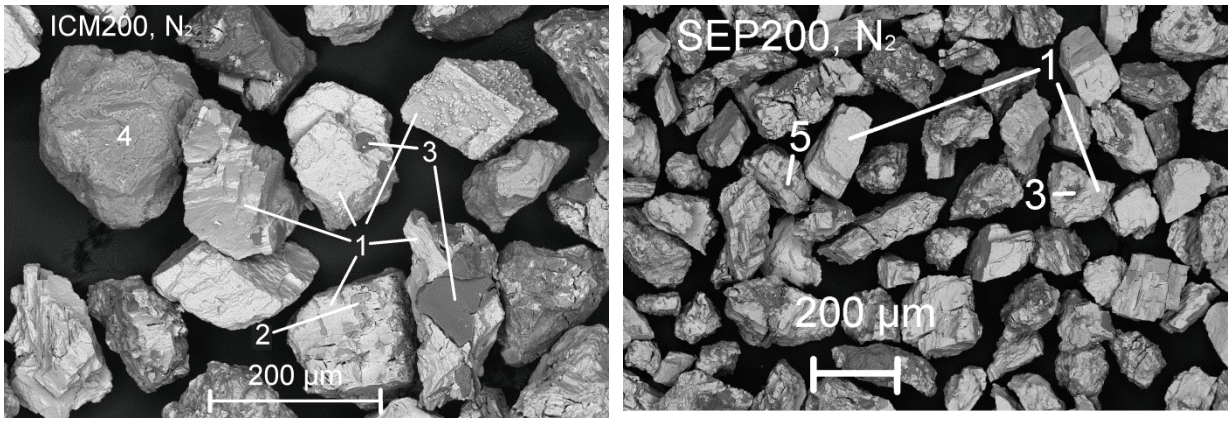

Figure 2-5: Scanning electron micrographs of the product of decomposition of ICM200 (left) and SEP200 (right) in N_2 atmosphere. The use of the HDAsB® detector allows identification of mineral phases by the brightness of the material in the micrograph. Positions where an EDXS spectrum was recorded are marked with numbers 1-5. 1: Fe, Mn, Mg, O (Mg-Mn substituted wuestite and magnetite) - 2: Ca, Fe, Mn, Mg, O (Mg-Mn substituted srebrodoloskite) – 3: Si, O (quartz) – 4: Ca, Mg, O (dolomite) – 5: K, Si, Al, Mg, O (muscovite). Samples demonstrate an irregular size and compound distribution.

Therefore, it is assumed that this mixed calcium iron oxide is the product of the thermal decomposition of ankerite. The elemental analysis (see Table 2-3) reveals that magnesium and manganese are present in the products of the thermal decomposition of ICM200 and SEP200. There are no significant signals for oxides of these elements in the XRD spectrum. A SEM/EDXS study evidences that magnesium and manganese are found together with the iron oxide phases (see Figure 2-5). It has been reported that manganese and magnesium can be incorporated into the lattice of iron oxides and stabilize iron(II)oxides [1,14]. Therefore, it is concluded that magnesium and manganese are also incorporated into the magnetite, wuestite, and srebrodoloskite phases of the investigated samples. This assumption is supported by the determination of the mixed composition of siderite $[Fe_{0.873}Mg_{0.073}Mn_{0.054}]CO_3$ and ankerite $(Ca_a,Fe_b,Mg_c,Mn_d)(CO_3)_y$ given in section 2.3.2.

2.3.4 Kinetics of the decomposition of Mg-Mn-siderite in nitrogen

Iron carbonate can form bivalent FeO and mixed bi-, trivalent Fe_3O_4, and trivalent Fe_2O_3 via oxidation with CO_2 during thermal decomposition (see Eq. 15) [29]. As evidenced by the XRD analysis of the decomposition product, Fe_2O_3 is neither formed from SEP200 nor from ICM200. Thus, only formation of FeO and Fe_3O_4 will be considered in the following discussion. Magnesium and manganese carbonate are not expected to form mixed bi-, trivalent or trivalent oxides during thermal decomposition. Therefore, the decomposition of Mg-Mn-siderite can be formally treated with the reaction model shown in Eq. 15. The stoichiometric parameter γ can range from 5/3 (only Fe_3O_4 is formed) to 2 (only FeO is formed) so that all combinations of FeO:Fe_3O_4 can be considered by adjusting the parameter γ. The weight ratio wr of FeO:Fe_3O_4 can be calculated by considering the validity of equation 16 and applying equation 17.

$$[FeCO_3]_a * [MgCO_3]_b * [MnCO_3]_c \rightarrow [FeO_{3-\gamma}]_a * [MgO]_b * [MnO]_c + (b + c + \gamma - 1)CO_2 + (2 - \gamma)CO \qquad (15)$$

$$FeO_{3-\gamma} = \rho FeO + \frac{\tau}{3} Fe_3O_4 \quad (16)$$

$$wr = \frac{\rho}{\frac{\tau}{3}} * \frac{MW(FeO)}{MW(Fe_3O_4)} = \frac{3\gamma-5}{2-\gamma} * \frac{MW(FeO)}{MW(Fe_3O_4)} \quad (17)$$

The relative mass loss for complete conversion of the Mg-Mn-siderite present in SEP200 can be calculated from the elemental composition determined by ICP-OES and applying Eq. 18, whereas the corrected mass fraction of magnesium $w_{Mg,Sid}$ was calculated with Eq. 19 assuming that all of the calcium is present as dolomite $CaMg(CO_3)_2$.

$$\Delta m_{max,rel} = \gamma * w_{Fe} \frac{AW(O)}{AW(Fe)} + w_{Fe} \frac{AW(C)}{AW(Fe)} + w_{Mg,Sid} \frac{MW(CO_2)}{AW(Mg)} + w_{Mn} \frac{MW(CO_2)}{AW(Mn)} \quad (18)$$

$$w_{Mg,Sid} = w_{Mg} - w_{Ca} * \frac{AW(Mg)}{AW(Ca)} \quad (19)$$

These equations allow for the calculation of the weight ratio wr_{TG} of $FeO:Fe_3O_4$ from the experimental mass loss results encountered in the thermogravimetric experiments. The results are compared with wr_{RIR} calculated from the XRD analysis with the RIR. The weight loss for the decomposition of Mg-Mn-siderite amounts to -34.0 wt.% in the case of SEP200 (see Figure 2-3). A mass loss of -34.0 wt.% correlates to wr_{TG} = 0.845 and a nominal composition of the iron species of $0.48FeO*0.17Fe_3O_4$. The value calculated from the RIR is consistent with this result, as w_{RIR} amounts to 0.64 corresponding to $0.40FeO*0.20Fe_3O_4$. For the four data sets used in the kinetic analysis the mean mass loss for the decomposition of Mg-Mn-siderite of SEP200 amounts to -34.6 ± 0.5 wt.%. As the molecular formula for ankerite present in ICM200 is known to vary [30], the calculations according to Eq. 18 and 19 cannot be applied to this material. Nevertheless, it can be assumed that the same reaction scheme (see Eq. 15) can be applied to the Mg-Mn-siderite present in ICM200 as for SEP200.

2.3.4.1 Isoconversional activation energy

For SEP200 decomposition the activation energy calculated with the Friedman approach $E_{\alpha,F}$ is nearly constant. The activation energy calculated with the KAS approach $E_{\alpha,KAS}$ slightly decreases (see Figure 2-6). In the case of ICM200, $E_{\alpha,KAS}$ decreases up to a conversion of approximately 0.8 and shows a minor increase thereafter (see Figure 2-6). $E_{\alpha,F}$ also decreases with increasing conversion, but shows a minimum at $\alpha \sim 0.65$. None of the E_α vs.α curves for ICM200 is strictly linear, but neither shows a pronounced shoulder nor peak.

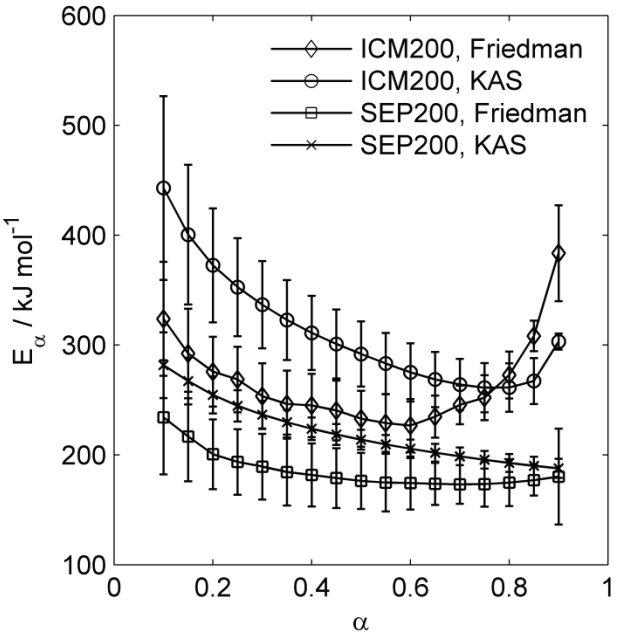

Figure 2-6: Friedman activation energy and KAS activation energy, calculated with Thermokinetics 3.1.

The mean value of the activation energy (see Table 2-4) calculated from the Friedman data $E_{m,F}$ accounts for 252 ± 20 kJ mol^{-1} for ICM200 and 182 ± 8 kJ mol^{-1} for SEP200. The mean value of the activation energy calculated from the KAS data $E_{m,KAS}$ accounts for 303 ± 40 kJ mol^{-1} for ICM200 and 218 ± 21 kJ mol^{-1} for SEP200 (see Table 2-4). Although only the decomposition of Mg-Mn-siderite present in both materials was considered in the evaluation of the isoconversional activation energy, the values calculated for the SEP200 are noticeably lower than for ICM200. This difference of approximately 70-80 kJ mol^{-1} seems to be systematic, and could therefore be contributed to compositional and physico-geometric difference in the two samples. The size range of both materials was fixed by sieving to the 100-200 µm fraction, hence differences in size of the reacting particles should cancel out on average. Nevertheless, at this size range the mineral phases are not completely separated into individual particles but several mineral phases can be present in one particle (see micrograph shown in Figure 2-5). An average particle of ICM200 can statistically contain more mineral phases and, thus, phase boundaries and specific surface area for each mineral phase, than an average particle of SEP200 due to the higher amount of accompanying minerals. As in heterogeneous solid-solid reaction the reaction interface plays a major role [21], this could be an explanation for the increase of the mean activation energy for the decomposition of the Mg-Mn-siderite and the variation of E_α with α. Although the evaluated temperature range was limited to 550 °C, the decomposition onset of trace amounts of dolomite present in SEP200 could lead to the slight non-linearity of E_α. Another explanation could be the formation of two solid products from Mg-Mn-siderite: Mg-Mn substituted wuestite and Mg-Mn substituted magnetite.

Table 2-4: Overview of activation energies used to describe the decomposition of Mn-Mg siderite present in ICM200 and SEP200. For the Friedman and KAS approaches the activation energy was calculated as the mean value in the interval 0.15 < α < 0.90; MVNR … multivariate non-linear regression.

	Activation energy kJ mol^{-1}
ICM200, Friedman	252 ± 20
ICM200, KAS	303 ± 40
ICM200, MVNR	301
SEP200, Friedman	182 ± 8
SEP200, KAS	218 ± 21
SEP200, MVNR	210

The non-linearity of the run of E_α with α is more pronounced for ICM200, which arises from the higher amount and number of accompanying mineral carbonates (dolomite and ankerite) present. Nevertheless, as $E_{\alpha,F}$ is relatively linear for SEP200, it is assumed that single step kinetics can be applied to the decomposition of Mg-Mn-siderite in both materials.

2.3.4.2 *Determination of the kinetic triplet via an isoconversional method*

In order to prepare the master plots y(α) (Eq. 6) and z(α) (Eq. 7) a constant value for the activation energy E_{iso} (also referred to as apparent activation energy) is needed as an input parameter. Therefore, the average values of the activation energy determined by the Friedman and the KAS approach in the interval 0.15 < α < 0.90 (see Table 2-4) were employed as E_{iso}.

All y(α) curves for SEP200 (Figure 2-7 and Figure 2-8) show a maximum of y(α) α_M (see Table 2-5) between 0.15 and 0.26 for E_{iso}=181 kJ mol^{-1} (mean of $E_{\alpha,F}$) and 0.11-0.23 for E_{iso}=218 kJ mol^{-1} (mean of $E_{\alpha,KAS}$). The maxima of the z(α) curve α_P vary between 0.54 and 0.64 independent of the value of E_{iso}. The shape and maxima of the y(α) curve, on the contrary, vary with the value of E_{iso} (see Eq. 7). An increase of E_{iso} from 181 kJ mol^{-1} to 218 kJ mol^{-1} leads to a shift of α_M to lower values for the same heating rate dataset. The y(α) curves for SEP200 do not show a change of shape depending on the heating rate dataset used. However, α_M decreases with increasing heating rate. This phenomenon can most possibly be attributed to the use of the apparent activation energy, as increased E_{iso} values lead to a more pronounced decrease of α_M with increasing heating rate.

Table 2-5: Maxima of the y(α) curve αM and of the z(α) curve αP in ascending order of the heating rate data sets used (0.8 – 1.8 – 5 – 10 °C min^{-1})

	E_{iso} / kJ mol^{-1}	α_M	α_P
ICM200	252	0.23-0.23-0.16-0.09	0.51-0.54-0.51-0.56
	303	0.19-0.19-0.08-0.04	0.51-0.54-0.51-0.56
SEP200	181	0.26-0.22-0.19-0.15	0.55-0.54-0.60-0.64
	218	0.23-0.19-0.16-0.11	0.55-0.54-0.60-0.64

The y(α) curves for ICM200 (see Figure 2-9 and Figure 2-10) are comparable to those calculated for SEP200, with respect to shape and peak position. The α_M and α_P values are decreased compared to SEP200. The decrease of α_M with increasing heating rate is more pronounced. Additionally, when the highest E_{iso} value (303 kJ mol^{-1}, mean from KAS method) is used, the shape of the y(α) curves for 5 and 10 °C min^{-1} differs from the y(α) curves calculated for the lower heating rate datasets and could possibly be also described with a reaction order model.

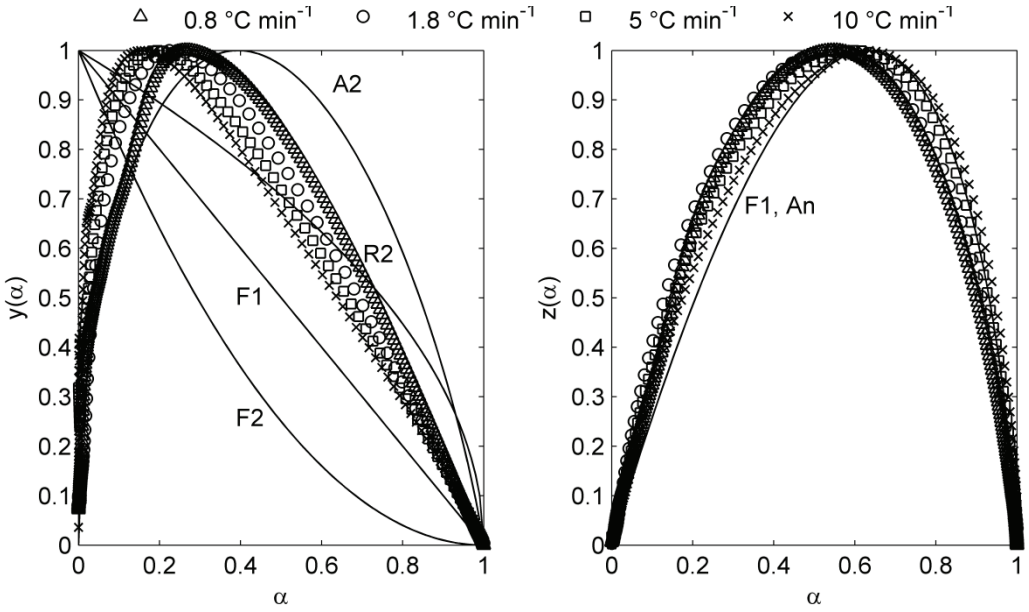

Figure 2-7: Master plots for the decomposition of Mg-Mn-siderite present in SEP200 and E_{iso} = 182 kJ mol^{-1} (determined from the mean value of $E_{\alpha,F}$).

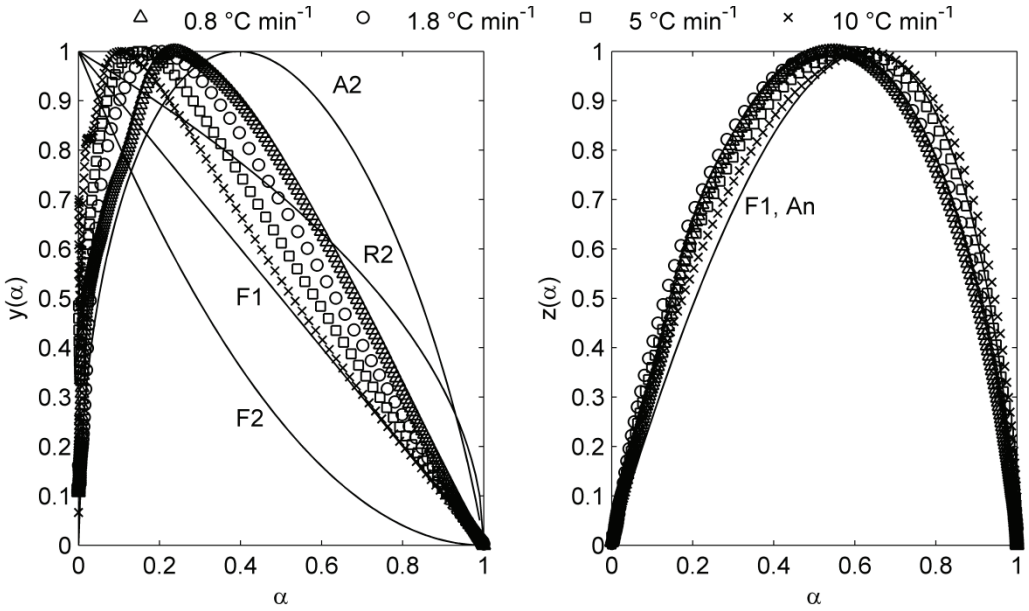

Figure 2-8: Master plots for the decomposition of Mg-Mn-siderite present in SEP200 and E_{iso} = 218 kJ mol^{-1}(determined from the mean value of $E_{\alpha,KAS}$).

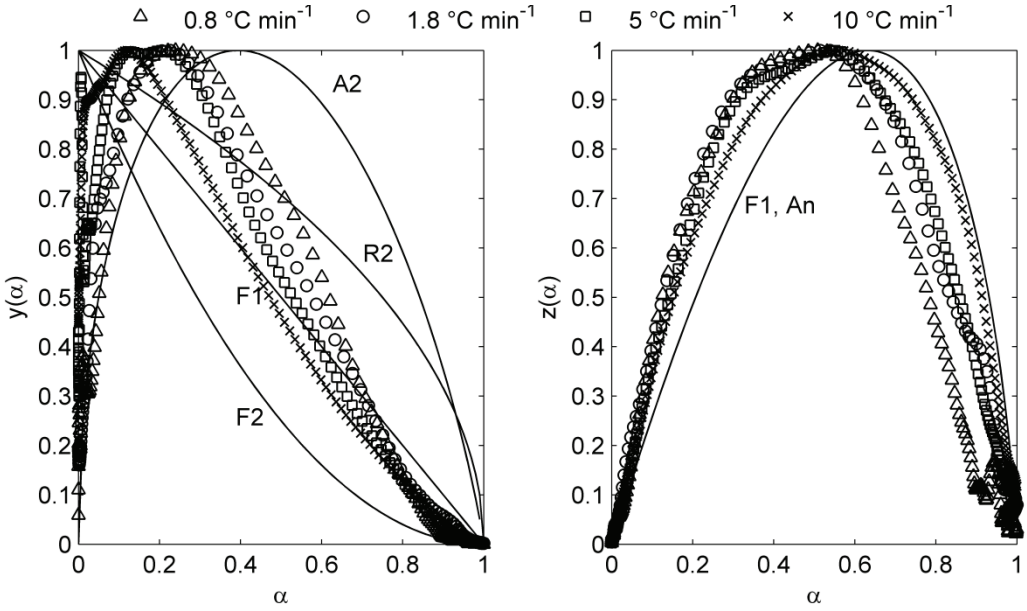

Figure 2-9: Master plots for the decomposition of Mg-Mn-siderite present in ICM200 and Eiso = 252 kJ mol^{-1} (determined from the mean value of $E_{\alpha,F}$).

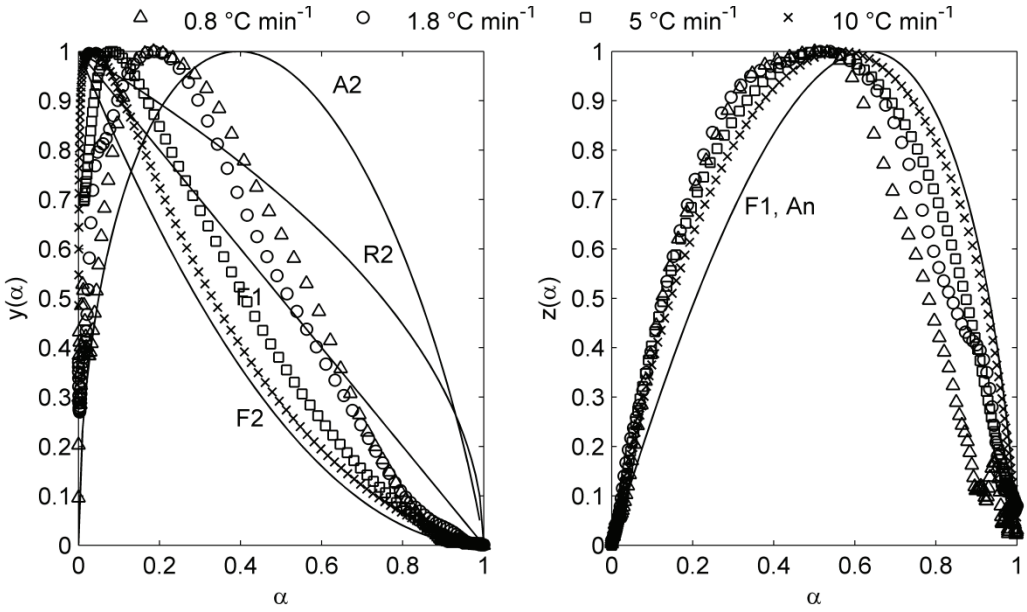

Figure 2-10: Master plots for the decomposition of Mg-Mn-siderite present in ICM200 and Eiso = 303 kJ mol^{-1}(determined from the mean value of $E_{\alpha,KAS}$).

If y(α) has a maximum either Bna or An models should be used [25]. The Bna model seems to be an appropriate selection for both materials due to two findings: (1) α_M is larger than 0 and smaller than α_P; (2) α_P is lower than the theoretical value for An models - α_P(An) = 0.632 (except for the SEP200 dataset at 10 °C min^{-1}). Furthermore, a Bna model with a low value for m can approximate a reaction order model (as for m ~ 0 it follows that: $\alpha^m(1-\alpha)^n \sim (1-\alpha)^n$) and, if expanded by a third parameter c, Pérez-Maqueda et al. could show [31] that the reaction model $f(\alpha)=c(1-\alpha)^n\alpha^m$ can be used to approximate most reaction models.

Table 2-6: Kinetic triplet calculated for the decomposition of Mg-Mn-siderite present in SEP200 with Bna as the reaction model $f(\alpha)=\alpha^m(1-\alpha)^n$.

Dataset	n	m	E_{iso} / kJ mol^{-1}	$\log_{10}(A_{iso})$ / s^{-1}
0.8 °C min^{-1}	1.061	0.389	182 (mean value of $E_{\alpha,F}$)	10.53
1.8 °C min^{-1}	1.056	0.305		10.48
5 °C min^{-1}	1.069	0.259		10.48
10 °C min^{-1}	1.042	0.189		10.42
0.8 °C min^{-1}	1.159	0.344	218 (mean value of $E_{\alpha,KAS}$)	13.21
1.8 °C min^{-1}	1.187	0.275		13.11
5 °C min^{-1}	1.234	0.231		13.05
10 °C min^{-1}	1.219	0.146		12.95

Table 2-7: Kinetic triplet calculated for the decomposition of Mg-Mn-siderite present in ICM200 with Bna as the reaction model $f(\alpha)=\alpha^m(1-\alpha)^n$.

Dataset	n	m	E_{iso} / kJ mol^{-1}	$\log_{10}(A_{iso})$ / s^{-1}
0.8 °C min^{-1}	1.965	0.598	252 (mean value of $E_{\alpha,F}$)	15.87
1.8 °C min^{-1}	1.768	0.519		15.69
5 °C min^{-1}	1.802	0.339		15.73
10 °C min^{-1}	1.586	0.158		15.62
0.8 °C min^{-1}	2.040	0.465	303 (mean value of $E_{\alpha,KAS}$)	19.60
1.8 °C min^{-1}	1.922	0.442		19.38
5 °C min^{-1}	1.894	0.172		19.32
10 °C min^{-1}	1.799	0.065		19.27

The values for n and m where calculated with Eq. 9 and 10 as a function of the apparent activation energy E_{iso} used (see Table 2-6 and Table 2-7). The pre-exponential factor A_{iso} was calculated as the mean value of A_{reg} (Eq. 10) and A_{der} (Eq. 11), as both values did not deviate strongly (see supplementary material for actual values of A_{reg} and A_{der}). Three aspects of the calculation results shown in Table 2-6 toTable 2-8 can now be compared: (a) the influence of activation energy on the model parameters n and m and the pre-exponential factor for each individual heating rate dataset; (b) the variation of the model parameters n and m and the pre-exponential factor for a constant E_{iso} within the four heating rate datasets for each material; (c) differences in the calculations results for SEP200 and ICM200.

With respect to matter (a), an increase of E_{iso} for the same heating rate dataset generally leads to a minor increase of reaction order and notable increase of the pre-exponential factor. The second Bna parameter m, on the contrary, decreases with increasing activation energy for the same heating rate dataset. Regarding matter (b), it was found that reaction order and pre-exponential factor do not vary significantly for a constant E_{iso} and the four heating rate datasets evaluated (see mean values in Table 2-8). This finding is supported by the low standard deviation, e.g. n=1.9 ± 0.1 and $\log_{10}(A_{iso})$ = 19.4 ± 0.2 s^{-1} for ICM200 and E_{iso} = 303 kJ mol^{-1} (see Table 2-8). The model parameter m, on the contrary, has a high relative standard deviation for constant E_{iso} and the four heating rate datasets evaluated, e.g. m=0.3±0.2 for ICM200 and E_{iso}=303 kJ mol^{-1} (see Table 2-8).

Table 2-8: Mean values and relative standard deviation (SD) of the model parameters n and m and of the pre-exponential factor A_{iso} for the results of the isoconversional method. For comparison, the results of the multi-variate nonlinear regression (MVNR) are shown.

	n	SD %	m	SD %	$\log_{10}(A_{iso})$ s^{-1}	SD %
ICM200, E_{iso} = 252 kJ mol^{-1}	1.780	8.7	0.403	48.7	15.73	0.7
ICM200, E_{iso} = 303 kJ mol^{-1}	1.914	5.2	0.286	69.4	19.39	0.8
ICM200, MVNR, E_a=301 kJ mol^{-1}	1.929	-	0.249	-	19.22	-
SEP200, E_{iso} = 182 kJ mol^{-1}	1.057	1.0	0.285	29.4	10.48	0.4
SEP200, E_{iso} = 218 kJ mol^{-1}	1.200	2.8	0.249	33.4	13.08	0.8
SEP200, MVNR, Ea=210 kJ mol^{-1}	1.258	-	0.325	-	12.55	-

(c) According to Table 2-8 the activation energy increased for ICM200 compared to SEP200, and the reaction order and pre-exponential factor increased as well. In the case of SEP200 the reaction order is approximately one, whereas it is approximately two for ICM200.

2.3.4.3 Comparison of the results of the multivariate non-linear regression and the isoconversional method

In 2000 Opfermann presented a MVNR method that evaluates the suitability of various reaction models based on multiple heating rate datasets [26]. The results of this MVNR method can be appraised statistically and the resulting kinetic triplet ranked by the regression coefficient (see Table 2-9 and Table 2-10). The calculations were performed with Thermokinetics 3.1 in the interval α = 0.01-0.99.

Table 2-9: Results of the MVNR for the decomposition of Mg-Mn-siderite present in SEP200. R … regression coefficient, F … F-test value for critical F-value of 1.19.

Model	R	F	E_a kJ mol^{-1}	$\log_{10}(A)$ s^{-1}	Model parameters
Bna	0.993	1.00	210	12.5	n=1.26, m=0.32
CnB	0.993	1.00	210	12.0	n=1.58, $\log_{10}(K_{cat})$=0.74
An	0.992	1.16	208	12.1	n=1.23
C1B	0.990	1.30	208	11.9	$\log_{10}(K_{cat})$=0.13
Fn	0.986	1.67	211	12.3	n=0.70
F1	0.980	2.09	223	13.2	n=1

Table 2-10: Results of the MVNR for the decomposition of Mg-Mn-siderite present in ICM200. R … regression coefficient, F … F-test value for critical F-value of x.

Model	R	F	E_a kJ mol^{-1}	$\log_{10}(A)$ s^{-1}	Model parameters
Bna	0.994	1.00	301	19.2	n=1.93, m=0.25
CnB	0.994	1.00	300	18.7	n=2.22, $\log_{10}(K_{cat})$=0.55
Fn	0.993	1.22	307	19.4	n=1.57
F2	0.990	1.53	336	21.6	n=2
An	0.989	1.74	294	18.3	n=0.85
F1	0.986	2.05	275	16.9	n=1

For both materials, the reaction models with two model parameters (Bna and n^{th}-order autocatalysis by product CnB) give the highest correlation coefficient and a similar fit result (the F-test does not show a significant difference between the models). Avrami-Erofeev An and reaction order Fn models also yield acceptable regression coefficients, but the fit quality is decreased compared to Bna and CnB. This finding is in accordance with the discussion of the form and peak position of the master plots (see Figure 2-7 to Figure 2-10). Furthermore, the value of the model parameters n and m of the Bna model are comparable for the mean value of the results of the isoconversional method based on $E_{\alpha,KAS}$ and the MVNR method (see Table 2-8) whereas the results based on $E_{\alpha,F}$ are systematically lower than results from the MVNR method. The increase of activation energy of 70-100 kJ mol^{-1} and the increase of the reaction order from approximately one to two was encountered independent of the calculation method (MVNR vs. isoconversional).

2.3.4.4 Validation of the calculation results and prediction of a dataset not included in the calculations (β = 3 °C min^{-1})

Figure 2-11a shows that for SEP200 and the datasets at 0.8 and 1.8 °C min^{-1} the results of the isoconversional method produce a poor prediction of the experimental curve when the mean value of $E_{\alpha,F}$ (182 kJ mol^{-1}) is used as the apparent activation energy E_{iso}. At 5 °C min^{-1} and 10 °C min^{-1} the model prediction based on $E_{\alpha,F}$ is acceptable. An increase of E_{iso} to the value of $E_{\alpha,KAS}$ (218 kJ mol^{-1}) leads to an improved agreement between experiment and computed kinetic triplet, whereas there is still a notable deviation for the data set at 1.8 °C min^{-1} (see Figure 2-11b). As can be seen in Fig. 11c, the MVNR method produces the best match of experimental curve and model prediction. In Figure 2-11a and Figure 2-11b the model parameters n and m determined for the individual heating rate data set were used (see Table 2-6). In the case of ICM200, however, the isoconversional method with Bna as the reaction model and the individual parameters n and m (see Table 2-7) results in good accordance of the experimental and calculated curve, independent of the apparent activation energy used (see Figure 2-12). The result of the MVNR method also produces a fair agreement between experimental and calculated curve, but the match is not as good as for the results of the isoconversional method. To evaluate the predictive capability of the kinetic triplets computed with the two methods, a heating rate dataset recorded at 3 °C min^{-1} was used for both materials (see Figure 2-13 and Figure 2-14). The mean model parameters m and n of the datasets at 0.8, 1.8, 5, and 10 °C min^{-1} were used in the case of the isoconversional method (see Table 2-8). Both approaches, isoconversional and MVNR, are able to predict the dataset at 3 °C min^{-1} (see Figure 2-13 and Figure 2-14), even though the validation showed notable deviations for SEP200 and $E_{iso} = E_{\alpha,F}$. A reason for this could possibly be found in the use of the mean value of m and n, so that deviations cancel out on average. Zakharov and Adonyi [15] reported a second order reaction model F2, an activation energy of 238 kJ mol^{-1}, and a pre-exponential factor A of $3*10^{13}$ s^{-1} for the kinetics of the decomposition of mineral siderite (87 %wt. $FeCO_3$). Feng et al. [18] used model free and multivariate non-linear regression approaches to determine the decomposition kinetics of Wangjiatan siderite of different particle size at 5, 15, 25, and 35 °C min^{-1}. An activation energy of

223 kJ mol^{-1} was determined with the Kissinger and Friedman method and a reaction order of approximately one was found to fit the kinetics best. However, Feng et al. [18] did not use blank-value corrected replicated data sets, nor applied a detailed analysis of the reactants and products. Although neither Zakharov and Adonyi [15] nor Feng et al. [18] adhered to the recommendations of the ICTAC Kinetics Committee [19,20], their results for activation energy and pre-exponential factor are comparable to the results of this study for SEP200. Feng et al. [18] also find a reaction order of one, whereas Zakharov and Adonyi [15] report a reaction order of two. The experimental technique and computation method of Zakharov and Adnoyi [15] is questionable from an current point of view, as only a single heating rate data set assuming nth-order kinetics was evaluated. Gotor et al. [14] demonstrated that kinetic calculations based on just one experimental data set, be it isothermal or non-isothermal, yield good correlation coefficients for whatever reaction model is used.

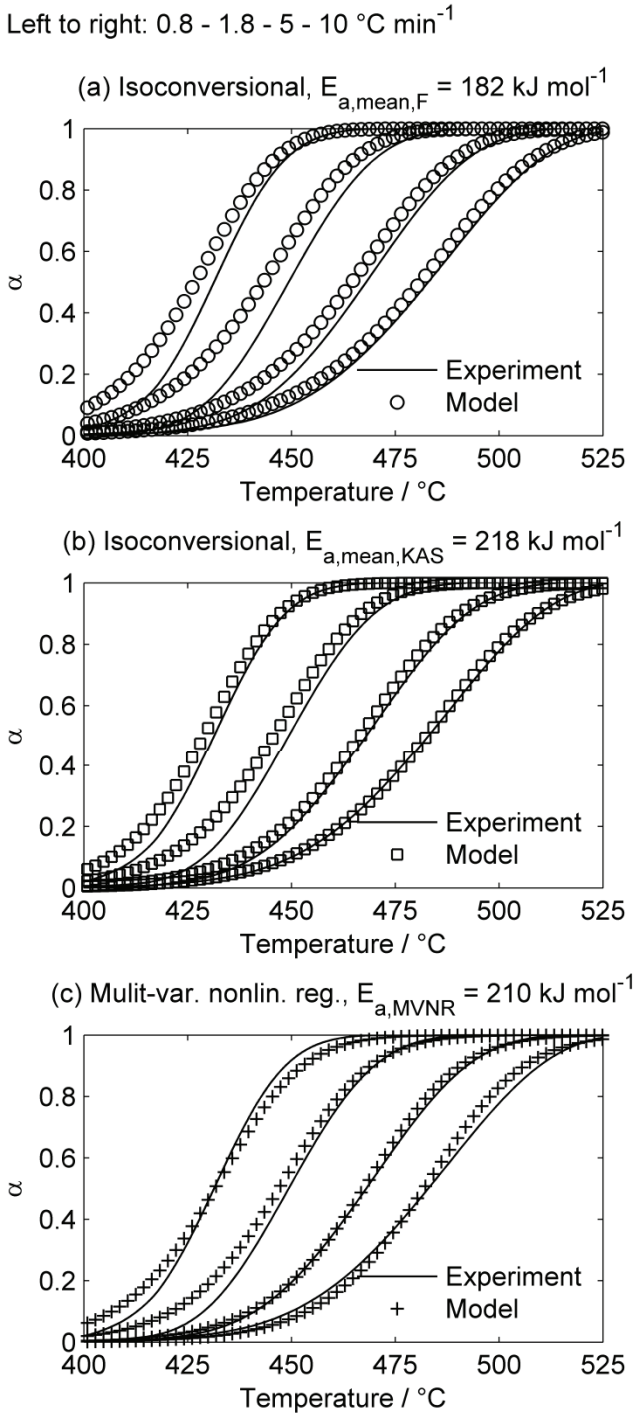

Figure 2-11: Comparison of the experimental curves (lines) and the calculated kinetic triplet (symbols) computed with the isoconversional method (a, b) and the MVNR method (c) for the decomposition of the Mg-Mn-siderite present in SEP200.The reaction model used is Bna.

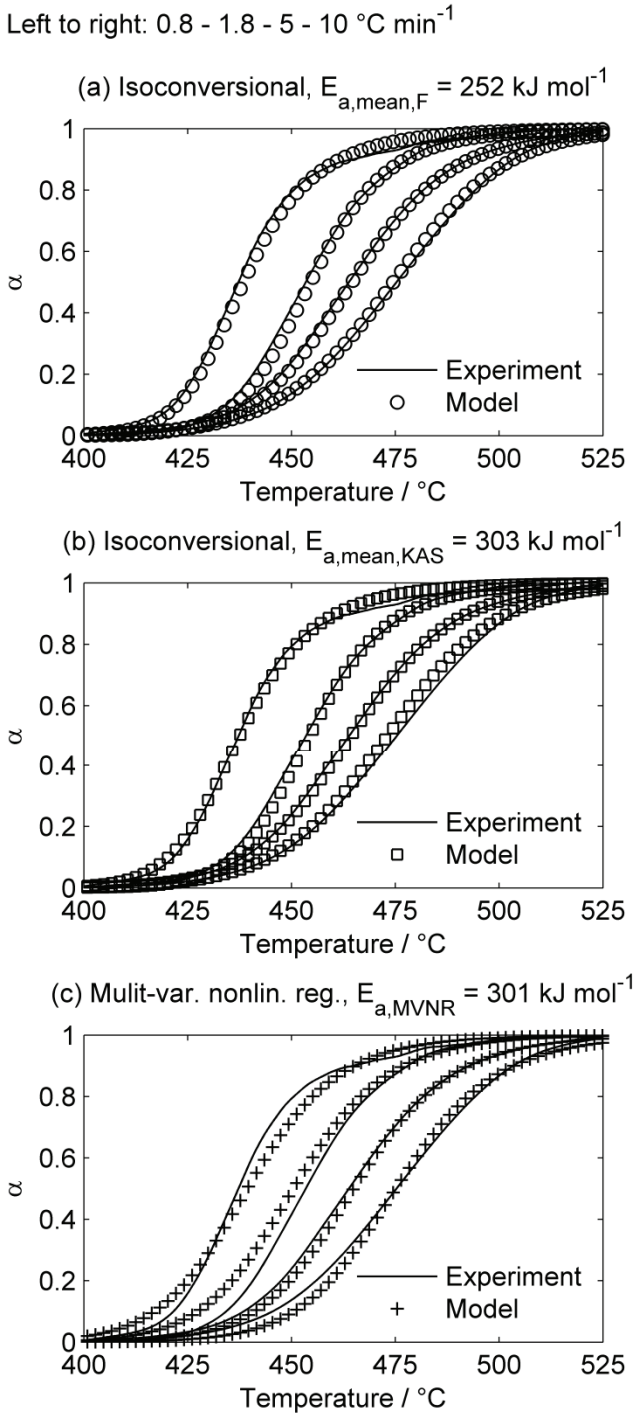

Figure 2-12: Comparison of the experimental curves (lines) and the calculated kinetic triplet (symbols) computed with the isoconversional method (a, b) and the MVNR method (c) for the decomposition of the Mg-Mn-siderite present in ICM200. The reaction model used is Bna.

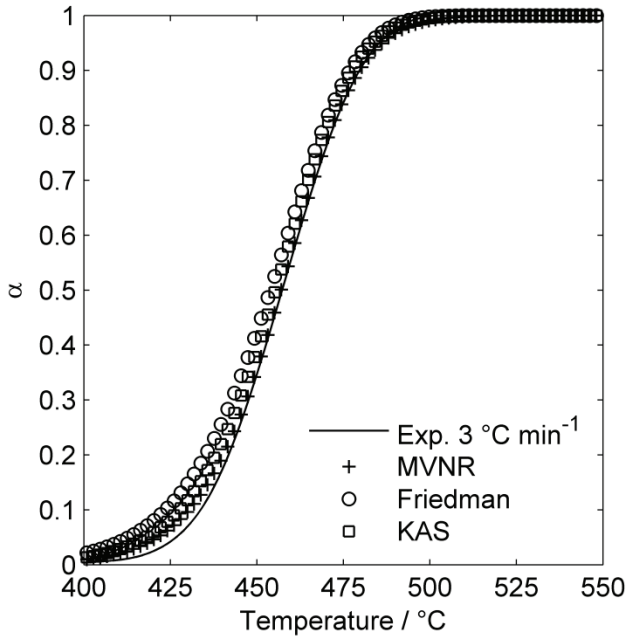

Figure 2-13: Prediction of a heating rate dataset not used in the kinetic computations for the decomposition of Mg-Mn-siderite present in SEP200. The model parameters are depicted in Table 2-8 (MVNR … results of the MVNR computed with Thermokinetics 3.1, Friedman … results for the isoconversional method with the mean of $E_{\alpha,F}$ as E_{iso} and mean values of m and n for the reaction model Bna, KAS … isoconversional method with the mean of $E_{\alpha,KAS}$ as E_{iso} and mean values of m and n for the reaction model Bna).

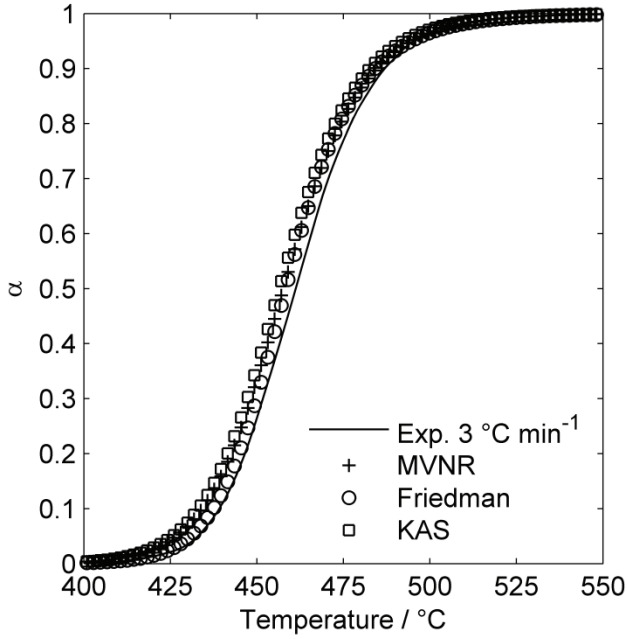

Figure 2-14: Prediction of a heating rate dataset not used in the kinetic computations for the decomposition of Mg-Mn-siderite present in ICM200. The model parameters are depicted in Table 2-8 (MVNR … results of the MVNR computed with Thermokinetics 3.1, Friedman … results for the isoconversional method with the mean of $E_{\alpha,F}$ as E_{iso} and mean values of m and n for the reaction model Bna, KAS … isoconversional method with the mean of $E_{\alpha,KAS}$ as E_{iso} and mean values of m and n for the reaction model Bna).

2.4 Conclusions

A combinatorial approach applying ICP-OES, XRD, SEM/EDXS, and TGA was used to characterize the materials used in this study. The iron carbonate mineral used (ICM200) consisted of three carbonates: Mg-Mn substituted siderite, ankerite, and dolomite. Enrichment of the Mg-Mn-siderite phase was achieved by grinding, separation of the 100-200 µm fraction, sorting by density, and electromagnetic separation in the isodynamic field (=siderite enriched phase, SEP200). The product of the thermal decomposition of Mg-Mn-siderite in nitrogen consists of the Mg-Mn substituted iron oxides wuestite and magnetite.

The formation of wuestite and magnetite can be treated as a single step reaction, as the isoconversional activation energy E_α for the purified Mg-Mn-siderite present in SEP200 does not vary significantly with conversion. An increase of accompanying minerals (ICM200 vs. SEP200) leads to an increase of the mean E_α and to a more pronounced non-linearity of E_α with conversion. The results of the KAS and Friedman approach systematically differ by 30 - 50 kJ mol^{-1} due to the different calculation method (integral vs. differential).

The shape and peak position of the master plots y(α) and z(α) suggest the use of the same reaction model as the MVNR method. The expanded Prout-Tompkins model Bna was confirmed as the most appropriate selection by both methods. The isoconversional method used in this work needs a constant value of the activation energy E_{iso} as an input parameter, the so-called apparent activation energy. The selection of an 'appropriate' value of E_{iso} is a key issue in the determination of the parameters of the reaction model selected by the interpretation of the master plots. Even though $E_{\alpha,F}$ did not vary significantly for SEP200 (mean of 182 ± 8 kJ mol^{-1}) and the master plots indicated the use of Bna as the reaction model, the validation showed a distinct deviation of calculated kinetic triplet and experimental data at 0.8 and 1.8 °C min^{-1}. An increase of E_{iso} to the mean value determined with the KAS method (218 kJ mol^{-1}) leads to a significant improvement of the conformity of model and experiment at heating rate 0.8 °C min^{-1} and 1.8 °C min^{-1}. The MVNR method makes use of the iterative calculation of the minimum of the sum of least squares to calculate an optimal combination of reaction model, activation energy, and pre-exponential factor. The selection and input of an 'appropriate' value of E_{iso} is not needed. Therefore, MVNR proved to be a more robust computational method, as the experimental values and a dataset not included in the computations (3 °C min^{-1}) could be predicted appropriately by the kinetic triplet determined. Nevertheless, if E_{iso} is in the same range of E_a calculated with MVNR, both methods (isoconversional and MVNR) give comparable results. This finding is supported by the results of the isoconversional method based on E_{iso} as the mean of $E_{\alpha,KAS}$ was always in the range of E_a determined with MVNR, for example $E_{a,MVNR,ICM200}$ = 301 kJ mol^{-1} and mean($E_{\alpha,KAS,ICM200}$) = 303 kJ mol^{-1}.

Independent of the computational method, the decomposition of Mg-Mn-siderite present in SEP200 cannot be described with the same kinetic triplet as for ICM200. In the case of SEP200 the reaction order was found to be approximately one and is increased to approximately two for

ICM200. Additionally, the activation energy is increased by 70-100 kJ mol^{-1}. This effect is attributed to the presences of higher amounts of decomposable accompanying carbonates in ICM200 compared to SEP200.

Acknowledgements

The project 'Reduzierende Kalzinierung' is funded by the Austrian 'Klima- und Energiefond' in the framework of the program 'ENERGY MISSION AUSTRIA'. The authors wish to thank Dr. H. Schmid (voestalpine Stahl GmbH, Austria) and Dr. A. Stadtschnitzer (VA Erzberg GmbH, Austria) for their valuable collaboration in the course of the project 'Reduzierende Kalzinierung'. The authors gratefully acknowledge the support from the NAWI Graz program. Thanks are also due to W. Aniser for his support in the performance of the experiments.

References

[1] P.K. Gallagher, S.S.J. Warne, Thermomagnetometry and thermal decomposition of siderite, Thermochim. Acta. 43 (1981) 253–267. doi:10.1016/0040-6031(81)85183-0.

[2] A.P. Dhupe, A.N. Gokarn, Studies in the thermal decomposition of natural siderites in the presence of air, Int. J. Miner. Process. 28 (1990) 209–220.

[3] J.M. Criado, M. Gonzalez, M. Macias, Influence of grinding on both the stability and thermal decomposition mechanism of siderite, Thermochim. Acta. 135 (1988) 219–223. doi:10.1016/0040-6031(88)87389-1.

[4] P.L. Fosbøl, K. Thomsen, E.H. Stenby, Review and recommended thermodynamic properties of FeCO3, Corros. Eng. Sci. Technol. 45 (2010) 115–135. doi:10.1179/174327808X286437.

[5] Y.H. Luo, D.Q. Zhu, J. Pan, X.L. Zhou, Thermal decomposition behaviour and kinetics of Xinjiang siderite ore, Miner. Process. Extr. Metall. Trans. Institutions Min. Metall. Sect. C. 125 (2016) 17–25. doi:10.1080/03719553.2015.1118213.

[6] J. V. Dubrawski, Thermal decomposition of some siderite-magnesite minerals using DSC, J. Therm. Anal. 37 (1991) 1213–1221. doi:10.1007/BF01913855.

[7] S.S.J. Warne, J. V. Dubrawski, Differential scanning calorimetry of the dolomite-ankerite mineral series in flowing nitrogen, Thermochim. Acta. 121 (1987) 39–49.

[8] J. V Dubrawski, S.S.J. Warne, Use of differential scanning calorimetry in measuring the thermal decomposition of mineral carbonates occurring in coal, Fuel. 66 (1987) 1733–1736. doi: 10.1016/0016-2361(87)90372-3.

[9] H.J. Hurst, J.H. Levy, J.H. Patterson, Siderite decomposition in retorting atmospheres, Fuel. 72 (1993) 885–890. doi: 10.1016/0016-2361(93)90097-L.

[10] Y.X. Pan, R.X. Zhu, Q.S. Liu, M.. Jackson, Low-temperature magnetic behavior related to thermal alteration of siderite, Geophys. Res. Lett. 29 (2002) 1–2.

[11] D. Alkaç, Ü. Atalay, Kinetics of thermal decomposition of Hekimhan-Deveci siderite ore samples, Int. J. Miner. Process. 87 (2008) 120–128. doi:10.1016/j.minpro.2008.02.007.

[12] S.B. Jagtap, A. R. Pande, A. N. Gokarn, Kinetics of thermal decomposition of siderite: effect of particle size, Int. J. Miner. Process. 36 (1992) 113–124. doi:10.1016/0301-7516(92)90068-8.

[13] G. Baldauf-Sommerbauer, S. Lux, M. Siebenhofer, Sustainable iron production from mineral iron carbonate and hydrogen, Green Chem. in press (2016). doi:10.1039/C6GC02160C.

[14] F. Gotor, M. Macias, A. Ortega, J. Criado, Comparative study of the kinetics of the thermal decomposition of synthetic and natural siderite samples, Phys. Chem. Miner. 27 (2000) 495–503. doi: 10.1007/s002690000093.

[15] V.Y. Zakharov, Z. Adonyi, Thermal decomposition kinetics of siderite, Thermochim. Acta. 102 (1986) 101–107.

[16] Y.-L. Pang, G.-X. Xiao, S.-W. Jiu, Study on thermal decomposition kinetics of siderite, Xi'an Jianzhu Keji Daxue Xuebao/Journal Xi'an Univ. Archit. Technol. 39 (2007) 136–139+144.

[17] Z.L. Feng, Y. Yu, G. Liu, W. Chen, Thermal decomposition kinetics of siderite in nitrogen, Wuhan Ligong Daxue Xuebao/Journal Wuhan Univ. Technol. 31 (2009) 11–14. doi:10.3963/j.issn.1671-4431.2009.17.004.

[18] Z. Feng, Y. Yu, G. Liu, W. Chen, Kinetics of the thermal decomposition of Wangjiatan siderite, J. Wuhan Univ. Technol. Sci. Ed. 26 (2011) 523–526. doi:10.1007/s11595-011-0261-x.

[19] S. Vyazovkin, A.K. Burnham, J.M. Criado, L. a. Pérez-Maqueda, C. Popescu, N. Sbirrazzuoli, ICTAC Kinetics Committee recommendations for performing kinetic computations on thermal analysis data, Thermochim. Acta. 520 (2011) 1–19. doi:10.1016/j.tca.2011.03.034.

[20] S. Vyazovkin, K. Chrissafis, M.L. Di Lorenzo, N. Koga, M. Pijolat, B. Roduit, et al., ICTAC Kinetics Committee recommendations for collecting experimental thermal analysis data for kinetic computations, Thermochim. Acta. 590 (2014) 1–23. doi:10.1016/j.tca.2014.05.036.

[21] S. Vyazovkin, Isoconversional Kinetics of Thermally Simulated Processes, 1st ed., Springer International Publishing Switzerland, Cham, 2015. doi:10.1007/978-3-319-14175-6.

[22] H.L. Friedman, Kinetics of thermal degradation of char-forming plastics from thermogravimetry. Application to a phenolic plastic, J. Polym. Sci. Part C Polym. Symp. 6 (1964) 183–195. doi:10.1002/polc.5070060121.

[23] T. Akahira, T. Sunose, Method of determining activation deterioration constant of electrical insulating materials, Res. Rep. Chiba Inst. Technol. (Sci. Technol.). 16 (1971) 22–31.

[24] J.M. Criado, J. Málek, A. Ortega, Applicability of the master plots in kinetic analysis of non-isothermal data, Thermochim. Acta. 147 (1989) 377–385. doi:10.1016/0040-6031(89)85192-5.

[25] J. Málek, The kinetic analysis of non-isothermal data, Thermochim. Acta. 200 (1992) 257–269. doi:10.1016/0040-6031(92)85118-F.

[26] J. Opfermann, Kinetic analysis using multivariate non-linear regression, J. Therm. Anal. Calorim. 60 (2000) 641–658. doi:10.1023/A:1010167626551.

[27] J. Málek, The applicability of Johnson-Mehl-Avrami model in the thermal analysis of the crystallization kinetics of glasses, Thermochim. Acta. 267 (1995) 61–73. doi:10.1016/0040-6031(95)02466-2.

[28] Outotec, HSC Chemistry 8.0.3, 2014.

[29] A. Reller, R. Emmenegger, C. Padeste, H.R. Oswald, Thermochemical reactivity of metal carbonates, Chimia (Aarau). 45 (1991) 262–266.

[30] A. Boehm, M. Boehm, A. Kogelbauer, Neutrons for mineral processing - Thermo diffractometry to investigate mineral selective magnetizing flash roasting, Chemie Ing. Tech. 86 (2014) 883–890. doi:10.1002/cite.201400024.

[31] L.A. Pérez-Maqueda, J.M. Criado, P.E. Sánchez-Jiménez, Combined kinetic analysis of solid-state reactions: A powerful tool for the simultaneous determination of kinetic parameters and the kinetic model without previous assumptions on the reaction mechanism, J. Phys. Chem. A. 110 (2006) 12456–12462. doi:10.1021/jp064792g.

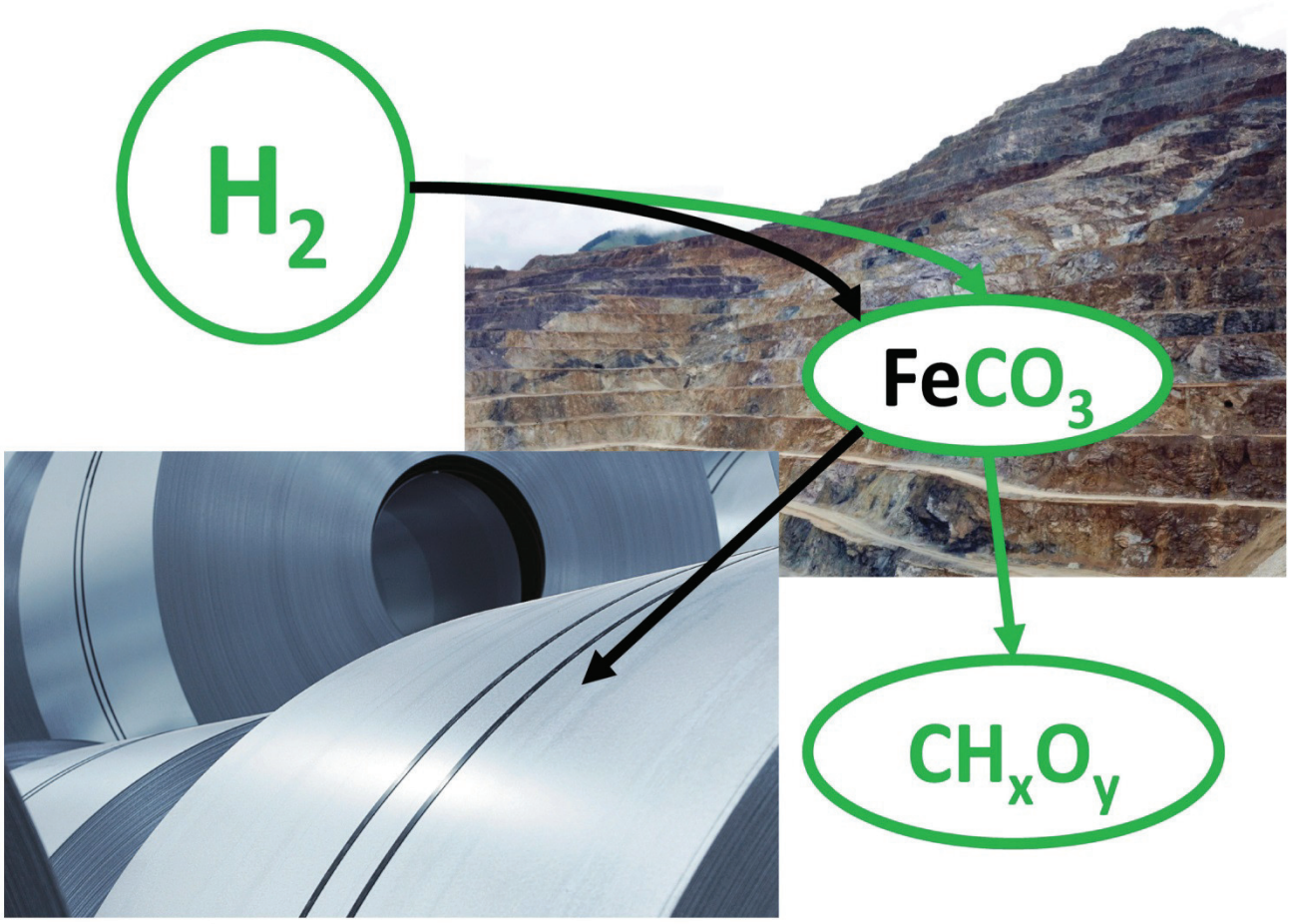

Research conducted at the Institute of Chemical Engineering and Environmental Technology in cooperation with the industrial partners VA Erzberg and voestalpine (all from Austria).

Sustainable iron production from mineral iron carbonate and hydrogen

The reduction of $FeCO_3$ with hydrogen suppresses intermediate Fe_2O_3 formation. CO_2 emission can be reduced by 60% and the amount of reducing agent can be reduced by 33% compared to state-of-the-art iron carbonate beneficiation. The kinetics and reaction mechanism of the reduction of mineral $FeCO_3$ with gaseous hydrogen were determined with a thermogravimetric method.

As featured in:

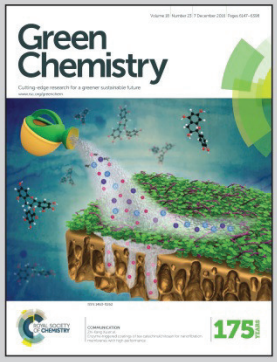

See G. Baldauf-Sommerbauer, S. Lux *et al.*, *Green Chem.*, 2016, **18**, 6255.

ROYAL SOCIETY OF CHEMISTRY

www.rsc.org/greenchem

Registered charity number: 207890

3 Sustainable iron production from mineral iron carbonate and hydrogen[2]

Abstract

The reduction of iron ores with hydrogen is considered a promising CO_2 breakthrough technology to mitigate CO_2 emissions from the iron and steel industry. The state-of-the-art production of iron and steel from mineral iron carbonates ($FeCO_3$) is based on the thermal decomposition of $FeCO_3$ in air to produce hematite (Fe_2O_3) suitable for iron production. Our approach is to directly reduce $FeCO_3$ with hydrogen to elemental iron, avoiding Fe_2O_3 formation. As a consequence, CO_2 emissions can be decreased by 60 % and up to 33 % less reducing agent is needed for iron production. The development of environmentally benign production pathways needs to be based on a fundamental understanding of the reaction kinetics and mechanism. Therefore, thermogravimetry was used to determine the kinetics of the formation of iron from mineral iron carbonate and the concomitant decomposition of the accessory matrix carbonates of calcium, magnesium, and manganese. The isoconversional kinetic analysis according to the Ozawa-Flynn-Wall, Kissinger-Akahira-Sunose, and Friedman approach confirms the proposed parallel kinetic model. Multi-variate non-linear regression was used to determine the appropriate kinetic parameters. The conversion of iron carbonate to iron can be described with the two-dimensional Avrami-Erofeev model A2. Therefore, a temperature-controlled nucleation and diffusional growth mechanism is suggested for iron formation from mineral iron carbonate and hydrogen. The multi-parameter reaction models Cn-X and Bna can be used to describe the concomitant iron, calcium oxide, magnesium oxide, and manganese oxide formation without applying multi-step kinetics. The multi-parameter reaction models predict a conversion above 95 % at 450 °C within less than 60 minutes reaction time. Unavoidably, 1 mole of carbon dioxide is always emitted when 1 mole of $FeCO_3$ is converted into iron. Catalytic carbon dioxide hydrogenation (CCDH) can be applied to diminish inevitable CO_2 emissions by chemical conversion into value-added carbon containing chemicals. Therefore, we propose a process that combines the improved iron production via direct $FeCO_3$ reduction with CCDH as a follow-up reaction.

[2] This chapter is based on an gold open access article published by The Royal Society of Chemistry under a Creative Commons Attribution-NonCommercial 3.0 Unported licence:
G. Baldauf-Sommerbauer, S. Lux, M. Siebenhofer, Sustainable iron production from mineral iron carbonate and hydrogen, Green Chem. 18 (2016) 6255–6265. doi:10.1039/C6GC02160C.

Symbols

α	-	Conversion
$\alpha_{Fe,calc}$	-	Fractional conversion for total iron carbonate reduction (Eq. 9)
A_α	s^{-1}	Frequency factor determined with a model-free/isoconversional method
A	s^{-1}	Frequency factor
β_i	K min^{-1}	Heating rate of the i^{th} temperature program
$\Delta_R G°$	kJ mol^{-1}	Standard free energy of reaction
$\Delta_R H_T$	kJ mol^{-1}	Reaction enthalpy at temperature T and 1.013 bar
Δm	%	Mass change: negative for loss, positive for gain
Δm_{TGi}	%	Mass change for i^{th} step of the thermogravimetric curve
$\Delta m_{FeCO3,Fe}$		%Mass loss for the direct hydrogen reduction of the iron carbonate content of CS to iron
$\Delta m_{MCO3,MO}$		%Mass loss for the conversion of Ca-, Mg-, and Mn-carbonates of CS to oxides
d_i	-	Degrees of freedom for model i
E_α	kJ mol^{-1}	Model-free/isoconversional activation energy
E_a	kJ mol^{-1}	Activation energy
$f(\alpha)$	-	Reaction model
h	-	Number of linear heating rate scans
k(T)	K s^{-1}	Arrhenius temperature dependency: $k(T) = A * e^{\frac{-E_a}{RT}}$
Kcat	-	Parameter for autocatalysis model Cn-X
m	%wt.	Mass
MW	g mol^{-1}	Molecular weight
n	-	Reaction order
n_{AE}	-	Parameter for Avrami-Erofeev reaction model
r	-	Parameter for expanded Prout-Tompinks model Bna
R_{gas}	J mol^{-1} K^{-1}	Ideal gas constant
T	°C/K	Temperature
T	min	Time
v	-	Number of datapoints
y	-	Measured value
wf_i	%	Mass fraction of compound i

Abbreviations

AISI	American iron and steel institute
BF	Blast furnace
BOF	Blast oxygen furnace
CCDH	Carbon dioxide hydrogenation
CS	Concentrated siderite
CO_2^e	Carbon dioxide equivalent
COURSE 50	CO_2 ultimate reductions in steelmaking process by innovative technology for cool earth 50
DIOR	Direct iron oxide reduction
ICP-OES	Inductively coupled plasma optical emission spectroscopy
IPCC	Intergovernmental Panel on Climate Change
KAS	Kissinger-Akahira-Sunose
MCO_3	Calcium, magnesium, and manganese carbonate present in OM
MO	Calcium, magnesium, and manganese oxide produced from MCO_3 present in OM
OFW	Ozawa-Flynn-Wall

OM	Original mineral
P	Product
POSCO	Pohang iron and steel company
R	Correlation coefficient
TG	Thermogravimetry
ULCOS	Ultra-low carbon dioxide steelmaking
XRD	X-ray diffraction

3.1 Introduction

According to the Fifth Assessment Report of the Intergovernmental Panel on Climate Change (IPCC), [1] the industrial sector is responsible for approximately one third of the total anthropogenic CO_2-equivalent (CO_2^e) emissions. Iron- and steelmaking accounts for 13 - 25 % [2,3] of these industrial CO_2^e emissions. Several approaches can contribute to a substantial decrease of CO_2^e emissions from the iron- and steel industry: (1) Reduction of steel production and demand [2], (2) increased steel recycling and scrap use [4], and (3) innovative iron- and steelmaking technologies, also called CO_2 breakthrough technologies. Global steel production and demand is not expected to decrease within the 21st century and an increase of the share of recycled steel (= secondary steel) on total steel production can be expected [4,5]. However, to meet global industrial demand for iron based products, primary steel production from iron ores will continue to contribute a major part of the CO_2^e emissions from the global iron and steel sector. Therefore, various research programs aiming at the development of CO_2 breakthrough technologies have been initiated: ULCOS I and II in the EU, COURSE 50 in Japan, the POSCO CO_2 breakthrough framework in South Korea, and the AISI program in the USA, to mention the most extensive ones [3,6,7]. Fu et al. [6] and Quader et al. [3,8] provide an overview and evaluation of these programs. The COURSE 50, POSCO framework, and the AISI CO_2 breakthrough program explicitly include hydrogen reduction of iron ores as a key future technology. To reach a substantial decrease of anthropogenic CO_2^e emission within the 21st century most nations adopted the 'Paris Pact' that includes a commitment to the transition of the global energy sector from fossil fuels to renewables [9]. Fischedick et al. [5] did show that direct hydrogen reduction of iron ores is an environmentally and economically promising iron and steel production route in a 100 % renewable energy system.

The world steel production increased from 1.53 Gt in 2013 [10] to 1.60 Gt in 2015 [11].[3] China makes up for approximately 50 % of the world steel and 57 % of the world iron production [11,12]. China [13] and Austria [14] have major mineral iron carbonate (= siderite) reserves, which are used as ores for iron and steel production. Siderite beneficiation is challenging, because of the low iron content of the ore compared to magnetite and hematite ores. The industrial practice is to blend siderite with other high-grade ores in the sinter plant [15,16]. During the sintering process, siderite is converted to hematite Fe_2O_3 through roasting in air according to Eq. 1. The sinter product is fed to the blast furnace where it is reduced with coal via CO, producing at least 1.5 mole CO_2 per mole of iron due to the stoichiometry of reaction 2. Consequently, at least 2.5 mole CO_2 are emitted during the production of 1 mole of iron from iron carbonate. The direct reduction of iron carbonate with hydrogen according to Eq. 3 reduces the carbon dioxide emissions by 60 % to one mole of CO_2 per mole of iron. As will be outlined in this work, the remaining CO_2 emissions can be limited by catalytic hydrogenation of carbon

[3] 39 countries which account for approximately 99 % (BF) and 90 % (DIOR) of the world production were considered in the calculation.

dioxide (CCDH) [17-19] according to equation 4 and 5 to value added products such as methane and higher hydrocarbons via Fischer-Tropsch synthesis.

$$FeCO_3 + 0.25\ O_2 \xrightarrow{Air} 0.5\ Fe_2O_3 + CO_2 \quad (1)$$

$$0.5\ Fe_2O_3 + 1.5\ CO \rightarrow Fe + 1.5\ CO_2 \quad (2)$$

$$FeCO_3 + H_2 \rightarrow Fe + H_2O + CO_2 \quad (3)$$

$$CO_2 + 4\ H_2 \rightarrow CH_4 + 2\ H_2O \quad (4)$$

$$CO_2 + 3\ H_2 \rightarrow -CH_2 - + 2\ H_2O \quad (5)$$

Improvement of siderite beneficiation has focused on innovative roasting technologies [14] and direct reduction with coal [13,20]. Neither of these processes greatly affects the CO_2 emissions and could be considered a CO_2 breakthrough technology. Nowadays (2016), most of the industrially used hydrogen is produced from fossil fuels by steam reforming ($CH_4 + H_2O \rightarrow 3\ H_2 + CO$) and the water-gas shift reaction ($H_2O + CO \rightarrow H_2 + CO_2$) with natural gas as the primary feedstock. At least 0.25 moles of CO_2 are produced per mole of hydrogen in combined steam reforming and water-gas shift (Eq. 6).

$$CH_4 + 2\ H_2O \rightarrow 4\ H_2 + CO_2 \quad (6)$$

Even when the hydrogen supply of direct carbonate reduction (Eq. 3) is covered by combined steam reforming and water-gas shift (Eq. 6), the stoichiometric CO_2 emission per mole of iron is decreased by 50 % compared to roasting of iron carbonate and subsequent reduction. Renewable and sustainable hydrogen production is extensively investigated [21-26]. The production of 'green' hydrogen is not only conceivable from a scientific point of view, but also necessary from an environmental point of view to meet the global CO_2 mitigation targets for the 21st century.

The detailed understanding of the reaction mechanism and kinetics of the fundamental reactions is the basis for the design of an environmentally benign industrial process. The kinetics for the direct hydrogen reduction of hematite Fe_2O_3 and magnetite F_3O_4 have been broadly investigated and discussed in literature [27-30]. The decomposition kinetics of mineral iron carbonate have been investigated in oxygen atmosphere [31-33], vacuum [34], and nitrogen atmosphere [35-38]. However, the direct reduction of mineral iron carbonate lacks kinetic and mechanistic investigation.

In this paper, we propose a kinetic model and a suggested reaction mechanism for the direct hydrogen reduction of mineral iron carbonate to elemental iron on the basis of thermogravimetric experiments. Based on the reaction kinetics developed in this work, a process concept and an outlook to a carbon dioxide utilization approach by coupling direct

hydrogen reduction of iron carbonate with catalytic carbon dioxide hydrogenation (CCDH) to value added products (e.g. methane, methanol, higher hydrocarbons) is presented.

3.2 Experimental and computational methods

Thermogravimetric measurements were performed on a Netzsch Jupiter STA 449C balance with alumina sample pans. Hydrogen and nitrogen were used in 99.999 % quality (AirLiquide). The X-ray diffraction (XRD) spectra were recorded on a Panalytical X'Pert Pro diffractometer equipped with a cobalt radiation tube (Co-Kα line at 0.178901 nm). The HighScore Plus software together with the Inorganic Crystal Structure Database was used for compound determination. The quantitative analysis was performed by means of Inductively Coupled Plasma - Optical Emission Spectroscopy (ICP-OES) using a Spectro Ametek Spectro Arcos device

3.2.1 Sample preparation for quantitative ICP-OES analysis

2.15 g of the concentrated siderite sample was reduced on the thermobalance in 70 %vol. hydrogen at a total flow rate of 100 cm^3 min^{-1}. The sample was heated to 725 °C at a linear heating rate of 3 °C min^{-1} and kept at 725 °C until a constant mass was reached, indicating complete reaction. The reaction product was dissolved in a mixture of concentrated hydrochloric and concentrated nitic acid ($HCl:HNO_3$=3:1, volumetric) for elemental analysis.

3.2.2 Kinetic computations

Four different linear heating rates (1.8, 3, 5, 10 °C min^{-1}) were used to generate a data set suitable for kinetic computations according to the recommendations of the International Committee of Thermal Analysis and Calorimetry (ICTAC) Kinetics Committee [39,40]. Before the data collection was started, a temperature calibration was performed at a linear heating rate of 5 °C min^{-1} and a nitrogen flow of 100 cm^3 min^{-1} with indium, tin, bismuth, zinc, and aluminum standard reference materials. A blank measurement was recorded every time the experimental conditions were changed and all kinetic measurements were replicated with a sample amount of 20 ± 2 mg for each run. The conversion α was calculated as the ratio of mass loss at temperature T and maximum mass loss of the experiment.

The model-free integral Ozawa-Flynn-Wall (OFW, Eq. 7) [41,42] and Kissinger-Akahira-Sunose (KAS, Eq. 8) [43] methods and the differential Friedman method [44] (Eq. 9) were used to check the suitability and separability of single step kinetic models.

$$\ln \beta_i = \text{const} - 1.052 * \frac{E_\alpha}{R_{gas} T_{\alpha,i}} \quad (7)$$

$$\ln \left[\frac{\beta_i}{T_{\alpha,i}^2}\right] = \text{const} - \frac{E_\alpha}{R_{gas} T_{\alpha,i}} \quad (8)$$

$$\ln \left[\frac{d\alpha}{dt}\right]_{\alpha,i} = \ln(f(\alpha) A_\alpha) - \frac{E_\alpha}{R_{gas} T_{\alpha,i}} \quad (9)$$

Table 3-1: Reaction models [39,45] considered in the analysis of the kinetic datasets.

Code	Description	Model equation f(α)
F1	Reaction of first order	$1- \alpha$
F2	Reaction of second order	$(1-\alpha)^2$
Fn	Reaction of n^{th} order	$(1- \alpha)^n$
R2	Two-dimensional phase boundary/contracting cylinder	$2(1- \alpha)^{1/2}$
R3	Three-dimensional phase boundary/contracting sphere	$3(1- \alpha)^{2/3}$
D1	One-dimensional diffusion	$1/(2\alpha)$
D2	Two-dimensional diffusion	$[-\ln(1- \alpha)]^{-1}$
D3J	Jander three-dimensional diffusion,	$3/2*(1- \alpha)^{2/3}[1-(1- \alpha)^{1/3}]^{-1}$
D3GB	Ginstling-Bronstein three-dimensional diffusion	$3/2*[(1- \alpha)^{-1/3}-1]^{-1}$
B1	Prout-Tompkins equation	$\alpha(1-\alpha)$
Bna	Expanded Prout-Tompkins equation	$\alpha^r(1-\alpha)^n$
C1-X	First order autocatalytic reaction with catalysis by final or intermediate product X expressed as function of α	$(1-\alpha)(1+K_{cat}*X(\alpha))$
Cn-X	n^{th} order autocatalytic reaction with catalysis by final or intermediate product X expressed as function of α	$(1-\alpha)^n(1+K_{cat}*X(\alpha))$
A2	Avrami-Erofeev two-dimensional nucleation	$2(1- \alpha)[-\ln(1- \alpha)]^{1/2}$
A3	Avrami-Erofeev three-dimensional nucleation	$3(1- \alpha)[-\ln(1- \alpha)]^{2/3}$
An	Avrami-Erofeev n^{th} dimensional nucleation	$n(1- \alpha)[-\ln(1- \alpha)]^{(n-1)/n}$

The multi-variate regression analysis presented by Opfermann [45] implemented in the software Thermokinetics 3.1 was used for the computation of an accurate combination of Arrhenius temperature dependency k(T) and reaction model f(α) for the general kinetic equation depicted in Eq. 10.

$$\frac{d\alpha}{dt} = \beta * \frac{d\alpha}{dT} = k(T) * f(\alpha) = A * e^{\frac{-E_a}{R_{gas}T}} * f(\alpha) \quad (10)$$

Evaluation of the suitability of models was done by computation of the coefficient of regression R according to Eq. 11 and performing the F-test according to Eq. 12.

$$R = \sqrt{1 - \frac{\sum_{i=1}^{h}\sum_{j=1}^{v}\left(y_{ij}-y_{calc,ij}\right)^2}{\sum_{i=1}^{h}\left(\sum_{j=1}^{v} y_{ij}^2 - \frac{\left(\sum_{j=1}^{v} y_{ij}\right)^2}{v}\right)}} \quad (11)$$

$$F(d_A, d_B) = \frac{\sum_{i=1}^{h}\sum_{j=1}^{v} d_A^{-1}(y_{ij}-y_{calc,ij}(model\ A))^2}{\sum_{i=1}^{h}\sum_{j=1}^{v} d_B^{-1}(y_{ij}-y_{calc,ij}(model\ B))^2} \quad (12)$$

3.3 Results and discussion

3.3.1 Comparison of direct iron carbonate reduction to the state-of-the-art from a thermodynamic point of view

Iron carbonate minerals are beneficiated industrially by roasting in air to produce hematite Fe_2O_3 (Eq. 1). Reduction of hematite with hydrogen requires 1.5 moles of hydrogen per mole of iron produced (Eq. 13), whereas the direct reduction of iron carbonate requires one mole of hydrogen per mole of iron produced (Eq. 3).

$$0.5\ Fe_2O_3 + 1.5\ H_2 \rightarrow Fe + 1.5H_2O \qquad (13)$$

Thus, the effectiveness of the reduction process is enhanced by 33 % less reducing agent consumption when the hematite route (Eq. 1 and 2) is bypassed by direct iron carbonate reduction (Eq. 3). The reduction of iron carbonate is favored over the hematite reduction at temperatures above 100 °C, due to the decreasing run of the standard free energy of reaction $\Delta_R G°$ with temperature (see Figure 3-1: green line with circles for hematite, red line with circles for iron carbonate). Mineral iron carbonates are often accompanied by calcium, magnesium, and manganese carbonates. Iron, calcium, magnesium, and manganese can either be present as separate carbonate phases or as solid solutions. The thermodynamic analysis for the carbonates shows, that $\Delta_R G°$ decreases linearly with temperature for $CaCO_3$, $(Ca,Mg)(CO_3)_2$, $MgCO_3$, $MnCO_3$, and $FeCO_3$. The temperature needed for high conversions increases in the order $FeCO_3$ < $MnCO_3$ < $MgCO_3$ < $(Ca,Mg)(CO_3)_2$ < $CaCO_3$.

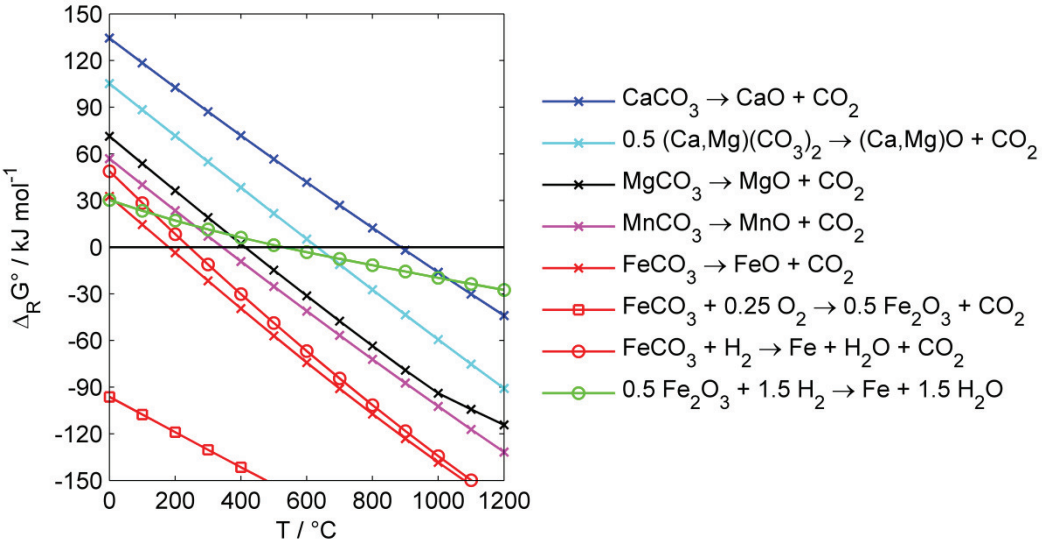

Figure 3-1: Standard free energy of reaction ΔRG° at ambient pressure calculated with HSC Chemistry 8 for the most stable solid phases. Roasting of iron carbonate (red squares) produces stable products, thus exhibits strongly negative values for ΔRG°. The reduction of iron carbonate (red circles) is thermodynamically favoured over the reduction of hematite (green circles) at temperatures above 200 °C. Decomposition of carbonates to bivalent oxides is expected to proceed in the order iron (red x) < manganese (magenta x) < magnesium (black x) < dolomite (cyan x) < calcite (blue x).

3.3.2 Reactant and product characterization

The original mineral from the Austrian Erzberg was provided by VA Erzberg GmbH. This mineral consists of three main carbonate components: siderite $FeCO_3$ with partial Mg and Mn substitution, ankerite $(Ca_aFe_bMg_cMn_d)CO_3$, and dolomite $(Ca,Mg)(CO_3)_2$. Potassium, aluminum, and silicon are present in the form of muscovite $KAl_2(AlSi_3O_{10})(OH)_2$, whereas major parts of the silicon can be found as quartz SiO_2 (see Figure 3-2a for XRD spectrum and Table 3-2 for composition). A 100-200 µm size fraction of the original mineral was sorted by density and separated electromagnetically in the isodynamic field. This procedure produced a concentrated siderite specimen (referred to as CS, see Figure 3-2b and Table 3-2), which was used for the kinetic analysis. The iron carbonate content of the CS is converted to elemental iron (79 ± 2 %wt., see Table 3-2) after reduction with hydrogen. Calcium, magnesium, and manganese carbonates are converted to oxides. Summation of the produced Fe, CaO, MgO, MnO, SiO_2, and Al_2O_3 results in 102 ± 3 %wt. (see last row of column P in Table 3-2). Consequently, the conversion can be considered quantitative.

3.3.3 Kinetic modelling

On the basis of the analysis of reactants and products, a parallel reaction scheme can be assumed to model the kinetics of the reduction of the concentrated mineral siderite. Iron carbonate is converted to iron (Eq. 3) and the metal carbonates of calcium, magnesium, and manganese are converted to oxides (Eq. 14).

$$FeCO_3 + H_2 \xrightarrow{k_1(T),f_1(\alpha)} Fe + H_2O + CO_2 \tag{3}$$

$$(Ca_xMg_yMn_z)CO_3 \xrightarrow{k_2(T),f_2(\alpha)} xCaO + yMgO + zMnO + CO_2 \tag{14}$$

The theoretical mass loss of the solid phase transformed in reaction 3 and 14 can be calculated from the reactant composition (see column CS in Table 3-2). The mass loss for the direct hydrogen reduction of the iron carbonate content of the concentrated siderite $\Delta m_{FeCO3,Fe}$ accounts for 42.8 ± 1.3 %wt (Eq. 15). The mass loss for the conversion of the Ca-, Mg-, and Mn-carbonates to oxides $\Delta m_{MCO3,MO}$ sum up to 6.5 ± 0.2 %wt (Eq. 16). Thus, the fractional conversion for total iron carbonate reduction $\alpha_{Fe,calc}$ can be calculated from Eq. 17 and accounts for 0.87 ± 0.03. These calculated values are in good agreement with the experimental thermogravimetric curves, as depicted in Figure 3-3.

$$\Delta m_{FeCO3,Fe} = wf_{FeCO3} * \frac{MW(CO_3)}{MW(FeCO_3)} \tag{15}$$

$$\Delta m_{MCO3,MO} = wf_{MCO3} * \frac{MW(CO_2)}{MW(MCO_3)} \tag{16}$$

$$\alpha_{Fe,calc} = \frac{\Delta m_{FeCO3,Fe}}{\Delta m_{FeCO3,Fe} + \Delta m_{MCO3,MO}} \tag{17}$$

Table 3-2: Results of the ICP-OES analysis (OM: original mineral, CS: concentrated siderite phase, P: product of the reduction of CS with hydrogen). Compared to the OM, the relative iron content of CS is increased and the relative content of calcium and magnesium are decreased. The reduction of CS with hydrogen yields a product with high iron content by quantitative carbonate reduction (see Eq. 3).

	OM / %wt. ±3 %rel.	CS / %wt. ±3 %rel.	P / %wt. ±3 %rel.
Fe	33.5	39.9	79.0
CaO	5.8	1.3	2.7
MgO	3.9	3.3	6.6
MnO	2.6	3.1	5.7
SiO_2	5.4	2.1	4.7
Al_2O_3	1.1	1.5	2.9
SUM	52.3	51.2	101.6

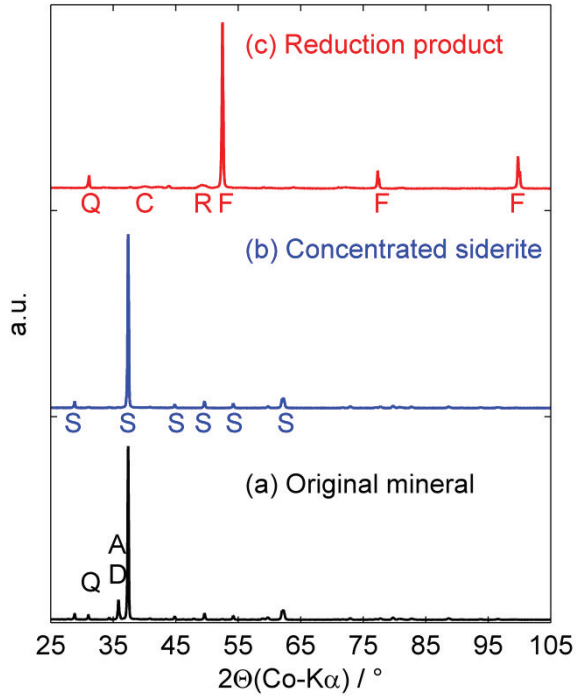

Figure 3-2: XRD pattern of the original mineral from Erzberg/Austria (a), the concentrated siderite (b), and the product of the reduction with H_2 of the concentrated siderite (c). Magnesium and manganese oxide cannot be distinguished, as both oxides are present in amounts below 7 %wt. The most intensive reflection for both oxides should appear at 48-50° but cannot be separated, as there is a broad peak ranging from 48.2-50.6° at this scattering angle. A: ankerite $(Ca_aFe_bMg_cMn_d)CO_3$; C: calcite, CaO; D: dolomite $(Ca,Mg)(CO_3)_2$; F: iron, Fe; R: magnesium/manganese oxide, MgO/MnO; S: siderite $FeCO_3$; Q: quartz, SiO_2.

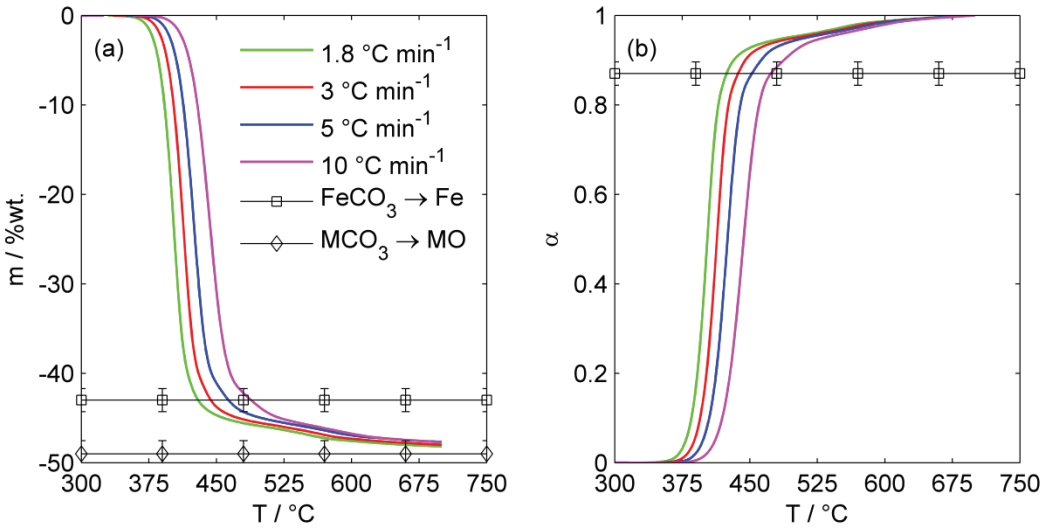

Figure 3-3: Thermogravimetric curves (a) and conversion α curves (b) used for the kinetic analysis. The calculated mass loss for the reduction of iron carbonate to iron (square) and for the decomposition of the Ca-, Mg-, and Mn-carbonate (diamond) are marked. The calculated total conversion (diamond) and the experiment (a) are in good agreement. Sample mass = 20 ± 2 mg, 100 cm^3min^{-1} total flow, 70 %vol. hydrogen at the inlet.

3.3.4 Model-free kinetic analysis

The Ozawa-Flynn-Wall (OFW) [41,42], Kissinger-Akahira-Sunose (KAS) [43], and Friedman [44] approach result in a model-free activation energy E_α vs. conversion α plot (Figure 3-4). If activation energy is roughly constant with the extent of reaction, the process can be described with one single step model. If two or more clearly separable E_α regimes can be observed, two or more step reactions seem to be appropriate approaches. Results from model-free E_α calculations can be used as input parameters for linear and non-linear model fitting purposes [39,46] and analysis of the variation of activation energy with extent of conversion [46]. The differential Friedman method can be applied to any temperature program, but is sensitive to experimental noise. The OFW and KAS methods do not tend to magnify experimental noise, as they are integral. But both methods introduce a systematic error in the value of model-free activation energy E_α due to the method of integration [46]. Therefore, a combinatorial interpretation of the outcome of these three methods should give a sound model-free kinetic analysis

The OFW and KAS analysis produce a comparable result, whereas the KAS method leads to slightly lower E_α values (2-3 kJ mol^{-1}, see Table 3-3). This can be expected from the different temperature integral approximation (Eq. 7 and 8). The calculations based on the Friedman approach result in a comparable run of E_α vs. conversion. Nevertheless, the value of E_α is systematically lower (17-25 kJ mol^{-1}, see Table 3-3) than the value for E_α calculated with the OFW and KAS method. The three model-free approaches result in the same trend of the model-free activation energy with extent of conversion. E_α is relatively constant from α=0.1 to α=0.8 and decreases by approximately 25 kJ mol^{-1}. In theory, reactions following single step kinetics result in constant values for E_α over the whole conversion range. The constant decrease over a

specific conversion range can be expected for heterogeneous mineral systems. This variation of activation energy is an indication for partially overlapping reactions, resulting in an effective, conversion dependent activation energy [46]. The shoulder starting at α≈0.80 (Friedman) and α≈0.85 (OFW, KAS) indicates the overlapping start of the second reaction. As shown in Figure 3-4, the occurrence of the shoulder is in good agreement with the fractional conversion for total iron carbonate reduction $\alpha_{Fe,calc}$=0.87±0.03. Hence, the model free kinetic analysis confirms the assumed kinetic model of two parallel reactions: the reduction of iron carbonate to iron (Eq. 3) and the decomposition of Ca-, Mg-, and Mn-carbonate (Eq. 14).

Table 3-3: Model-free activation energy E_α calculated with the Friedman (FM), Ozawa-Flynn-Wall (OFW), and Kissinger-Akahira-Sunose (KAS) method.

	E_α / kJ mol^{-1}		
α	FM	OFW	KAS
0.1	164±3	184±1	182±1
0.4	143±7	168±2	165±3
0.5	138±8	164±3	161±3
0.7	134±9	156±4	152±4
0.8	143±4	151±5	147±5
0.9	104±10	128±5	122±5

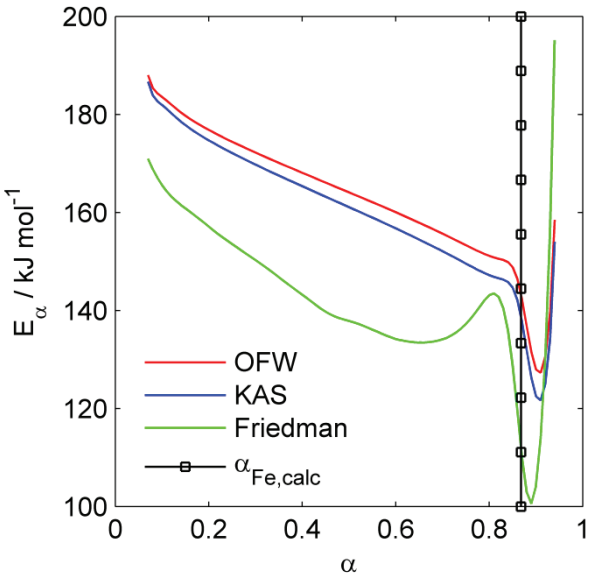

Figure 3-4: Model-free activation energy Eα calculated with the Ozawa-Flynn-Wall [41,42] (OFW, red), the Kissinger-Akahira-Sunose (KAS, blue) [43], and Friedman [44] (green) approach. The shoulder starting at α ≈ 0.80-0.83 indicates the overlap of a second reaction. The black line with squares at α =0.87 demarks the calculated partial mass loss (0.87±0.03) for complete iron carbonate conversion to iron $\alpha_{Fe,calc}$ and the start for the decomposition of Ca-, Mg-, and Mn-carbonate calculated from the sample composition

3.3.5 Determination of a reaction model f(α) and proposed reaction mechanism

A multivariate non-linear regression analysis [45] of 16 commonly used single step reaction models (Table 3-1) was performed on the conversion range α=0.01-0.99 to find suitable reaction models. As shown in Table 3-4 and Figure 3-5, the multi-parameter n^{th}-order autocatalysis model Cn-X and the expanded Prout-Tompkins model Bna can adequately describe the whole conversion range. The model parameters (Table 3-4), however, are not very plausible for single step kinetics. A fractional reaction order of 2.65 (Cn-X) and 2.56 (Bna) is an indication for overlapping reactions, as expected from the model-free analysis. Nevertheless, Cn-X and Bna can adequately describe the concomitant conversion of iron carbonate to iron and the decomposition of the matrix carbonates of Ca, Mg, and Mn to oxides without applying multi-step kinetics (see Figure 3-5).

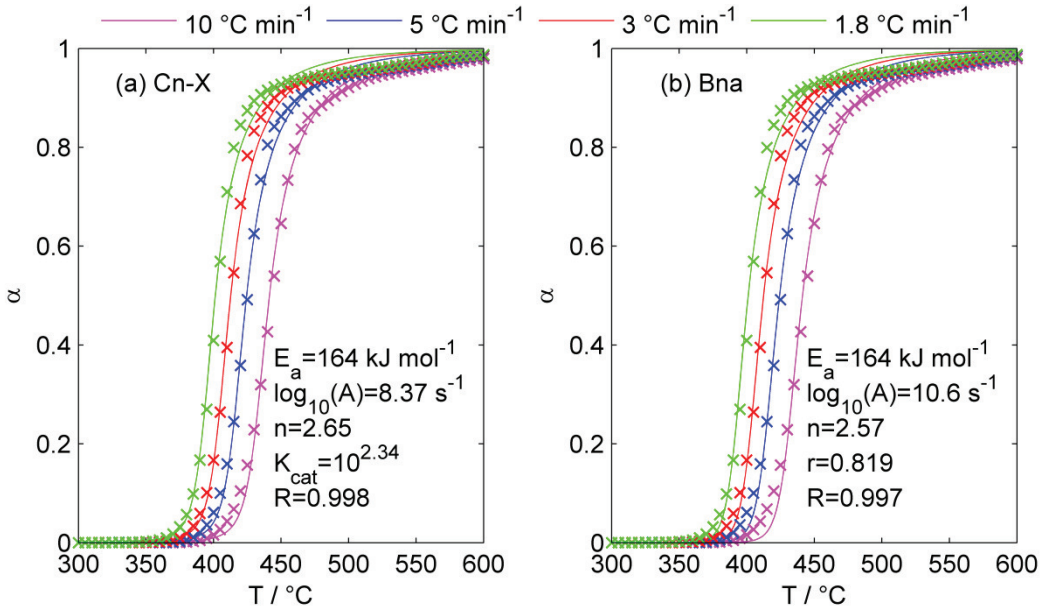

Figure 3-5: Model prediction (solid lines) and experimental (x) conversion of CS into iron and conversion of calcium, magnesium, and manganese carbonate to the corresponding oxides at four different heating rates. The multi-parameter models considering autocatalysis (a: Cn-X) and the expanded Prout-Tompkins model (b: Bna) accurately predict the experimental curves.

Table 3-4: Results of the regression analysis for single step kinetics in the conversion range α = 0.01-0.99. 16 commonly used reaction models for solid state kinetics were considered; see Tab. 5 for model description and equations. The correlation coefficient (R, see Eq. 11) and the F-test (F, see Eq. 12) are used for model comparison. Critical F-value = 1.11

Model	R	F	Ea kJ mol^{-1}	$\log_{10}$(A) s^{-1}	Model parameters
Cn-X	0.9977	1.00	164.3	8.374	n = 2.652, $\log_{10}(K_{cat})$ = 2.340, autocatalysis by product: X = α
Bna	0.9972	1.26	163.7	10.58	n = 2.566, r = 0.819
An	0.9874	5.56	162.3	9.546	n = 1.554
A2	0.9859	6.22	151.8	8.751	
Fn	0.9829	7.53	201.9	12.55	n = 1.08

The multi-parameter models Cn-X and Bna are helpful for global kinetics calculations broadly used in chemical reaction engineering applications, e.g. reactor design. Insight into intrinsic kinetics and reaction mechanism, though, is easier achieved by applying simpler models with physico-chemical background. As shown in the plot of the standard free reaction energy (Figure 3-1), reduction of iron carbonate according to Eq. 3 is expected to proceed at lower temperatures than the decomposition of magnesium, manganese, and calcium carbonate (see Eq. 14). This behavior, expected from thermodynamics, can be experimentally confirmed by the shape of the thermogravimetric curves shown in Figure 3-3. The iron carbonate reduction is represented by a distinct mass loss Δm_{TG1} below 450 °C, which is followed by small relative mass loss Δm_{TG2} spanning over a broad temperature range (450-650 °C). The second mass loss Δm_{TG2} can be allocated to the concomitant decomposition of manganese, magnesium, and calcium carbonate. This proposed reaction mechanism is confirmed by the results of the model-free kinetics analysis. The shoulder in the E_α vs. α plot of the model-free analysis at a conversion of 0.8-0.9 (Figure 3-4) is a strong indication for two separable, independent reactions. Thus, a limitation of the evaluated conversion range for model regression should result in an improvement of the goodness of fit for simple reaction models that describe the single step iron carbonate reduction according to Eq. 3.

Table 3-3 shows that the n^{th}-dimensional Avrami-Erofeev models An and the n^{th} order model Fn produced the best results for single step kinetic models. For both models, the evaluation range for the regression analysis was gradually reduced to α=0.8 (Table 3-5). The dimension n_{AE} of the An model converged to 2, as the evaluated conversion range was reduced. For the Fn model, on the contrary, the order n diverged from approximately one for α=0.01-0.99 to values below 0.01 for α=0.01-0.80/0.90. Therefore, the A2 model was further investigated and compared to the Fn model in Tab. 5. E_a and A show a clear increasing tendency with increasing conversion range for the A2 model. E_a and A for the Fn model, however, decrease when the upper limit of the conversion range α_u is increased from 0.80 to 0.90 but increase between α_u=0.90 and α_u=0.99. The correlation coefficient R is significantly higher for the A2 model compared to the Fn model in all evaluated conversion ranges shown in Table 3-5. As a result, the Avrami-Erofeev two dimensional nucleation model A2 is superior to the Fn model in describing the kinetics of the reduction of iron carbonate to iron with hydrogen. The correlation coefficient for the A2 model shows an optimum when the upper boundary of the conversion range $\alpha_{u,opt}$ is between 0.85 and 0.87 (see Table 3-5 and Figure 3-6). This range of $\alpha_{u,opt}$ coincides with the fractional conversion for complete iron carbonate reduction $\alpha_{Fe,calc}$=0.84-0.90 calculated from the elemental analysis (Figure 3-6). Gotor et al. [34] state that n_{AE}=2 describes two reaction mechanisms, depending on the reaction temperature. At low reaction temperatures, nuclei are formed at a constant rate and grow by one-dimensional diffusion. At elevated reaction temperatures, nucleation can be considered instantaneous and growth of nuclei proceeds by two-dimensional diffusion. Thus, it can be concluded that the formation of iron from iron carbonate via hydrogen reduction proceeds via nucleus formation and diffusional growth of nuclei. Nucleus formation and diffusional growth can be controlled by the reaction temperature.

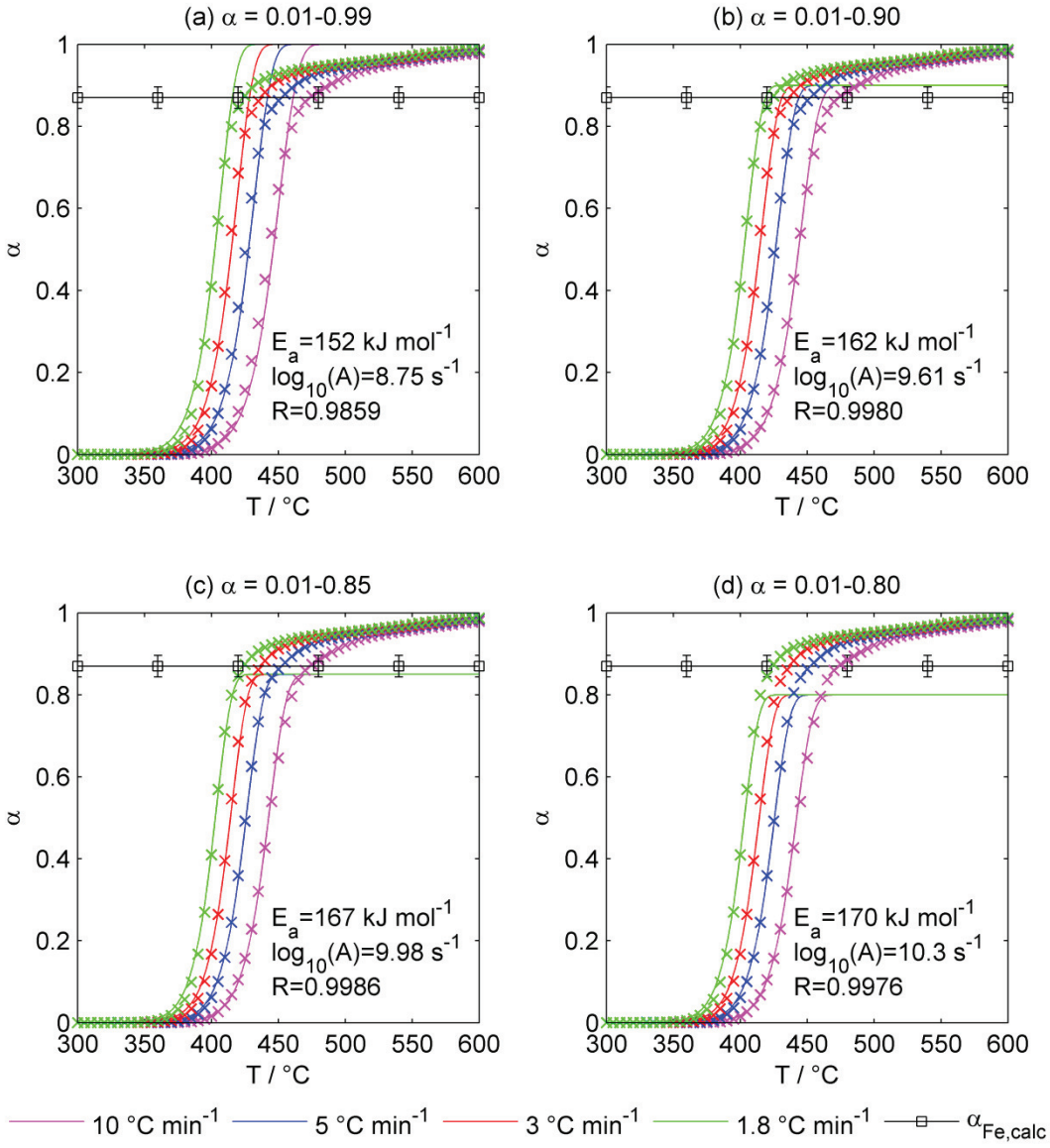

Figure 3-6: Validation of the two-dimensional Avrami-Erofeev model A2 (solid lines) with the experimental TG curves (crosses). The adaption of the evaluated conversion range leads to an optimum between α=0.85. (c) and α=0.90 (d) of the correlation coefficient R in the range of the calculated complete conversion of iron carbonate to iron $\alpha_{Fe,calc}$ (black line with squares and error bar). Experimental conditions for TG: 20 ± 2 mg, 100 $cm^3 min^{-1}$ total inlet gas flow (70 % H2 + 30 % N2).

Table 3-5: Dependency of the correlation coefficient R, the activation energy E_a, and frequency factor A on the evaluated conversion range for the two-dimensional Avrami-Erofeev model A2 and the n^{th}-order model Fn.

α	A2: $f(\alpha)= 2(1-\alpha)[-\ln(1-\alpha)]^{1/2}$			Fn: $f(\alpha)=(1-\alpha)^n$			
	R	E_a kJ mol^{-1}	$\log_{10}(A)$ s^{-1}	R	E_a kJ mol^{-1}	$\log_{10}(A)$ s^{-1}	n
0.01-0.80	0.9976	170.1	10.27	0.9768	185.4	11.23	0.000116
0.01-0.83	0.9983	168.1	10.11	0.9797	183.1	11.03	0.000213
0.01-0.85	0.9986	166.6	9.98	0.9824	182.4	10.97	0.00445
0.01-0.87	0.9987	164.9	9.84	0.9848	180.8	10.83	0.000153
0.01-0.90	0.9980	162.2	9.61	0.9868	177.5	10.56	0.000153
0.01-0.99	0.9859	151.8	8.75	0.9830	201.8	12.55	1.084

3.3.6 Process concept and comparison to the state-of-the-art

The Cn-X model parameters found in the regression analysis can be used to predict the shape and trend of the conversion of CS according to Eq. 3 and 14 with time at fixed temperature (Figure 3-7). After the same reaction time, conversion increases with temperature. Even at temperatures that can be considered to be low for metallurgical processes, e.g. 450 °C, industrially relevant conversions of more than 95 % can be obtained within less than 60 minutes reaction time. For comparison, the Midrex© process for direct iron oxide reduction (DIOR) with natural gas is run at 780-900 °C [47] and a typical blast furnace (BF) is run at more than 1500 °C [16]. Direct hydrogen reduction of mineral iron carbonates can save up to 33 % of the reducing agent compared to the established iron production routes (BF, DIOR) due to the abolition of sinter production (= roasting in air, Eq. 1). Due to its magnetic properties, iron can be easily separated from MgO, MnO, CaO, and SiO_2 by magnetic separation (Figure 3-8) and processed in the steel mill. The off-gas of the reduction reactor, as depicted in Figure 3-8, consists of carbon dioxide, water, and excess hydrogen if the reduction reactor is run at $n(H_2):n(FeCO_3) > 1$. By virtue of its chemical nature conversion of iron carbonate into iron is always coupled to the emission of 1 mole of CO_2 per mole of iron produced (Eq. 3). Two possible ways for carbon dioxide mitigation are conceivable: (1) carbon capture and storage and (2) carbon dioxide utilization. Carbon dioxide utilization is preferable, as this could possibly add value to the whole process.

Owing to the fact, that hydrogen is already used for iron carbonate reduction and available on-site, catalytic carbon dioxide hydrogenation (CCDH) is suggested (green frame in Figure 3-8). The reduction reactor shown in Figure 3-8 can either be run with the stoichiometric amount of hydrogen ($n(H_2)$: $n(FeCO_3)=1$), or with excess hydrogen for the CCDH reactor. A variety of products is accessible with CCDH [17-19]: methanol, methane, higher hydrocarbons via Fischer-Tropsch-Synthesis, etc. Evaluation of the most suitable final product depends on environmental and economic factors and is out of the scope of this paper. Moreover, heat recovery can be achieved by transferring the heat of reaction produced in exothermal CCDH reactions, for instance methane synthesis (Eq. 10) or higher hydrocarbon formation via RWGS and Fischer-Tropsch synthesis (Eq. 11), to the reduction reactor.

$$CO_2 + 4\,H_2 \rightarrow CH_4 + 2\,H_2O \qquad \Delta_R H_{573K} = -177\ \text{kJ mol}^{-1} \qquad (4)$$

$$CO_2 + 3\,H_2 \rightarrow -CH_2- + 2\,H_2O \qquad \Delta_R H_{573K} = -128\ \text{kJ mol}^{-1} \qquad (5)$$

Baldauf-Sommerbauer et al. [48] could show that reductive calcination of mineral magnesium carbonate in 90 % hydrogen produces a temperature- and pressure-dependent mixture of CO, CH_4, and CO_2. Jagadeesan et al. revealed that synthetic $(Fe,Ca)(CO_3)_2$ can be directly converted into methane [49] and C1-C3[50] hydrocarbons [50] when heated to 300-600 °C in 100 % H_2 flow. Thus, it can be expected that partial conversion of carbon dioxide into CO, CH_4, and/or higher hydrocarbons is possible already in the reduction reactor.

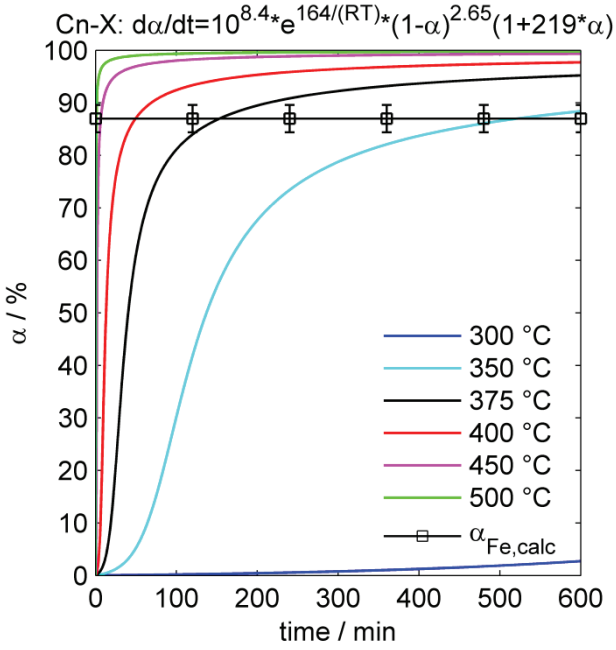

Figure 3-7: Prediction of the conversion α of CS into iron and Ca-, Mg-, and Mn-oxide based on the Cn-X model with the best parameters found in the regression analysis. At a total conversion of 87 ± 3 %, quantitative iron carbonate conversion to iron ($\alpha_{Fe,calc}$) can be expected, the remaining 13 ± 3 % of conversion are attributed to the conversion of calcium, magnesium, and manganese carbonate to the respective oxide.

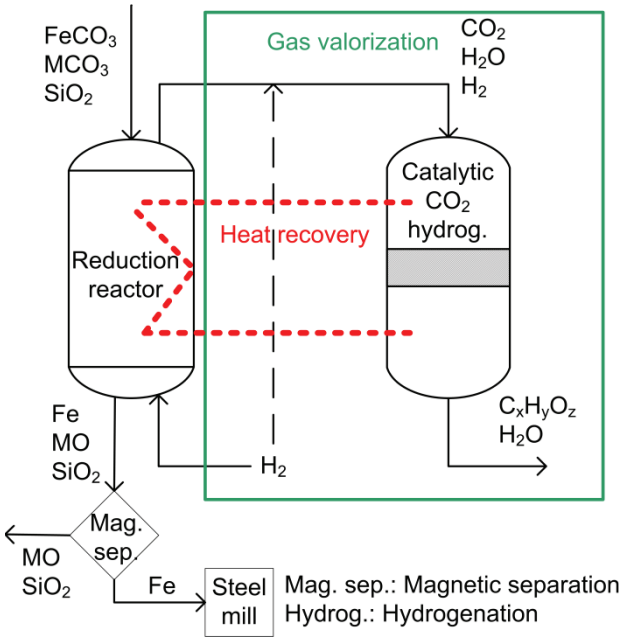

Figure 3-8: Process concept for the direct hydrogen reduction of mineral iron carbonate coupled to catalytic carbon dioxide hydrogenation.

3.4 Conclusions

The production of iron and steel is one of the most energy- and emission-intensive industrial branches worldwide. Consequently, CO_2 breakthrough technologies have to be developed and improved to substantially decrease the CO_2^e emission from this sector. The direct hydrogen reduction of mineral iron carbonate was proven feasible and can be considered such a breakthrough technology that could foster green steelmaking. Multi-parameter kinetic models (Cn-X, Bna) can be applied to predict the conversion of mineral iron carbonate into iron and matrix calcium, magnesium, and manganese carbonate into oxides. The iron carbonate reduction to iron can be described with the two-dimensional Avrami-Erofeev A2 model. As a consequence, a temperature controlled nucleation and diffusional growth mechanism for iron formation from iron carbonate in hydrogen atmosphere is proposed. Compared to the state-of-the-art, iron carbonate beneficiation via direct hydrogen reduction can save up to 60 % of the CO_2 emissions and 33 % of the reducing agent. Compared to other metallurgical iron carbonate beneficiation processes (BF, DIOR), direct hydrogen reduction can be run at relatively low (400-500 °C) temperatures. Furthermore, a concept is outlined to recycle inevitably produced carbon dioxide by catalytic carbon dioxide hydrogenation (CCDH). Exothermal CCDH reactions can provide the necessary heat for direct hydrogen reduction of mineral iron carbonate.

Acknowledgements

The project 'Reduzierende Kalzinierung' is funded by the Austrian 'Klima- und Energiefond' in the framework of the program 'ENERGY MISSION AUSTRIA'. The authors wish to thank Dr. H. Schmid (voestalpine Stahl GmbH, Austria) and Dr. A. Stadtschnitzer (VA Erzberg GmbH, Austria) for their valuable collaboration in the course of the project 'Reduzierende Kalzinierung'. The authors gratefully acknowledge the support from the NAWI Graz program. Thanks are also due to W. Aniser for his support in the performance of the experiments.

References

[1] IPCC, Climate Change 2014 Synthesis Report, Geneva, 2014.

[2] J.M. Allwood, J.M. Cullen, R.L. Milford, Options for achieving a 50% cut in industrial carbon emissions by 2050, Environ. Sci. Technol. 44 (2010) 1888–1894. doi:10.1021/es902909k.

[3] M.A. Quader, S. Ahmed, R.A.R. Ghazilla, S. Ahmed, M. Dahari, A comprehensive review on energy efficient CO2 breakthrough technologies for sustainable green iron and steel manufacturing, Renew. Sustain. Energy Rev. 50 (2015) 594–614. doi:10.1016/j.rser.2015.05.026.

[4] S. Pauliuk, R.L. Milford, D.B. Mu, J.M. Allwood, The Steel Scrap Age, Environ. Sci. Technol. 47 (2013) 3448–3454. doi:10.1021/es303149z.

[5] M. Fischedick, J. Marzinkowski, P. Winzer, M. Weigel, Techno-economic evaluation of innovative steel production technologies, J. Clean. Prod. 84 (2014) 563–580. doi:10.1016/j.jclepro.2014.05.063.

[6] J. Fu, G. Tang, R. Zhao, W. Hwang, Carbon reduction programs and key technologies in global steel industry, J. Iron Steel Res. Int. 21 (2014) 275–281. doi:10.1016/S1006-706X(14)60042-X.

[7] N. Pardo, J.A. Moya, Prospective scenarios on energy efficiency and CO2 emissions in the European Iron & Steel industry, Energy. 54 (2013) 113–128. doi:10.1016/j.energy.2013.03.015.

[8] M. Abdul Quader, S. Ahmed, S.Z. Dawal, Y. Nukman, Present needs, recent progress and future trends of energy-efficient Ultra-Low Carbon Dioxide (CO2) Steelmaking (ULCOS) program, Renew. Sustain. Energy Rev. 55 (2016) 537–549. doi:10.1016/j.rser.2015.10.101.

[9] United Nations Framework Convention on Climate Change FCCC/CP/2015/L.9, Adoption of the Paris Agreement, Paris, 2015.

[10] U. N. conference on Trade and Development, Iron ore statistics 2013, New York/Geneva, 2013.

[11] Monthly crude steel production 2015 and 01-06/2016, http://www.worldsteel.org/statistics/statistics-archive/monthly-steel-archive.html (accessed July 2016).

[12] Monthly iron production 2015 and 01-06/2016, http://www.worldsteel.org/statistics/statistics-archive/monthly-steel-archive.html (accessed July 12, 2016).

[13] D. Zhu, X. Zhou, J. Pan, Y. Luo, Direct reduction and beneficiation of a refractory siderite lump, Miner. Process. Extr. Metall. 123 (2014) 246–250. doi:10.1179/1743285514Y.0000000081.

[14] A. Boehm, M. Boehm, A. Kogelbauer, Neutrons for mineral processing - Thermo diffractometry to investigate mineral selective magnetizing flash roasting, Chemie Ing. Tech. 86 (2014) 883–890. doi:10.1002/cite.201400024.

[15] F. Oeters, M. Ottow, D. Senk, A. Beyzavi, J. Gunther, H.B. Lungen, et al., Iron, 1. Fundamentals and principles of reduction processes, Ullmann's Encycl. Ind. Chem. 19 (2011) 578–655. doi:10.1002/14356007.a14_461.pub5.

[16] H.B. Lüngen, J.-I. Yagi, Iron, 2. Blast furnace process, Ullmann's Encycl. Ind. Chem. 19 (2012) 657–707. doi:10.1002/14356007.o14_o01.

[17] I. Dimitriou, P. García-Gutiérrez, R.H. Elder, R.M. Cuéllar-Franca, A. Azapagic, R.W.K. Allen, Carbon dioxide utilisation for production of transport fuels: process and economic analysis, Energy Environ. Sci. 8 (2015) 1775–1789. doi:10.1039/C4EE04117H.

[18] M.D. Porosoff, B. Yan, J.G. Chen, Catalytic reduction of CO2 by H2 for synthesis of CO, methanol and hydrocarbons: Challenges and opportunities, Energy Environ. Sci. (2016) 62–73. doi:10.1039/c5ee02657a.

[19] W. Wang, S. Wang, X. Ma, J. Gong, Recent advances in catalytic hydrogenation of carbon dioxide., Chem. Soc. Rev. 40 (2011) 3703–27. doi:10.1039/c1cs15008a.

[20] D. Zhu, Y. Luo, J. Pan, X. Zhou, Reaction mechanism of siderite lump in coal-based direct reduction, High Temp. Mater. Process. 35 (2016) 185–194. doi:10.1515/htmp-2014-0176.

[21] G. Gahleitner, Hydrogen from renewable electricity: An international review of power-to-gas pilot plants for stationary applications, Int. J. Hydrogen Energy. 38 (2013) 2039–2061. doi:10.1016/j.ijhydene.2012.12.010.

[22] S. Dutta, A review on production, storage of hydrogen and its utilization as an energy resource, J. Ind. Eng. Chem. 20 (2013) 1148–1156. doi:10.1016/j.jiec.2013.07.037.

[23] R. Chaubey, S. Sahu, O.O. James, S. Maity, A review on development of industrial processes and emerging techniques for production of hydrogen from renewable and sustainable sources, Renew. Sustain. Energy Rev. 23 (2013) 443–462. doi:10.1016/j.rser.2013.02.019.

[24] K. Christopher, R. Dimitrios, A review on exergy comparison of hydrogen production methods from renewable energy sources, Energy Environ. Sci. 5 (2012) 6640. doi:10.1039/c2ee01098d.

[25] O. Bičáková, P. Straka, Production of hydrogen from renewable resources and its effectiveness, Int. J. Hydrogen Energy. 37 (2012) 11563–11578. doi:10.1016/j.ijhydene.2012.05.047.

[26] T. Abbasi, S.A. Abbasi, "Renewable" hydrogen: Prospects and challenges, Renew. Sustain. Energy Rev. 15 (2011) 3034–3040. doi:10.1016/j.rser.2011.02.026.

[27] A. Pineau, N. Kanari, I. Gaballah, Kinetics of reduction of iron oxides by H2. Part I: Low temperature reduction of hematite, Thermochim. Acta. 447 (2006) 89–100. doi:10.1016/j.tca.2005.10.004.

[28] A. Pineau, N. Kanari, I. Gaballah, Kinetics of reduction of iron oxides by H2. Part II. Low temperature reduction of magnetite, Thermochim. Acta. 456 (2007) 75–88. doi:10.1016/j.tca.2007.01.014.

[29] H. Zuo, C. Wang, J. Dong, K. Jiao, R. Xu, Reduction kinetics of iron oxide pellets with H2 and CO mixtures, Int. J. Miner. Metall. Mater. 22 (2015) 688–696. doi:10.1007/s12613-015-1123-x.

[30] F. Chen, Y. Mohassab, S. Zhang, H.Y. Sohn, Hydrogen reduction kinetics of hematite concentrate particles relevant to a novel flash ironmaking process, Metall. Mater. Trans. B Process Metall. Mater. Process. Sci. 46 (2015) 1133–1145. doi:10.1007/s11663-015-0332-z.

[31] A.P. Dhupe, A.N. Gokarn, Studies in the thermal decomposition of natural siderites in the presence of air, Int. J. Miner. Process. 28 (1990) 209–220.

[32] D. Alkaç, Ü. Atalay, Kinetics of thermal decomposition of Hekimhan-Deveci siderite ore samples, Int. J. Miner. Process. 87 (2008) 120–128. doi:10.1016/j.minpro.2008.02.007.

[33] S.B. Jagtap, A. R. Pande, A. N. Gokarn, Kinetics of thermal decomposition of siderite: effect of particle size, Int. J. Miner. Process. 36 (1992) 113–124. doi:10.1016/0301-7516(92)90068-8.

[34] J.M. Criado, F.J. Gotor, M. Macias, A. Ortega, J. Criado, Comparative study of the kinetics of the thermal decomposition of synthetic and natural siderite samples, Phys. Chem. Miner. 27 (2000) 495–503. doi:10.1007/s002690000093.

[35] V.Y. Zakharov, Z. Adonyi, Thermal decomposition kinetics of siderite, Thermochim. Acta. 102 (1986) 101–107.

[36] Y.-L. Pang, G.-X. Xiao, S.-W. Jiu, Study on thermal decomposition kinetics of siderite, Xi'an Jianzhu Keji Daxue Xuebao/Journal Xi'an Univ. Archit. Technol. 39 (2007) 136–139+144.

[37] Z.L. Feng, Y. Yu, G. Liu, W. Chen, Thermal decomposition kinetics of siderite in nitrogen, Wuhan Ligong Daxue Xuebao/Journal Wuhan Univ. Technol. 31 (2009) 11–14. doi:10.3963/j.issn.1671-4431.2009.17.004.

[38] Z. Feng, Y. Yu, G. Liu, W. Chen, Kinetics of the thermal decomposition of Wangjiatan siderite, J. Wuhan Univ. Technol. Sci. Ed. 26 (2011) 523–526. doi:10.1007/s11595-011-0261-x.

[39] S. Vyazovkin, A.K. Burnham, J.M. Criado, L. a. Pérez-Maqueda, C. Popescu, N. Sbirrazzuoli, ICTAC Kinetics Committee recommendations for performing kinetic computations on thermal analysis data, Thermochim. Acta. 520 (2011) 1–19. doi:10.1016/j.tca.2011.03.034.

[40] S. Vyazovkin, K. Chrissafis, M.L. Di Lorenzo, N. Koga, M. Pijolat, B. Roduit, et al., ICTAC Kinetics Committee recommendations for collecting experimental thermal analysis data for kinetic computations, Thermochim. Acta. 590 (2014) 1–23. doi:10.1016/j.tca.2014.05.036.

[41] T. Ozawa, A new method of analyzing thermogravimetric data, Bull. Chem. Soc. Japan 38 (1965) 1881–1886. doi:10.1246/bcsj.38.1881.

[42] J.H. Flynn, L.A. Wall, General treatment of the thermogravimetry of polymers, J. Res. Natl. Bur. Stand. Sect. A Phys. Chem. 70A (1966) 487. doi:10.6028/jres.070A.043.

[43] T. Akahira, T. Sunose, Method of determining activation deterioration constant of electrical insulating materials, Res. Rep. Chiba Inst. Technol. (Sci. Technol.). 16 (1971) 22–31.

[44] H.L. Friedman, Kinetics of thermal degradation of char-forming plastics from thermogravimetry. Application to a phenolic plastic, J. Polym. Sci. Part C Polym. Symp. 6 (1964) 183–195. doi:10.1002/polc.5070060121.

[45] J. Opfermann, Kinetic analysis using multivariate non-linear regression, J. Therm. Anal. Calorim. 60 (2000) 641–658. doi:10.1023/A:1010167626551.

[46] S. Vyazovkin, A time to search: finding the meaning of variable activation energy, Phys. Chem. Chem. Phys. 18 (2016) 18643–18656. doi:10.1039/C6CP02491B.

[47] L. Formanek, F. Rose, J. Prölß, Iron , 3 . Direct reduction processes, Ullmann's Encycl. Ind. Chem. 20 (2013) 1–14. doi:10.1002/14356007.o14_o02.pub2.

[48] G. Baldauf-Sommerbauer, S. Lux, W. Aniser, M. Siebenhofer, Reductive calcination of mineral magnesite: hydrogenation of carbon dioxide without catalysts, Chem. Eng. Technol. 39 (2016) 2035–2041. doi:10.1002/ceat.201600094.

[49] D. Jagadeesan, M. Eswaramoorthy, C.N.R. Rao, Investigations of the conversion of inorganic carbonates to methane., ChemSusChem 2 (2009) 878–82. doi:10.1002/cssc.200900152.

[50] D. Jagadeesan, Y. Sundarayya, G. Madras, C.N.R. Rao, Direct conversion of calcium carbonate to C1-C3 hydrocarbons, RSC Adv. 3 (2013) 7224–7229. doi:10.1039/c3ra40264a.

4 Reductive calcination and its application to mineral iron carbonate beneficiation

Abstract

A generalized reaction equation for the reductive calcination of metal carbonates is introduced. The chemical thermodynamics of the reductive calcination of iron and magnesium are discussed. The influence of temperature and pressure on equilibrium conversion is reviewed together with the accessible products. Results from the reductive calcination of mineral iron carbonate in a tubular reactor setup are presented. An optimization of the methane yield via design of experiments is discussed. A first approach for the reaction kinetics of the reductive calcination of mineral Mg-Mn siderite is depicted, as well as the design of a tube bundle reactor. Results from the reductive calcination of two different mineral magnesium carbonates will be presented in chapters 5 and 6.

Greek symbols

$\Delta_R G°$	kJ mol^{-1}	Standard free energy of reaction
Δm_i	-	Mass loss: reference (i=ref), experiment (i=exp)
$\Delta n_{i,j}$	mmol	Amount of substance i in stream j
Δt	s	Time segment of data recording (=5 s)
ϵ_i	-	Generalized stoichiometric coefficient
ρ_{ICM}	g cm^{-3}, t m^{-3}	Apparent density of the ICM
τ_{MD}	-	Molar ratio of carbon monoxide and carbon dioxide

Symbols

A	min^{-1}	Pre-exponential factor for Arrhenius approach
$c_{i,j}$	%vol.	Concentration of compound i in stream j
$d_{j,i}$	%	y-axis intercept for either pre-factor (j=a) or order (j=b) for compound i
d_R	m	Diameter of one reactor tube
d_{tot}	m	Diameter of tube bundle reactor
E_a	kJ mol^{-1}	Activation energy
F	cm$^3_{STP}$min^{-1}	Feed flow rate; feed
$f(X_i)$	-	Reaction model
f_{ref}	-	Margin of error, reference line in DoE bar plots
f_{SP}	-	Split factor
f_D	-	Tube distance factor
$g(X_i)$	-	Integral form of the reaction model f
h_R	m	Height of one reactor tube
$h_{ICM,TR}$	mm	Bed height of ICM in the reactor tube for TR experiments
ID_{RT}	mm	Inner diameter of the TR
k(T)	min^{-1}	Arrhenius approach
m_i	g	Mass of compound i
$\dot{m}_{i,j,R}$	t m^{-3} h^{-1}	Mass flow of the compound i in the stream j for one reactor tube
$\dot{m}_{ICM,tot}$	t year^{-1}	Total throughput of ICM
N_R	-	Number of reactor tubes
$N_{R,tot}$	-	Number of reactor tubes in circular tube bundle reactor
$n_{i,t}$	(m)mol	Molar amount of compound i at time t
$n_{Sid,0}$	(m)mol	Amount of Mg-Mn siderite present in the starting material
OC_{TC}	mm	Outer diameter of the thermocouple casing
P	cm$^3_{STP}$min^{-1}	Product flow rate; product stream
R^2	-	Coefficient of determination
R_{gas}	kJ mol^{-1} K^{-1}	Ideal gas constant
$r_{WM,GA}$	-	Weight ratio of wuestite to magnetite calculated from gas analysis
$s_{j,i}$	% K^{-1}	Slope for either pre-factor (j=a) or order (j=b) for compound i
t_{react}	min	Reaction time, calculated with Eq. 33
T	°C, K	Temperature
T_{tar}	°C, K	Target temperature
T1-T6	-	Temperature measured inside the reactor tube from top (T6) to bottom (T1)
V_n	dm^{3}mol^{-1}	Molar volume = 22.414 for STP
v_s	m h^{-1}	Sinking rate
$x_{i,j}$	-	Mole fraction of compound i in stream j
$X_{ICM\text{-}WM,ml}$		Relative conversion of Mg-Mn siderite present in ICM into a solid product containing wuestite and magnetite, calculation based on ratio of experimental to reference mass loss according to Eq. 22

$X_{Sid\text{-}Ox,t}$		Relative, time dependent conversion of Mg-Mn xiderite present in ICM into Mg-Mn iron oxides according to Eq. 24
Y_i	%, -	Yield of compound i

Abbreviations

barg	Bar gauge, overpressure
C1	Compound containing one carbon atom
DoE	Design of experiments
Exp[Nr].	Abbreviation used to refer to a specific experiment
ICM	Iron carbonate mineral
ICP-OES	Inductively-coupled-plasma optical-emission-spectroscopy
MW	Molecular weight
P	Product stream
PSE	Lenth Pseudo-Standard-Error
r.h.s.	Right hand side
RWGS	Reverse water-gas-shift
SEP	Siderite enriched phase of the ICM
STP	Standard temperature and pressure, 0 °C and 1.013 bar absolute
wt.	Weight
TG	Thermogravimetry, thermogravimetric
TOC	Total organic carbon
TR	Tubular reactor (used in the experiments)
vol.	Volume
XRD	X-ray diffraction
XRF	X-ray fluorescence spectroscopy

4.1 Introduction

The term *reductive calcination* describes the conversion of a metal carbonate into a metal oxide or elemental metal via calcination in hydrogen atmosphere (Eq. 1). Thus, it is a combination of carbonate calcination (Eq. 2) and/or carbonate reduction (Eq. 3) with carbon dioxide hydrogenation (Eq. 4). Solely the formation of products containing one carbon atom (= C1 products) will be considered. Reductive calcination is applicable to any carbonate within thermodynamic feasibility. In this thesis, the focus lies on iron and magnesium carbonate (M = Fe and Mg).

$$(a+b)MCO_3 + \left[(a+b)\left(\frac{c}{2}+d\right)+b\right]H_2 \rightarrow$$

$$a\,MO + b\,M + (a+b)CH_cO_{2-d} + [b+d(a+b)]H_2O \quad (1)$$

$$a\,MCO_3 \rightarrow a\,MO + a\,CO_2 \quad (2)$$

$$b\,MCO_3 + b\,H_2 \rightarrow b\,M + b\,CO_2 + b\,H_2O \quad (3)$$

$$CO_2 + \left(\frac{c}{2}+d\right)H_2 \rightarrow CH_cO_{2-d} + d\,H_2O \quad (4)$$

4.2 Chemical thermodynamics of the reductive calcination of magnesium carbonate and iron carbonate

4.2.1 Influence of temperature on the equilibrium composition

Figure 2-1 shows that the standard free energy of reaction $\Delta_R G°$ for the formation of the bivalent iron oxide FeO (wuestite) and the mixed bi/trivalent oxide Fe_3O_4 (magnetite) is in a comparable range and that the formation of FeO and Fe_3O_4 is favored over the formation of Fe_2O_3 (hematite). Magnesium carbonate is not known to form stable oxides other than the bivalent MgO. Furthermore, the reduction of $MgCO_3$ with hydrogen to form elemental magnesium according to Eq. 3 is thermodynamically not feasible below 2000 °C. The formation of elemental iron is feasible from a thermodynamic point of view, whereas iron oxide formation is slightly favored over iron formation. Due to the difference in $\Delta_R G°$ the calcination temperature can be expected to be 200-300 °C higher for magnesium carbonate compared to iron carbonate (see Figure 4-1). The general Eq. 4 for the hydrogenation of carbon dioxide to C1 products can be applied to represent the formation of carbon monoxide (Eq. 5), formic acid (Eq. 6), formaldehyde (Eq. 7), methanol (Eq. 8), and methane (Eq. 9).

$$CO_2 + H_2 \rightarrow CO + H_2O \quad (5)$$

$$CO_2 + H_2 \rightarrow HCOOH \quad (6)$$

$$CO_2 + 2\,H_2 \rightarrow HCHO + H_2O \quad (7)$$

$$CO_2 + 3\,H_2 \rightarrow H_3COH + H_2O \quad (8)$$

$$CO_2 + 4H_2 \rightarrow CH_4 + 2\,H_2O \quad (9)$$

The temperature dependency of $\Delta_R G°$ for the hydrogenation reactions (Eq. 5-9) is approximately linear in the range T = 0-1000 °C at ambient pressure (Table 4-1). In the case of CO formation (Eq. 5, also referred to as reverse water-gas-shift RWGS) $\Delta_R G°$ decreases with temperature, whereas for all other reactions (Eq. 6-9) $\Delta_R G°$ increases. The formation of formic acid and formaldehyde is thermodynamically not favorable, as $\Delta_R G°$ is above + 40 kJ mol^{-1} at 0 °C and increases with temperature. Methanol formation could proceed at low temperatures (<150 °C) as $\Delta_R G°$ is ~ 0 at 0 °C, but it shows a strong increase with temperature ($d(\Delta_R G°)/dT$ = 0.2 kJ mol^{-1} °C^{-1}). Methane formation is highly favorable below 450 °C ($\Delta_R G°_{450\,°C}$ = -30 kJ mol^{-1}) and shows a gradient of $d(\Delta_R G°)/dT$ = 0.2 kJ mol^{-1} °C^{-1}, comparable to methanol formation. Carbon monoxide formation can be expected in the whole temperature range evaluated (0-1000 °C) as $\Delta_R G°$ decreases with a low gradient of $d(\Delta_R G°)/dT$ = -0.04 kJ mol^{-1} °C^{-1} compared to the other products (HCOOH, HCHO, H_3COH, CH_4) from approx. +30 kJ mol^{-1} at 0 °C to approx. -5 kJ mol^{-1} at 1000 °C.

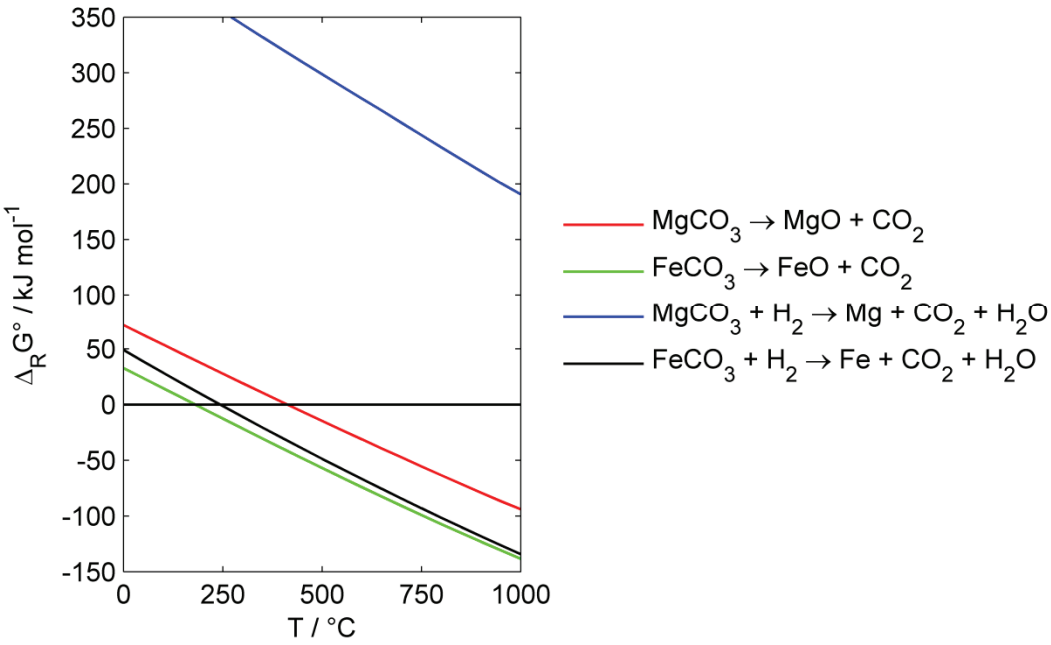

Figure 4-1: Standard free energy of reaction $\Delta_R G°$ for the conversion of magnesium and iron carbonate into bivalent oxides and elements at ambient pressure. Calculations were performed with HSC Chemistry 8.0.6 assuming formation of gaseous CO_2 and H_2O.

Table 4-1: Linear fit data to temperature dependency of $\Delta_R G°$ for the formation of carbon monoxide (CO, Eq. 5), formic acid (HCOOH, Eq. 6), formaldehyde (HCHO, Eq. 7), methanol (H_3COH, Eq. 8), and methane (CH_4, Eq. 9).

	Slope kJ mol^{-1} °C^{-1}	y-axis intercept kJ mol^{-1}	R^2
CO	-0.035	28.54	0.9974
HCOOH	0.106	40.62	0.9999
HCHO	0.087	58.90	0.9984
H_3COH	0.209	-4.81	0.9994
CH_4	0.210	-122.3	0.9991

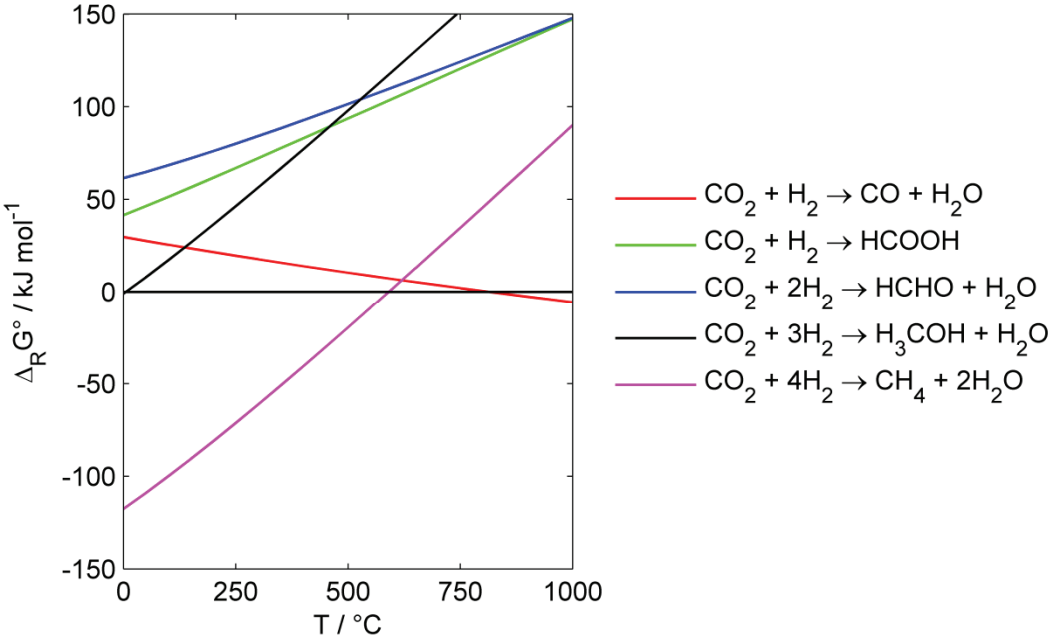

Figure 4-2: Standard free energy of reaction $\Delta_R G°$ for the hydrogenation of carbon dioxide to produce carbon monoxide (red), formic acid (green), formaldehyde (blue), methanol (black), and methane (magenta) at ambient pressure. Calculations were performed with HSC Chemistry 8.0.6 assuming gaseous compounds.

4.2.2 Influence of pressure on the equilibrium composition

A first insight into the influence of an increase in pressure to a closed reaction system can be evaluated by applying Le Chatelier's principle assuming ideal gas behavior. A stoichiometric equation can be generalized as expressed in Eq. 10 for i compounds I with the respective stoichiometric coefficient ϵ_i. The stoichiometric coefficient is positive for products and negative for reactants.

$$\sum_i \epsilon_i I = 0 \qquad (10)$$

As a first approximation, volume changes can be neglected for liquid and solid reactants and products. Therefore, change of reaction volume in a closed system only depends on the change

of gaseous reactants. A positive change in gaseous reactants ($\sum_i \epsilon_i(\text{gaseous}) > 0$) would lead to a volume increase, a negative change in gaseous reactants ($\sum_i \epsilon_i(\text{gaseous}) < 0$) would lead to a volume decrease. For a closed system, Le Chatelier's principle states that for $\sum_i \epsilon_i(\text{gaseous}) > 0$ the equilibrium product yield would decrease and for $\sum_i \epsilon_i(\text{gaseous}) < 0$ the equilibrium yield would increase when the pressure is increased. Consequently, increase of pressure negatively affects calcination (Eq. 2) and metal formation via reduction with hydrogen (Eq. 3) as $\sum_i \epsilon_i(\text{gaseous}) = 1$ for Eq. 2 and 3 if H_2O is considered to be gaseous. Carbon monoxide formation according to Eq. 5 is not affected by pressure increase as $\sum_i \epsilon_i(\text{gaseous}) = 0$. The equilibrium yield of formic acid (Eq. 6), formaldehyde (Eq. 7), methanol (Eq. 8), and methane (Eq. 9) can be expected to be increased by pressure as $\sum_i \epsilon_i(\text{gaseous}) = -1$ if H_2O is considered to be gaseous and even lower if water is partially condensed.

4.3 Investigations on the reductive calcination of mineral iron carbonate

4.3.1 Materials and methods

The iron carbonate mineral (ICM) from the Erzberg (Austria) was supplied by VA Erzberg GmbH in four size ranges: 0.5-1 mm, 1-2 mm, 2-5 mm, and 5-10 mm. A 100-200 µm fraction of the material and a siderite enriched phase of the iron carbonate mineral (SEP; for preparation method see section 3.2) were used in the studies presented in chapters 2 and 3. Wavelength dispersive X-ray fluorescence spectroscopy (XRF) was performed by VA Erzberg GmbH on a PW4400 Axios max (Panalytical) device. X-ray diffraction analysis (XRD) was performed at the voestalpine Stahl Linz GmbH on an X'Pert Pro (Panalytical) device using a cobalt radiation source ($K\alpha_1$ = 0.178901 nm, $K\alpha_2$ = 0.179290 nm) and the HighScore Plus software for phase detection and quantification by either the reference intensity ratio (RIR) or Rietveld refinement. Elemental analysis of solid samples was performed by means of ICP-OES (Spectro Acros, Spectro Ametek) at voestalpine Stahl GmbH and by chemical wet analysis (iron determination according to the procedure of Zimmermann-Reinhardt) at VA Erzberg GmbH. The sample preparation method for ICP-OES analysis is described in section 5.5.4. A Netzsch Jupiter STA 449C thermobalance and alumina sample beakers were used in all thermogravimetry (TG) experiments. The organic carbon content of liquid reaction products of tubular reactor (TR) experiments was analyzed by means of automated total organic carbon analysis (TOC-L-CPH, Shimadzu). Nitrogen and hydrogen of 99.999 %vol. grade and carbon dioxide of 99.998 %vol. grade were supplied by AirLiquide. An ABB AO2020 online gas analysis system was used in tubular reactor experiments. Infrared absorption spectroscopy (ABB Uras26) was used to quantify the CO, CO_2, and CH_4 content (0.0-100.0 %vol.). A thermal conductivity module (ABB Caldos27) was used to quantify H_2 (0.0-100.0 %vol.). The online gas analyzer was frequently recalibrated with three different standard gas mixtures containing certified amounts of CO, CO_2, CH_4, H_2, and N_2 supplied by AirLiquide.

Table 4-2: Average value and absolute standard deviation of the elemental composition determined by XRF calculated from 20 samples of the size ranges 0.5-1, 1-2, 2-5, 5-10 mm. The elemental composition of the size range 0.1-0.2 mm was determined by ICP-OES and is taken from Table 2-1.

Size range mm		Fe %wt.	Ca %wt.	Si %wt.	Mg %wt.	Mn %wt.	Al %wt.	S %wt.	P %wt.	Na %wt.	K %wt.
0.5-1	Av.	33.3	4.14	2.70	2.15	1.97	0.80	0.04	0.02	0.02	0.48
	SD	0.2	0.07	0.02	0.01	0.01	0.01	0.00	0.00	0.00	0.01
1-2	Av.	33.1	4.08	2.84	2.16	1.97	0.78	0.03	0.02	0.02	0.47
	SD	0.2	0.06	0.04	0.01	0.01	0.01	0.00	0.00	0.00	0.01
2-5	Av.	33.5	3.82	2.75	2.15	2.00	0.73	0.03	0.02	0.02	0.44
	SD	0.3	0.30	0.11	0.04	0.03	0.04	0.00	0.00	0.00	0.02
5-10	Av.	33.5	3.66	2.78	2.19	2.00	0.72	0.03	0.02	0.02	0.43
	SD	1.0	0.62	0.23	0.10	0.07	0.09	0.01	0.01	0.00	0.05
0.5-10	Av.	33.4	3.92	2.77	2.16	1.99	0.76	0.03	0.02	0.02	0.45
	SD	0.20	0.22	0.06	0.02	0.02	0.04	0.00	0.00	0.00	0.02
0.1-0.2	-	33.5	4.1	2.5	2.4	2.0	0.3	n.d.	n.d.	n.d.	n.d.

n.d. … not determined; Av. … average value; SD … absolute standard deviation

Mercury porosimetry measurements were carried out on a Pascal 140/440 device provided by Thermo Finnigan with mercury in 99.9995 % quality (Roth) and a dry sample mass of ~ 100 mg. Validation of the device and calculation procedures applied to the porosimetry results are described in section 7.2.

The composition of the 100-200 µm size fraction of the ICM used in the study presented in chapter 2 is quite comparable to the composition of the four size fractions (0.5-1, 1-2, 2-5, 5-10 mm) used in the tubular reactor (TR) experiments discussed in this chapter. Table 4-2 shows that iron is the main constituent of the ICM and calcium, silicon, magnesium, and manganese are accompanying elements at a level of 2 to 4 %wt. Aluminum, sulfur, phosphorus, and potassium are present at levels below 0.5 %wt. The variation of the metal content is small as verified by the small values of the absolute standard deviation (see Table 4-2). There is only a minor difference between mean of each size range (e.g. w_{Fe} = 33.3 ± 0.2 for size range 0.5-1 mm) and the mean of the size ranges 0.5-10 mm (e.g. w_{Fe} = 33.4 ± 0.2 for all size ranges). As all samples were taken from the same deposit and do show a comparable elemental distribution, the phase composition is not expected to vary significantly between samples and size ranges. As pointed out in section 2.3.2, iron is present in two different carbonate phases: Mg-Mn-substituted siderite and ankerite, a Ca-Fe-Mg-Mn carbonate with the same crystal structure [1] as dolomite. Mg-Mn-substituted siderite is the main iron containing phase (see Figure 2-2). The iron content is distinctly higher in Mg-Mn siderite compared to ankerite. It is challenging to determine the ratio of siderite to ankerite for each sample of the ICM used in reductive calcination experiments. The reflection signals of dolomite and ankerite overlap in the XRD pattern. Therefore, quantification of phases via the reference intensity ratio (as applied in chapter 2) or Rietveld refinement (as applied in this chapter and chapter 7) is challenging as either dolomite or ankerite has to be used for quantification, as the reflections are hardly to be distinguished. Iron, magnesium, and

manganese are present in both, siderite and ankerite, therefore the elemental analysis cannot be used for distinguishing phases. Decomposition steps encountered in thermogravimetric curves (see Figure 4-8) can give a hint for the phase ratio as siderite decomposes at lower temperature than ankerite. But also in the thermogravimetric approach, a stoichiometric formula for siderite and ankerite is needed to calculate molar compositions.

4.3.1.1 Reactor setup

The setup delineated in Figure 4-3 and pictured in Figure 4-4 to Figure 4-6 was used for tubular reactor experiments described in this chapter and chapters 5, 6, and 7. As chapter 5 and 6 were published as journal articles [2,3], and chapter 7 is intended for publication, comparable sketches can be found in these chapters. A detailed written description of the setup is given in section 5.5.1. A detailed sketch of the reactor tube and the thermocouple positioning can be found in Figure 7-1.

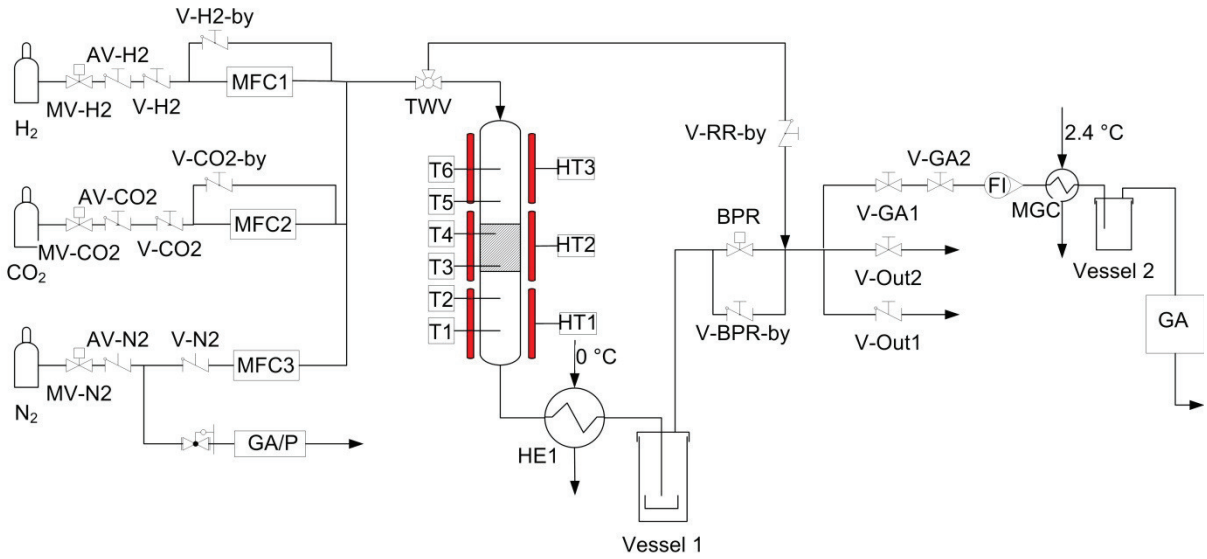

MV-i	…	Magnetic valve	Tj	…	Thermocouple position inside the reactor (j=1-6)
AV-i	…	On-off valve outside the fume hood	HTj	…	Thermocouple position at the reactor outside wall (j=1-3)
V-i	…	On-off valve			
V-i-by	…	On-off valve in a bybass tube	HE	…	Double pipe heat exchanger
TWV	…	Three-way valve	BPR	…	Back pressure regulator
MFC	…	Mass flow controller	FI	…	Rotameter
GA/P	…	Protective gas for gas analyzer	MGC	…	Measuring gas cooler
			GA	…	Gas analyzer

Figure 4-3: Sketch of the tubular reactor setup.

Figure 4-4: Picture of the tubular reactor setup [4] including (from left to right) the online gas analyzer, condensing vessels, double pipe heat exchanger with cryostat, reactor furnace, and process controller.

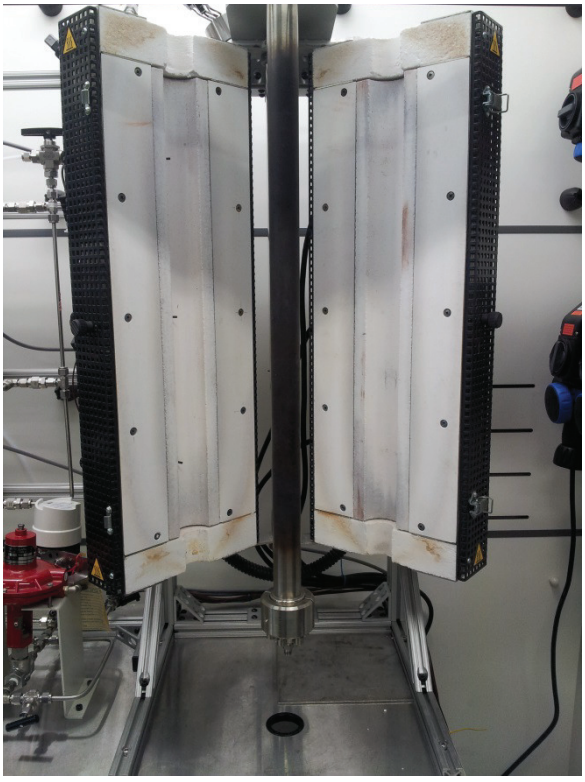

Figure 4-5: Picture of the reactor tube [5] with open heating mantle. The gas enters from top.

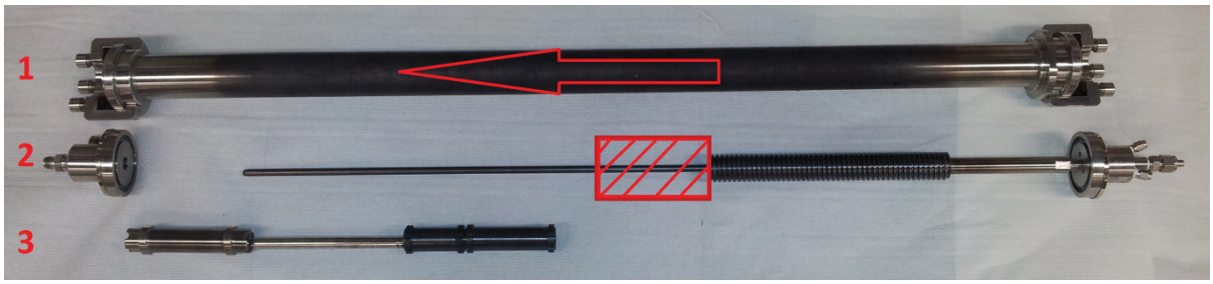

Figure 4-6: Picture of the reactor tube [5] to demonstrate the gas flow direction (1), placement of the solid bed (2), and spacers (3).

Table 4-3: Apparent densities of the four size fractions of the ICM.

Size fraction mm	Apparent density kg m^{-3}
0.5 – 1	1710
1 – 2	1690
2 – 5	1670
5 – 10	1670

4.3.1.2 Experimental procedures for tubular reactor experiments

Stainless steel spacers (see Figure 4-6) were used to place the ICM bed inside the reactor tube. For the size fraction 0.5-1 mm glass wool tori were employed above and below the solid bed, to avoid carry over of the particles. The ICM bed forms a hollow cylinder inside the reactor tube. The bed height h_{ICM} can be estimated with Eq. 11 from the mass m_{ICM}, the apparent density ρ_{ICM}, (~1.69 g cm^{-3}, see Table 4-3) the outer diameter of the thermocouple casing OD_{TC}, and the inner diameter of the reactor tube ID_{RT}.

$$h_{ICM,TR} = \frac{4}{\pi*(ID_{RT}^2 - OD_{TC}^2)} * \frac{m_{ICM}}{\rho_{ICM}} \quad (11)$$

The feed composition of gas mixtures was adjusted with the gas analyzer. The feed gas flow was directed into the gas analyzer, bypassing the reactor tube and the set points of the mass flow controller (MFC) adjusted so that the desired feed gas composition was achieved under the prerequisite that the total flow was as defined. After setting up the desired inlet gas flow, the feed flow was directed into the reactor tube. This procedure was employed to overcome possible deviations of the MFC. The MFC could not be calibrated in-house, whereas the gas analyzer was checked and re-calibrated frequently. Several operation modes were employed:

a) ***Exp1-Exp5***. 104 g of the ICM of the size fraction 2-5 mm were used, corresponding to a height of the ICM bed of 125 mm. The mean value of T3 and T4 was used as T_{tar}, as this was the temperature nearest to the mid of the ICM bed. The feed flow rate was set to 500 $cm^3_{STP}min^{-1}$ and the feed gas composition was either 100 %vol. N_2 or H_2:N_2=9:1. The

shut-off and weighing procedure was the same as for the scanning experiments. Liquid products collected in vessels 1 and 2 (see Figure 4-3) were saved for TOC analysis.

b) *Controlled increase of a target temperature T_{tar}:* ***scanning experiment***. 115 g of the ICM were used, which corresponds to a bed of 147 mm for ρ_{ICM} = 1.685 g cm^{-3} (mean value of the for size ranges). The feed flow rate was set to 500 $cm^3_{STP}min^{-1}$ and the feed gas was either pure N_2 or a mixture of hydrogen and nitrogen with a composition of H_2:N_2=9:1. Starting from room temperature and after an initial heating phase of 25-35 minutes the heating power of all heating zones was adjusted manually, so that the average gradient of the target temperature T_{tar} was at 1.5 K min^{-1}. The mean value of T3 and T4 was used as T_{tar}, as this was the temperature nearest to the center of the ICM bed. When T_{tar} = 530 °C was reached, the reactor was operated at this target temperature for 1 hour before it was flushed with nitrogen and cooled to room temperature overnight. The next day, the solid product was filled into a polypropylene container under nitrogen flow and the output weight determined immediately. Liquid products collected in vessels 1 and 2 (see Figure 4-3) were stored for TOC analysis.

c) ***Steady state*** *reductive calcination for statistically planned (DoE) parameter study*. 60/104 g of ICM were used, corresponding to a height of the ICM bed of 76/132 mm for size fraction 0.5-1 mm and 78/135 mm for size fraction 5-10 mm. The mean value of T3 and T4 was used as T_{tar}, as this was the temperature nearest to the mid of the ICM bed (see Figure 4-7). The feed flow rate was set to 500/867 $cm^3_{STP}min^{-1}$ and the feed gas composition was H_2:N_2=9:1/6:4. The reactor was heated to T_{tar} + 1 = 350/375 °C and operated for 6 hours at the target temperature. The shut-off and weighing procedure was the same as for the scanning experiments. Liquid products collected in vessels 1 and 2 (see Figure 4-3) were saved for TOC analysis.

d) *Reductive calcination at 375-415 °C for* ***kinetic analysis*** *presented in section 4.3.2.3*. 104 g of the 5-10 mm size fraction of the IM were used. The mean value of T3 and T4 was used as T_{tar} and the feed flow was set to 867 $cm^3_{STP}min^{-1}$ with a composition of H_2:N_2=9:1. The reactor was heated to T_{tar} + 1 = 375/395/415 °C and operated for several hours at the target temperature. Experiments were performed at ambient pressure and 8 barg (ovepressure). The shut-off and weighing procedure was the same as for the scanning experiments. Liquid products collected in vessels 1 and 2 (see Figure 4-3) were saved for TOC analysis.

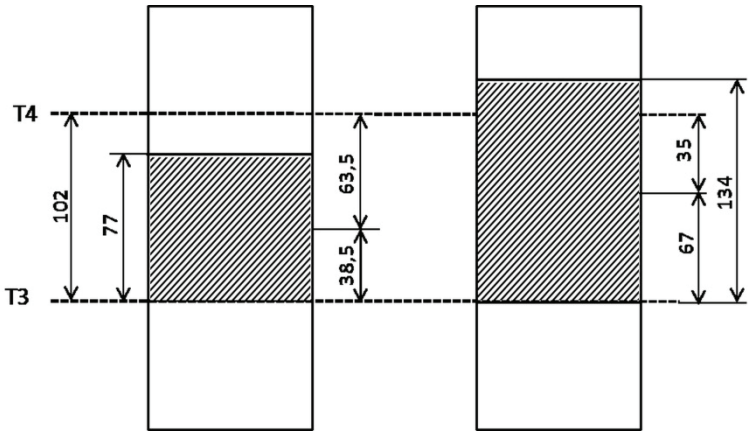

Figure 4-7: Position of the ICM bed [4] for an initial mass of 60 g (left) and 104 g (right). The mean value of the apparent density for the size fractions 0.5-1 mm and 5-10 mm was used to calculate the height of the bed.

4.3.1.3 Design of experiments for statistically planned parameter optimization of methane yield

A two-level fractional factorial 2^{6-1} design for six factors was used. The factors were: A = gauge pressure, B = temperature, C = amount of solid, D = H_2:N_2 feed ratio, E = feed flow rate, and F = size range. The two levels (+/-) for each factor are shown in Table 4-4. Factors A through F were varied under otherwise constant experimental conditions and the effect on mass loss of the solid product (=a measure for the total conversion), CO-, and CH_4-yield was evaluated statistically. The statistical evaluation was performed according to the methodology introduced by Lenth [6] and applied i.a. by Frontistis et al. [7] A fractional design with the generator ABCDE = F was chosen to decrease the number of experiments compared to a full factorial design. A full factorial design for six factors includes 64 experiments, whereas a 2^{6-1} fractional design includes 32 experiments. This design was chosen because of the high information output – no main effects or two-effect interactions are aliased [8] – while the necessary experimental time is cut by half. The Lenth Pseudo-Standard-Error PSE was calculated as described in reference [6].

Table 4-4: Experimental parameters (=factors) that were varied (-/+ level) in the steady state reductive calcination of the ICM in a study planned by design of experiments.

Factor	Dimension	-	+
A: Gauge pressure	bar	0	8
B: Temperature	°C	350	375
C: Amount of solid	g	60	104
D: H_2:N_2 ratio	-	60:40	90:10
E: Feed flow	$cm^3_{STP}min^{-1}$	500	867
F: Size range	mm	0.5-1.0	5-10

The value of the reference line f_{ref} (also referred to as margin of error) in the bar plots (Figure 4-16 to Figure 4-18) was calculated from the PSE and the value $t_{0.95,d}$ 2.22 (for d=31) for a 95 % confidence interval of a standard student T-distribution according to Eq. 12.

$$f_{ref} = PSE * t_{0.95,d} \quad (12)$$

4.3.1.4 Calculation of CO and CH_4 yield

The procedure and equations applied to calculate the amount of carbon monoxide, carbon dioxide, and methane formed during experiments from the online gas analysis of the tubular reactor setup is described in section 5.5.3.1. The yield of carbon monoxide after time t $Y_{CO,t}$ was calculated with Eq. 13 and the yield of methane after time t $Y_{CH4,t}$ was calculated with Eq. 14 from the produced amounts $n_{i,t}$ of CO, CH_4, and CO_2 during the reaction.

$$Y_{CO,t} = \frac{n_{CO,t}}{n_{CO2,t}+n_{CO,t}+n_{CH4,t}} \quad (13)$$

$$Y_{CH4,t} = \frac{n_{CH4,t}}{n_{CO2,t}+n_{CO,t}+n_{CH4,t}} \quad (14)$$

4.3.2 Results and discussion

4.3.2.1 Product characterization and proposed reaction mechanism

All liquid samples of tubular reactor experiments collected in vessel 1 and 2 were color- and odorless. The TOC was below 1000 ppm in all cases. According to the reaction equations, water is the only condensable (at 0 °C) non-carbonaceous compound that is formed during reductive calcination (Eq. 1). Therefore, it is concluded that the liquids collected in vessel 1 and 2 consist of > 99 %wt. H_2O.

Results of the product characterization of thermogravimetric experiments already presented in section 2.3.3 and 3.3.2 will be supplemented with further findings. Additionally, the transferability of thermogravimetric results to tubular reactor results will be discussed. Figure 4-8 shows the thermogravimetric curve for five linear heating rate experiments (3 K min^{-1}) with 2 g of ICM and SEP (100-200 µm) in nitrogen and hydrogen atmosphere. The solid products of these experiments were analyzed by XRD and ICP-OES (Figure 4-9 and Table 4-5). As pointed out in chapter 2, calcination in nitrogen leads to the formation of wuestite and magnetite (both with Mg and Mn substitution) from the Mg-Mn siderite. The calcium-iron oxide srebrodoloskite $Ca_2Fe_2O_5$ (with Mg and Mn substitution) is produced from ankerite (see Figure 4-9). When the ICM is heated at 3 K min^{-1} to 640 °C and immediately cooled to 300 °C at a rate of approx. -11.4 K min^{-1} (see black lines in Figure 4-8 and Figure 4-9) ankerite is present besides Mg-Mn-substituted wuestite and magnetite, whereas srebrodoloskite is formed in traces only. This means that below 640 °C ankerite is only partially converted and low conversion of ankerite is expectable during calcination in nitrogen at lower temperatures.

Reductive calcination with an inlet flow of 70 %vol. H_2 leads to a shift of the thermogravimetric curves of 40-50 °C compared to pure N_2 inlet flow (Figure 4-8). This can be explained by the higher thermal conductivity and heat capacity of H_2 compared to N_2 and the chemical interaction of H_2 with the solid reactant. The reaction temperature is decreased in reductive calcination compared to calcination in nitrogen, and the mass loss is increased (see Figure 4-8). This can be explained by the formation of iron instead of iron oxides (see Figure 4-9). Iron formation can be described with a single step A2 reaction for SEP as derived in chapter 2. In the case of ICM two clearly separable steps are detected in the thermogravimetric curve (Figure 4-8). Though in ICM iron is present in siderite and ankerite, after reductive calcination at a maximum temperature of 740 °C, iron is formed as one phase and the accompanying elements are present in separate, oxidic phases (see Figure 4-9). The elemental analysis (Table 4-5) is in good accordance with the XRD analysis. As expected, the iron content of the product of reductive calcination is increased compared to the product of calcination in nitrogen due to the formation of iron instead of iron oxides (see Table 4-5). Taking the results of the XRD analysis into account, the formal composition of the reaction products can be calculated from the elemental analysis (Table 4-6). A consistent result is generated, as summation of the proposed solid products is in the range of 100 ± 2 %wt.

Table 4-5: Elemental analysis by means of ICP-OES of the products of the thermogravimetric (TG) experiments presented in Figure 4-8, corresponding to the XRD patterns presented in Figure 4-9.

Experiment	Fe %wt.	Mg %wt.	Mn %wt.	Ca %wt.	SiO_2 %wt.	Al_2O_3 %wt.
Partial calcination of ICM in N_2 on TG	47.6	3.36	2.97	5.83	6.33	1.15
Full calcination of ICM in N_2 on TG	52.6	3.72	3.23	6.15	7.80	1.44
Full calcination of SEP in N_2 on TG	62.2	3.13	3.60	1.62	4.00	1.23
Reductive calcination of ICM in 70%vol. H_2 on TG	64.6	4.37	3.77	6.70	9.00	1.59
Reductive calcination of SEP in 70%vol. H_2 on TG	79.0	3.96	4.39	1.96	4.72	1.44

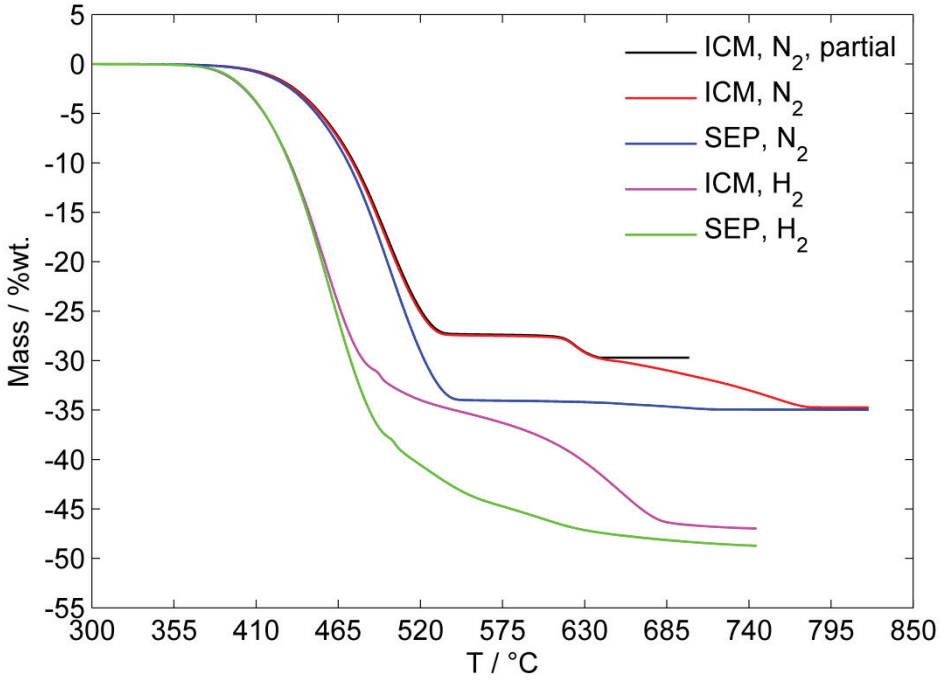

Figure 4-8: Thermogravimetric curves for the calcination of the iron carbonate mineral (ICM) and the siderite enriched phase (SEP) in nitrogen (black, red, blue) and 70 %vol. hydrogen (magenta, green). All samples were heated at linear rate of 3 K min^{-1} to either 640 °C (ICM, N_2, partial), 745 °C (ICM and SEP, H_2), or 825 °C (ICM and SEP, N_2). Initial weight = 2 g, 100 $cm^3_{STP}min^{-1}$ total inlet flow rate, N_2 … 100 %vol. nitrogen at the inlet, H_2 … 70 %vol. hydrogen + 30 %vol. nitrogen at the inlet.

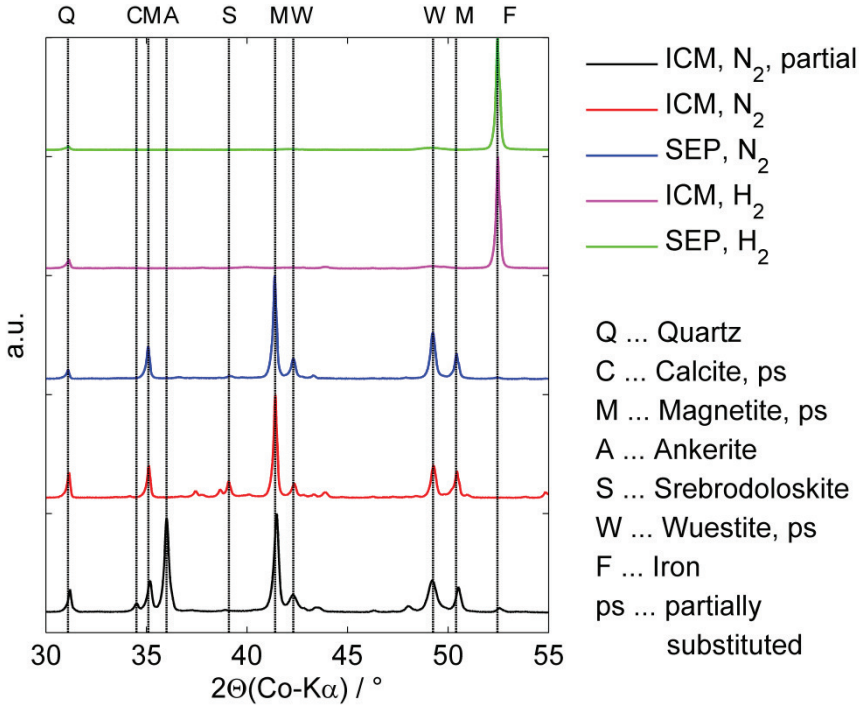

Figure 4-9: XRD pattern in the 30-55° range of the products of the thermogravimetric experiments presented in Figure 4-8. 'Partially substituted' means that the main element (e.g. iron in wuestite FeO) can be partially substituted by magnesium or manganese.

Table 4-6: Composition of the solid products of the thermogravimetric calcination of a 100-200 µm fraction of ICM and SEP in nitrogen (column 2 and 3) and 70 %vol. hydrogen (column 4 and 5) calculated from the ICP-OES analysis.

	ICM, N_2	SEP, N_2	ICM, H_2	SEP, H_2
Fe, %wt.	0	0	64.6	79.0
FeO, %wt.^{RIR}	30.5	32.6	0	0
Fe_3O_4, %wt.^{RIR}	39.9	51.0	0	0
MgO, %wt.	6.17	5.19	7.25	6.57
MnO, %wt.	4.17	4.65	4.87	5.67
CaO, %wt.	8.61	2.27	9.37	2.74
SiO_2, %wt.	7.81	4.00	9.00	4.73
Al_2O_3, %wt.	2.87	2.46	3.17	2.87
Sum, %wt.	100	102	98	102

RIR … The phase ratio determined via RIR analysis of the XRD pattern was used to distinguish FeO and Fe_3O_4.

The transferability of the results from thermogravimetric experiments to calcination performed with the tubular reactor shall be discussed on the basis of five tubular reactor experiments Exp1-Exp5 (Figure 4-12). The general experimental procedure is described in point a) of section 4.3.1.2 and operation conditions are given below:

Exp1. ICM was calcined in 100 %vol. nitrogen feed with a final temperature of 500 °C.

Exp2. ICM was calcined at a maximum temperature of 500 °C with a feed of H_2:N_2=9:1 until the product gas concentration of CO_2 was below 0.2 %vol.

Exp3. Experiment Exp2 was repeated with an additional final holding time of 2 hours.

Exp4. Day1 = repetition of experiment Exp2; Day2 = reduction of the solid product of Day1 with a feed of H_2:N_2=6:4 at 400 °C for 5 hours.

Exp5. Day1 = repetition of experiment Exp2; Day2 = oxidation of the solid product of Day1 with a feed of CO_2:N_2=1:4 at 400 °C for 5 hours.

Hg-porosimetry measurements were performed with the iron carbonate mineral and the solid products of Exp1-Exp3. The ICM did not reveal any porosity. During calcination in N_2 (Exp1) and reductive calcination (Exp2, Exp3) a porous solid is formed due to the release of carbon dioxide from the solid. The specific surface area varies between 5 and 7 m^2g^{-1}, whereas the porosity is higher for the products of reductive calcination (42-47 %) compared to the product of calcination in nitrogen (27 %, see Table 4-7). The pore size distribution is relatively narrow for all products (Figure 4-10). The average pore diameter is lower for the product of calcination in N_2 (72 nm) compared to the products of reductive calcination (128-155 nm, see Table 4-7).

Table 4-7: Results of the porosimetry measurements of the solid products of Exp1-Exp3.

Solid product	Porosity[a] %	Spec. surface area[b] $m^2\ g^{-1}$	Av. pore diameter[b] nm
Exp1: Calcination in N_2	27.4	6.7	72
Exp2: Reductive calcination, short	46.8	7.2	128
Exp3: Reductive calcination, long	42.0	5.3	155

[a] Ratio of pore volume to total external volume of the sample

[b] Equations for the calculation procedure are given in chapter 7.2.

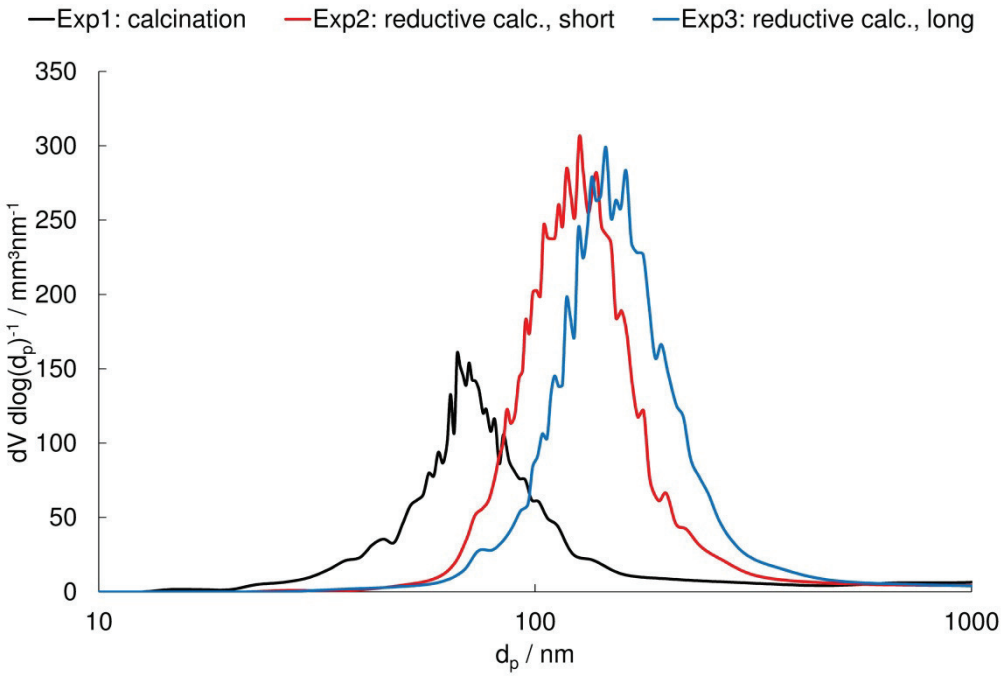

Figure 4-10: Differential mercury intrusion over $\log_{10}$ of the pore diameter dp determined via Hg-porosimetry for the solid product of Exp1-Exp3.

Table 4-9 and Figure 4-11 show that comparable XRD results are obtained with the 2-5 mm size fraction of the ICM calcined in the tubular reactor and the 100-200 µm size fraction investigated in thermogravimetric experiments. Calcination in nitrogen leads to the formation of a mixture of wuestite and magnetite. Ankerite is not decomposed in tubular reactor experiment as the reaction temperature is limited to 500 °C (see Table 4-9, Exp1). This finding is conceivable from the thermogravimetric results (see Figure 4-9). Reductive calcination at 500 °C, until the product gas composition decreases to 0.2 %vol. CO_2 (= Exp2), leads to the formation of wuestite, iron, and magnetite, whereas the wuestite to magnetite ratio is increased, compared to calcination in nitrogen (see Table 4-9, Exp2). When the reductive calcination is performed for 2 more hours in a single experiment (see Table 4-9, Exp3), the iron content is increased, the wuestite level decreases, and magnetite is not present due to reduction of the oxides with hydrogen. If Exp2 is repeated and the reduction with hydrogen is performed for 5 hours at 400 °C in a different experiment, iron formation from the iron oxides produced in Exp2 is confirmed. The lower iron

content of the product of Exp3 compared to Exp4 (see Table 4-9) can be explained by the lower reaction temperature applied in Exp4 (400 °C) compared to Exp3 (500 °C). If Exp2 is repeated and the solid product is treated with a feed gas containing 20 %vol. CO_2 in a follow-up experiment (=Exp5), wuestite and iron levels decrease and magnetite levels increase due to oxidation of iron and wuestite with CO_2 (Eq. 15). The mass loss of the ICM after Exp1-Exp3 coincides with the XRD results. The mass loss is higher for short reductive calcination (31.92 %wt. for Exp2, see Table 4-8) compared to calcination in N_2 (27.98 %wt. for Exp1) due to the higher amount of wuestite and iron formed in reductive calcination compared to calcination in N_2 (see Table 4-9). Mass loss decreases further (35.16 %wt. for Exp3 compared to 31.92 %wt. for Exp2, see Table 4-8) when the reaction time for reductive calcination is extended. This can be explained by the increase in iron and decrease in wuestite and magnetite content (see Table 4-9) due to their reduction with H_2.

Table 4-8: Several experimental results from tubular reactor experiments Exp1-Exp3.

Nr.	Parameter	Exp1 N_2	Exp2 H_2:N_2=9:1, short	Exp3 H_2:N_2=9:1, long
1	H_2O(exp), g	0	4.14	6.32
2	H_2O(calc), g	2.18	2.83	2.79
3	CO, mmol	120	154	151
4	CO_2, mmol	468	443	435
5	CH_4, mmol	0	1.4	1.8
6	CO+CO_2+CH_4, mmol	588	598	588
7	Mass loss, %wt.	27.98	31.92	35.16
8	Fe(ICM), %wt.	33.23	34.09	32.96
9	$FeCO_3$(ICM,calc), mmol	619	635	614

1: Amount of condensed water
2: Amount of water calculated from produced amounts of CO and CH_4 ($m_{H2O,calc}*MW_{H2O} = n_{CO} + 2*n_{CH4}$)
3-6: Amounts of CO, CO_2, and CH_4 produced in each experiment and sum thereof
7: Mass loss of the ICM after the experiment
8: Iron content of the ICM before the experiment
9: Theoretical $FeCO_3$ content of the ICM before the experiment ($n_{FeCO3,ICM,calc} = n_{Fe,ICM} = m_{0,ICM}*w_{Fe}/MW_{Fe}$)

Table 4-9: Solid phase composition calculated from XRD data applying Rietveld refinement. All experiments were performed on the tubular reactor setup with 104 g of a 2-5 mm sample of the ICM, a total feed flow rate of 500 $cm^3_{STP}min^{-1}$, and ambient pressure.

Compound	%wt. according to Rietveld refinement				
	Exp1 N_2	Exp2 H_2:N_2=9:1, short	Exp3 H_2:N_2=9:1, long	Exp4 H_2:N_2=9:1, short + H_2 (2days)	Exp5 H_2:N_2=9:1, short + CO_2 (2days)
Mg-Mn wuestite $Fe_{1-x-y}Mg_xMn_yO$	19.3	39.8	27.4	35.1	9.8
Magnetite Fe_3O_4	39.8	4.3	0	0	47.8
Iron Fe	0	9.5	25.6	17	2.5
Ankerite $CaFe_xMg_yMn_z(CO_3)_2$	16	19.8	24.1	23.7	18.2
Calcite $CaCO_3$	2.9	4.0	4.0	3.4	4.0
Quartz low SiO_2	6.9	8.5	8.7	7.8	7.2
Remainder	15.1	14	10.3	12.9	7.2

Exp1: ICM was calcined in 100 %vol. nitrogen feed with a final temperature of 500 °C.
Exp2: ICM was calcined at a maximum temperature of 500 °C with a feed of H_2:N_2=9:1 until the product gas concentration of CO_2 was below 0.2 %vol.
Exp3: Experiment Exp2 was repeated with a final holding time of 2 hours.
Exp4: Day1 = repetition of experiment Exp2; Day2 = reduction of the solid product of Day1 with a feed of H_2:N_2=6:4 at 400 °C for 5 hours.
Exp5: Day1 = repetition of experiment Exp2; Day2 = Oxidation of solid product of Day1 with a feed of CO_2:N_2=1:4 at 400 °C for 5 hours.

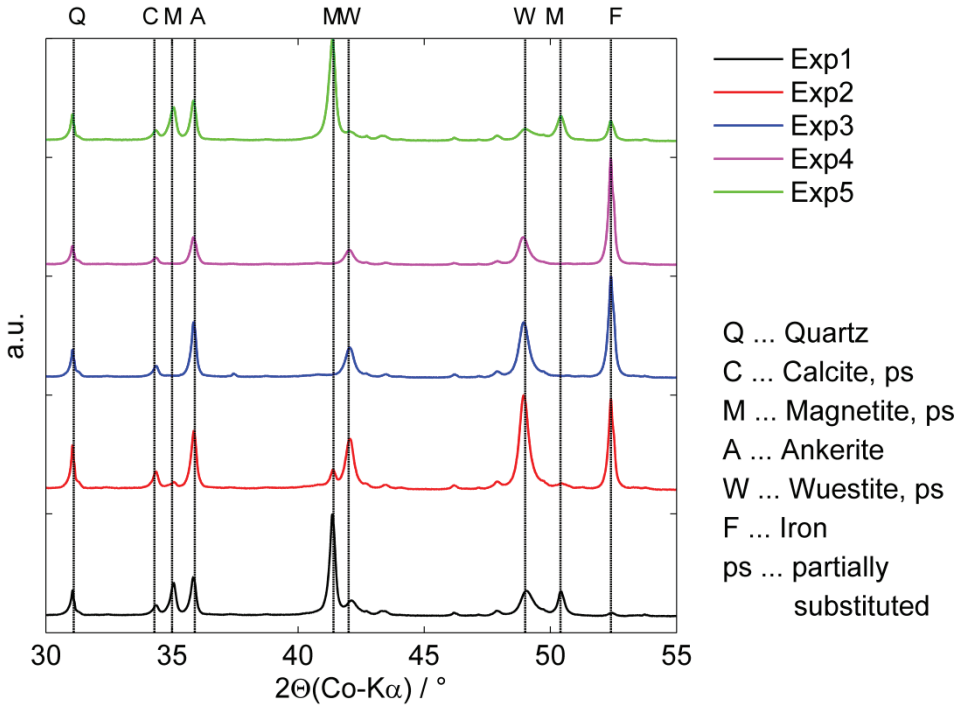

Figure 4-11: XRD pattern in the 30-55° range of the solid products of Exp1-Exp5.

As pointed out in the in section 4.1 the formation of methanol, formic acid, and formaldehyde is not expectable at the reaction temperatures of 400-500 °C applied in the tubular reactor experiments Exp1-Exp5 (see Figure 4-12). This was confirmed, as only CO, CO_2, and CH_4 were detected in the product gas and the TOC value of the condensed liquids was well below 1000 ppm. In Exp1-Exp3, CO_2 formation started in the heat-up phase and CO formation was observed subsequently (see Figure 4-12). CH_4 formation in traces was observed during the heat-up phase of reductive calcination (Exp2 and Exp3) but not during calcination in N_2 (see Table 4-8). Regardless of the calcining atmosphere (N_2 vs. H_2) both, the total amount of C1 products formed ($CO+CO_2+CH_4$ = 588-598 mmol) and the ratio of total C1 products to calculated $FeCO_3$ content of the ICM, are in a comparable range (0.94-0.96). CO formation can be explained by two reactions: wuestite oxidation (Eq. 15) and RWGS (Eq. 5). Calcination of the ICM in N_2 (Exp1) did not lead to the formation of water (see Table 4-8) and magnetite was detected in the solid product besides wuestite. Thus, the carbon monoxide produced can be attributed to the formation of magnetite via Eq. 15.

$$FeO + \frac{1}{3}CO_2 \rightarrow \frac{1}{3}Fe_3O_4 + \frac{1}{3}\,CO \qquad (15)$$

$$CO_2 + H_2 \rightarrow CO + H_2O \qquad (5)$$

Application of Eq. 16 and 17 allows for the calculation of the mass ratio of wuestite to magnetite $r_{WM,GA}$ from the molar ratio of CO and CO_2 τ_{MD} (see Table 4-8) for calcination in N_2.

$$FeCO_3 \rightarrow (1-x)FeO + \frac{x}{3}Fe_3O_4 + \left(1-\frac{x}{3}\right)CO_2 + \frac{x}{3}CO, \qquad x = 0-1 \qquad (16)$$

$$\frac{m_{FeO}}{m_{Fe3O4}} = \frac{MW(FeO)}{MW(Fe_3O_4)} * \frac{3*\left(1-\frac{3\tau_{MD}}{1+\tau_{MD}}\right)}{\frac{3\tau_{MD}}{1+\tau_{MD}}} \qquad (17)$$

The mass ratio of wuestite to magnetite was determined to be 0.485 based on the XRD analysis (see Table 4-9) and 0.589 based on the gas analysis (see Table 4-8). These values are in a comparable range and the increase of the magnetite content between the end of the experiment and after XRD analysis can be explained by oxidation of magnetite in air during sample preparation for XRD analysis (grinding, storage time, etc.). In reductive calcination (Exp2 and Exp3), on the contrary, water was formed. Carbon monoxide formation in a RWGS reaction (Eq. 5) and methane formation (Eq. 9) are coupled to the formation of water. The amount of water calculated from the amount of CO and CH_4 according to Eq. 5 and 9, however, is lower than the amount of water produced during reductive calcination in Exp2 and Exp3 (see Table 4-8). As evidenced by XRD, iron is formed in Exp2 and Exp3. This is a possible explanation for the increased water amount, as H_2O is the hydrogen sink during reduction of iron oxides (see Eq. 18).

$$FeO_{1+x} + (1+x)H_2 \rightarrow Fe + (1+x)H_2O \qquad (18)$$

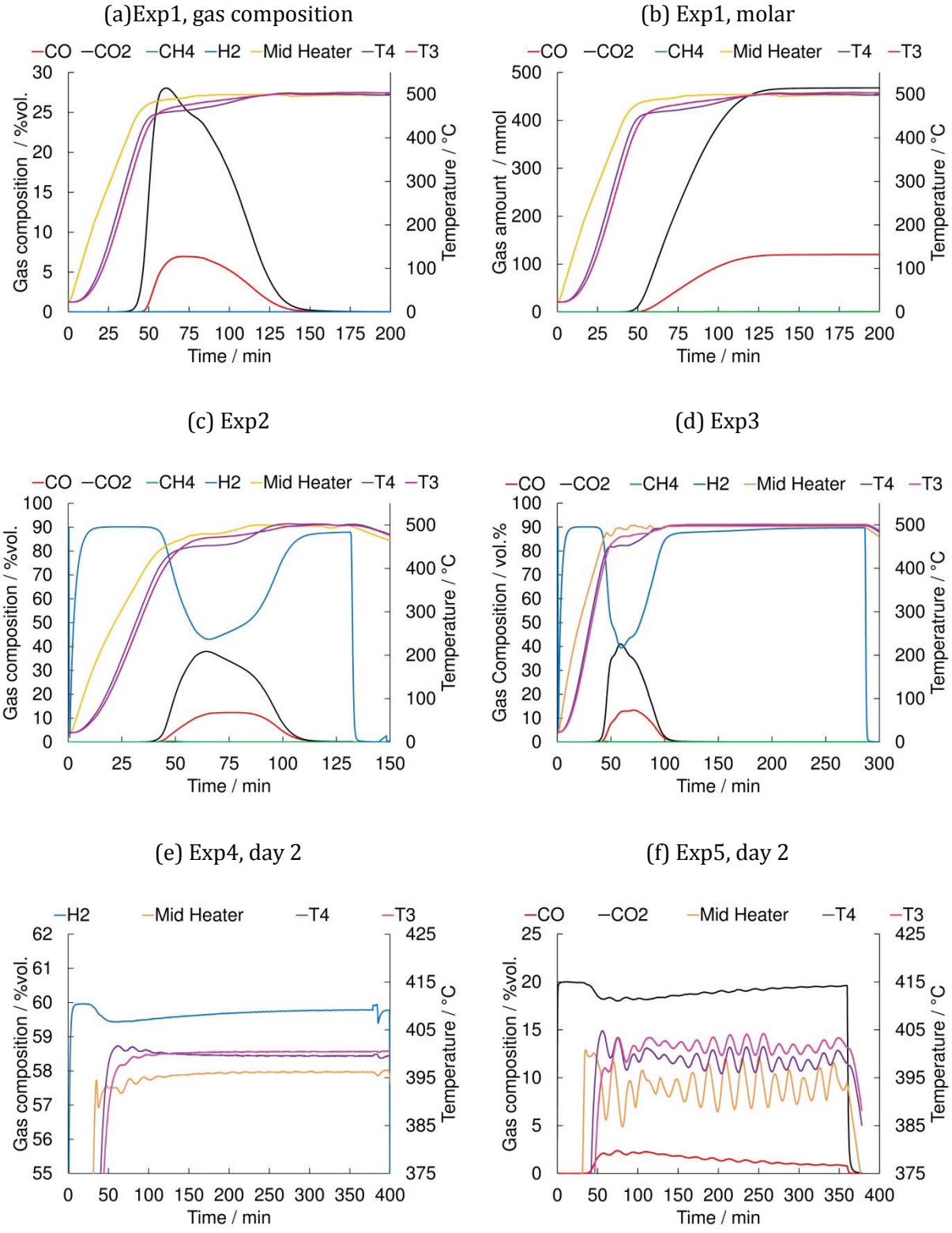

Figure 4-12: Tubular reactor experiments Exp1-Exp5. Gas composition data (CO/red, CO_2/black, CH_4/green, H_2/blue) refer to the left ordinate, temperature data (mid heater/orange, T4/purple, T3/magenta) to the right ordinate.

During thermogravimetric experiments the mass change is measured online, whereas during tubular reactor experiments the product gas composition is measured online. Both signals are linked to the relative conversion via the general reaction equation 1. A balance on the C1 products of tubular reactor experiments allows for the calculation of conversion of the carbonate into the oxide. Iron formation, however, is only detectable online during thermogravimetric experiments from the mass loss. A hydrogen balance could be applied to account for iron formation during tubular reactor experiments. The calculation of such a balance has some limitations, as shall be derived on the basis of Exp3. The hydrogen balance for the tubular reactor setup can be calculated with Eq. 19. As derived in section 5.5.3.1, the amounts leaving the reactor during Δt are calculated according to Eq. 20.

$$\Delta n_{H2,P} - \Delta n_{H2,F} = F * \Delta t * V_n^{-1} * \left(x_{H2,P} \frac{x_{N2,F}}{x_{N2,P}} - x_{H2,F} \right) \quad (19)$$

$$\Delta n_{i,P} = x_{i,P} * \frac{x_{N2,F}}{x_{N2,P}} * F * \Delta t * V_n^{-1} \quad (20)$$

For an entering flow with 90 %vol. hydrogen this balance is very sensitive to the value of the nitrogen concentration, whereas the error in the carbon balance is acceptable. This shall be demonstrated on the basis of the experimental data of Exp3 (see Table 4-10). The concentration of nitrogen in the reactor feed gas and the product gas is determined with Eq. 21. For Exp3, the concentration of nitrogen in the feed was determined to equal 9.9 %vol., hydrogen was at 90.1 %vol. in the feed, and the total feed flow rate was at 503 cm^3_{STP} min^{-1}.

$$c_{N2,i} = 100 - c_{CO2,i} - c_{CO,i} - c_{CH4,i} - c_{H2,i} \quad (21)$$

Table 4-10: Influence of the variation of the inlet concentration of nitrogen of ±0.1 %vol. on the calculated value of the produced amounts of CO, CO_2, and CH_4, and the hydrogen balance.

$c_{N2,F}$	9.8	9.9	10	%vol.
H_2 balance, total	709	658	608	mmol
H_2 balance, reduction (t=116-286 min)	333	298	263	mmol
CO	150	151	153	mmol
CO_2	431	435	440	mmol
CH_4	2	2	2	mmol

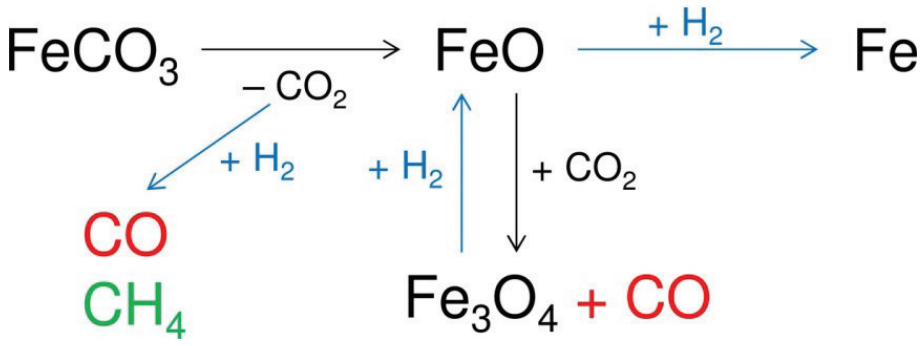

Figure 4-13: Proposed reaction scheme for the reductive calcination of mineral iron carbonate. To keep the sketch clear, the partial substitution of iron with magnesium and manganese in iron carbonate, wuestite, and magnetite is not depicted.

The detection error of the gas analyzer is ± 0.1 %vol. Thus, the nitrogen concentration in the inlet could vary at least between 9.9 ± 0.1 %vol. If $c_{N2,F}$ = 9.9 %vol. is taken as the reference case, the total H_2 balance has a relative variation of ± 7.7 %, whereas the produced amounts of CO, CO_2, and CH_4 only vary with ± 1 % compared to the reference case (see Table 4-10). However, the online-gas analysis of tubular reactor experiments provides important information on the reaction mechanism. Firstly, the balance on CO, CO_2, and CH_4 provides a measure for the consumption of decomposable carbonates. As long as one of these compounds is measured in the product gas, decomposable carbonates must be present in the ICM fixed in the tubular reactor. Secondly, as long as the hydrogen content of the product gas is below the content of the entering gas, hydrogen is consumed in either hydrogenation reactions (Eq. 5-9) or in iron formation (Eq. 1, Eq. 18). During reductive calcination of the ICM in the tubular reactor (Exp2 and Exp3), most of the CO, CO_2, and CH_4 has been produced 125 minutes after start of the heating phase (see Figure 4-12c). This finding is fortified by the hydrogen consumption evidenced in day 2 of Exp4 (see Figure 4-12d).

Based on the findings, the reaction mechanism depicted in Figure 4-13 is proposed. Wuestite and carbon dioxide are the products of the thermal decomposition of the Mg-Mn siderite present in the ICM. Carbon dioxide produced during thermal decomposition can either undergo hydrogenation to CO and CH_4 or leads to a partial oxidation of wuestite to magnetite. Iron formation can be treated as a follow-up reaction. At first, wuestite and carbon dioxide are formed from iron carbonate. Subsequently, wuestite can then either react with hydrogen to form iron or react with carbon dioxide to form magnetite.

4.3.2.2 Optimization of the methane yield based on design of experiments

Figure 4-14 demonstrates that the onset temperature for CO_2 formation[4] in scanning experiments increases with the size range of the ICM. This can be explained by transport limitations with increasing particle diameter. Furthermore, the formation rate of carbon dioxide and monoxide $\frac{dy_{COx}}{dt} = \frac{dy_{COx}}{dT} * \frac{dT}{dt}$ is higher than the formation rate of methane (see Figure 4-14

[4] and thus for carbonate decomposition and succeeding hydrogenation reactions in the gas phase

and Figure 4-15). The relative methane content of the product gas passes a peak at approximately 400 °C and decreases with increasing time and temperature. Several preliminary steady-state experiments between 330 and 415 °C proofed the assumption drawn from the thermodynamic analysis: CO yield increases with temperature, whereas CH_4 yield decreases. However, in the preliminary experiments, only temperature was varied under otherwise constant conditions. Therefore, a statistically planned study on the influence of temperature, gauge pressure, size fraction, initial mass of the ICM, feed flow rate, and feed flow composition (see Table 4-4 for value of the factors) on mass loss of the solid sample, CO-, and CH_4-yield was performed. The mass loss of the ICM due to calcination is a direct measure for the conversion of the solid. The use of a reference mass loss for a specific reaction product Δm_{ref} allows for the calculation of the conversion $X_{i\text{-}j,calc}$ of reactant ICM into into a product containing wuestite and magnetite (Eq. 22) with the experimental mass loss Δm_{exp}.

$$X_{ICM-WM,ml} = \frac{\Delta m_{exp}}{\Delta m_{ref}} \tag{22}$$

As pointed out in the discussion of the results from scanning experiments (see section 4.3.1.2 b), the reactor was held at 530 °C for approximately 1 hour. After this hold time, practically no CO, CO_2 or CH_4 was detected in the product-gas for calcination in nitrogen. The average mass loss encountered in scanning experiments with pure nitrogen feed was 27.5 %wt. This value can be interpreted as the maximum mass loss corresponding to complete conversion of the Mg-Mn siderite present in ICM into wuestite and magnetite $X_{ICM\text{-}WM,ml}$. Consequently, Eq. 22 with Δm_{ref} = 27.5 %wt was applied to quantify the conversion of the siderite fraction of the ICM into iron oxides after each experiment.

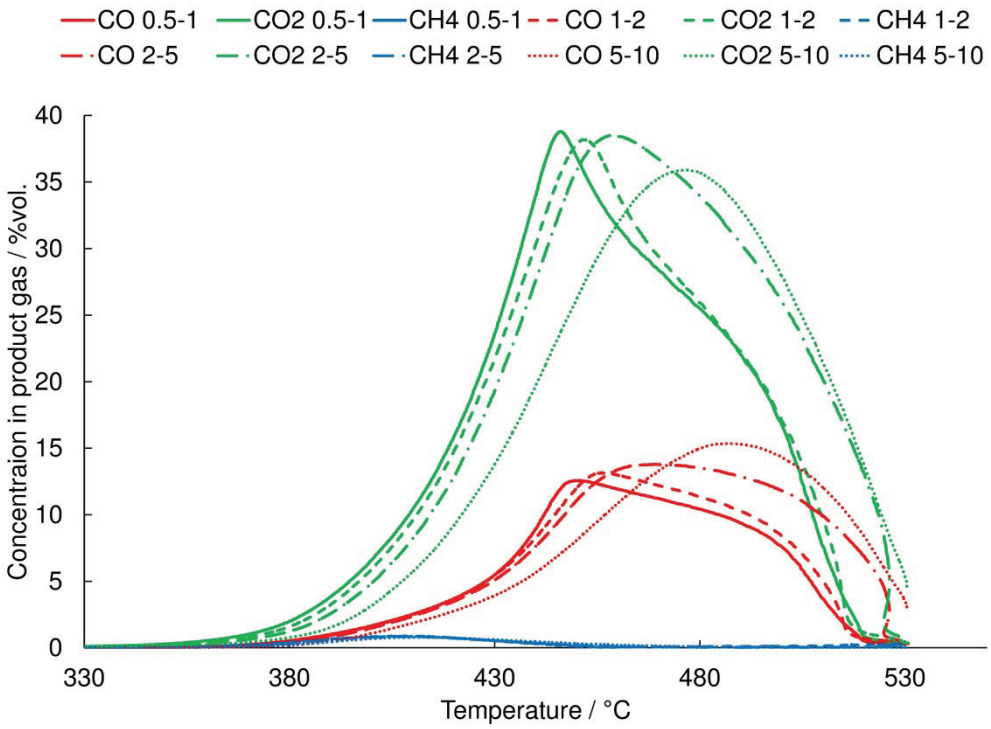

Figure 4-14: Scanning experiment with four size ranges (0.5-1 mm, 1-2 mm, 2-5 mm, 5-10 mm) of the ICM in a feed flow of 500 $cm^3_{STP}min^{-1}$ with a composition of H_2:N_2=9:1. Only the heat-up phase with a gradient of 1.5 K min^{-1} is plotted, hence the reaction time increases with temperature.

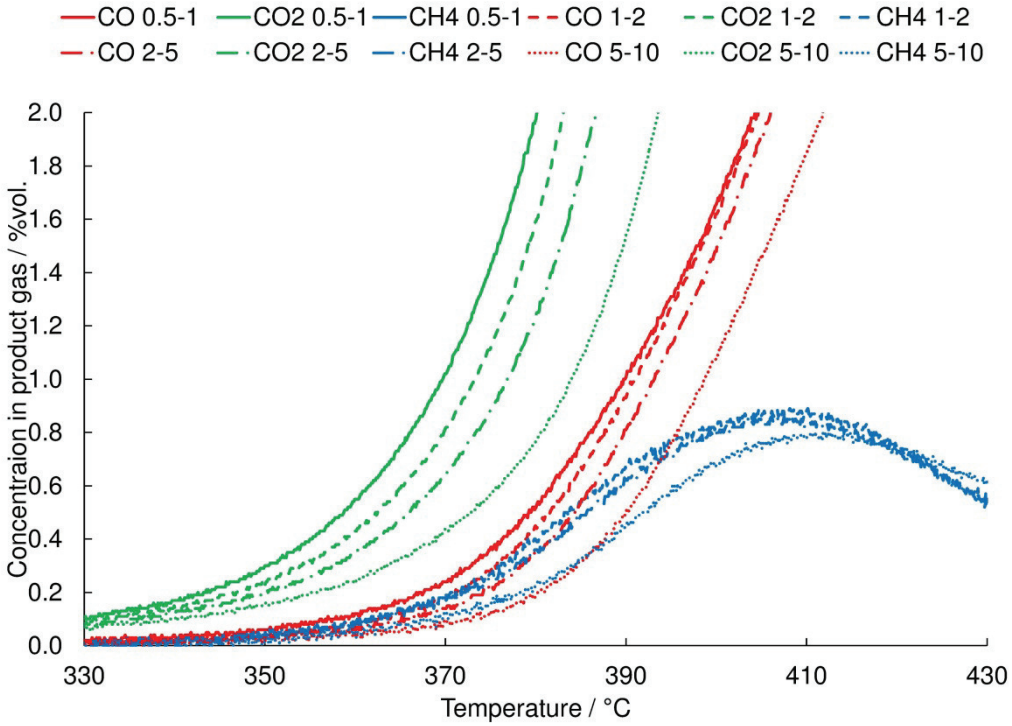

Figure 4-15: Zoom into Figure 4-14 to demonstrate the range of CH_4 formation.

The main findings of the statistically planned study are shown in the bar plots Figure 4-16 – Figure 4-18 and the experimental results are summarized in Table 4-11. Negative effects are shown in red, positive effects are shown in green color. Every effect with an absolute value higher than the margin of error is statistically significant in a 95 % confidence interval of the Student's T-distribution. Thus, gauge pressure and temperature show a statistically significant effect on total conversion $X_{ICM\text{-}WM,calc}$ (Figure 4-16). On average, the conversion is decreased by 20 % when the pressure is increased from ambient to 0.8 MPa gauge pressure. On the contrary, conversion is increased by 25 % when the temperature is increased from 350 to 375 °C. Carbon monoxide yield is primarily influenced by temperature and pressure (Figure 4-17). Increase of pressure leads to an average 10 % decrease of CO yield, whereas increase of temperature leads to an average 4 % increase of CO yield. Methane yield is increased by pressure by 20 % and decreased by temperature by 13 % (Figure 4-18). Increase of hydrogen in the feed positively affects methane yield at a level of 12 %. Initial amount of ICM and feed flow rate show an opposing trend. A low amount of ICM and a high feed flow rate positively affect methane yield at a level of 6 %. The highest methane yield of 75 % (marked bold in Table 4-11) was achieved under conditions that could be predicted from the bar plot shown in Figure 4-18: high pressure, low temperature, low amount of ICM, high size range, high amount of hydrogen in the feed, and high feed flow rate.

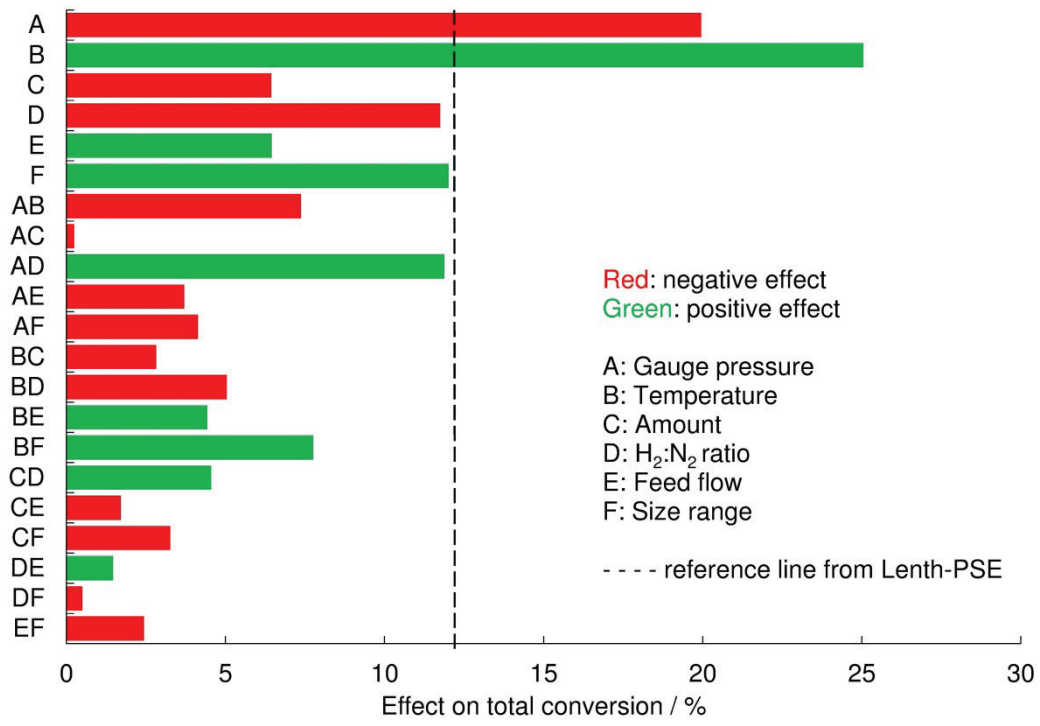

Figure 4-16: Effect of factors A-F on the total conversion of the ICM into iron oxides.

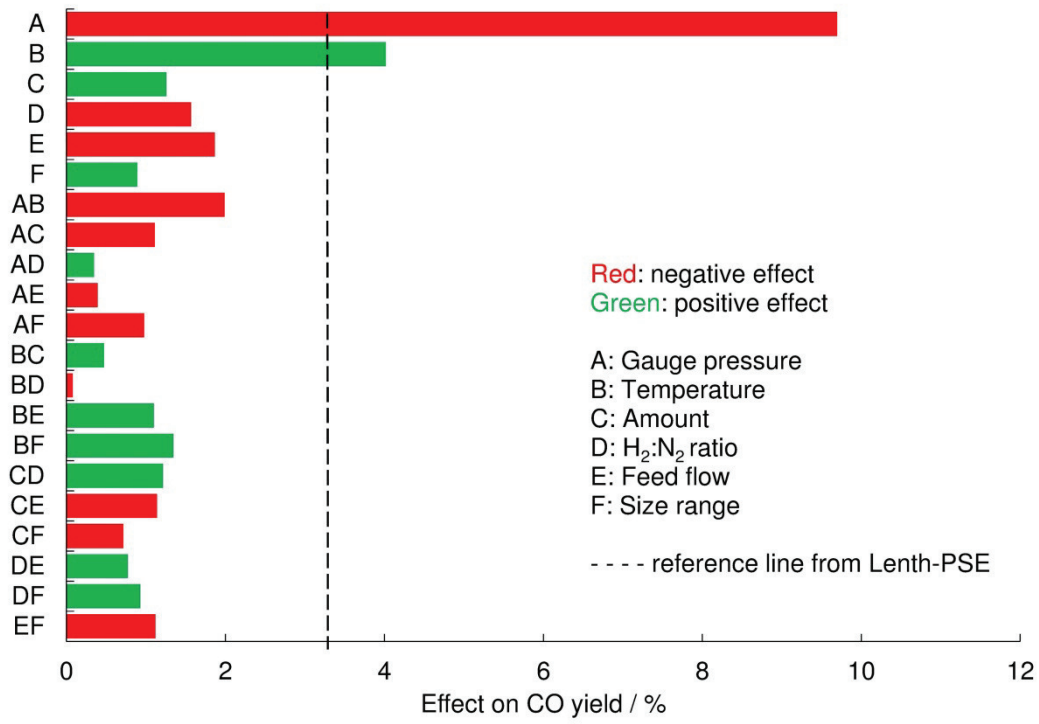

Figure 4-17: Effect of factors A-F on the carbon monoxide yield.

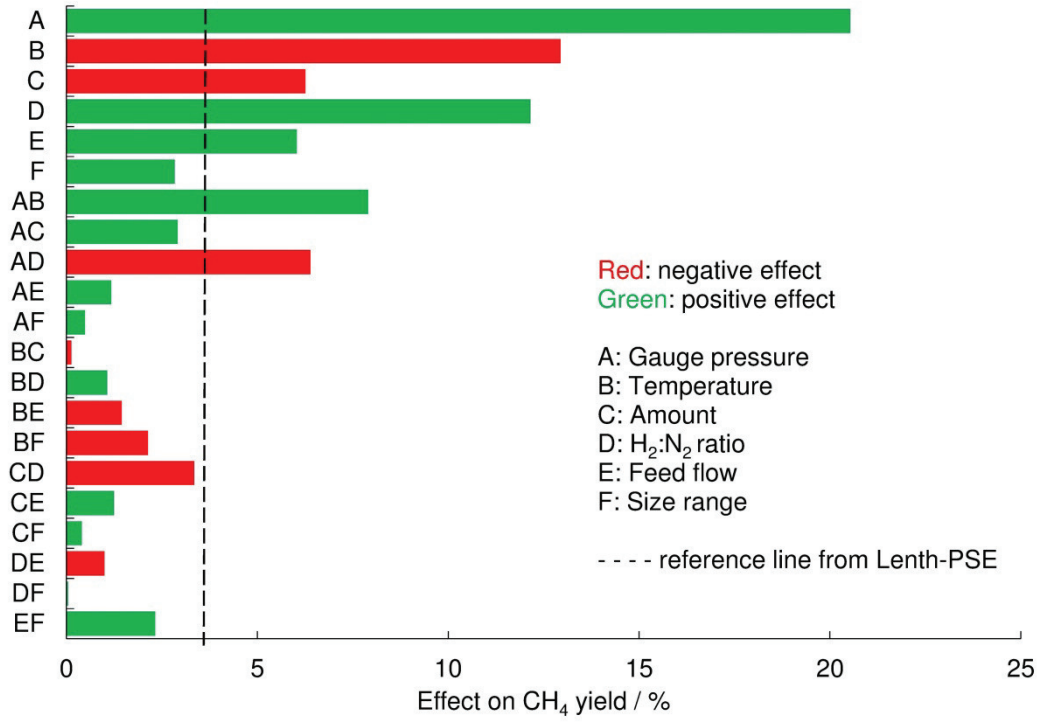

Figure 4-18: Effect of factors A-F on the methane yield.

Table 4-11: Results of the statistically planned reductive calcination of ICM.

A	B	C	D	E	F	$X_{ICM-WM,calc}$	Y_{CH4}	Y_{CO}
Pressure	Temp.	Amount	Size range	H_2:N_2	Feed			
bar	°C	g	mm	-	cm^3min^{-1}	%	%	%
0	350	60	0.5-1.0	60:40	500	22.18	37.69	15.26
8	350	60	0.5-1.0	60:40	867	9.85	59.39	6.19
0	375	60	0.5-1.0	60:40	867	87.64	17.66	21.70
8	375	60	0.5-1.0	60:40	500	20.40	50.64	8.69
0	350	104	0.5-1.0	60:40	867	23.82	37.14	15.35
8	350	104	0.5-1.0	60:40	500	3.09	51.85	7.65
0	375	104	0.5-1.0	60:40	500	40.40	13.57	20.36
8	375	104	0.5-1.0	60:40	867	21.13	50.38	8.80
0	350	60	5-10	60:40	867	13.38	62.49	12.52
8	350	60	5-10	60:40	500	4.76	62.22	4.95
0	375	60	5-10	60:40	500	3.09	51.85	7.65
8	375	60	5-10	60:40	867	33.27	58.99	8.13
0	350	104	5-10	60:40	500	10.95	46.14	15.05
8	350	104	5-10	60:40	867	5.13	59.98	6.02
0	375	104	5-10	60:40	867	39.20	26.92	23.99
8	375	104	5-10	60:40	500	13.02	54.90	7.01
0	350	60	0.5-1.0	90:10	867	35.53	49.43	11.60
8	350	60	0.5-1.0	90:10	500	6.25	62.86	4.70
0	375	60	0.5-1.0	90:10	500	71.82	20.98	18.70
8	375	60	0.5-1.0	90:10	867	38.73	59.42	6.45
0	350	104	0.5-1.0	90:10	500	20.00	41.09	11.89
8	350	104	0.5-1.0	90:10	867	7.38	62.99	4.44
0	375	104	0.5-1.0	90:10	867	74.40	21.19	18.77
8	375	104	0.5-1.0	90:10	500	14.33	56.57	6.36
0	350	60	5-10	90:10	500	13.16	62.17	9.93
8	350	60	5-10	90:10	867	10.62	75.10	2.84
0	375	60	5-10	90:10	867	59.27	47.33	19.16
8	375	60	5-10	90:10	500	24.44	61.94	5.88
0	350	104	5-10	90:10	867	12.58	60.15	10.36
8	350	104	5-10	90:10	500	3.82	62.93	3.51
0	375	104	5-10	90:10	500	35.13	30.03	19.68
8	375	104	5-10	90:10	867	27.09	64.18	5.20

$X_{ICM-WM,calc}$ … Conversion of ICM into wuestite/magnetite according to Eq. 22, Y_i … Yield of compound i

4.3.2.3 Steady-state kinetics of the Mg-Mn iron oxide formation from Mg-Mn siderite at 375–415 °C and 0-8 bar overpressure determined from tubular reactor experiments

The reductive calcination of any metal carbonate according to Eq. 1 is directly linked to the formation of gaseous carbonaceous products (CH_cO_{2-d} on the r.h.s. of Eq. 1).[5] Even if carbon dioxide produced from thermal decomposition is converted to carbon monoxide (via wuestite oxidation, Eq. 16, or RWGS, Eq. 5) or methane (Eq. 9), the carbon balance (Eq. 23) must be valid.

$$n_{MCO3,0} - n_{MCO3,t} = n_{CO2,t} + n_{CO,t} + n_{CH4,t} \quad (23)$$

Eq. 23 shows that every carbon atom that is released from the metal carbonate is either transferred to CO or CO_2 or CH_4 in the product gas. As lined out in section 4.3.2.1, this assumption can be made as no carbon containing products were found in the condensed liquids. Thus, the conversion $X_{Sid\text{-}Ox,t}$ of Mg-Mn siderite present in the ICM into Mg-Mn iron oxides can be calculated with Eq. 24. A comparable approach is used in chapters 5 and 6.

$$X_{Sid-Ox,t} = \frac{n_{Sid,0} - n_{Sid,t}}{n_{Sid,0}} = \frac{n_{CO2,t} + n_{CO,t} + n_{CH4,t}}{n_{Sid,0}} \quad (24)$$

The amount of CO, CO_2, and CH_4 $n_{i,t}$ produced can be quantified as a function of time with the online gas analysis data (details on the calculation procedure are given in section 5.5.3.1). The amount of Mg-Mn siderite present in the starting material $n_{Sid,0}$, however, cannot be determined straightforward. In order to minimize analysis time, the following procedure was used to quantify the Mg-Mn siderite sample on the basis of the iron content of the sample and the results from tubular reactor experiments discussed in section 4.3.2.1. The scanning experiment described in section 4.3.1.2b) was performed with pure nitrogen feed with one sample of every size fraction (see Table 4-12 for results). As the experiments were performed until negligible amounts of CO and CO_2 were detected in the product gas, it can be assumed, that the reaction of Mg-Mn siderite according to Eq. 25 was completed. As a consequence, the amount of CO_2 and CO produced is equal to the initial amount of Mg-Mn siderite (see Table 4-12). To account for varying iron contents of the samples a normalization with the initial iron content was performed. As a result, a value of 18 ± 1 mmol Mg-Mn siderite per gram of iron present in the ICM could be determined and the starting amount of Mg-Mn siderite can be determined for any ICM sample in the size range 0.5-10 mm with Eq. 26.

$$FeCO_3 * yMgCO_3 * zMnCO_3 \rightarrow$$

$$(1-x)FeO + \frac{x}{3}Fe_3O_4 + \left(1 - \frac{x}{3} + y + z\right)CO_2 + \frac{x}{3}CO + yMgO + zMnO \quad (25)$$

[5] Given that no carbon compound is added in the feed gas or any other carbonate is decomposed at the respective reaction temperature.

Table 4-12: Determination of the average Mg-Mn siderite content of the ICM normalized to the iron content of the sample (last column).

Size range mm	m_{Fe} g	$n_{CO,end}+n_{CO2,end}+n_{CH4,end}$ mmol	$\frac{\sum_i n_{i,end}}{m_{Fe}}$ mmol g^{-1}
0.5-1	38.1	688	18.0
1-2	37.7	699	18.5
2-5	38.6	705	18.3
5-10	39.8	682	17.1
		Average ± SD =	18 ±1

m_{Fe} … iron content of the ICM before calcination in N_2
$n_{i,end}$ … amount of compound i produced during calcination in N_2

$$n_{Sid,0}[\text{mmol}] = 18\ \left[\frac{\text{mmol}}{\text{g}}\right] * m_{Fe}[\text{g}] \qquad (26)$$

Figure 4-19a and Figure 4-20a show that the reaction rate dX/dt increases from 375 to 415 °C both at ambient pressure and 8 bar overpressure. The yield of methane decreases with increasing temperature and increases with increasing pressure, whereas yield of CO increases with increasing temperature and decreases with increasing pressure (see Figure 4-19b and Figure 4-20b). This behavior is in agreement with the discussion of the thermodynamics of reductive calcination given in section 4.1 and the results of section 4.3.2.2. A catalytic activity of the iron oxides formed during the reaction could give an explanation for the increasing tendency of CO and CH_4 yield with conversion (the higher the conversion, the more oxides are present).

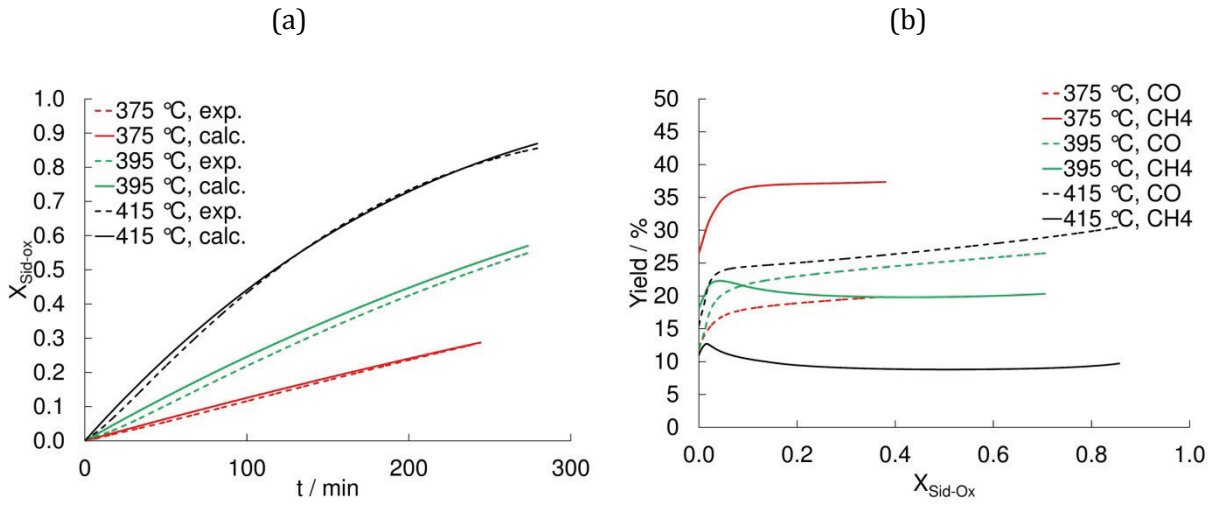

Figure 4-19: Conversion of Mg-Mn siderite into iron oxides (a) and yield of CO and CH_4 (b) at ambient pressure and 375-415 °C. The contracting volume reaction model R3 (dotted line in a) yields a reliable fit to the experimental dataset independent of the temperature. exp … experiment, calc … values calculated with R3 model

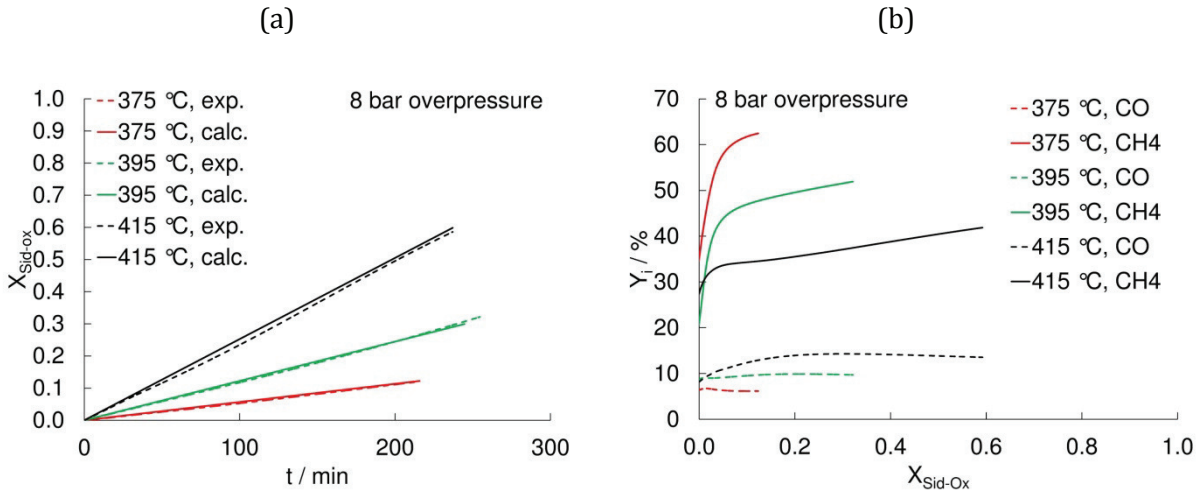

Figure 4-20: Conversion of Mg-Mn siderite into iron oxides (a) and yield of CO and CH_4 (b) at 8 bar overpressure and 375-415 °C. The zero order reaction model F0 (dotted line in a) yields a reliable fit to the dataset independent of the temperature. exp … experiment, calc … values calculated with F0 model

As lined out in chapters 2 and 3, the kinetics of solid state reactions can be described with Eq. 27. The relative conversion[6] $X_{Sid\text{-}Ox}$ is related to a temperature dependent function k(T) and a reaction model $f(X_{Sid\text{-}Ox})$. The Arrhenius approach (Eq. 28) with pre-exponential factor A and activation energy E_a is used for k(T).

$$\frac{dX_{Sid-Ox}}{dt} = k(T) * f(X_{Sid-Ox}) = A * e^{\frac{-E_a}{R_{gas}T}} * f(X_{Sid-Ox}) \quad (27)$$

$$k(T) = A * e^{\frac{-E_a}{R_{gas}T}} \quad (28)$$

Separation of variables and integration results in the integral form of the rate law (Eq. 29). The function $g(X_{Sid\text{-}Ox})$ represents the integral reaction model as defined in Eq. 30.

$$k(T) * t = g(X_{Sid-Ox}) \quad (29)$$

$$g(X_{Sid-Ox}) \equiv \int_0^{X_{Sid-Ox}} \frac{dX_{Sid-Ox}}{f(X_{Sid-Ox})} \quad (30)$$

Table 4-13: Differential $f(X_{Sid\text{-}Ox})$ and integral $g(X_{Sid\text{-}Ox})$ form the reaction models [9,10] evaluated.

Reaction model		$f(X_{Sid\text{-}Ox})$	$g(X_{Sid\text{-}Ox})$
Zero order	F0=R1	1	X
First order	F1	1-X	-ln(1-X)
Second order	F2	$(1-X)^2$	(1/(1-X)) - 1
Contracting area	R2	$2(1-X)^{1/2}$	$1-(1-X)^{1/2}$
Contracting volume	R3	$3(1-X)^{2/3}$	$1-(1-X)^{1/3}$
1-dimensional diffusion	D1	1/2X	X^2
2-dimensional diffusion	D2	-(1/ln(1-X))	((1-X)ln(1-X))+X

[6] Instead of α, which is used as the abbreviation for the relative conversion in chapters 2 and 3, the symbol $X_{Sid\text{-}Ox}$ is used to emphasize that the conversion of Mg-Mn siderite present in ICM into Mg-Mn iron oxides is modelled and discussed.

Geometrical contraction (R2, R3), diffusion (D1, D2), and reaction order (F0, F1, F2) models (see Table 4-13 for equations) were evaluated with respect to their suitability to fit the reaction run. Even though it was not possible to achieve relative conversions above 90 % in the experiments due to procedural aspects, a methodology was developed to describe and predict the relative conversion of Mg-Mn siderite and the CO- and CH_4-yield within several limits:

1. The reaction time was plotted as a function of the analytical solution of $g(X_{Sid\text{-}Ox})$ for the reaction models presented in Table 4-13 and k(T) determined from the slope (see Eq. 29).
2. A Arrhenius plot – ln(k) vs. $1/(R_{gas}*T)$), see Eq. 28 – was generated from the three temperature datasets available for ambient and 8 bar overpressure and the pre-exponential factor and activation energy calculated.
3. The values of A and E_a calculated in Step 2 and the respective analytical solution of $g(X_{Sid\_Ox})$ were inserted in Eq. 29 and compared against the experimental values.

This methodology revealed that a contracting volume model R3 describes the kinetics best at ambient pressure (Figure 4-19a and Table 4-14) and a zero order model describes the kinetics best at 8 bar overpressure (Figure 4-20a and Table 4-14). The CO and CH_4 yield were assumed to depend on the relative conversion in the form of a power function with order b and pre-factor a (Eq. 31). The order and pre-factor revealed a proximate linear behavior in the temperature region investigated. Therefore, a linear equation with slope $s_{a,i}$ and intercept $d_{a,i}$ for the pre-factor a_i, and slope $s_{b,i}$ and intercept $d_{b,i}$ for the order b_i was used to account for the temperature dependency of CO and CH_4 yield. The coefficient of determination R^2 was above 0.936 for all conditions, except for the intercept of the methane yield at ambient pressure $d_{b,CH4,amb}$ for which R^2 equals 0.771 (see Table 4-15). This leads to a slight underestimation of methane yield at ambient pressure (see Figure 4-21b).

$$Y_i = a_i * X_{Sid-Ox}^{b_i} \tag{31}$$

$$Y_i(T) = \left[s_{a,i} * T[K] + d_{a,i}\right] * X_{Sid-Ox}^{\left[s_{b,i}*T[K]+d_{b,i}\right]} \tag{32}$$

Table 4-14: Arrhenius parameters for the reductive calcination of Mg-Mn siderite.

	Ambient pressure	8 bar overpressure
Reaction model	R3: $k(T)*t = 1-(1-X_{Sid\text{-}Ox})^{1/3}$	F0: $k(T)*t=X_{Sid\text{-}Ox}$
Activation energy E_a, kJ mol^{-1}	129.176	138.489
Pre-exponential factor A, min^{-1}	$1.13*10^7$	$8.22*10^8$

Table 4-15: Linear parameters used to describe the dependency of CO and CH_4 yield (in %) on temperature and conversion.

	Y_{CH4} (ambient) %	Y_{CH4}(8 barg) %	Y_{CO} (ambient) %	Y_{CO}(8 barg) %
$s_{a,i}$, % K^{-1}	-0.722	-0.706	0.212	0.215
$d_{a,i}$, %	504	529	-115	-133
R^2	0.977	0.999	0.936	1.000
$s_{b,i}$, % K^{-1}	-0.001	0.001	0.001	0.001
$d_{b,i}$ %	0.592	-0.730	-0.753	-0.921
R^2	0.771	0.986	0.969	0.945

$s_{j,i}$ … slope of linear function for pre-factor (j=a) and order (j=b) for compound i
$d_{j,i}$ … intercept of linear function for pre-factor (j=a) and order (j=b) for compound i

At ambient pressure, the trend of conversion with time is approximately linear for 375 °C, but shows a decelerating tendency for 395 and 415 °C (see Figure 4-19a). At 8 bar overpressure, however, conversion increases linearly with time independent of the temperature (see Figure 4-20a). As the same rate law is used for all three temperatures, it seems plausible that the extrapolation of conversion outside the experimental dataset is applicable, as depicted exemplarily in Figure 4-21a for T = 415 °C. Furthermore, the power approach for the yield of CO and CH_4 describes the experimental dataset satisfactorily and can cautiously be used to interpolate the yield in the temperature region 375-415 and extrapolate the yield for higher conversions (Figure 4-21b). As a result, the reaction model for ambient and 8 bar overpressure can be used to predict both the time needed to reach a certain conversion (Figure 4-22a) and the yield of CO and CH_4 at that conversion (Figure 4-22b). Figure 4-22a shows that the reaction time needed to reach a relative conversion of 0.95 decreases exponentially with increasing reaction temperature and that the difference between reaction time at ambient pressure and 8 bar overpressure decreases with increasing temperature. Figure 4-22b shows that the methane selectivity can be substantially increased by an increase of pressure to 8 bar overpressure.

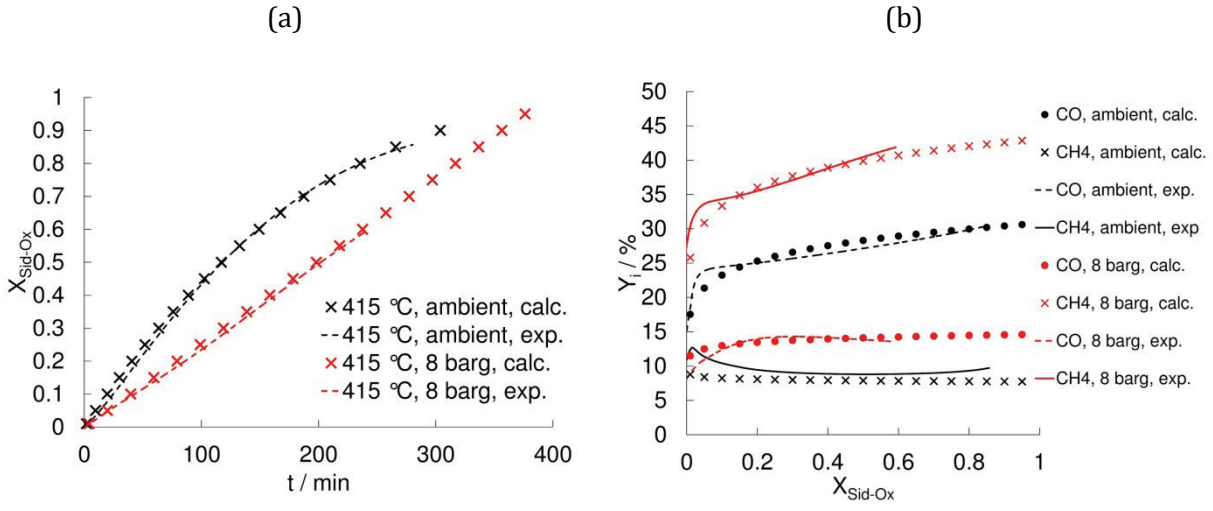

Figure 4-21: Comparison of experimental (exp) conversion (a) and yield (b) with values calculated (calc) from the model described in section 4.3.2.3.

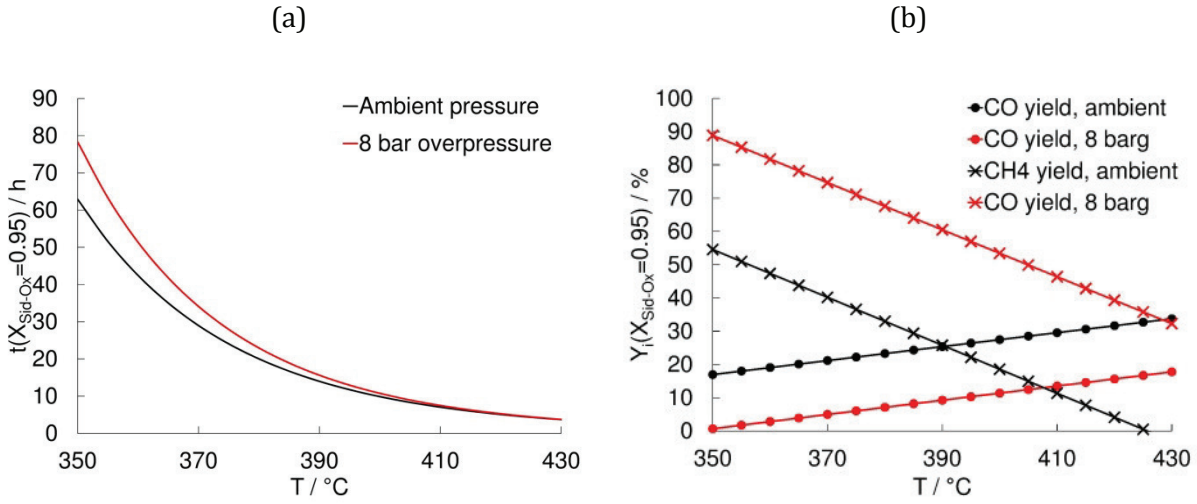

Figure 4-22: Prediction of the reaction time necessary to reach 95 % conversion (a) and yield of carbon monoxide and methane (b) at 95 % conversion.

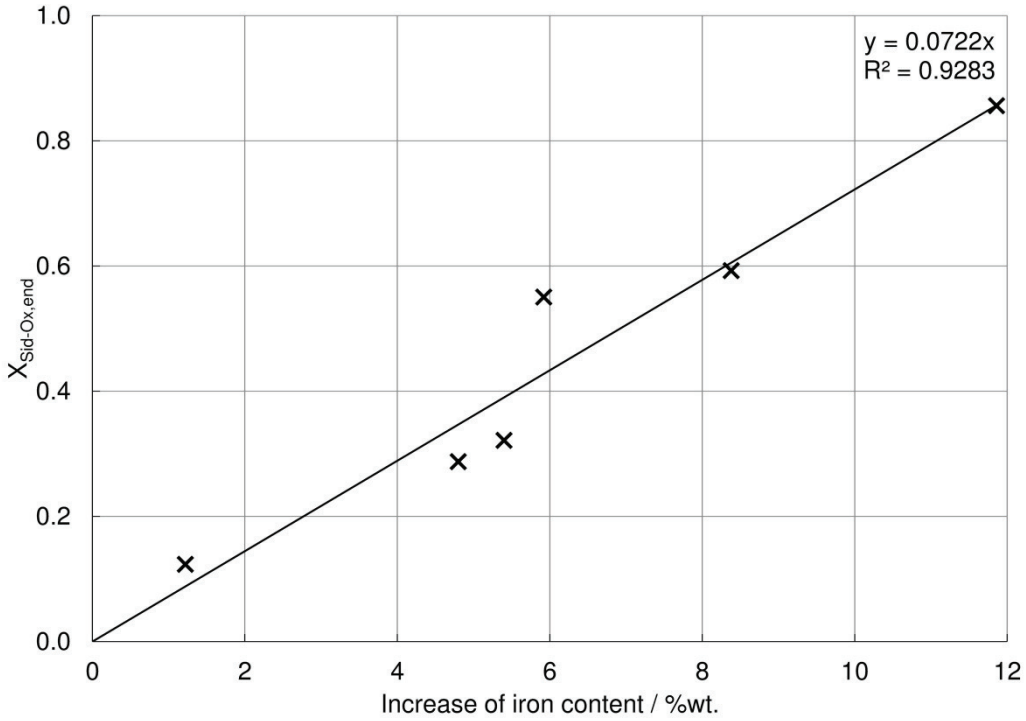

Figure 4-23: The increase of iron content of the solid due to reductive calcination is directly proportional to the conversion at the end of the experiment calculated with Eq. 24.

For validation purposes, the increase of the relative iron content of the solid reactant was determined. The relative iron content increases due to the loss of carbon dioxide. The relative conversion at the end of each experiment, as calculated with Eq. 24, is directly proportional to the increase of iron content (Figure 4-23). This finding confirms the calculation approach used to determine the rate law. Furthermore, the phase composition of the solid products was determined semi-quantitatively from the XRD pattern applying Rietveld refinement (Table 4-16). In general, the phase composition depends on the final conversion that was obtained in the experiment $X_{Sid\text{-}Ox,end}$ (as the reaction time was roughly constant the $X_{Sid\text{-}Ox,end}$ increases with temperature) and not on the pressure applied. The siderite content decreases with increasing conversion $X_{Sid\text{-}ox,end}$, whereas the ankerite content increases. This supports the assumption, that ankerite does not react in the temperature and pressure regime investigated. Wuestite is formed as the main iron oxide phase; magnetite is formed at low levels and only at high conversions. As expected, the iron oxide content increases with conversion. Iron is already formed in the low temperature regime (375-415 °C). There is no clear indication wether iron is formed directly from siderite or from the iron oxides. The detection of cohenite and its increase with conversion indicates a possible partial direct reduction of siderite with hydrogen to form iron, as depicted in a modified reaction scheme (Figure 4-24).

Table 4-16: Phase composition of the solid product of the experiments used to determine the reaction kinetics of iron oxide formation.

	375	395	415	375	395	415	°C
	0	0	0	8	8	8	barg
$X_{Sid\text{-}Ox,end}$	28.7	55.0	85.6	12.3	32.1	59.3	%
Siderite, $FeCO_3$	58.6	42.1	13.8	62.7	55.2	33.1	%wt.[a]
Wuestite, FeO	5.5	13.5	24.2	1.9	6.2	16.6	%wt.[a]
Magnetite, Fe_3O_4	0.0	0.0	6.7	0.0	0.0	3.2	%wt.[a]
Iron	1.2	1.2	4.2	0.8	1.5	2.9	%wt.[a]
Ankerite, mixed carbonate	16.0	16.9	26.9	16.5	14.9	20.3	%wt.[a]
Cohenite, Fe_3C	0.0	4.0	7.3	0.0	1.3	4.9	%wt.[a]
Calcite, $CaCO_3$	3.6	2.8	4.1	3.3	4.1	4.0	%wt.[a]
Phengite, mixed silicate	12.3	15.1	4.6	11.6	12.2	7.9	%wt.[a]
Quartz, SiO_2	2.4	3.6	3.5	3.1	3.7	5.4	%wt.[a]
Graphite	0.4	0.8	4.8	0.0	0.9	1.6	%wt.[a]

[a] Determined by Rietveld refinement

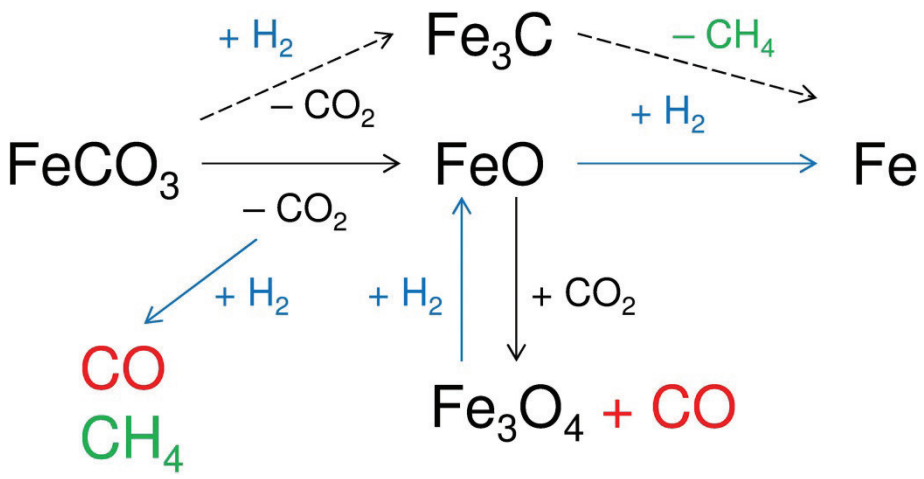

Figure 4-24: Modified reaction scheme which includes iron carbide Fe_3C (cohenite) formation.

4.4 Design of a tube bundle reactor

4.4.1 Design equations

Based on the kinetics derived in section 4.3.2.3 it is possible to evaluate a first design of a steady state, counter current, isothermal tube bundle reactor with continuous feed of ICM and hydrogen, and continuous removal of the solid and gaseous products (Figure 4-25). The reaction time t_{react} to reach a certain relative conversion can be calculated with Eq. 33.

$$t_{react} = \frac{g(X_{Sid-Ox})}{k(T)} \tag{33}$$

The reactor height h_R can be calculated as the product of reaction time t_{react} and rate of the the discharge of solids v_s (Eq. 34). Assuming that the bulk volume is constant (Eq. 35, with $\dot{m}_{ICM,F,R}$ as the mass flow of the ICM in the feed, ρ_{ICM} as the apparent density of ICM in the feed, $\dot{m}_{S,P,R}$ as the mass flow of the calcined solid product, and $\rho_{S,P}$ as the apparent density of the calcined solid product), the mass flow of ICM that can be converted in one reactor tube $\dot{m}_{ICM,F,R}$ can be calculated with Eq. 36.

$$h_R = t_{react} * v_s \tag{34}$$

$$\frac{m_{ICM,F,R}}{\rho_{ICM}} = \frac{m_{S,P,R}}{\rho_{S,P}} \tag{35}$$

$$\dot{m}_{ICM,F,R} = \pi * \frac{d_R^2}{4} * \rho_{ICM} * v_s \tag{36}$$

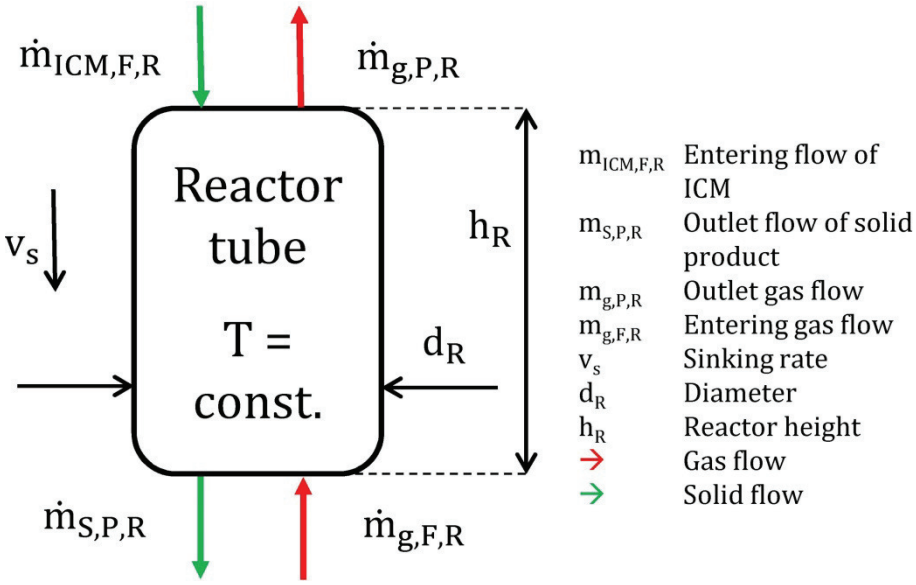

Figure 4-25: Sketch of one reactor tube.

For a given total throughput of ICM $\dot{m}_{ICM,tot}$, the number of reactor tubes N_R is calculated with Eq. 37. The number of tubes in a tube bundle $N_{R,tot}$ depends on the split factor f_{SP} (Eq. 38). The total diameter of the tube bundle d_{tot} is thus calculated from the single reactor tube diameter d_R, a factor quantifying the single tube distance f_D, and the arrangement factor f_{SP} with Eq. 39.

$$N_R = \frac{\dot{m}_{ICM,tot}}{\dot{m}_{ICM,R}} \quad (37)$$

$$N_{R,tot} = 6 * (f_{SP} + 1) * \frac{f_{SP}}{2} - 5 \quad (38)$$

$$d_{tot} = f_{SP} * d_R * f_D \quad (39)$$

4.4.2 Case study

In order to evaluate the size of an industrial scale reactor a throughput of 1,000,000 t of ICM year^{-1} (size range 5-10 mm), and an operation time of 8000 h year^{-1} is assumed. A conversion $X_{Sid\text{-}Ox,end}$ = 0.95 is desired, for a reactor tube diameter of 0.1 m and a discharge rate of 2 m h^{-1}. Essential design parameters are summarized in Table 4-17 and results are presented in Table 4-18. An increase of reaction temperature from 375 °C to 415 °C results in a decrease of reactor height by a factor of approximately 4 at both ambient pressure (48 m vs. 12 m) and 8 barg (56 m vs. 13 m). An increase of reactor pressure results in a slight increase of reactor height for both 375 °C (48 m vs. 56 m) and 415 °C (12 m vs. 13 m). The methane yield, however, is substantially affected by reactor pressure, as already discussed in section 4.3.2.3 (see Figure 4-22b).

Table 4-17: Selected design parameters for the case study.

Throughput	1,000,000	t year^{-1}
Operation time	8000	h year^{-1}
Apparent density ρ_{ICM}	1.67	t m^{-3}
Conversion $X_{Sid\text{-}Ox}$	0.95	
Tube diameter d_R	0.100	m
Sinking rate v_s	2	m h^{-1}
Single tube distance factor f_D	1.3	

Table 4-18: Results of the case study.

	375 °C		415 °C	
	Ambient	8 barg	Ambient	8 barg
t_{react}, h	24.0	27.9	6.0	6.3
Y_{CO}, %	22.2	6.0	30.6	14.6
Y_{CH4}, %	36.6	71.1	7.7	42.8
h_R, m	48.1	55.9	11.9	12.5
N_R	4766	4766	4766	4766
$N_{R,tot}$	4915	4915	4915	4915
f_{SP}	40	40	40	40
d_{tot}, m	5	5	5	5

As the discharge rate and tube diameter were fixed, the number of tubes is relatively high (N_R=4766) and independent of the reaction conditions. The number of tubes can only be reduced by either increasing the discharge rate or increasing the single tube diameter, or decreasing the throughput (see Eq. 40).

$$N_R = \frac{4}{\pi * \rho_{ICM}} * \frac{\dot{m}_{ICM,tot}}{d_R^2 * v_s} \quad (40)$$

The number of tubes in a tube bundle $N_{R,tot}$ depends on the arrangement factor: $N_{R,tot}(f_{SP}=39)$=4675 vs. $N_{R,tot}(f_{SP}=40)$=4915 (see Eq. 37). Therefore, the minimum arrangement factor to house the 4766 tubes needed equals 40. As a consequence, the total diameter of the tube bundle was calculated to equal 5 m. The reactor height, however, increases from 12 m at 415 °C and ambient pressure to 56 m at 375 °C and 8 barg.

4.5 Conclusions

The thermodynamic analysis of the reductive calcination of iron and magnesium carbonate revealed that in the temperature range of 0-1000 °C the accessible products are MgO, FeO, Fe_3O_4, Fe, CO, CO_2, and CH_4. Methane formation is expected to be favoured at low temperature and increased pressure. This expectation was confirmed experimentally and reaction conditions for increased methane yield were optimized via design of experiments. A steady-state kinetic model was derived and applied to the Mg-Mn iron oxide formation from mineral Mg-Mn siderite during reductive calcination at 375-415 °C and 0-8 barg. At ambient pressure, a volume contraction reaction model R3 describes the kinetics best, whereas at 8 barg a zero order reaction mode F0

fits experiments better. The kinetic model is expanded to predict the methane and carbon monoxide yield via a power approach. The kinetic model is applied to design an isothermal tube bundle reactor and execute a case study. This case study revealed that the reactor size can be decreased by factor of 4, when the design temperature is increased from 375 to 415 °C. The decrease in reactor size is yet coupled to a substantial decrease in methane yield.

References

[1] S.S.J. Warne, J. V. Dubrawski, Differential scanning calorimetry of the dolomite-ankerite mineral series in flowing nitrogen, Thermochim. Acta. 121 (1987) 39–49. doi:10.1016/0040-6031(87)80160-0.

[2] G. Baldauf-Sommerbauer, S. Lux, W. Aniser, M. Siebenhofer, Reductive calcination of mineral magnesite: hydrogenation of carbon dioxide without catalysts, Chem. Eng. Technol. 39 (2016) 2035–2041. doi:10.1002/ceat.201600094.

[3] G. Baldauf-Sommerbauer, S. Lux, W. Aniser, M. Siebenhofer, Synthesis of carbon monoxide from hydrogen and magnesite/dolomite, Chemie Ing. Tech. 89 (2017) 172–179. doi:10.1002/cite.201600078.

[4] B. Ottitsch, Die reduzierende Kalzinierung ausgewählter Kornklassen eines eisenkarbonathaltigen Erzes, Master‘s Thesis, Graz University of Technology, 2016.

[5] G. Kaufmann, Charakterisierung von Ni/MgO mit einer Ni-Beladung von 16 Gew.% zur katalytischen CO2 Methanisierung, Bachelor‘s Thesis, Graz University of Technology, 2016.

[6] R. V. Lenth, Quick and easy analysis of unreplicated factorials, Technometrics. 31 (1989) 469–473. doi:10.2307/1269997.

[7] Z. Frontistis, E. Hapeshi, D. Fatta-Kassinos, D. Mantzavinos, Ultraviolet-activated persulfate oxidation of methyl orange: A comparison between artificial neural networks and factorial design for process modelling, Photochem. Photobiol. Sci. 14 (2015) 528–535. doi:10.1039/c4pp00277f.

[8] D.C. Montgomery, Design and analysis of experiments, 4th ed., John Wiley & Sons, Inc., 1997.

[9] A. Khawam, D.R. Flanagan, Solid-state kinetic models: Basics and mathematical fundamentals, J. Phys. Chem. B. 110 (2006) 17315–17328.

[10] S. Vyazovkin, Isoconversional kinetics of thermally stimulated processes, 1st ed., Springer International Publishing Switzerland, Cham, 2015. doi:10.1007/978-3-319-14175-6.

5 Reductive calcination of mineral magnesite: hydrogenation of carbon dioxide without catalysts[7]

Abstract

This paper discusses the conversion of mineral magnesite to magnesium oxide, methane, carbon dioxide, and carbon monoxide in hydrogen atmosphere between 748 K and 778 K at ambient to 1.2 MPa overpressure without catalysts. Low temperature and elevated pressure facilitate methane formation, whereas moderate to high temperature and low pressure facilitate carbon monoxide formation. Methane is formed directly without any additional catalyst. Carbon dioxide emissions are decreased substantially in reductive calcination. Additional experiments revealed that reductively calcined magnesium oxide is a highly active reverse water gas shift catalyst. Carbon monoxide formation from gaseous carbon dioxide and hydrogen at catalytically active magnesium oxide has been reproducibly confirmed. Further reduction of carbon monoxide to methane is not catalyzed by reductively calcined magnesium oxide.

[7] This chapter is based on an article published by John Wiley & Sons and is reprinted under licence number 4038830601127 of Jan. 30, 2017:
G. Baldauf-Sommerbauer, S. Lux, W. Aniser, M. Siebenhofer, Reductive calcination of mineral magnesite: hydrogenation of carbon dioxide without catalysts, Chem. Eng. Technol. 39 (2016) 2035–2041. doi:10.1002/ceat.201600094.

Symbols

T	K	temperature
OP	MPa	overpressure
Δt	s	time interval
F	$dm^3\ s^{-1}$	feed flow rate
P	$dm^3\ s^{-1}$	dry product gas flow rate
T1-T6	-	temperature measurement position inside the reactor tube
HT1-HT3	-	temperature measurement position in the mid of the heating zone
X	%	magnesite conversion
t_{iso}	min	time at isothermal temperature
t_{20}	min	time needed to reach 20 % conversion of magnesite calculated from online gas analysis
$Y_{i,20}$	%	yield of compound i after t_{20}
$Y_{i,end}$	%	yield of compound i at the end of the experiment
C_{CO2}	%	conversion of CO_2 into CO
na	-	ambient pressure
$X_{end,\Delta m}$	%	conversion of magnesite after t_{iso} calculated from mass loss and LOI
$X_{end,GA}$	%	conversion of magnesite after t_{iso} calculated from online gas analysis

Abbreviations

i	-	compound examined
mid	-	mid of the packed bed
iso	-	quantity examined at isothermal conditions
MW_i	$g\ mol^{-1}$	molecular weight of compound i
MS	-	mass spectroscopy
GC	-	gas chromatography
GA	-	online gas analysis
FID	-	flame ionization detector
TCD	-	thermal conductivity detector
ICP-OES	-	inductively coupled plasma optical emission spectroscopy
XRD	-	X-ray diffraction analysis
STP	K, MPa	standard temperature of 273.15 K and absolute pressure of 0.1 MPa
LOI	%wt.	loss on ignition

5.1 Introduction

In several industrial processes the calcination of inorganic carbonates is used as a preparation method for metal and metal oxide production. Carbon dioxide is emitted as a byproduct and released into the environment with the flue gas. The production of magnesium oxide from mineral magnesite (Eq. 1) for refractory production, for example, accounted for direct process CO_2 emissions of 6.7 Mt from the calcination process alone (2005) [1]. The accumulation of carbon dioxide in the atmosphere and its detrimental effect on global climate is a commonly acknowledged challenge for society in the 21st century [2,3]. Instead of emitting carbon dioxide into the atmosphere, it would be beneficial to use it as a raw material for the production of carbon containing chemicals [4-6]. As a first step, carbon dioxide has to be reduced with hydrogen to platform chemicals such as methane or carbon monoxide/syngas [7]. Methane could also be directly used as a fuel. The catalytic hydrogenation of CO_2 has gained major interest, but there are significant challenges in catalyst development [8]. Instead of separating carbon dioxide from the flue gas for catalytic hydrogenation, our approach is to directly convert CO_2-containing carbonates. The gaseous products of this conversion termed 'reductive calcination' are methane, carbon dioxide, and carbon monoxide (Eq. 2). Compared to calcination, the CO_2 emission per unit $MgCO_3$ is significantly decreased in reductive calcination.

$$MgCO_3 \rightarrow MgO + CO_2 \quad (1)$$

$$(a + b + c)MgCO_3 + (b + 4c)H_2 \rightarrow$$

$$(a + b + c)MgO + aCO_2 + bCO + cCH_4 + (b + 2c)H_2O \quad (2)$$

The reducing agent in reductive calcination is hydrogen. Hydrogen can be produced renewably and sustainably from various sources [9-15] but storage is challenging [16] and would require a completely new distribution system. Therefore, reductive calcination of inorganic carbonates is a direct CO_2-utilization approach as well as a means of chemical hydrogen storage as either methane [17] or fuels produced from syngas [18-19]. The advantage of this hydrogen storage technology is the availability of storage and distribution systems for natural gas and liquid hydrocarbon fuels. Furthermore, reductive calcination could even be applied as a novel means of carbon dioxide capture and utilization, for magnesium oxide can be used as a carbon dioxide sorbent [20]. The use of sustainably produced hydrogen in the reductive calcination step would provide a powerful measure to produce methane or carbon monoxide/syngas from carbon dioxide emitted at large point sources, for instance fossil fuel fired power plants.

In the following, we want to provide an overview of relevant research that has been conducted so far. Reller et al. [21] investigated the calcination of mineral magnesite (Ural, former Soviet Union) and mineral magnesite mixed with 10 %wt. of cobalt, nickel, and copper in hydrogen atmosphere. Calcination in hydrogen atmosphere produced magnesium oxide, equal amounts of carbon monoxide and carbon dioxide, and water. The calcination temperature decreased considerably — more than 150 K — compared to calcination in non-reducing atmosphere.

Admixture of 10 %wt. of the transition metals copper, nickel, and cobalt to the mineral revealed a further reduction of the calcination temperature in the range of 200 to 400 K. Admixture of transition metals had a significant influence on the gaseous products. Copper led to the formation of carbon monoxide and carbon dioxide. Doping with cobalt produced mostly methane, some carbon monoxide, and low concentrations of carbon dioxide. In the case of 10 %wt. nickel, the main product was methane.

Reller et al. [22] also examined the influence of temperature and gas atmosphere on the calcination of synthetic alkaline earth metal and transition metal carbonates. Experiments were conducted with a combined thermogravimetry/mass spectrometry unit. The calcination temperature increased with the atomic mass of the cation of the alkaline earth metal carbonate. Reductive hydrogen atmosphere significantly lowered the calcination temperature. Decomposition of synthetic $MgCO_3$ in hydrogen atmosphere produced carbon dioxide and carbon monoxide, with a CO_2:CO ratio of approximately 3.

Padeste et al. [23] investigated two forms of decomposition of the basic magnesium carbonate hydromagnesite $Mg_5(OH)_2(CO_3)_4*4H_2O$. First, the decomposition of hydromagnesite in nitrogen and carbon dioxide atmosphere. Second, the decomposition of nickel-doped hydromagnesite in nitrogen and hydrogen atmosphere. As expected, decomposition of hydromagnesite in nitrogen and carbon dioxide produced carbon dioxide and water. Decomposition of nickel-doped hydromagnesite in carbon dioxide produced carbon dioxide and water, while hydrogen atmosphere led to methane as the major gaseous product.

Tsuneto et al. [24] reported on the catalytic reduction of hydromagnesite with hydrogen at atmospheric pressure. The experiments were carried out with powder samples mixed with 2 %wt. of nickel catalyst for methanation in a fixed bed flow reactor. Decomposition of hydromagnesite with 2 %wt. nickel produced a gas mixture with a CO_2:CH_4 ratio of approximately 1.5 after 0.5-1.0 hours reaction time.

Jagadeesan et al. [25] examined the catalytic conversion of synthetic $MgCO_3$ to methane with the catalyst Co/Ca/CoO. The experiments were conducted in a tubular reactor with $MgCO_3$ and Co/Ca/CoO in a ratio of 1:1 (50 mg each) at 823 K for 5 hours. At a hydrogen flow rate of 8 ml min^{-1} 100 % of the CO_2 from decomposition of $MgCO_3$ were catalytically converted to methane.

Furthermore, there have been reports on the conversion of calcium carbonate to methane by introducing solid catalysts. Jagadeesan et al. [26] found that admixture of iron oxides to calcium carbonate catalyze the direct formation of C1-C3 hydrocarbons. Yoshida et al. [27] reported on the calcination of synthetic calcium carbonate in hydrogen with and without noble-metal catalysis. Decomposition of $CaCO_3$ in hydrogen produced a mixture of carbon monoxide and dioxide. Addition of 5 %wt. of iridium and palladium led to a lower calcination temperature and the production of methane.

In this work, we report on the direct conversion of magnesite to carbon monoxide and methane without the admixture of catalysts. As far as to our knowledge, the direct conversion of magnesite or any other carbonate into methane without admixture of catalysts has not been published yet.

5.2 Experimental

Mineral magnesite samples (size range 5-8mm, Eskişehir/Turkey; 98.40 %wt. $MgCO_3$ see Table 5-1 for composition) were used as the carbonate carrier. The carbonate carrier and solid products were characterized with ICP-OES (Spectro Arcos, Spectro Ametek) and XRD (X'Pert Pro, Panalytical, Co-$K_{\alpha1}$=0.178901 nm, data collection at 298 K). Liquid reaction products were analyzed with GC-FID/TCD (Shimadzu GC2010Plus, Supelco Q-Plot 30m*0,53m, fused silica). The dry product gas was analyzed at a time interval of 5 seconds using online IR absorption (ABB Uras26) for CO, CO_2, and CH_4 (0.0-100.0 %vol.) and TCD detection (ABB Caldos27) for H_2 (0.0-100.0 %vol.). Nitrogen and hydrogen were used in 99.999 % quality and were supplied by Air Liquide. The test gas for periodical check-up of the online gas analyzer consisted of 2.5 %vol. CO, 2.5 %vol. CO_2, and 2.5 %vol. CH_4 in nitrogen and was supplied by Linde. Deionized water and dried (0.3 nm molecular sieve, Metrohm) 1,4-dioxane (99.5 %, Merck) were used for liquid sample preparation for GC analysis. Experiments were carried out at 748-778 K and ambient to 1.2 MPa overpressure. Details of the GC, ICP-OES, and XRD analysis can be found in section 5.5.

5.2.1 Reactor setup, experimental procedure, and calculations performed

A fixed bed tubular reactor setup (see Figure 5-1) was used for all experiments. The reductive calcination experiments were carried out with 115.00 ± 0.50 g of the mineral magnesite placed in the mid of the tubular reactor. Experiments on the catalytic activity of magnesium oxide produced via reductive calcination were carried out using 25.00 ± 0.20 g of MgO as the catalyst bed. The feed flow rate was maintained at $8.33*10^{-3}$ dm^3s^{-1} (at standard temperature and pressure, STP) in all experiments. Details on the experimental procedures and the tubular reactor setup can be found in the section 5.5. The procedure applied for the calculation of the CO, CO_2, and CH_4 amount over time as well as the calculation of the magnesite conversion *X* during reaction time is described in section 5.5.3.

Table 5-1: Composition of the mineral magnesite sample used in this study. $MgCO_3$ content calculated from Mg content according to ICP-OES analysis and a Mg:$MgCO_3$ ratio of 0.29. $CaCO_3$ content calculated from the Ca content according to the ICP-OES analysis and a Ca:$CaCO_3$ ratio of 0.40.

	Content / %wt.
Magnesium	28.37
$MgCO_3$	98.40
CO_2 content of $MgCO_3$	51.36
Calcium	0.49
$CaCO_3$	1.22
Remains (<0.4%wt. total)	Fe, Mn, Si, Al

5.2.2 Characterization of the mineral magnesite samples

According to the results of the ICP-OES analysis, the mineral magnesite sample consisted of 98.40 %wt. $MgCO_3$ (Table 5-1). This is in good agreement with the XRD spectrum depicted in Figure 5-2. All signals at higher angles than 35° 2Θ could be assigned to $MgCO_3$, whereas two minor signals below 35° 2Θ could be assigned to $CaCO_3$ and $Mg,Ca(CO_3)_2$. The semi-quantitative XRD analysis based on the reference intensity ratio resulted in a $MgCO_3$ content of 98 %wt.

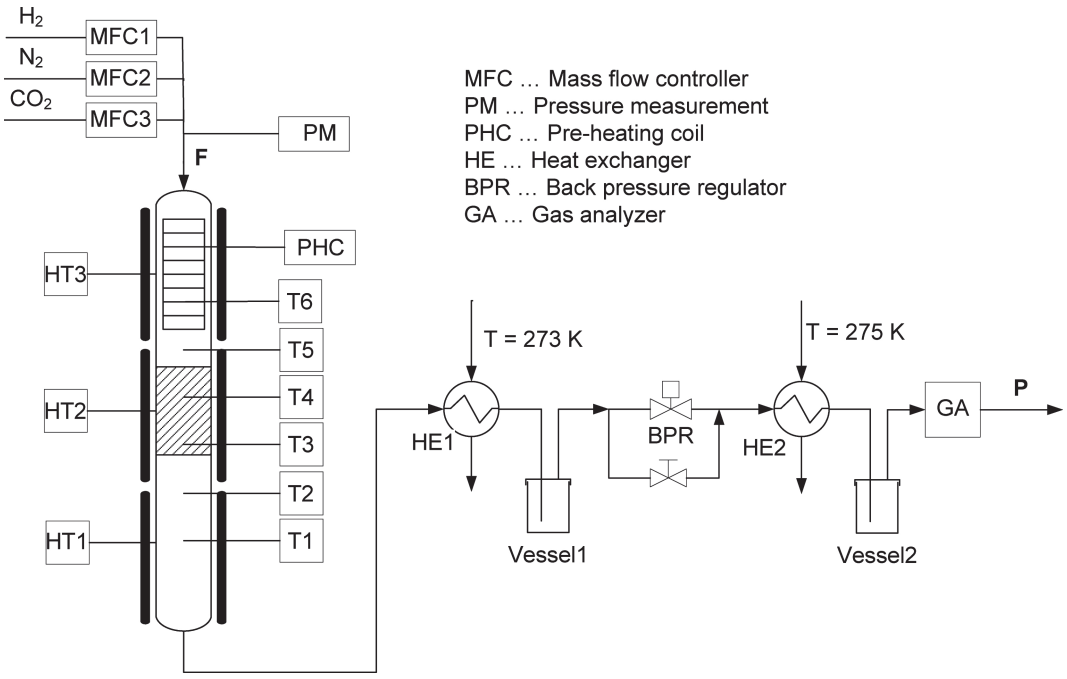

Figure 5-1: Scheme of the tubular reactor setup. Feed (F) and Product (P) gas stream are delineated. The feed flow rate was maintained at $8.33*10^{-3}$ dm^3s^{-1} (at standard temperature and pressure, STP) in all experiments. Details on the reactor setup are given in section 5.5.1.

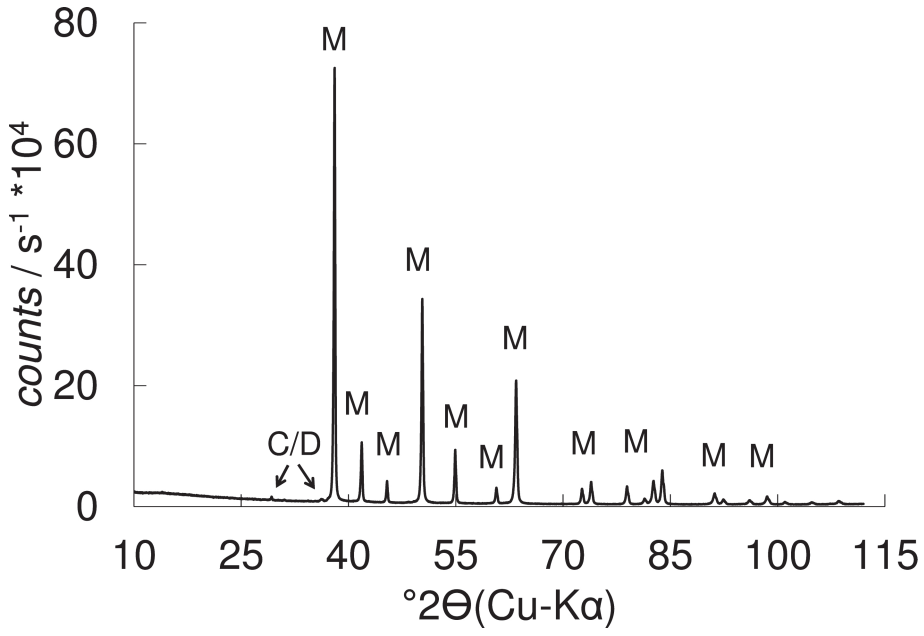

Figure 5-2: XRD spectrum of the mineral magnesite sample used in this study. All major signals can be assigned to Magnesite (M), trace amounts of calcium carbonate (C) and dolomite (D) are present.

5.3 Results and discussion

5.3.1 Isothermal reductive calcination of magnesite

The conversion of magnesite *X* increases with rising reaction temperature (e.g. from 45 % at 748 K to 96 % at 778 K, see Table 5-2 and Figure 5-3). At isothermal conditions, the conversion decreases with increasing pressure (e.g. from 76 % at ambient pressure and 763 K to 67 % at 1.2 MPa overpressure and 763 K, see Table 5-2 and Figure 5-3). In all experiments, carbon dioxide, carbon monoxide, and methane were detected in the product gas. Figure 5-4 -Figure 5-6 show the mole fraction of methane x_{CH4} and carbon monoxide x_{CO} produced as a function of magnesite conversion *X* at 748-778 K and 0-1.2 MPa overpressure. Methane formation decreases with magnesite conversion and reaches a constant level after 10-20% magnesite conversion. At higher temperatures, this constant level is reached at lower magnesite conversions. At isothermal conditions, methane formation increases with pressure (solid lines in Figure 5-4 - Figure 5-6). Carbon monoxide formation increases with magnesite conversion. As a first approximation, this increase shows a logarithmic behavior. When the pressure is increased, carbon monoxide formation reaches a constant level after 20-30 % magnesite conversion. At ambient pressure conditions, however, carbon monoxide formation keeps increasing until high magnesite conversions (see dashed lines with diamonds in Figure 5-4 -Figure 5-6). Carbon monoxide formation slightly increases from ambient to 0.3 MPa overpressure, and decreases at higher pressures.

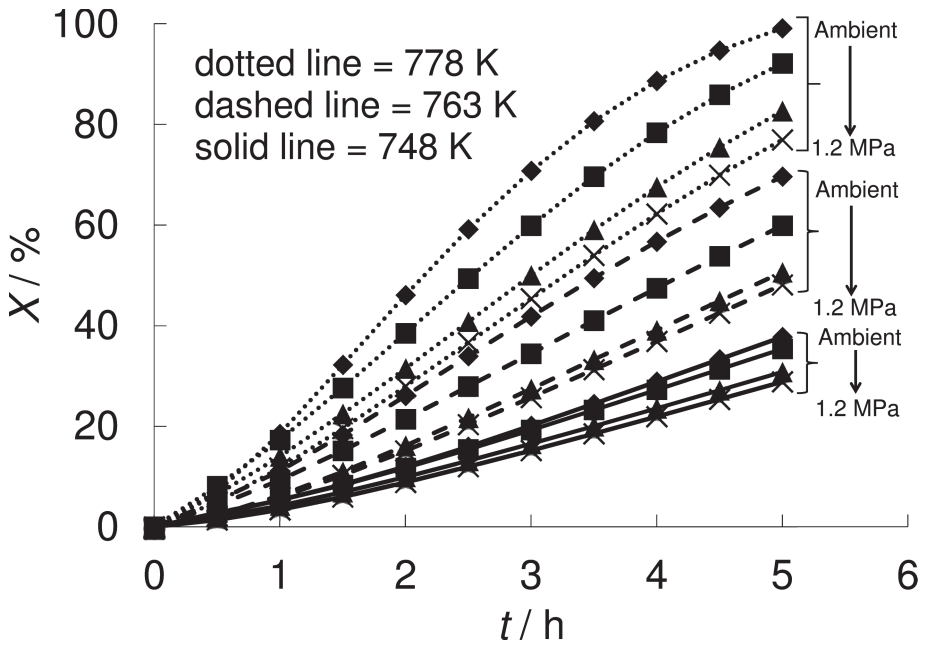

Figure 5-3: Conversion *X* of magnesite at 748 K (solid line), 763 K (dashed line), and 778 K (dotted line) and ambient pressure (diamond), 0.3 MPa overpressure (square), 0.8 MPa overpressure (triangle), and 1.2 MPa overpressure (X); 90 %vol. H_2 at the reactor inlet, $8.33*10^{-3}$ dm^3s^{-1} total feed flow rate, *t* = time.

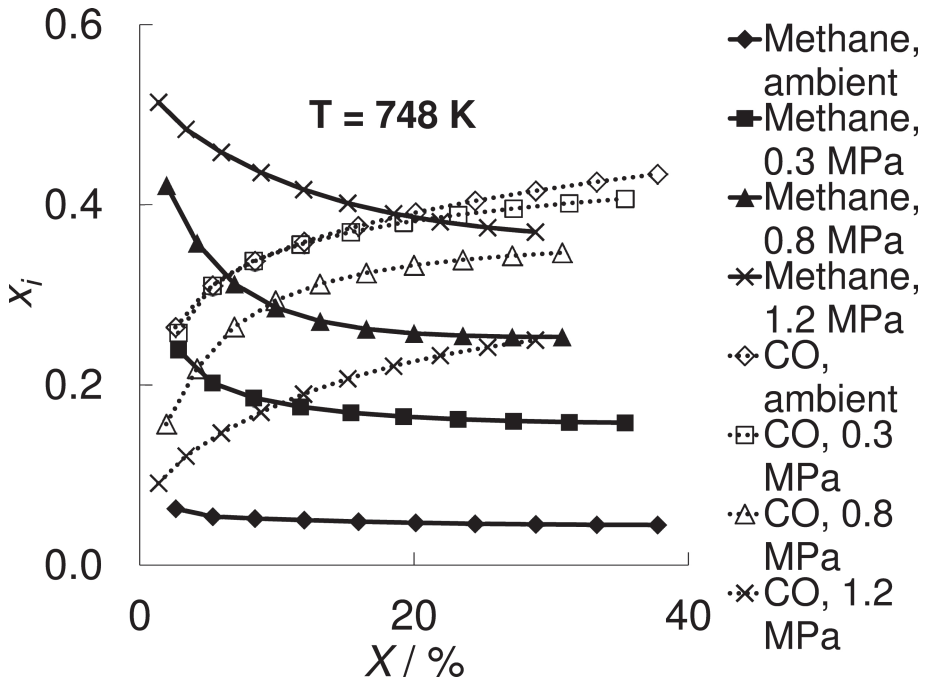

Figure 5-4: Dependency of the dry product gas composition on the reaction pressure at 748 K during reductive calcination of 115 g magnesite with 90 %vol. H_2 at the reactor inlet and $8.33*10^{-3}$ dm^3s^{-1} total feed flow; x_i = mole fraction of compound i, X = magnesite conversion; mole fraction of CO_2 (x_{CO2}) not shown: $x_{CO2} = 1 - x_{CO} - x_{CH4}$.

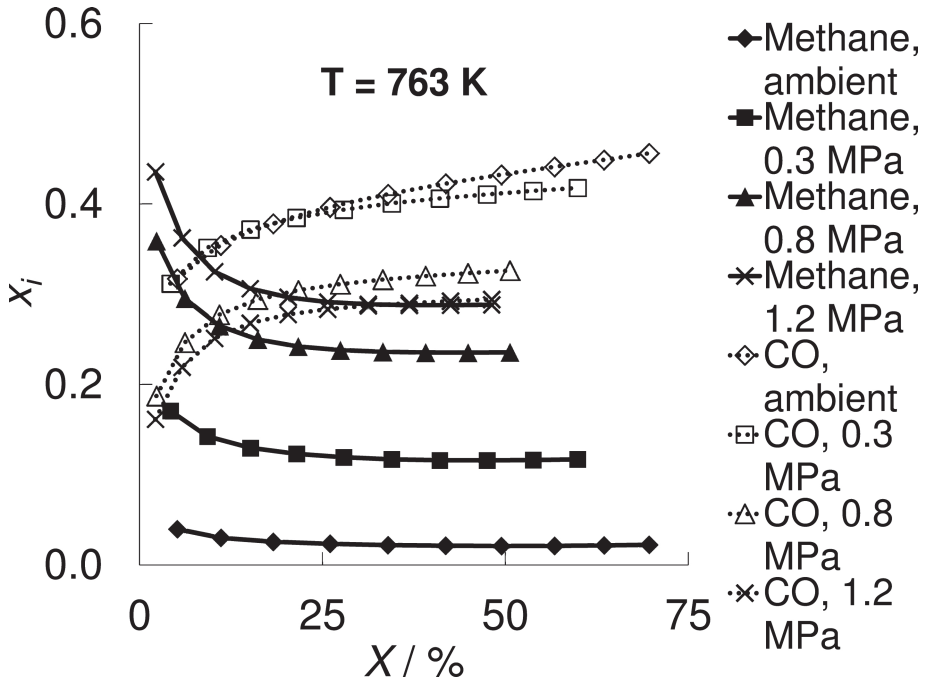

Figure 5-5: Dependency of the dry product gas composition on the reaction pressure at 763 K during reductive calcination of 115 g magnesite with 90 %vol. H_2 at the reactor inlet and $8.33*10^{-3}$ dm^3s^{-1} total feed flow; x_i = mole fraction of compound i, X = magnesite conversion; mole fraction of CO_2 (x_{CO2}) not shown: $x_{CO2} = 1 - x_{CO} - x_{CH4}$.

Table 5-2: Experimental conditions and results from the reductive calcination of 115.00 ± 0.50 g magnesite with 90 %vol. H_2 at the reactor inlet.

T_{mid}	OP	t_{iso}	$X_{end,\Delta m}$	$X_{end,GA}$	ε_{rel}	t_{20}	Mg
K	MPa	min	%	%	%	min	%wt.
748	na	348	44.6	47.0	5.5	179	34.32
748	0.3	328	40.6	40.6	0.0	186	32.69
748	0.8	338	40.0	37.1	-7.4	210	35.18
748	1.2	337	40.4	35.6	-11.8	223	36.19
763	na	345	75.7	80.1	5.8	96	43.62
763	0.3	354	73.3	74.3	1.3	113	43.39
763	0.8	350	66.0	62.6	-5.1	140	43.55
763	1.2	345	65.7	60.3	-8.3	148	40.78
778	na	365	95.6	104.4	9.2	63	53.40
778	0.3	360	94.8	102.8	8.3	68	51.62
778	0.8	360	94.6	97.9	3.5	81	52.53
778	1.2	344	91.2	88.2	-3.3	92	52.56
T_{mid}	OP	$Y_{CO,20}$	$Y_{CO2,20}$	$Y_{CH4,20}$	$Y_{CO,end}$	$Y_{CO2,end}$	$Y_{CH4,end}$
K	MPa	%	%	%	%	%	%
748	na	39.1	56.2	4.7	44.1	50.9	4.9
748	0.3	38.2	45.4	16.4	40.6	43.2	16.2
748	0.8	33.3	41.0	25.7	34.6	39.7	25.7
748	1.2	22.7	38.8	38.6	25.7	37.8	36.6
763	na	38.3	59.2	2.5	46.1	51.2	2.7
763	0.3	38.2	49.4	12.4	42.3	45.7	12.0
763	0.8	30.2	45.4	24.4	43.2	32.9	23.9
763	1.2	27.7	42.6	29.7	29.6	41.3	29.2
778	na	36.1	62.7	1.3	46.8	51.7	1.5
778	0.3	41.6	53.6	4.8	46.1	48.3	5.7
778	0.8	35.4	48.8	15.8	37.9	45.8	16.3
778	1.2	30.3	46.9	22.9	32.9	44.9	22.2

T_{mid} = temperature in the mid of the packed bed; OP = overpressure in reactor system; na = ambient pressure; t_{iso} = time at isothermal temperature; $X_{end,\Delta m}$ = conversion of magnesite after t_{iso} calculated from mass loss and LOI; $X_{end,GA}$ = conversion of magnesite after t_{iso} calculated from gas analysis; t_{20} = time needed to reach 20 % conversion of magnesite, the conversion of magnesite was calculated from gas analysis; $Y_{CO,20}$ = carbon monoxide yield after t_{20}; $Y_{CO2,20}$ = carbon dioxide yield after t_{20}; $Y_{CH4,20}$ = methane yield after t_{20} ; $Y_{CO,end}$ = carbon monoxide yield after t_{iso} at the end of the experiment; $Y_{CO2,end}$ = carbon dioxide yield after t_{iso} at the end of the experiment; $Y_{CH4,end}$ = methane yield after t_{iso} at the end of the experiment; Mg = magnesium content of the solid product according to ICP-OES analysis. Calculations applied are described in section 5.5.3.

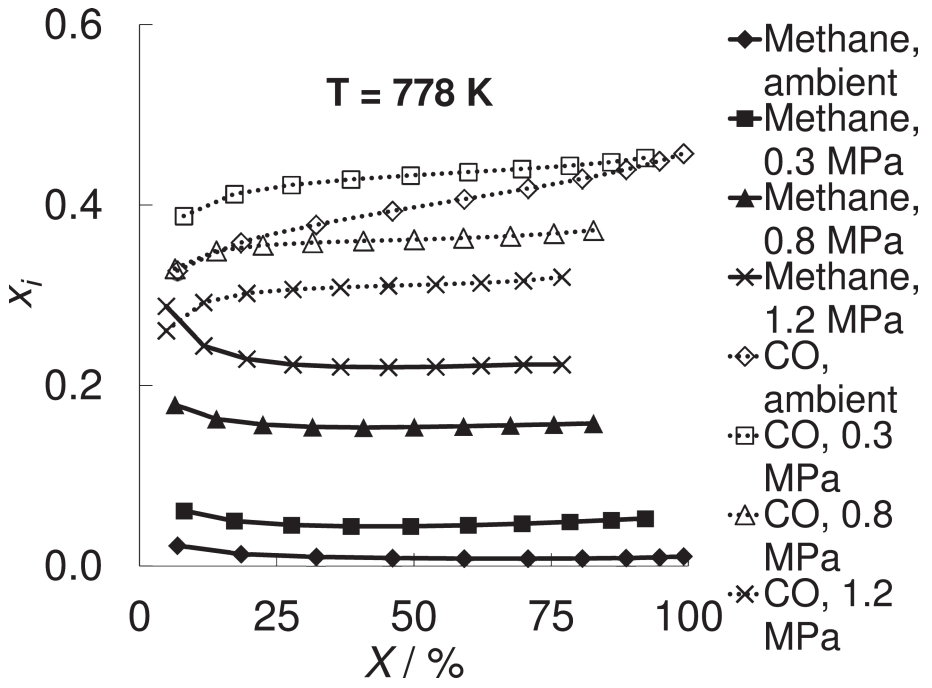

Figure 5-6: Dependency of the dry product gas composition on the reaction pressure at 778 K during reductive calcination of 115 g magnesite with 90 %vol. H_2 at the reactor inlet and $8.33*10^{-3}$ dm^3s^{-1} total feed flow; x_i = mole fraction of compound i, X = magnesite conversion; mole fraction of CO_2 (x_{CO2}) not shown: $x_{CO2} = 1 - x_{CO} - x_{CH4}$.

Table 5-2 shows that methane yield at 20 % magnesite conversion (see Table 5-2, column $Y_{CH4,20}$) increases with pressure at the same temperature and decreases with temperature at the same pressure. This characteristic does not substantially change at higher conversions (see Table 5-2, column $Y_{CH4,end}$). As a consequence, high pressure and low temperature facilitate methane formation (e.g. increase of methane yield from 4.9 % to 36.6 % at 748 K when pressure is increased from ambient to 1.2 MPa overpressure, see Table 5-2). At 748 K and 763 K carbon monoxide yield decreases with pressure at 20 % magnesite conversion (see Table 5-2, column $Y_{CO,20}$). Carbon monoxide yield is increased when magnesite conversion increases (see Table 5-2, column $Y_{CO,end}$). At 778 K and 20 % magnesite conversion, carbon monoxide yield increases when the pressure is increased from ambient to 0.3 MPa, but decreases at higher overpressures of 0.8-1.2 MPa. Thus, low to moderate temperature and pressure facilitate carbon monoxide formation. Carbon dioxide formation increases with temperature and decreases with pressure.

With respect to the reaction mechanism, the decrease of methane formation with increasing magnesite conversion suggests a dependency of methane formation on the amount of magnesite present. The increase of carbon monoxide with magnesite conversion can also be interpreted as an increase of carbon monoxide formation with increasing magnesium oxide formation. Therefore, reductively calcined magnesium oxide was investigated for its catalytic properties in separate experiments.

5.3.2 Liquid and solid products

The liquid products of all reductive calcination experiments were analyzed with a GC-TCD/FID standard routine described in section 5.5.5. The TCD signal confirmed that the liquid products consisted of water. The mean value for the amount of water produced was approximately 15 %wt. below the value that could be calculated from Eq. 2. This effect could be explained by incomplete condensation of water vapour in vessels 1 and 2 (see Figure 5-1). The FID signal of the chromatograms did not reveal any hydrocarbon based by-products. As expected, the magnesium content of the solid products increases with the calculated conversion (see last column in Table 5-2). The XRD spectra confirmed the formation of magnesium oxide. Minor formation of magnesium hydroxide and hydromagnesite can be explained by reaction of magnesium oxide with humidity during sample preparation for ICP-OES analysis in air. XRD spectra of all solid products can be found in the Supporting Information of the original article.

5.3.3 Catalytic properties of reductively calcined magnesium oxide for the conversion of CO_2 with H_2 (1:1)

Figure 5-7 shows that the CO_2 conversion to CO C_{CO2} increases from 763 to 778 K. It increases from ambient to 0.3 MPa overpressure and decreases slightly from 0.3 to 0.8 MPa. This can be explained by a general concept from heterogeneously catalyzed gas-phase reactions. Moderate pressures facilitate adsorption of the reactants on the catalyst surface, whereas elevated pressure impede desorption of the gaseous product. However, only carbon monoxide was detected in the product gas at ambient pressure and 0.3 MPa overpressure. At 0.8 MPa overpressure, traces of methane were detected besides the major product carbon monoxide. These findings imply that reductively calcined magnesium oxide catalyzes the reverse water gas shift reaction (see Eq.3) but does not catalyze conversion of carbon dioxide to methane. Calculations of the equilibrium conversion of CO_2 to CO according to Eq. 3 were performed with HSC Chemistry 8. The CO_2 conversion increases from approximately 80 % to nearly 100 % of the equilibrium conversion when the pressure is increased from ambient pressure to 0.3 MPa overpressure (see Fig. 7).

$$CO_2 + H_2 \xrightarrow{MgO} CO + H_2O \qquad (3)$$

The experiments also confirm that CO_2 conversion during reductive calcination of magnesium carbonate cannot be catalyzed by any trace elements. Hence, methane formation from magnesite in reductive calcination appears to proceed in a different mechanism. One possibility is the formation of reactive transition species either in the gas or solid phase or at the gas-solid interface.

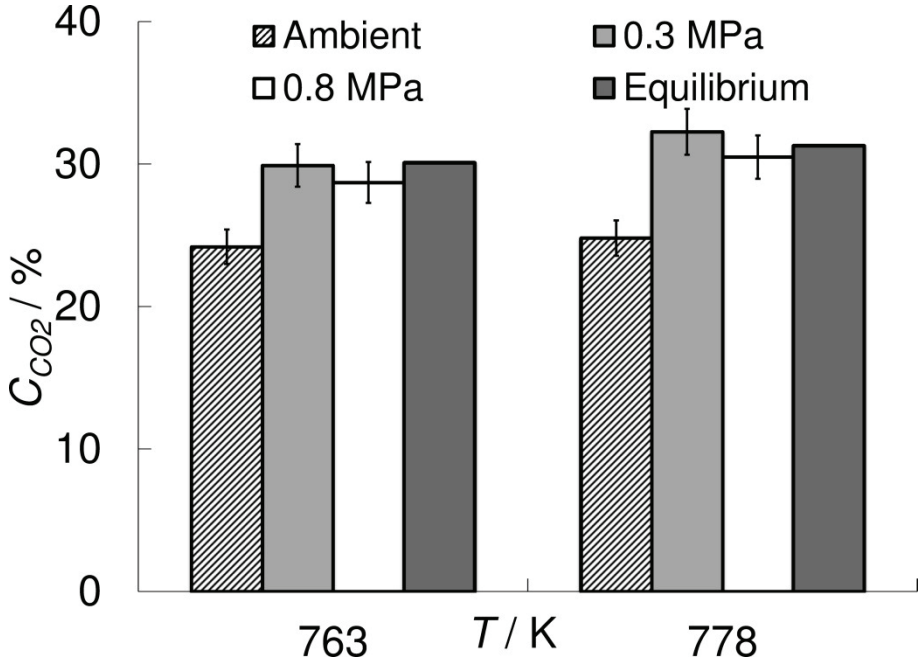

Figure 5-7: CO_2 conversion to CO C_{CO2} with reductively calcined MgO (25 g) as a fixed bed catalyst. Gas feed: 50 %vol. N_2, 25 %vol. H_2, 25%vol. CO_2, 8.33*10^{-3} dm^{3}s^{-1} (STP) total flow, T = reaction temperature.

5.4 Conclusions

The direct partial conversion of magnesite into magnesium oxide and methane without admixture of catalyst is feasible, which has not been reported in the literature, as far as to our knowledge. The product gas composition in the reductive calcination of magnesite can be easily adjusted by temperature and pressure. Reductive calcination substantially decreases carbon dioxide emissions from magnesite calcination and gives access to storing hydrogen either as methane or syngas. Experiments with carbon dioxide and hydrogen in the feed and reductively calcined magnesium oxide revealed significant reverse water gas shift activity. Methane formation from CO_2 in H_2 atmosphere over magnesium oxide was monitored in traces only. This implies that methane formation in reductive calcination of magnesite proceeds via a different mechanism that has not been reported yet and has to be further investigated.

5.5 Appendix: Extract of the Supporting Information

5.5.1 Details on the tubular reactor setup used in the study

The reductive calcination experiments were carried out in a fixed bed tubular reactor (see Figure 5-1) made of T316 steel with a total length of 800 mm, a reaction zone of 508 mm (T6-T1 in Fig. 2 in the original article), and an inner diameter of 25 mm. The setup is rated up to 34.5 MPa at 823 K and was manufactured by Parr Instrument Company (Moline, Illinois, USA). The gas flow at the inlet can be controlled with three separate thermal mass flow controllers for each gas (Bronkhorst El-Flow). At the inlet of the reactor tube a pre-heating coil (length 200 mm, largest diameter 24.05 mm) is installed. The reactor tube can be heated with a three-segmented electric furnace (Vecstar Ltd.) and the temperature is measured in the mid of each segment

(HT1-HT3 in Fig. 2 in the original article). The temperature inside the reactor is measured at six equally spaced positions with a multipoint Type J thermocouple (T1-T6 in Fig. 2 in the original article, distance between measurement points 101.6 mm). The pressure in the reactor can be controlled with a back pressure regulator (Badger Meter Europa GmbH). The product gas is cooled in two stages and condensable liquids are collected in vessels 1 and 2. Heat exchanger 1 is a double-pipe heat exchanger run with Kryo 30 (ethylene glycol/water mixture supplied by Lauda) at 273 K using a Microcool MC 250 cryostat (Lauda). For quantitative water removal, a sample gas cooler (heat exchanger 2, Hartmann and Braun CGEK 5, coolant R12) run at 275 K is used. A Parr 4871 process controller coupled with control software (SpecView HMI) was used to read out, save (time interval 10 sec), and control temperature, pressure, and gas flow rate. This software allowed for the visualization of the level of each process variable and for the variation of the controller output.

5.5.2 Experimental procedures

5.5.2.1 Isothermal conversion of magnesite

In all isothermal calcination experiments fresh magnesite starting material (115.00 ± 0.50 g) was used. The magnesite bed was placed at 278 mm from the reactor tube outlet with stainless steel spacers. The temperature of the bed was measured at two positions approximately 60 mm from the end (T3) and approximately 40 mm from top (T4). The gaseous feed was maintained at 90 %vol. hydrogen and 10 %vol. nitrogen, with a total flow rate of $8.33*10^{-3}$ dm^3s^{-1} (at standard temperature and pressure, STP). The temperature T_{mid} in the mid of the fixed bed was calculated by position-weighted linear interpolation of the temperature at the measurement positions next to the bed (T3 and T4 in Fig. 2 in the original article). T_{mid} is the reference temperature for all experiments.

Each experimental run consisted of a heat-up phase and an isothermal phase of 330-360 minutes. In the heat-up phase, conversion of magnesite was below 0.5 %. At the end of each isothermal phase, the reactor was flushed with nitrogen and cooled to room temperature overnight. Liquids condensed at 273 K (vessel 1 in Figure 5-1) and 275 K (vessel 2 in Figure 5-1) were collected, weighed, and analyzed with GC-TCD/FID. Solid products were transferred to a container under nitrogen flow and weighed.

5.5.2.2 Catalytic activity of reductively calcined magnesium oxide

The magnesium oxide bed (25.0 ± 0.2 g, reductively calcined at 808 K and stored under nitrogen in between experiments) was placed at 340 mm from the reactor tube outlet. The temperature T_{mid} in the mid of the fixed bed was calculated by position-weighted linear interpolation of the temperature at the measurement positions next to the bed (T3 and T4 in Figure 5-1). The flow rate at the inlet of the reactor was maintained at $8.33*10^{-3}$ dm^3s^{-1} (STP) with a gas composition of 50 %vol. nitrogen, 25 %vol. hydrogen, and 25 %vol. carbon dioxide. Liquids condensed at 273 K (vessel 1 in Figure 5-1) and 275 K (vessel 2 in Figure 5-1) were collected, weighed, and analyzed with GC-TCD/FID.

5.5.3 Calculation procedures

5.5.3.1 Calculation of the CO, CO_2, and CH_4 amount over reaction time

Nitrogen was used as an inert gas (Eq. SI1) to establish the reactor balance (Eq. SI2), assuming ideal gas behavior (Eq. SI2 and SI3). By means of equation SI4, the molar quantities of CO, CO_2, and CH_4 leaving the reactor at each time interval Δt (5 sec) of data acquisition was calculated. Cumulative summation of these quantities over the reaction time gives the produced amounts of CO, CO_2, and CH_4 (Eq. SI5). As no nitrogen detector was used, the nitrogen concentration was calculated with Eq. SI6.

$$x_{N2,P} * P = x_{N2,F} * F \quad \text{(SI1)}$$

$$n_{i,P} = \frac{\Delta n_{i,P}}{\Delta t} = x_{i,P} * P * V_n^{-1} \quad \text{(SI2)}$$

$$x_{i,j} = \frac{c_{i,j}[\%\text{vol.}]}{100[\%\text{vol.}]} \quad \text{(SI3)}$$

$$\Delta n_{i,P} = x_{i,P} * \frac{x_{N2,F}}{x_{N2,P}} * F * \Delta t * V_n^{-1} \quad \text{(SI4)}$$

$$n_{i,P}(t) = \sum_{t_{start}}^{t} \Delta n_{i,P} \quad \text{(SI5)}$$

$$c_{N2,P} = 100 - c_{CO2,P} - c_{CO,P} - c_{CH4,P} - c_{H2,P} \quad \text{(SI6)}$$

P = product stream, dm^3s^{-1} (at standard temperature and pressure, STP); F = feed stream, dm^3s^{-1} (STP); $x_{i,j}$ = mole fraction of compound i in stream j; $n_{i,j}$ = molar stream of compound i in stream j, mol s^{-1}; $c_{i,j}$ = concentration of compound i in stream j, %vol.; $\Delta n_{i,P}$ = amount of compound i leaving the reactor in the product stream during time interval Δt, mole; V_n = molar volume (STP), 22.71 dm^3mole^{-1}; $n_{i,P(t)}$ = molar quantity of compound i at time t, mole.

5.5.3.2 Calculation of magnesite conversion during reaction from gas analysis

The theoretical mass loss accounting for total conversion of magnesite (Eq. SI7) $\Delta m_{magn,max}$ was calculated using the loss on ignition (LOI) of 51.36 %wt. for fresh magnesite (decomposition of 2.00 g in air in a crucible at T = 1323 K). Alternatively, the theoretical mass loss accounting for total conversion could be calculated from the CO_2 content of the magnesium carbonate present in the sample (see Table 5-1). As both values account for 51.36 %wt. this would not affect the calculated conversion values. Magnesite is not known to form non-stoichiometric oxides. Therefore direct production of CO without consumption of H_2 can be neglected. The reduction of MgO to magnesium with H_2 is thermodynamically highly unfavorable in the examined temperature range ($\Delta_R^\circ G_{573\,K} = 324$ kJ mol^{-1} ;$\Delta_R^\circ G_{823\,K} = 311$ kJ mol^{-1}, values calculated with HSC Chemistry 8). Hence, a carbon balance according to Eq. 1 can be applied. The sum of the amount of CO_2, CO, and CH_4 produced can thus be directly linked to the amount of magnesite consumed during reaction (Eq. SI8). As a consequence, the conversion during reaction can be calculated by applying Eq. SI9.

$$\Delta m_{magn,max} = LOI * m_{magn,start} \quad \text{(SI7)}$$

$$n_{magn,start} - n_{magn}(t) = n_{MgO}(t) = n_{(CO+CO_2+CH_4),GA}(t) \quad \text{(SI8)}$$

$$X(t) = \frac{n_{magn,start} - n_{magn}(t)}{\left(\frac{\Delta m_{magn,max}}{MW_{CO2}}\right)} = \frac{n_{(CO+CO_2+CH_4)}(t)}{\left(\frac{\Delta m_{magn,max}}{MW_{CO2}}\right)} * 100\% \quad \text{(SI9)}$$

$\Delta m_{magn,max}$ = mass loss at total conversion, g; $m_{magn,start}$ = amount of magnesite used in the experiment, g; $n_{magn,start}$ = amount of magnesite used in the experiment, mole; $n_{magn}(t)$ = amount of magnesite present at time t, mole; $n_{MgO}(t)$ = amount of magnesium oxide present at time t, mole; $n_{(CO+CO2+CH4),GA}(t)$ = amount of CO, CO_2, and CH_4 produced at time t according to gas analysis (GA), mole; MW_{CO2} = molecular weight of CO_2, 44.01 g mole^{-1}; X(t) = conversion of magnesite at time t.

5.5.3.3 Verification of the calculation algorithm

To check the calculation approach derived above, the relative deviation ε_{rel} between the calculated amount of CO_2, CO, and CH_4 produced until the end of the experiment was compared to the mass loss of the solid sample at the end of each experiment (Eq. SI10).

$$\varepsilon_{rel} = \frac{n_{(CO+CO_2+CH_4),GA}(t_{end}) - \left(\frac{m_{magn,start} - m_{magn}(t_{end})}{MW_{CO2}}\right)}{\left(\frac{m_{magn,start} - m_{magn}(t_{end})}{MW_{CO2}}\right)} * [100\%] \quad \text{(SI10)}$$

The mean standard deviation of ε_{rel} for all experiments accounted for ± 7.0 %.

5.5.4 Sample preparation for ICP-OES Analysis

The samples were grinded to powders before analysis. 200 mg of each sample were digested with 15 ml of HCl and 5 ml of HNO_3 in a volumetric flask (500 ml). 20 ml $HClO_4$ were added to decrease the volume. Then, the volumetric flask was filled with H_2O up to the 500 ml marking.

5.5.5 Analysis of liquid products by GC-TCD/FID

5.5.5.1 Method

A Supel-P-Plot column (30 m, inner diameter 0.53 mm, layer 30 µm) was used as the stationary phase. Helium (5.0, Air Liquide) was used as the mobile phase. The thermal conductivity (523 K, 70 mA) and flame ionization detector (523 K) were connected in series. 0.3 µL of each sample were injected at an injection temperature of 513 K.

5.5.5.2 Calibration for quantitative analysis via the TCD-signal

Standard solutions of water in 1,4-dioxane were prepared in concentrations of 0, 0.05, 0.1, 0.2 und 0.3 mg H_2O per 0.3 µL injection volume. These standard solutions were prepared and measured in duplicate to calculate a linear calibration function, depicted in Figure 5-8. Figure 5-9 shows the chromatograms of one 0.2 mg H_2O per 0.3 µL injection volume sample. The water signal is detected after approximately 4.0 minutes and the 1,4-dioxane signal is detected after approximately 14.8 minutes.

Table 5-3: Temperature program of the GC method

Heating rate [K min^{-1}]	Temperature [K]	Holding time [min]
-	313	2
15	423	5,7
30	473	1

5.5.5.3 Results of the GC-TCD/FID analysis

Table 5-4 summarizes the experimental results of the liquid products of the reductive calcination of magnesite.

Table 5-4: Results of the GC analysis.

Experiment	H_2O [%wt.]	Recovery 1,4-dioxane [%]
Calcination 748 K ambient pressure	98	110
Calcination 748 K 0.3 MPa overpressure	100	107
Calcination 748 K 0.8 MPa overpressure	96	105
Calcination 748 K 1.2 MPa overpressure	93	97
Calcination 763 K ambient pressure	96	109
Calcination 763 K 0.3 MPa overpressure	99	102
Calcination 763 K 0.8 MPa overpressure	96	102
Calcination 763 K 1.2 MPa overpressure	96	110
Calcination 778 K ambient pressure	97	106
Calcination 778 K 0.3 MPa overpressure	99	108
Calcination 778 K 0.8 MPa overpressure	97	98
Calcination 778 K 1.2 MPa overpressure	94	106

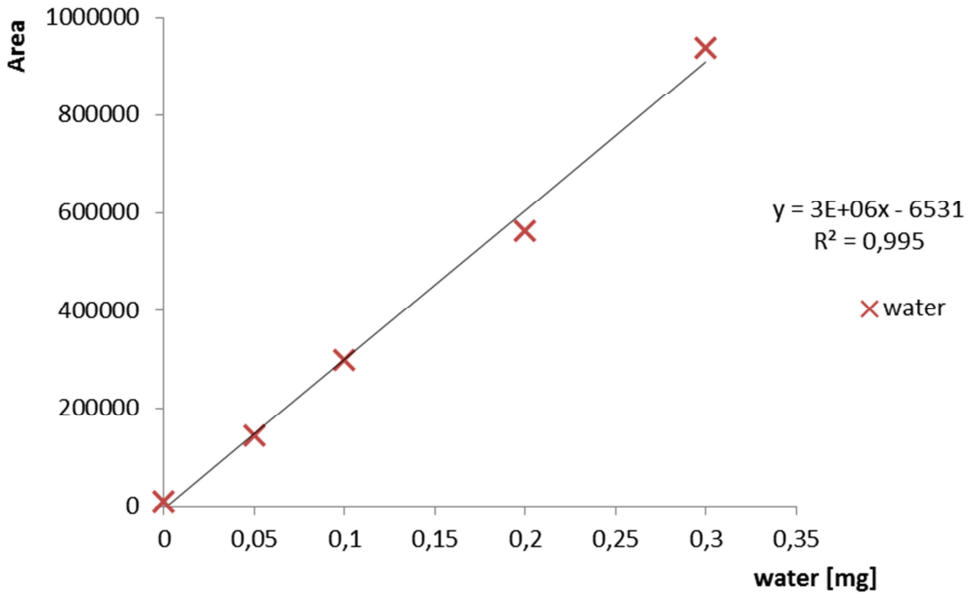

Figure 5-8: Calibration curve used for the calculation of the water content via GC.

SHIMADZU LabSolutions **Analysis Report**

<Sample Information>

Sample Name	: RedK_St0,2_2_2		
Sample ID	:		
Data Filename	: RedK_St0,2_2_2_2015_12-09_Dani_FID_26.gcd		
Method Filename	: Dani_FID.gcm		
Batch Filename	: 2015_12-09.gcb		
Vial #	: 83	Sample Type	: Unknown
Injection Volume	: 0,3 uL		
Date Acquired	: 10.12.2015 02:07:42	Acquired by	: System Administrator
Date Processed	: 10.12.2015 02:29:27	Processed by	: System Administrator

<Chromatogram>

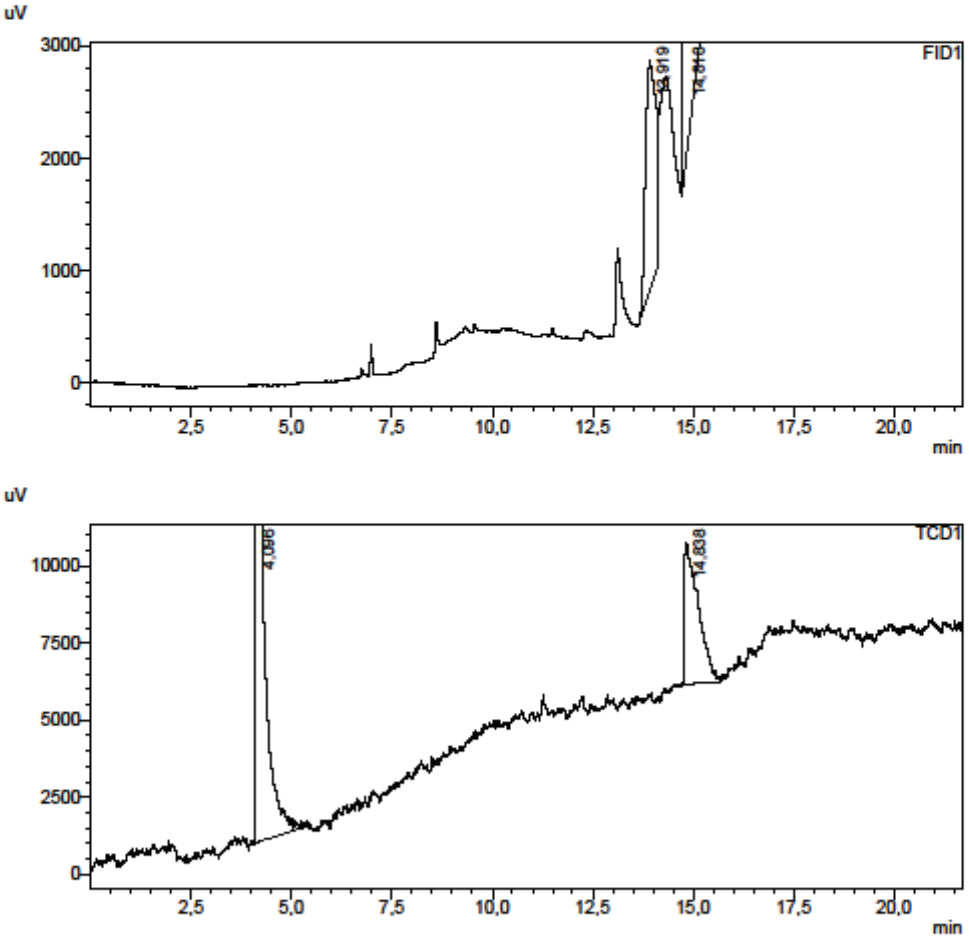

<Peak Table>

FID1

C:\LabSolutions\Data\2015-10-20\RedK_St0,2_2_2_2015_12-09_Dani_FID_26.gcd

Figure 5-9: Chromatograms of the standard with 0.2 mg H_2O per 0.3 µl injection volume.

References

[1] I. Szednyj, D. Brandhuber, Stand der Technik zur Kalk-, Gips und Magnesiaherstellung: Beschreibung von Anlagen in Österreich. Umweltbundesamt, Wien, 2007.

[2] M. Fischedick, J. Roy, A. Abdel-Aziz, A. Acquaye, J. M. Allwood, J.-P. Ceron, Y. Geng, H. Kheshgi, A. Lanza, D. Perczyk, L. Price, E. Santalla, C. Sheinbaum, K. Tanaka, 2014: Industry. In: Climate Change 2014: Mitigation of Climate Change. Contribution of Working Group III to the Fifth Assessment Report of the Intergovernmental Panel on Climate Change [O. Edenhofer, R. Pichs-Madruga, Y. Sokona, E. Farahani, S. Kadner, K. Seyboth, A. Adler, I. Baum, S. Brunner, P. Eickemeier, B. Kriemann,J. Savolainen, S. Schlömer, C. von Stechow, T. Zwickel and J.C. Minx [eds.]]. Cambridge University Press, Cambridge, United Kingdom and New York, NY, USA 2014.

[3] United Nations Framework Convention on Climate Change FCCC/CP/2015/L.9. Adoption of the Paris Agreement; Paris 2015.

[4] X. Xiaoding, J. Moulijn, Mitigation of CO2 by chemical conversion: Plausible chemical reactions and promising products, Energy Fuels 20 (1996) 305–325.

[5] H. Arakawa, M. Aresta, J.N. Armor et al., Catalysis research of relevance to carbon management: progress, challenges, and opportunities, Chem. Rev. 101 (2001) 953–996. doi: 10.1021/cr000018s.

[6] A. Otto, T. Grube, S. Schiebahn, D. Stolten, Closing the loop: captured CO2 as a feedstock in the chemical industry, Energy Environ. Sci., 8 (2015) 3283–3297. doi: 10.1039/C5EE02591E.

[7] W. Wang, S. Wang, X. Ma, J. Gong, Recent advances in catalytic hydrogenation of carbon dioxide., Chem. Soc. Rev. 40 (2011) 3703–27. doi: 10.1039/c1cs15008a.

[8] M. D. Porosoff, B. Yan, J.G. Chen, Catalytic reduction of CO2 by H2 for synthesis of CO, methanol and hydrocarbons: Challenges and opportunities, Energy Environ. Sci. 9 (2016) 62–73. doi: 10.1039/C5EE02657A.

[9] A. Melis, T. Happe, Hydrogen production. Green algae as a source of energy, Plant Physiol. 127 (2001) 740–748. doi:10.1104/pp.010498.740.

[10] R.M. Navarro, M.C. Sánchez-Sánchez, M.C. Alvarez-Galvan, F. del Valle, J.L.G. Fierro, Hydrogen production from renewable sources: biomass and photocatalytic opportunities, Energy Environ. Sci. 2 (2009) 35–54. doi:10.1039/B808138G.

[11] T. Abbasi, S.A. Abbasi, "Renewable" hydrogen: Prospects and challenges, Renew. Sustain. Energy Rev. 15 (2011) 3034–3040. doi:10.1016/j.rser.2011.02.026.

[12] A. Miltner, W. Wukovits, T. Pröll, A. Friedl, Renewable hydrogen production: a technical evaluation based on process simulation, J. Cleaner Prod. 18 (2010) S51–S62. doi: 10.1016/j.jclepro.2010.05.024.

[13] I. K. Kapdan, F. Kargi, Bio-hydrogen production from waste materials, Enzyme Microb. Technol. 38 (2006) 569–582. doi: 10.1016/j.enzmictec.2005.09.015.

[14] O. Bičáková, P. Straka, Production of hydrogen from renewable resources and its effectiveness, Int. J. Hydrogen Energy, 37 (2012) 11563–11578. doi: 10.1016/j.ijhydene.2012.05.047.

[15] A. Steinfeld, Solar thermochemical production of hydrogen - a review, Sol. Energy, 78 (2005) 603–615. doi: 10.1016/j.solener.2003.12.012.

[16] N. Armaroli, V. Balzani, The hydrogen issue, ChemSusChem. 4 (2011) 21–36. doi:10.1002/cssc.201000182.

[17] M. Sterner, Bioenergy and renewable power methane in integrated 100% renewable energy systems Ph.D. Thesis, University Kassel, 2009.

[18] O.S. Joo, K.D. Jung, I. Moon, a Y. Rozovskii, G.I. Lin, S.H. Han, et al., Carbon dioxide hydrogenation to form methanol via a reverse-water-gas-shift reaction (the CAMERE process), Ind. Eng. Chem. Res. 38 (1999) 1808–1812. doi:10.1021/ie9806848.

[19] K.M.K. Yu, I. Curcic, J. Gabriel, S.C.E. Tsang, Recent advances in CO2 capture and utilization, ChemSusChem. 1 (2008) 893–899. doi:10.1002/cssc.200800169.

[20] B. Dou, C. Wang, Y. Song, H. Chen, B. Jiang, M. Yang, et al., Solid sorbents for in-situ CO2 removal during sorption-enhanced steam reforming process: A review, Renew. Sustain. Energy Rev. 53 (2016) 536–546. doi:10.1016/j.rser.2015.08.068.

[21] A. Reller, C. Padeste, P. Hug, Formation of organic carbon compounds from metal carbonates, Nature 329 (1987) 527–529.

[22] A. Reller, R. Emmenegger, C. Padeste, H.R. Oswald, Thermochemical reactivity of metal carbonates, Chimia (Aarau) 45 (1991) 262–266.

[23] C. Padeste, H.R. Oswald, A. Reller, The thermal behaviour of pure and nickel-doped hydromagnesite in different atmospheres, Mater. Reserach Bull. 26 (1991) 1263–1268.

[24] A. Tsuneto, A. Kudo, N. Saito, T. Sakata, Hydrogenation of solid state carbonates, Chem. Lett. (1992) 831–834.

[25] D. Jagadeesan, M. Eswaramoorthy, C.N.R. Rao, Investigations of the conversion of inorganic carbonates to methane, ChemSusChem 2 (2009) 878–882. doi: 10.1002/cssc.200900152.

[26] D. Jagadeesan, Y. Sundarayya, G. Madras, C.N.R. Rao, Direct conversion of calcium carbonate to C1-C3 hydrocarbons, RSC Adv. 3 (2013) 7224–7229. doi:10.1039/c3ra40264a.

[27] N. Yoshida, T. Hattori, E. Komai, T. Wada, Methane formation by metal-catalyzed hydrogenation of solid calcium carbonate, Catal. Letters 58 (1999) 119–122.

6 Synthesis of carbon monoxide from hydrogen and magnesite/dolomite[8]

Abstract

The calcination of magnesite and dolomite is a state of the art technology step in minerals processing. The concomitantly produced carbon dioxide is released into the flue gas, with all its negative effects on the global carbon balance. Reductive calcination of magnesite and dolomite to carbon monoxide and methane would open a window to re-use carbon dioxide and produce value-added carbonaceous products. The conversion of more than 70 % of the carbon dioxide emitted during reductive calcination of the magnesite content of a mixed magnesite/dolomite (1:1 mol/mol) to carbon monoxide at moderate temperature is feasible without admixture of catalyst.

[8] This chapter is based on an article published by John Wiley & Sons and is reprinted under licence number 4038830122449 of Jan. 30, 2017:
G. Baldauf-Sommerbauer, S. Lux, W. Aniser, M. Siebenhofer, Synthesis of carbon monoxide from hydrogen and magnesite/dolomite, Chemie Ing. Tech. 89 (2017) 172–179. doi:10.1002/cite.201600078.

Symbols

$\Delta_R G°$	kJ mol^{-1}	Standard free energy of reaction
$\Delta_R H°$	kJ mol^{-1}	Standard enthalpy of reaction
Δm	%wt.	Mass change/loss
$\Delta m_{carb,max}$	mg	Mass loss after total conversion
Δt	min	Time step
F	cm^{3}min^{-1}	Feed stream (STP)
m	%wt.	Mass
$m_{carb,start}$	mg	Amount of magnesite used in the experiment
$n_{i,j}$	mmol min^{-1}	Molar flow of compound i in stream j
$n_i(t)$	mmol	Amount of compound i at the time t
$n_{carb,start}$	mmol	Amount of carbonate
$n_{carb}(t)$	mmol	Amount of carbonate present at time t
$n_{(CO+CO2+CH4),GA}(t)$	mmol	Amount of CO, CO_2, and CH_4 produced at time t according to gas analysis (GA)
MW_{CO2}	mg mmol^{-1}	Molecular weight of CO_2: 44.01 mg mmol^{-1}
OP	bar	Overpressure, gauge pressure
P	bar	Absolute pressure
PS	cm^{3}min^{-1}	Dry product gas stream (STP)
T	°C	Temperature
t_0	min	Starting time
$t_{r,iso}$	min	Reaction time at isothermal conditions
V_m	cm^{3}mmol^{-1}	Molar volume of an ideal gas at STP: 22.414 cm^{3}mmol^{-1}
X(t)	%	Conversion at time t
$X_{m.l.}$	%	Conversion calculated on the basis of the mass loss
X_{GA}	%	Conversion calculated on the basis of the gas analysis
$X_{GA,100min}$	%	Conversion calculated on the basis of the gas analysis at $t_{r,iso}$=100 minutes
Y_{CO}	%	Yield of carbon monoxide
$y_{i,j}$	-	Mole fraction of compound i in stream j
Θ	°	Diffraction angle
ϵ_i	-	Stoichiometric coefficient of compound i in any reaction equation, positive for products, negative for educts

Abbreviations

a.u.	Arbitrary units
Cat.	Catalyst
FID	Flame ionization detector
GC	Gas chromatography
IR	Infrared
RWGS	Revers water-gas-shift
STP	Standard temperature and pressure: 0 °C, 1.013 bar
TCD	Thermal conductivity detector
TG	Thermogravimetry
XRF	X-ray fluorescence
XRD	X-ray diffraction

6.1 Introduction

The mineral carbonates magnesite $MgCO_3$ and dolomite $(Ca,Mg)(CO_3)_2$ are important raw materials for diverse industrial applications. These two minerals are often found together in varying compositions of $xMgCO_3*y(Ca,Mg)(CO_3)_2$. Calcination of magnesite in air (Eq. 1) produces magnesia. Magnesia is mainly needed in refractory production [1]. Magnesia and calcite produced by calcination of magnesite and/or dolomite in air (Eq. 2) are used on a large scale as refractory liner or slag formers for pig iron production in the blast furnace process [2].

$$MgCO_3 \xrightarrow{\Delta T,Air} MgO + CO_2 \quad (1)$$

$$(Ca,Mg)(CO_3)_2 \xrightarrow{\Delta T,Air} MgO + CaO + 2CO_2 \quad (2)$$

Both calcination processes depicted in Eq. 1 and 2 produce a metal oxide as the product and carbon dioxide as a by-product. The technological state of the art is to release carbon dioxide into the flue gas. From an environmental point of view, liberation of carbon dioxide from carbonates is unfavorable, due to the detrimental effect on the global carbon balance and the climate [3]. Instead of emitting carbon dioxide into the atmosphere it would be beneficial to make use of it as a carbon source for hydrogen storage and production of chemicals, avoiding coal and oil consumption [4-7]. The carbon atom of CO_2 is in the highest oxidation state possible. Therefore, it has to be reduced for further utilization. Several C1 components, for instance carbon monoxide, methane, methanol, and formaldehyde, are accessible (Eq. 3), whereas the product selectivity depends on reaction conditions and catalysts [8]. A promising reducing agent is renewably produced hydrogen [9-13]. The use of hydrogen, favorably produced by water electrolysis run on excess renewable energy, would combine carbon dioxide utilization and chemical hydrogen storage.

$$CO_2 + \left(\frac{x}{2} + z\right) H_2 \xrightarrow{\Delta T,\Delta P,Cat.} CH_xO_y + z\,H_2O \quad | \quad z = 2 - y \quad (3)$$

$$CO_2 + H_2 \xleftrightarrow{\Delta T,\Delta P,Cat.} CO + H_2O \quad | \quad x = 0, y = 1;\ \text{RWGS} \quad (4)$$

$$CO + 3H_2 \xrightarrow{\Delta T,\Delta P,Cat.} CH_4 + H_2O \quad | \quad x = 2, y = 0;\ CO - \text{Methanation} \quad (5)$$

$$CO_2 + 4H_2 \xrightarrow{\Delta T,\Delta P,Cat.} CH_4 + 2H_2O \quad | \quad x = 4, y = 0;\ CO_2 - \text{Methanation} \quad (6)$$

Production of organic chemicals from syngas (CO/H_2) is an industrially established technology. A variety of products is accessible, whereas methanol, aliphatic aldehydes [14], and hydrocarbons [15] are the favored products. The current production of carbon monoxide for syngas applications is based on coal and oil gasification, steam reforming, and partial oxidation of hydrocarbons [14]. Alternatively, carbon monoxide production via the reverse water-gas-shift reaction shown in Eq. 4 is possible when suitable catalysts are applied [5]. Due to the standard free energy of reaction (Figure 6-1) an elevated temperature of at least 900 °C is needed for high

CO_2-conversion with H_2 to CO. A drawback of high operation temperature is the need for robust catalysts. Catalytic carbon monoxide and dioxide methanation (Eq. 5 and 6) with renewably produced hydrogen is broadly discussed in the Power-to-Gas concept [16, 17]. The conversion of CO and CO_2 to CH_4 is highly exothermic, but thermodynamically unfavorable above 600 °C. Due to kinetic hindrance, heterogeneous catalysis is needed for high CO/CO_2 conversion in catalytic methanation [8]. Catalyst development and stability are key issues in the catalytic reverse water-gas-shift reaction and the methanation reaction [5,18]. Therefore, a non-catalytic or a hybrid process with in-situ conversion would be beneficial.

Earlier research [19] revealed that conversion of pure mineral magnesite to magnesium oxide and carbon dioxide, carbon monoxide, and methane is feasible in single step reductive calcination according to Eq. 7.

$$(a + b + c)MgCO_3 + (b + 4c)H_2 \leftrightarrow$$

$$(a + b + c)MgO + aCO_2 + bCO + cCH_4 + (b + 2c)H_2O \quad (7)$$

The product composition CO_2:CO:CH_4 depends on the reaction temperature and pressure. It was shown that MgO is an active and stable RWGS catalyst at temperatures above 450 °C [19]. Conversion of metal carbonates to CO and CH_4 in hydrogen atmosphere with catalysts has been reported in [20-24] and conversion without catalysts is reported in [19,21,25].

From a process point of view, single-step reductive calcination would be advantageous over a two-step process of (1) calcination and (2) catalytic flue gas conversion with a reverse water-gas-shift catalyst. State of the art calcination of $MgCO_3$ is performed in directly fired kilns that run on combustion air and a carbonaceous (fossil) fuel, which leads to an increase of the overall CO_2 emissions. Furthermore, the nitrogen present in air increases the gas stream that needs to be processed thermally and catalytically and thus leads to a bigger plant size for the same amount of MgO to be produced.

In this work, the influence of temperature and pressure on the product composition for the reductive calcination of magnesite from mineral magnesite/dolomite (1:1 mol/mol) was investigated. Thermogravimetric experiments were performed to identify the calcination behavior in nitrogen and hydrogen atmosphere. The experimental verification of syngas production from magnesite/dolomite mineral with hydrogen was performed in a tubular reactor setup.

6.2 Thermodynamic calculations

As shown in Figure 6-1, the conversion of H_2 with metal carbonates (= reductive calcination) does significantly decrease the onset temperature of syngas formation to less than 500 °C in the case of $MgCO_3$. At a temperature of 500 °C, the reductive calcination of metal carbonates to methane is thermodynamically feasible.

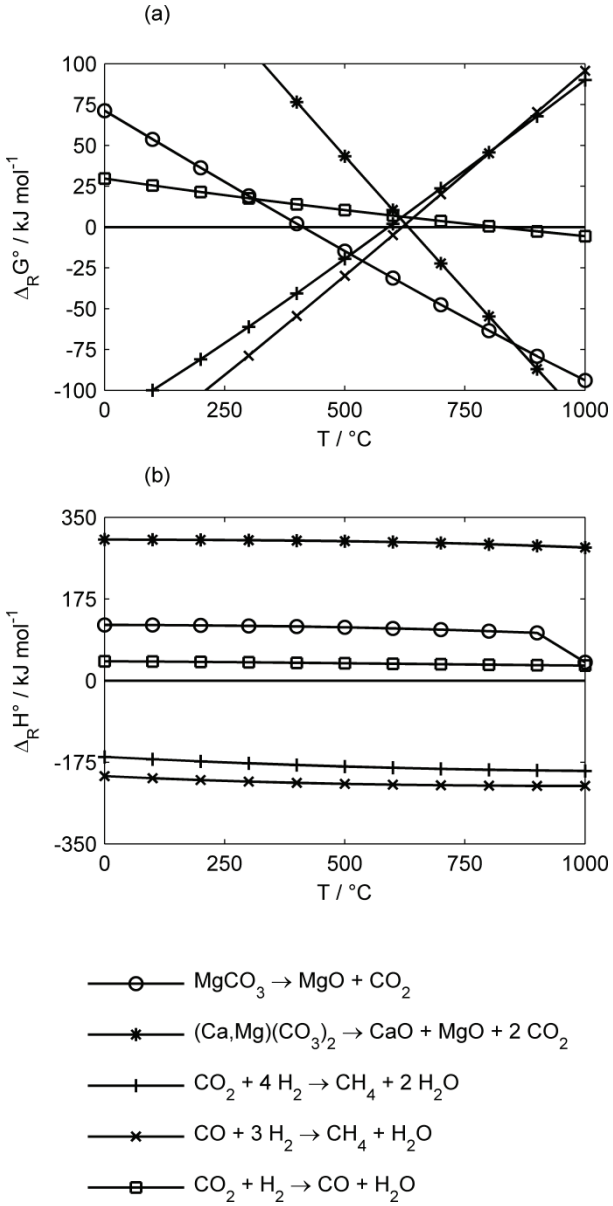

Figure 6-1: (a) Standard free energy of reaction $\Delta_R G°$ and (b) standard enthalpy of reaction $\Delta_R H°$ for the calcination of the carbonates present in the mineral sample investigated, the reverse water-gas-shift reaction, and the methanation of CO and CO_2 [26].

According to Le Chatelier's principle, increase of pressure does not positively affect the equilibrium composition of the reverse water-gas-shift reaction 4 ($\sum_i \epsilon_i(\text{gaseous}) = 0$ for T > 100 °C, P = ambient), but should increase equilibrium methane yield of the methanation reactions 5 and 6 ($\sum_i \epsilon_i(\text{gaseous}) < 0$ for T > 100 °C, P = ambient). Consequently, formation of methane and carbon monoxide from magnesite/dolomite and hydrogen is thermodynamically feasible.

6.3 Experimental

Mineral magnesite/dolomite samples (supplied by RHI, Breitenau, Austria) and solid products were characterized with X-ray fluorescence (XRF, Bruker S8 Tiger) and X-ray diffraction (XRD, X'Pert Pro, Panalytical, Co-$K_{\alpha 1}$=0.178901 nm, data collection at 298 K). Nitrogen and hydrogen

were used in 99.999 % quality and were supplied by Air Liquide. Deionized water and dried (with 0.3 nm molecular sieve, Metrohm) 1,4-dioxane (99.5 %, Merck) were used for liquid sample preparation for gas chromatography (GC) analysis. Liquid reaction products were analyzed with GC-FID/TCD (Shimadzu GC2010Plus, Supelco Q-Plot 30m*0,53m, fused silica). Thermogravimetry (TG) was carried out with a sample weight of 20 ± 2 mg of a 63-100 µm size fraction of magnesite/dolomite in 100 cm^3 min^{-1} total gas flow on a Netzsch Jupiter STA 449C thermobalance and alumina sample pans.

6.3.1 Reactor setup

Reductive calcining experiments in H_2 atmosphere were carried out with a tubular reactor setup manufactured by Parr Inc., USA, shown in Figure 6-2. The reactor tube made of T316 stainless steel has an inner diameter of 25 mm and a length of 800 mm. Experiments were carried out with 121.0 ± 0.5 g mineral feed material (5-8 mm size fraction, height in reactor 200 ± 10 mm) at temperatures close to the onset temperature of the RWGS reaction between 495 to 535 °C, at ambient pressure, 3 bar, and 8 bar overpressure. The feed gas flow was fixed at 500 cm^3 min^{-1} at standard temperature and pressure (STP: 0 °C, 1.013 bar). The feed gas composition was set to 90 %vol. hydrogen and 10 %vol. nitrogen as an internal standard for balancing purposes. The temperature of the solid feed mineral was monitored at two positions within the bed with a multipoint type J thermocouple. A Parr process control system was used for temperature and pressure control, as well as data recording. The dry product gas was analyzed by online IR absorption (ABB Uras26) for CO, CO_2, and CH_4 (0.0-100.0 %vol.) and TCD detection (ABB Caldos27) for H_2 (0.0-100.0 %vol.). The product gas composition was logged every 5 seconds.

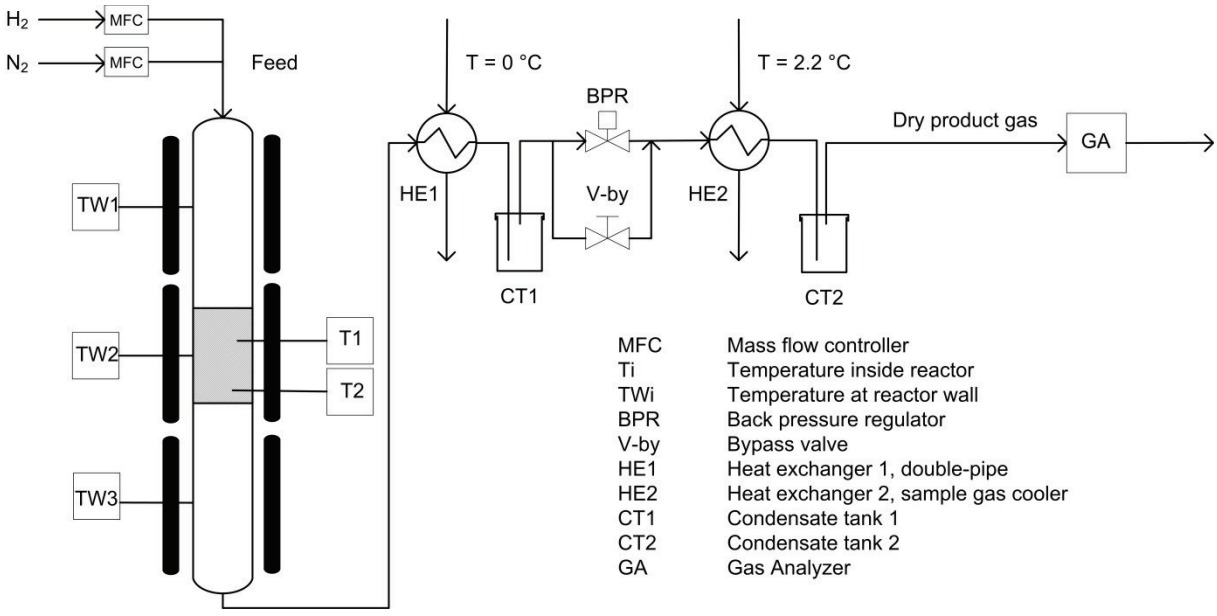

Figure 6-2: Tubular reactor setup used for reductive calcining experiments.

6.3.2 Reactor balance

The gaseous product streams $n_{i,j}$ were calculated with the help of the internal standard nitrogen by balancing the reactor assuming ideal gas behavior (Eq. 8). Numeric integration by summation of the discrete data points for $n_{i,j}$ allowed for the calculation of the produced amounts $n_i(t)$ of CO, CO_2, and CH_4 until any time t during the experiment (Eq. 9).

$$n_{i,PS} = y_{i,PS} * \frac{y_{N2,F}}{y_{N2,PS}} * \frac{F}{V_m} \quad (8)$$

$$n_i(t) = \int_{t_0}^{t} n_i \, dt \approx \sum_{t_o}^{t} n_{i,PS} * \Delta t \quad (9)$$

The carbonate conversion during the experiment can be calculated with a carbon balance: The sum of the amount of CO_2, CO, and CH_4 produced can be directly linked to the amount of carbonate consumed according to Eq. 10. Consequently, the conversion during the experiment can be calculated with Eq. 11. This approach can be verified by comparing the conversion at the end of the experiment with the conversion calculated from the mass loss according to Eq. 12.

$$n_{carb,start} - n_{carb}(t) = n_{(CO+CO_2+CH_4),GA}(t) \quad (10)$$

$$X(t) = \frac{n_{carb,start} - n_{carb}(t)}{\left(\frac{\Delta m_{carb,max}}{MW_{CO2}}\right)} = \frac{n_{(CO+CO_2+CH_4)}(t)}{\left(\frac{\Delta m_{carb,max}}{MW_{CO2}}\right)} \quad (11)$$

$$X(t_{end}) = \frac{n_{(CO+CO_2+CH_4)}(t_{end})}{\left(\frac{\Delta m_{carb,max}}{MW_{CO2}}\right)} \approx \frac{\Delta m_{carb}}{\Delta m_{carb,max}} \quad (12)$$

6.4 Results and Discussion

6.4.1 Mineral feed

The XRD pattern of the mineral feed material (Figure 6-3) evidences that two different carbonates are present: magnesite $MgCO_3$ and dolomite $(Ca,Mg)(CO_3)_2$. The elemental analysis by means of XRF (see Table 6-1) confirms the presence of magnesium (17.05 %wt.) and calcium (14.52 %wt.). Iron (1.75 %wt.) and manganese (0.33 %wt.) can also be detected as carbonate forming elements. As iron and manganese are only present at low concentrations, iron and manganese carbonate cannot be found in the XRD pattern of the mineral feed material. Furthermore, the most intensive XRD peak for iron carbonate overlaps with magnesite at 37.7-38.4 °2Θ and manganese carbonate overlaps with dolomite at 35.7-36.5 °2Θ [27]. Hence, the formal composition of the mineral carbonate can be represented by the formula $0.46[MgCO_3]*0.49[(Ca,Mg)(CO_3)_2]*0.04[FeCO_3]*0.01[MnCO_3]$.

Table 6-1: Elemental composition of the mineral feed material according to XRF analysis and calculated carbonate and CO_2 content, assuming $MgCO_3$, $(Ca,Mg)(CO_3)_2$, $FeCO_3$, and $MnCO_3$ as the stoichiometric carbonate formulas for Mg, Ca, Fe, and Mn.

	Mg	Ca	Fe	Mn	Sum
Element / %wt.	17.05	14.52	1.75	0.33	33.65
Carbonate / %wt.	28.60	66.79	3.64	0.68	99.71
CO_2 / %wt.	14.93	31.88	1.38	0.26	48.45
Mole fraction of carbonate	0.46	0.49	0.04	0.01	1.00

The thermogravimetric curve shows two decomposition steps, independent of the gas atmosphere (see Figure 6-4). Hydrogen atmosphere leads to a decrease of decomposition temperature of approximately 60 °C for the first TG step and approximately 100 °C for the second TG step. The first TG step is interpreted as the concomitant decomposition of $MgCO_3$, $FeCO_3$, and $MnCO_3$ to the respective bivalent oxide and carbon dioxide. The second TG step is assigned to the decomposition of $(Ca,Mg)(CO_3)_2$ to calcium and magnesium oxide and carbon dioxide. This supposed reaction behavior is consistent with the mass loss calculated from the CO_2-content of the carbonates (Table 6-1 and Figure 6-4) and the standard free reaction energy for the carbonate decomposition depicted in Figure 6-1.

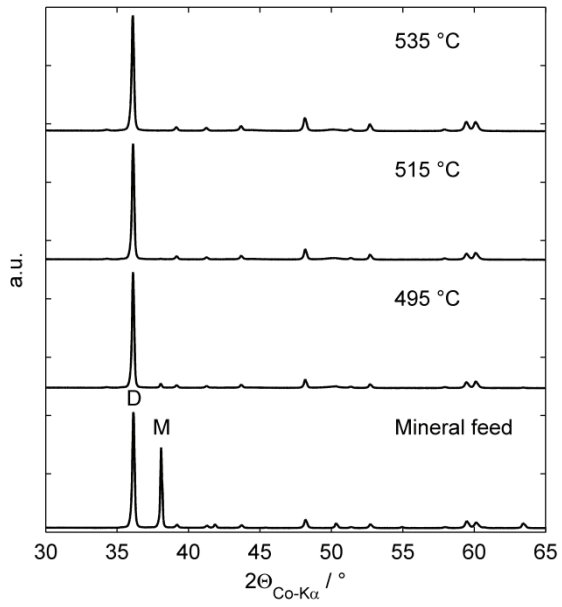

Figure 6-3: XRD pattern of mineral feed and products after reductive calcination with 90 %vol. hydrogen at 495-535 °C and ambient pressure. All peaks in the spectra can solely be assigned to magnesite (M) and dolomite (D), therefore only the most intensive peak is marked to distinguish between compounds.

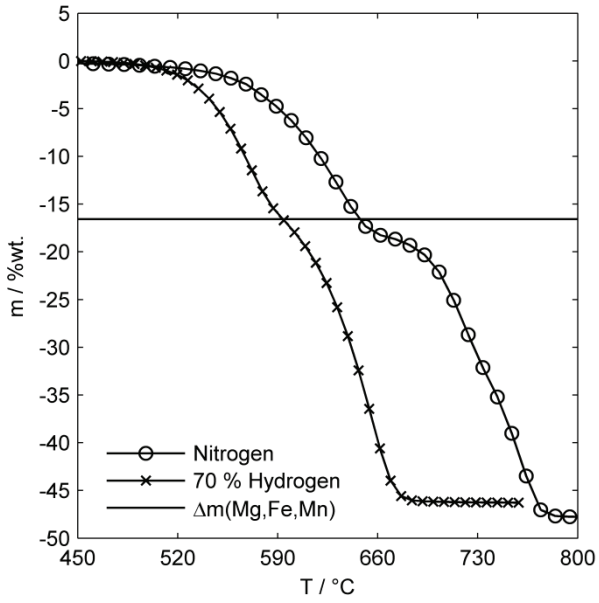

Figure 6-4: Calcination behavior of the mineral feed determined by thermogravimetry in nitrogen and 70 %vol. hydrogen, at a constant heating rate of 10 °C min^{-1}, 100 cm^3 min^{-1} total inlet flow, and ambient pressure. The solid line at -16.57 %wt. shows the calculated mass loss for the decomposition of $MgCO_3$, $FeCO_3$, and $MnCO_3$ to the respective bivalent oxide and CO_2.

6.4.2 Reaction products

The decomposition of dolomite is expected to proceed at temperatures above 535 °C (Figure 6-4). This assumption can be proved with the XRD pattern of the solid reaction products from tubular reactor experiments (Figure 6-3). At 495 °C, magnesite can be detected, even after more than 390 minutes reaction time. At 515 and 535 °C only dolomite can be detected (Figure 6-3). The XRD patterns of the solid products at 495-515 °C and 3-8 bar overpressure are similar to the patterns at ambient pressure.

The main gaseous products found in all experiments were carbon monoxide and carbon dioxide and water. Methane could only be detected in traces for experiments at 3 and 8 bar overpressure. Increase of temperature expectedly yields an increase in the reaction rate and thus in the product gas flow (Figure 6-5). In all experiments, carbon dioxide was formed prior to carbon monoxide. This indicates a sequential reaction mechanism. At first, carbon dioxide is formed by calcination (Eq. 1). Carbon dioxide is subsequently converted to carbon monoxide in a reverse water-gas-shift reaction (Eq. 4). This suggested mechanism is in accordance with our earlier work [19] that revealed the catalytic activity of MgO in the reverse water-gas-shift reaction. A possible role of accompanying trace elements (Fe, Mn) on the mechanism of carbon monoxide formation needs further investigation.

$$MgCO_3 \rightarrow MgO + CO_2 \quad (1)$$

$$CO_2 + H_2 \overset{MgO}{\longleftrightarrow} CO + H_2O \quad (4)$$

At 495 °C, an increase of pressure from ambient to 3 and 8 bar overpressure does not influence the product gas flow (Figure 6-5a). An increase of pressure leads to an expected retardation of reaction 1 at 515 and 535 °C. As a consequence, the gaseous product flow curves are retarded with increasing pressure (see Figure 6-5 b and c).

To calculate the conversion over time, Eq. 8 was applied, assuming complete decomposition of $MgCO_3$, $FeCO_3$, and $MnCO_3$, corresponding to a maximum mass loss of 16.57 %wt. Increasing the temperature leads to an increase in conversion, as shown in Fig. 6. At 495 °C the reaction rate dX/dt increases from ambient to 3 bar overpressure but decreases again from 3 to 8 bar overpressure because of thermodynamics. At 515 and 535 °C the reaction rate slightly decreases with increasing pressure. The calculation of the conversion X_{GA} from gas analysis data was experimentally validated with the conversion calculated from the mass loss $X_{m.l.}$ (column $X_{m.l.}$ and X_{GA} in Table 6-2). A comparison of conversion for different reaction conditions can be fulfilled after the same reaction time at isothermal conditions $t_{r,iso}$. Exemplarily, the total conversion increases from 23±2 % at 495 °C to 50±8 % at 515 °C and 80±4 % at 535 °C (Table 6-2) after 100 minutes $t_{r,iso.}$ Increase of pressure does not affect the rate of isothermal conversion. At 495 °C and 100 minutes $t_{r,iso}$, the conversion slightly increases from ambient to 3 bar overpressure (22 vs. 26 %) and decreases from 26 to 22 % when the pressure is increased from 3 to 8 bar overpressure (see Table 6-2). Expectedly, conversion slightly decreases with pressure after $t_{r,iso}$ = 100 minutes for 515 and 535 °C .

Table 6-2: Experimental results from the partial reductive calcination of magnesite/dolomite in 90 %vol. hydrogen.

T °C	OP bar	$t_{r,iso}$ min	$X_{m.l.}$ %	X_{GA} %	$X_{GA,100min}$ %	Y_{CO} %
495	0	390	76	76	22	72.1
495	3	376	86	86	26	73.2
495	8	375	82	80	22	73.3
515	0	240	83	84	57	66.2
515	3	247	83	84	50	68.1
515	8	247	85	88	42	67.6
535	0	324	94	96	83	61.1
535	3	316	96	93	82	62.8
535	8	315	96	89	75	61.7

T… temperature in the center of the solid bed; OP … overpressure; $t_{r,iso}$ … time at isothermal reaction conditions; $X_{m.l.}$ … conversion of Mg-Fe-Mn carbonates at the end of experiment calculated from the mass loss; X_{GA} … conversion of Mg-Fe-Mn carbonates at the end of experiment calculated from gas analysis results; $X_{GA,100min}$ … conversion of Mg-Fe-Mn carbonates at the end of experiment calculated from gas analysis at $t_{r,iso}$=100 minutes; Y_{CO} … yield of carbon monoxide

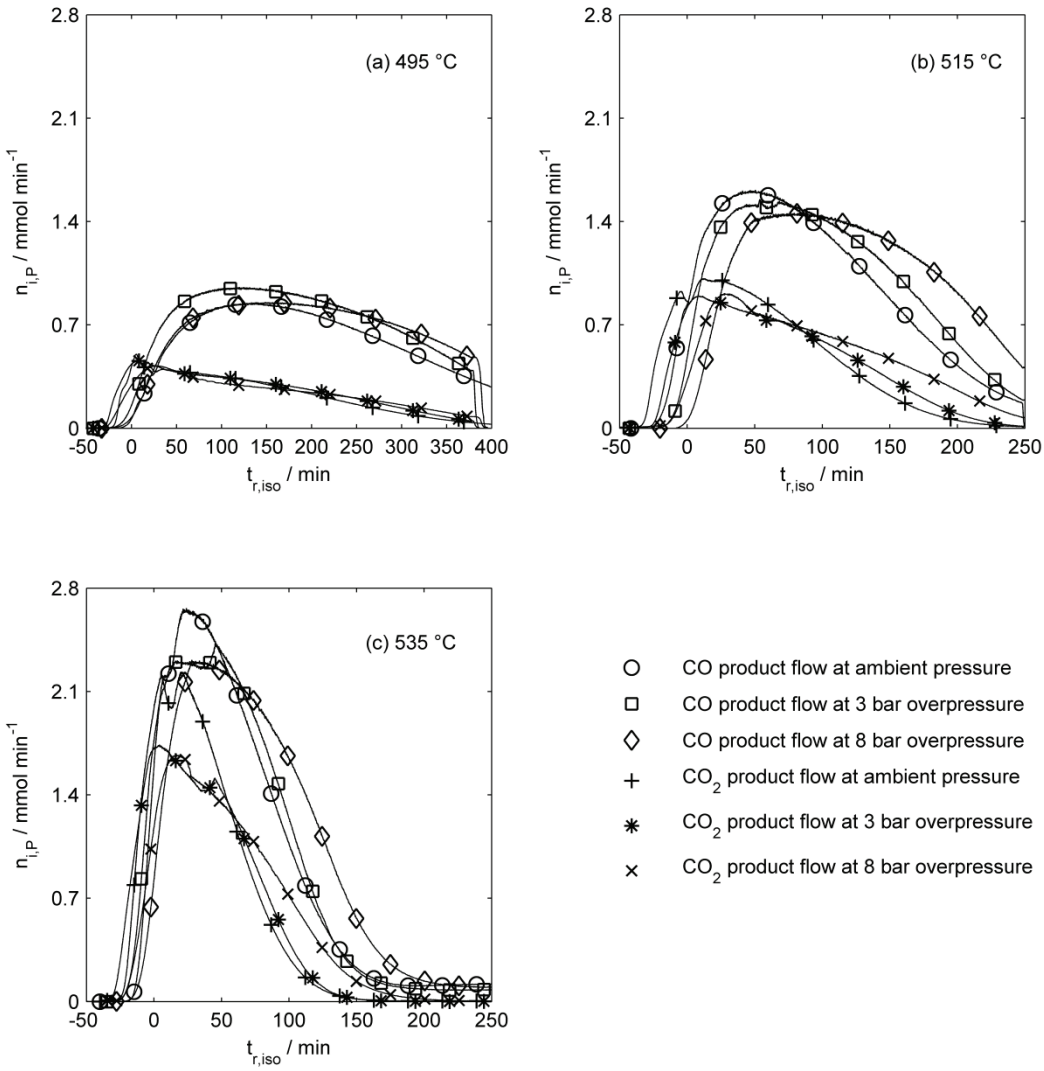

Figure 6-5: Dry gaseous product flow at 495 °C (a), 515 °C (b), and 515 °C (c) and ambient pressure, three, and eight bar overpressure; 121 g mineral feed, 500 cm^3 min^{-1} total inlet gas flow with 90 %vol. hydrogen content. Negative values in the abscissa indicate the heat-up phase to reach the isothermal temperature.

Compared to our earlier work [19] on the reductive calcination of relatively pure mineral magnesite (98 wt % $MgCO_3$), the reaction temperature for CO_2 liberation needs to be increased when a second mineral phase (dolomite) is present in the carbonate material. Furthermore, structural and compositional changes in the carbonate material result in a different product gas composition. Reductive calcination of 113 g $MgCO_3$ for 350 min at 490 °C and 8 bar overpressure resulted in a methane yield of 24 % and a carbon monoxide yield of 33 % at 66 % $MgCO_3$-conversion [19]. In this work, on the contrary, reductive calcination of 35 g of $MgCO_3$ for 375 min at 495 °C and 8 bar overpressure leads to a carbon monoxide yield of 73 % at 82 % $MgCO_3$-conversion and methane formation only in traces.

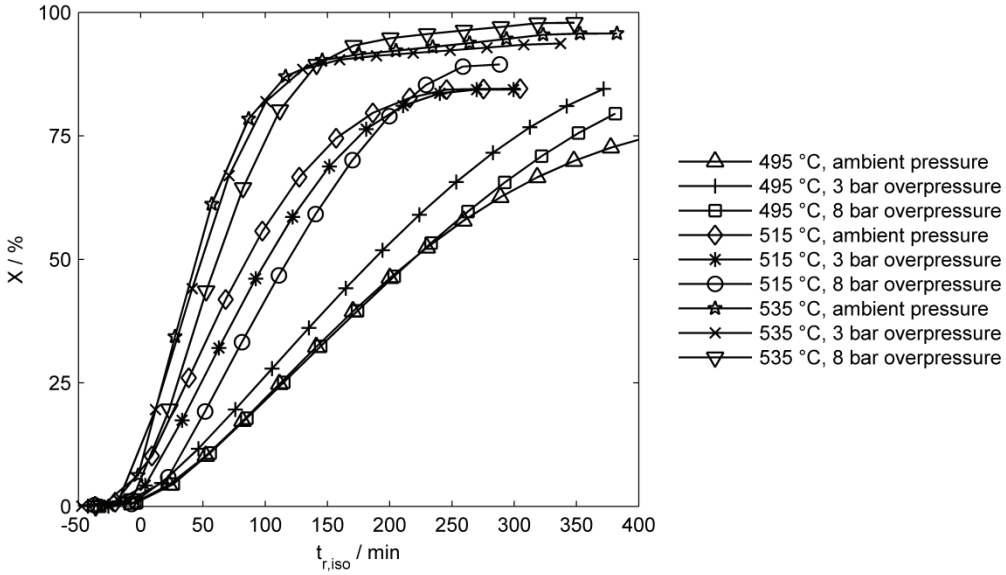

Figure 6-6: Conversion X of the $MgCO_3$+$FeCO_3$+$MnCO_3$ content of 121.0 ± 0.5 g magnesite/dolomite mineral feed material at 495-515 °C and ambient pressure, three, and eight bar overpressure and 500 cm^3min^{-1} total inlet gas flow with a 90 %vol. hydrogen content.

In all experiments performed for this work, liquid products were collected in condensate tank 1 (see Figure 6-2). All liquid products consisted of pure water, as verified by GC-TCD. The formation of water was expected due to the hydrogenation reaction 4-6.

6.5 Conclusions

The analysis of the standard free energy of reaction revealed that reductive calcination of magnesite with hydrogen to form carbon monoxide and methane is thermodynamically feasible at 500 ± 100 °C. Thermogravimetry confirmed that hydrogen atmosphere leads to a significant decrease of calcination temperature, compared to inert nitrogen atmosphere. Reductive calcination experiments in hydrogen atmosphere in the tubular reactor indicate a sequential mechanism of calcination followed by hydrogenation of carbon dioxide. According to Le Chatelier's principle, the formation of carbon monoxide in a reverse water-gas-shift reaction should not be affected by increase of pressure, except when the carbonate mineral participates in the reaction (Eq. 1 plus Eq. 2). CO and CO_2 methanation should be enhanced by increase of pressure. Experiments revealed, however, that methane is formed only in traces, even at elevated pressures. This finding suggests that methane formation is kinetically hindered. Carbon monoxide formation was experimentally verified. A carbon monoxide yield of 61-73 % was achieved for the partial reductive calcination of the magnesite content of a mixed magnesite/dolomite below 540 °C. Increase of pressure does not affect carbon monoxide formation, but for a slight retardation of the reaction.

Acknowledgements

The project 'Reduzierende Kalzinierung' is funded by the Austrian 'Klima- und Energiefond' in the framework of the program 'ENERGY MISSION AUSTRIA'. The authors wish to thank Dr. H. Schmid (voestalpine Stahl GmbH, Austria) and Dr. A. Stadtschnitzer (VA Erzberg GmbH, Austria) for their valuable collaboration in the project 'Reduzierende Kalzinierung'. The authors gratefully acknowledge the support from the NAWI Graz program. Thanks are also due to L. Rechberger from RHI AG Technology Center (Leoben, Austria) for the provision of the mineral samples.

References

[1] I. Szednyj, D. Brandhuber, Stand der Technik zur Kalk-, Gips und Magnesiaherstellung: Beschreibung von Anlagen in Österreich. Umweltbundesamt, Wien, 2007.

[2] H.B. Lüngen, J.-I. Yagi, Iron, 2. Blast furnace process, Ullmann's Encycl. Ind. Chem. 19 (2000), 656–707. doi: 10.1002/14356007.o14_o01.

[3] Climate Change 2014 Synthesis Report. IPCC Fifth Assess. Rep., IPCC, Geneva, 2014.

[4] A. Otto, T. Grube, S. Schiebahn, D. Stolten, Closing the loop: captured CO2 as a feedstock in the chemical industry, Energy Environ. Sci., 8 (2015) 3283–3297. doi: 10.1039/C5EE02591E.

[5] M. D. Porosoff, B. Yan, J.G. Chen, Catalytic reduction of CO2 by H2 for synthesis of CO, methanol and hydrocarbons: Challenges and opportunities, Energy Environ. Sci. 9 (2016) 62–73. doi: 10.1039/C5EE02657A.

[6] N.A.M Razali, K.T. Lee, S. Bhatia, A.R. Mohamed, Heterogeneous catalysts for production of chemicals using carbon dioxide as raw material: A review, Renewable Sustainable Energy Rev. 16 (2012) 4951–4964. doi: 10.1016/j.rser.2012.04.012.

[7] X. Xiaoding, J. Moulijn, Mitigation of CO2 by chemical conversion: Plausible chemical reactions and promising products, Energy Fuels 20 (1996) 305–325.

[8] W. Wang, S. Wang, X. Ma, J. Gong, Recent advances in catalytic hydrogenation of carbon dioxide., Chem. Soc. Rev. 40 (2011) 3703–27. doi: 10.1039/c1cs15008a.

[9] O. Bičáková, P. Straka, Production of hydrogen from renewable resources and its effectiveness, Int. J. Hydrogen Energy, 37 (2012) 11563–11578. doi: 10.1016/j.ijhydene.2012.05.047.

[10] S. Dutta, A review on production, storage of hydrogen and its utilization as an energy resource, J. Ind. Eng. Chem. 20 (2013) 1148–1156. doi: 10.1016/j.jiec.2013.07.037.

[11] I. K. Kapdan, F. Kargi, Bio-hydrogen production from waste materials, Enzyme Microb. Technol. 38 (2006) 569–582. doi: 10.1016/j.enzmictec.2005.09.015.

[12] A. Miltner, W. Wukovits, T. Pröll, A. Friedl, Renewable hydrogen production: a technical evaluation based on process simulation, J. Cleaner Prod. 18 (2010) S51–S62. doi: 10.1016/j.jclepro.2010.05.024.

[13] A. Steinfeld, Solar thermochemical production of hydrogen - a review, Sol. Energy, 78 (2005) 603–615. doi: 10.1016/j.solener.2003.12.012.

[14] J. Bierhals, Carbon monoxide, Ullmann's Encycl. Ind. Chem. 6 (2012) 679–693. doi: 10.1002/14356007.a05_203.

[15] A. de Klerk, Fischer-Tropsch Refining, 1st ed., Wiley VCH, Weinheim, 2011.

[16] M. Sterner, Bioenergy and renewable power methane in integrated 100% renewable energy systems Ph.D. Thesis, University Kassel, 2009.

[17] M. Götz, J. Lefebvre, F. Mörs et al., Renewable Power-to-Gas: A technological and economic review, Renewable Energy 85 (2016) 1371–1390. doi: 10.1016/j.renene.2015.07.066.

[18] H. Arakawa, M. Aresta, J.N. Armor et al., Catalysis research of relevance to carbon management: progress, challenges, and opportunities, Chem. Rev. 101 (2001) 953–996. doi: 10.1021/cr000018s.

[19] G. Baldauf-Sommerbauer, S. Lux, W. Aniser, M. Siebenhofer, Reductive calcination of mineral magnesite: hydrogenation of carbon dioxide without catalysts, Chem. Eng. Technol. 39 (2016) 2035–2041. doi:10.1002/ceat.201600094.

[20] A. Reller, C. Padeste, P. Hug, Formation of organic carbon compounds from metal carbonates, Nature 329 (1987) 527–529.

[21] A. Tsuneto, A. Kudo, N. Saito, T. Sakata, Hydrogenation of solid state carbonates, Chem. Lett. (1992) 831–834.

[22] D. Jagadeesan, M. Eswaramoorthy, C.N.R. Rao, Investigations of the conversion of inorganic carbonates to methane, ChemSusChem 2 (2009) 878–882. doi: 10.1002/cssc.200900152.

[23] D. Jagadeesan, Y. Sundarayya, G. Madras, C.N.R. Rao, Direct conversion of calcium carbonate to C1-C3 hydrocarbons, RSC Adv. 3 (2013) 7224–7229. doi:10.1039/c3ra40264a.

[24] N. Yoshida, T. Hattori, E. Komai, T. Wada, Methane formation by metal-catalyzed hydrogenation of solid calcium carbonate, Catal. Letters 58 (1999) 119–122.

[25] A. Reller, R. Emmenegger, C. Padeste, H.R. Oswald, Thermochemical reactivity of metal carbonates, Chimia (Aarau) 45 (1991) 262–266.

[26] HSC Chemistry 8.0.3, Software, Outotec 2014.

[27] H. Effenberger, J. Zemann, K.. Mereiter, Crystal structure refinements of magnesite, calcite, rhodochrosite, siderite, smithonite, and dolomite, with discussion of some aspects of the stereochemistry of calcite type carbonates, Zeitschrift Fur Krist. - New Cryst. Struct. 156 (1981) 233–243. doi:10.1524/zkri.1981.156.3-4.233.

7 Steady state and controlled heating rate methanation of CO_2 on Ni/MgO in a bench scale fixed bed tubular reactor[9]

Abstract

Chemical hydrogen storage via conversion of carbon dioxide into methane is a promising technology in an energy management system that relies on renewable energy resources. From the technical point of view robust heterogeneous catalysts are needed for methanation reactions to proceed at relevant levels. Ni/MgO is a promising catalyst in terms of activity and stability. Although several promising microscale catalyst studies exist, there is a lack of knowledge on catalyst performance and reactor control at larger scale for carbon dioxide methanation at ambient pressure and a technically relevant stoichiometric H_2:CO_2 (4:1) feed. Two catalysts with a loading of 11 and 17 wt.% nickel were prepared by wet impregnation, producing a Ni/MgO solid solution with a cubic lattice. Controlled increase ('scanning experiment') of the catalyst temperature from ambient to 500 °C for the highly exothermic CO_2 methanation was compared to steady state methanation experiments in a plug flow reactor (PFR). Scanning and steady state experiments yield comparable results in terms of carbon dioxide conversion and methane selectivity, whereas scanning experiments lead to considerable time saving. At a moderate temperature of 325 °C, CO_2 conversion and CH_4 selectivity near thermodynamic equilibrium are achievable. A first insight into the reaction kinetics is provided. A rate law that includes the equilibrium of forward and backward reaction at 260-375 °C and ambient pressure has been derived from the results of PFR experiments. In bench scale the long-term stability of Ni/MgO (17 wt.% Ni) at 330 °C was proven for a time span of several days.

[9] This chapter is intended for publication.

Greek symbols

γ_{Hg}	dyn cm^{-1}	Mercury surface tension
Θ_{Hg}	°	Mercury contact angle
ρ_{cat}	g cm^{-3}	Apparent density of catalyst bed
δ_{cat}	mm	Wall thickness
ε_{CO2}	%	Error of the carbon balance relative to the dry product gas stream

Symbols

A_S	$m^2\ g^{-1}$	Specific surface area determined by Hg-porosimetry
A_i	$m^3 kgc_{at}^{-1} s^{-1}$	Pre-exponential factor for Arrhenius equation
B_i	$m^3 kgc_{at}^{-1} s^{-1}$	Pre-exponential factor for van' Hoff equation
am_{cat}	mg	Amount of catalyst used in studies cited
c_i	mol m^{-3}	Concentration of compound i
d_{cat}	µm	Diameter of catalyst particle
d_p	nm	Pore diameter
$E_{a,i}$	kJ mol^{-1}	Activation energy
F	$cm^3_{STP} min^{-1}$	Feed flow rate at standard temperature and pressure
F_{CO2}	mol min^{-1}	Feed flow rate of carbon dioxide
h_{cat}	mm	Height of catalyst bed inside the reactor tube
H_{ads}	kJ mol^{-1}	Adsorption enthalpy
$\Delta H°_{R,i}$	kJ mol^{-1}	Standard enthalpy of reaction i
k_i	$m^3 kg_{cat}^{-1} s^{-1}$	Rate constant
K_i	$m^3 kg_{cat}^{-1} s^{-1}$	Adsorption constant
m_{cat}	g, kg	Amount of catalyst used in experiments
n_i	-	Reaction order with respect to compound i
P	$cm^3_{STP} min^{-1}$	Dry product gas flow rate at standard temperature and pressure
P_{Hg}	MPa	Absolute mercury pressure applied in Hg-porosimetry
R^2	-	Coefficient of determination
r_{CO2}	mol $kg_{cat}^{-1} s^{-1}$	Reaction rate of carbon dioxide
S_{CH4}	-	Methane selectivity
t_{steady}	h	Time of steady state operation
t_{store}	h	Storage time of catalyst
T_{tar}	°C	Target temperature
$v_{i,j}$	vol.%	Volume fraction of compound i in stream j
w_{Ni}	wt.%	Nickel loading
X_{CO2}	-	Relative conversion of carbon dioxide
$y_{i,j}$	-	Mole fraction of compound i in stream j

Abbreviations

AAS	-	Atomic absorption spectroscopy
cat	-	Catalyst
(EF)TEM	-	(Energy filtering) transmission electron microscopy
FID	-	Flame ionization detector
GC	-	Gas chromatography
HT[Nr]	-	Numbered (Nr=1-3) thermocouple position at reactor wall as specified in Figure 7-1
ICP-OES	-	Inductively-coupled-plasma optical-emission-spectroscopy
ID	mm	Inner diameter
IR	-	Infrared

Ni[Nr]-MgO		Nickel/Magnesium oxide catalyst with nickel loading specified in wt.% as [Nr]=11, 17
OD	mm	Outer diameter
$O(F,T_{tar})$	-	Operation point: one specific combination of feed flow rate and target temperature
PtG	-	Power-to-gas
RT	-	Reactor tube
sccm	$cm^3_{STP}min^{-1}$	Standard cubic centimeter per minute
STP	-	Standard temperature and pressure: 0 °C, 0.1 MPa
SNG	-	Synthetic natural gas
TC	-	Thermocouple casing
TCD	-	Thermal conductivity detector
T[Nr]	-	Numbered (1-6) thermocouple position inside the reactor as specified in Figure 7-1
TOC	-	Total organic carbon
WHSV	$cm^3\ g_{cat}^{-1}h^{-1}$	Weight hourly space velocity
XRD	-	X-ray diffraction

7.1 Introduction

The catalytic conversion of carbon dioxide with renewably produced hydrogen into methane (also referred to as CO_2 methanation or production of synthetic natural gas SNG, see Eq. 1) has gained major interest in recent years [1-4]. One of the reasons for this growing interest can be found in the quest for alternative hydrogen storage systems. In the power-to-gas (PtG) concept [5-8], renewably produced hydrogen is stored as methane, benefitting from the readily available natural gas storage and distribution infrastructure.

$$CO_2 + 4H_2 \rightarrow CH_4 + 2H_2O \quad (1)$$

$$CO + 3H_2 \rightarrow CH_4 + H_2O \quad (2)$$

Due to the time dependent availability of renewable (wind, hydro, and solar) energy, either large hydrogen buffer storage facilities, making the whole PtG concept questionable, or robust methanation catalysts are needed. The term 'robust' in this context refers to stable CO_2 conversion and CH_4 selectivity during long-term operation and also during several operation/down time cycles.

Catalytic methanation of CO_2 and CO (Eq. 1 and 2) using nickel was first reported more than 110 years ago [9]. Until the beginning of the 21st century, CO and CO_2 methanation was investigated and applied in the context of SNG production from coal, fossil resources, and biomass [10]. Furthermore, catalytic methanation has been used for decades in gas chromatographic analysis of CO and CO_2, first reported by Porter and Volman 1962 [11]. A multitude of different Ni-based catalysts have been reported [4,12-15]. Ni(O)/MgO catalysts exhibit high stability in methane and ethanol reforming [16-24] and for CO [25,26] and CO_2 [26-30] methanation and therefore seem to be a promising candidate for large scale implementation.

Table 7-1 summarizes experimental data of studies performed on CO and CO_2 methanation with Ni/MgO catalysts [25-30] relevant for this work. All studies [25-30] were performed with low amounts of catalysts (100-300 mg) in quartz micro-reactors at ambient pressure. Different synthesis approaches (co-precipitation [25,27,28], wet impregnation [26,28,30], mechanical mixing and melting [28]) were applied. In some cases, promoters (tungsten [27], carbon nanotubes [25]) or special structures (SiO_2 shell [29]) were used to enhance the catalytic activity. The focus of these studies [25-30] lies on the demonstration of the catalytic activity on a small scale and its dependency on temperature and/or synthesis method and/or catalyst formulation. However, these small scale investigations lack information relevant for technical implementation of Ni/MgO in a fixed bed reactor. The position of temperature measurement referred to in temperature vs. conversion plots was not mentioned [25-30]. The feed flow rate was only varied in one case [29]

In this work, experiments were performed with a bench scale stainless steel tubular reactor with several temperature measurement positions to demonstrate the applicability of Ni/MgO

catalysts in CO_2 methanation with a stoichiometric ratio of H_2:CO_2 = 4:1 feed. Two experimental procedures are compared: (1) scanning experiments with controlled increase of catalyst temperature and (2) steady state operation. Furthermore, the long-term catalyst stability was evaluated. Two Ni/MgO catalysts with 11 and 17 wt.% nickel loading were prepared by wet impregnation and characterized by X-ray diffraction (XRD), energy filtering transmission electron microscopy (EFTEM), mercury porosimetry, inductively-coupled-plasma optical-emission-spectroscopy (ICP-OES), and atomic absorption spectroscopy (AAS).

Table 7-1: Overview of Ni/MgO catalysts for CO and CO_2 methanation. All studies were performed with powders without detailed specification (e. g. size fraction) at ambient pressure. The position of the measurement of the catalyst temperature was not specified [25-30].

Catalyst	am_{cat} mg	w_{Ni} wt.%	Prep. meth.	Gas feed	Inlet flow $cm^3_{STP}min^{-1}$	Equipment	Ref.
Ni/MgO + carbon nanotubes	100	40	co-p.	H_2:CO: CO_2:N_2 75:15:5:5	66.7	Quartz reactor tube (ID n/a), online GC (TCD, FID), quantification after 2 hours of 'steady state'[c]	[25]
Ni/MgO	300	10	wi	H_2:CO_2=4:1 H_2:CO = 19:1	n/a GHSV = 10000 h^{-1}	Quartz reactor tube (ID 4 mm), online micro GC	[26]
W/Ni/MgO	100	Ni-W-Mg[a] 0.3:1:0.1	co-p.	He:H_2:CO_2 15:4:1	100	Quartz micro reactor (ID n/a), online GC, quantification after 2 hours 'steady state'[c]	[27]
Ni/MgO	150	10- 90	th, co-p.	H_2:CO_2 8:1 4:1	180	Glass reactor tube (ID 18 mm), online GC-TCD for CO, CO_2, CH_4, off-line GC-FID for CH_4, C_2H_6, C_2H_4	[28]
Ni/MgO @SiO_2, core-shell	50	26-65	co-p.	H_2:CO_2:N_2 4:1:4	90	Quartz reactor tube (ID 6 mm), 60 minutes 'steady state'[c], online GC-TCD, off-line GC-FID for hydrocarbon byproducts	[29]
Ni/MgO	n/a	1-40	wi[b]	H_2:CO_2 19:1	100	Not further specified 'flow system'	[30]

[a] Several catalysts with varying amount of Ni and promoter (W, Cu, Mo, Mn, Fe, Co) were synthesized, the catalyst composition giving the best result is shown.
[b] Two impregnation methods were compared.
[c] The 'steady state' is not further specified.
am_{cat} … amount of catalyst, w_{Ni} … nickel loading and/or catalyst composition, Prep. meth. … preparation method, co-p. … co-precipitation, wi … wet impregnation, th … thermal, n/a. … not applicable

7.2 Materials and Methods

Nickel nitrate hexahydrate ($Ni(NO_3)_2$*$6H_2O$, 99 %, p.a., Lactan), granulated spherical (0-8 wt.% <150 µm, 0-15 wt.% = 150-250 µm, 55-80 wt.% = 250-600 µm) MagGran© (4 $MgCO_3$*$Mg(OH)_2$*$4H_2O$, Ph. Eur., Magnesia AG, Switzerland), deionized water, and concentrated nitric acid (HNO_3, p.a., J.T. Baker) were used. Nitrogen (99.999 %), hydrogen (99.999 %), and carbon dioxide (99.998 %) were supplied by AirLiquide.

Online gas analysis during experiments on the tubular reactor setup was carried out by means of IR absorption (ABB Uras26) for the quantification of CO, CO_2 and CH_4 (0.0-100.0 vol.%), and thermal conductivity detection (ABB Caldos27) for the quantification of H_2 (0.0-100.0 vol.%). The online gas analyzer was frequently recalibrated with three different standard gas mixtures containing certified amounts of CO, CO_2, CH_4, H_2, and N_2 supplied by AirLiquide. Liquid reaction products were analyzed by means of total organic carbon analysis (TOC-L-CPH, Shimadzu). Atomic absorption spectroscopy was performed on an AAnalyst 400 (Perkin Elmer) device equipped with a nickel hollow cathode lamp set to 25 mA current at a wavelength of 232 nm, applying a compressed air/ethylene flame. Inductively-coupled-plasma optical-emission-spectroscopy was performed on a Spectro Ametek (Spectro Arcos) device. Solid samples for quantification of the nickel content were dissolved in a 1:1 (vol) mixture of HNO_3 (conc.) and H_2O prior to analysis. The TEM investigations were carried out with a Philips CM20, 200kV, LaB_6 cathode. The microscope is equipped with a Gatan 678 imaging filter for the acquisition of energy filtered images (elemental distribution maps). X-ray diffraction (XDR) patterns of the Ni/MgO catalyst powders were measured on a D8 Advance X-ray diffractometer (Bruker) using CuKα radiation. XRD data were collected in the range of 30–135 °2Θ at a step size of 0.02 °2Θ and a counting time of 2 seconds per step. Rietveld analysis was performed with the software X'Pert Highscore Plus (PANalytical) and with Topas (Bruker). Mercury porosimetry was carried out on a Pascal 140/440 (Thermo Finnigan) with mercury in 99.9995 % quality (Roth) and a sample mass of ~ 100 mg. The porosimetry measurements were validated with certified reference material ERM®-FD121 provided by the 'Bundesanstalt für Materialforschung und –prüfung' (Germany). Prior to porosimetry measurements solid samples were dried >12 hours at 110 °C, and cooled to room temperature over a desiccant. The Washburn equation assuming a Hg surface tension of γ_{Hg} = 480 dyn cm^{-1} and a contact angle of Θ_{Hg} =141.3 ° was used to calculate the pore diameter d_p for cylindrical pores with Eq. 3 from the applied absolute Hg pressure P_{Hg}. The Rootare and Prenzlow methodology [31] was used to calculate the specific surface area A_s from porosimetry measurements (Eq. 4).

$$d_p = \frac{-\gamma_{Hg} * \cos(\theta_{Hg})}{2 * P_{Hg}} \quad (3)$$

$$A_s = -\frac{1}{\gamma_{Hg} cos\theta} \int_O^V P_{Hg} dV \quad (4)$$

7.2.1 Catalyst preparation

The catalysts referred to as Ni11-MgO and Ni17-MgO were prepared in a four step sequence: (a) preparation of granular magnesium oxide; (b) impregnation; (c) thermal decomposition; (d) reduction in hydrogen atmosphere.

(a) Fresh granular magnesium oxide was prepared by thermal decomposition of MagGran© granulate in the tubular reactor in N_2 flow (500 $cm^3_{STP}min^{-1}$) at 535 °C until CO_2 was not detected in the product gas any more.

(b) 24.7 g of the magnesium oxide granulate (white color) was put in a 2-neck glass flask equipped with a dropping funnel containing 70 ml of an aqueous nickel nitrate solution (c(Ni) = 50 g L^{-1} for Ni11-MgO, c(Ni) = 100 g L^{-1} for Ni17-MgO) and connected to a vacuum pump. The setup was evacuated for 10 minutes to empty the pores of the granules. The nickel solution was added dropwise. The setup was allowed to regain ambient pressure by disconnecting the vacuum pump after 5 minutes. After 60 minutes impregnation time at ambient pressure, the catalyst precursor (green color) was separated by filtration and dried at room temperature for 24 hours.

(c) The catalyst precursor produced in step b was transferred to a muffle furnace (Heraeus M110), dried at 130 °C for 1 hour and calcined at 400 °C for 5 hours in static air.

(d) The product of step c (dark gray color) was reduced in the tubular reactor at 500 °C (temperature in the mid of the fixed bed) for 4 hours with a gas feed of 1000 $cm^3_{STP}min^{-1}$ H_2.

7.2.2 Experimental setup for catalytic experiments

A fixed-bed tubular reactor setup including a stainless steel (T316) reactor tube and an electric furnace with three heating zones (Figure 7-1) was used. A sketch and details of the reactor setup can be found in reference [32] and the supporting information thereof. The temperature was measured at the outer wall of the reactor tube in the middle of each heating zone at HTx (x = 1-3) and at two positions Ty (y = 1-6) within each zone inside the reactor tube (see Figure 7-1). The electric heating power of each zone can be controlled linearly in the range 0 % = 0 W and 100 % = 600 W.

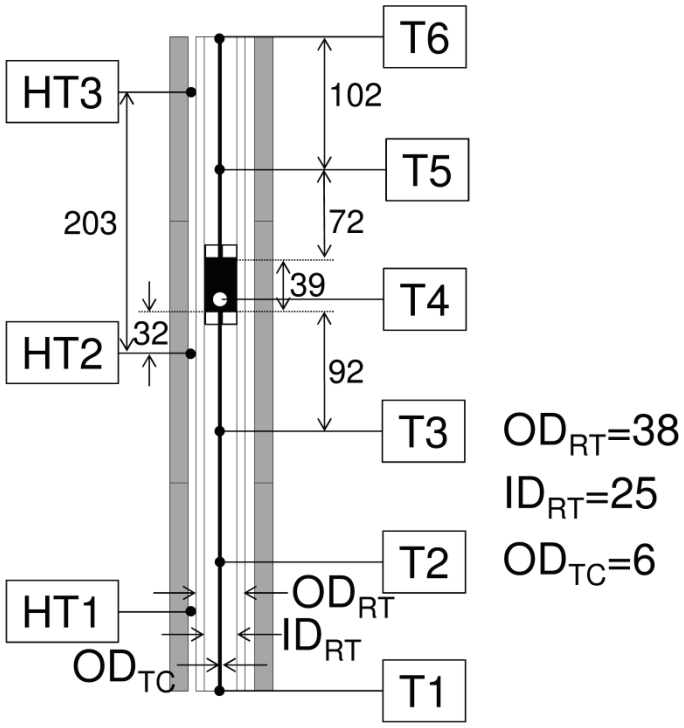

Figure 7-1: Position of the thermocouples T1-T6 inside the reactor tube and HT1-HT3 outside of the reactor tube. The catalyst bed is shown in black. The glass wool tori above and below the catalyst bed are shown as black framed rectangles. Gas enters from top at T6. The gray bars left and right of the reactor tube represent the heater segments. For simplicity, the pre-heating coil and the spacers are not shown. Dimensions are given in mm.

In all experiments 12.09 g of each catalyst (m_{cat}) of the size fraction 200-800 µm (weight based mean diameter d_{cat} = 500 µm) with an apparent density ρ_{cat} of 0.68 g cm^{-3} was used. The catalyst granulate bed forms a hollow cylinder inside the reactor tube. As the inner diameter of the reactor tube ID_{RT} and the outer diameter of the thermocouple casing OD_{TC} inside the reactor tube are specified, the height of the catalyst bed h_{cat} (39 mm) can be calculated with Eq. 5a and the wall thickness δ_{cat} (9.5 mm) with Eq. 5b.

$$h_{cat} = \frac{4}{\pi*(ID_{RT}^2 - OD_{TC}^2)} * \frac{m_{cat}}{\rho_{cat}} = 39\ \text{mm} \quad (5a)$$

$$\delta_{cat} = \frac{1}{2} * (ID_{RT} - OD_{TC}) = 9.5\ \text{mm} \quad (5b)$$

Four stainless steel spacers of a total length of 422 mm were used to place the catalyst bed appropriately inside the reactor tube. Glass wool tori with a height of 10 mm were placed above and below the catalyst bed to prevent carryover of the catalyst granulate. Therefore, the catalyst bed spans from mm 432 to mm 471(calculated from the reactor outlet) inside the reactor tube. Figure 7-1 shows that T4 is placed at the end of the catalyst bed at mm 441 (calculated from the reactor outlet) and that T5 is 72 mm above, whereas T3 is 92 mm below the catalyst bed. HT2 records the temperature 32 mm below the catalyst at the outer wall of the reactor tube.

The catalytic performance of Ni/MgO was determined with three experimental procedures.

(1) Scanning experiments (section 7.3.2.1): The purpose was to gain a first insight into the temperature dependency of carbon dioxide conversion and product selectivity for a gas feed of H_2:CO_2:N_2 = 4:1:5 (vol) and 1000 cm^3_{STP} min^{-1}. After an initial constant heating phase (~25-30 minutes) the heating power of each heating zone was adjusted manually, so that the average temperature gradient at T4 was at 1.9 °C min^{-1}.
(2) Steady-state experiments (section 7.3.2.2 and 7.3.2.3): The reactor was heated to a target temperature of 260, 290, 325, and 375 °C measured at T4 and the inlet flow rate was varied between 250, 500, 750, and 1000 $cm^3_{STP}min^{-1}$ at a constant gas feed composition of H_2:CO_2:N_2 = 4:1:5 (vol).
(3) The stability (section 7.3.2.4) of Ni17-MgO was determined over a total time span of 210 hours. The target temperature was 330 °C at the end of the catalyst bed (T4) and the inlet flow rate was fixed at 1000 $cm^3_{STP}min^{-1}$ with a composition of H_2:CO_2:N_2=4:1:5 (vol).

Nitrogen was used as an inert gas (Eq. 6) for heat transport and balancing purposes and ideal gas mixing was assumed for calculation of the molar composition (Eq.7) of the inlet flow F and dry product gas flow P. It was assumed, that the dry product gas did not contain any constituents in a concentration above 0.1 vol.% other than N_2, CO, CO_2, CH_4 and H_2. To prove this assumption, the error of the carbon balance relative to the dry product gas stream ε_{CO2} was calculated (see Eq. 8). The resulting value ε_{CO2} did not exceed ± 1 % in any experiment described in this work. Therefore, it is assumed that no other bulk gaseous products than methane and carbon monoxide were formed during the experiments. Consequently, the carbon dioxide conversion X_{CO2} can be calculated with Eq. 9 from the dry product gas composition. The methane selectivity S_{CH4} was calculated with Eq. 10.

$$F * y_{N2,F} = P * y_{N2,P} \quad (6)$$

$$y_{i,j} = 0.01 * v_{i,j} \quad (7)$$

$$\varepsilon_{CO2} = y_{CO2,F} * \frac{F}{P} - \left(y_{CO2,p} + y_{CO,P} + y_{CH4,P}\right) * 100[\%] \quad (8)$$

$$X_{CO2} = \frac{y_{CO2,F} - y_{CO2,P} * \frac{P}{F}}{y_{CO2,F}} \quad (9)$$

$$S_{CH4} = \frac{y_{CH4,P}}{y_{CH4,P} + y_{CO,P}} \quad (10)$$

7.3 Results and Discussion

7.3.1 Characterization of the catalyst

The impregnation of magnesium oxide with aqueous nickel nitrate leads to the formation of mixed nickel/magnesium hydroxide (see Figure 7-3a and Eq. 11). The thermal decomposition of this hydroxide results in the formation of mixed nickel-magnesium oxide (see Figure 7-3b and Eq. 12). MgO and NiO crystallize in a NaCl structure type. The reduction of the mixed nickel-

magnesium oxide in hydrogen atmosphere leads to the formation of a nickel/magnesium oxide solid solution with cubic lattice (see Figure 7-3d and Eq. 13). The nickel content of the reduced catalyst (= product of step d in the preparation) was determined in triplicate, twice by means of AAS and once by means of ICP-OES. The mean value of these three measurements resulted in the determination of the nickel content of catalyst Ni11-MgO of 11 ± 2 wt.% and for catalyst Ni17-MgO of 17 ± 2 wt.%. The lattice constant of pure cubic Ni a_{Ni} = 0.3525 nm [33] is considerably smaller than the lattice constant for MgO a_{MgO} = 0.4211 nm [34]. Rietveld refinement was performed on the fresh catalysts Ni11-MgO and Ni17-MgO. Adding Ni-atoms to the MgO starting model and refining the occupation factor of Mg and Ni at the 0 0 0 position gave an excellent fit, the refined occupation factors are in good agreement with the determined Ni content. This supports the presumed formation of a Ni-MgO solid solution.

$$MgO(s) + Ni(NO_3)_2(aq) \rightarrow (Mg_{1-x}Ni_x)(OH)_2(s) \quad (11)$$

$$(Mg_{1-x}Ni_x)(OH)_2 \xrightarrow{4h,400\,°C} Mg_{1-x}Ni_xO \quad (12)$$

$$Mg_{1-x}Ni_xO + H_2 \xrightarrow{3h,500\,°C} [Ni]_x * [Mg_{1-x}O] + H_2O \quad (13)$$

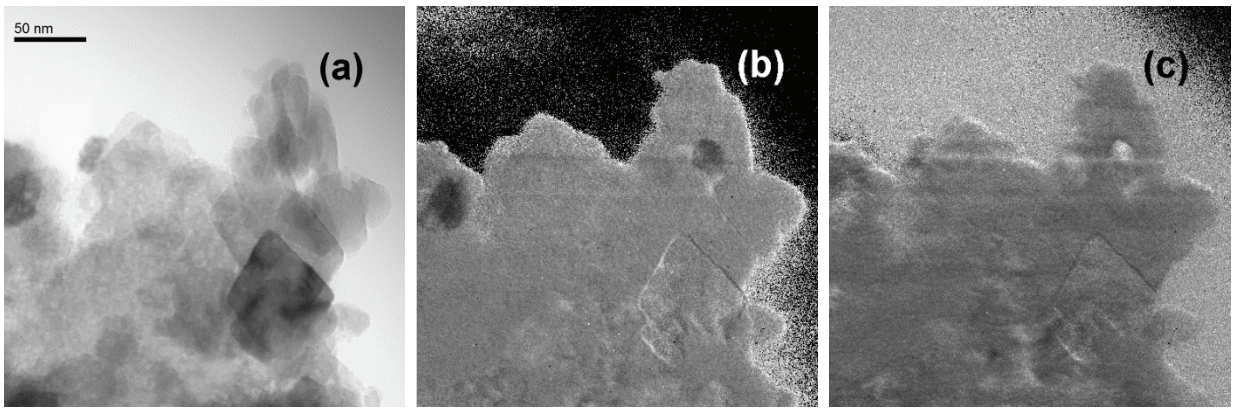

Figure 7-2: (a) TEM bright field image of catalyst Ni17-MgO and elemental maps of magnesium (b) and nickel (c) of the same field of view. The elements are uniformly distributed within the powder, fortifying the supposed formation of a Ni-MgO solid solution.

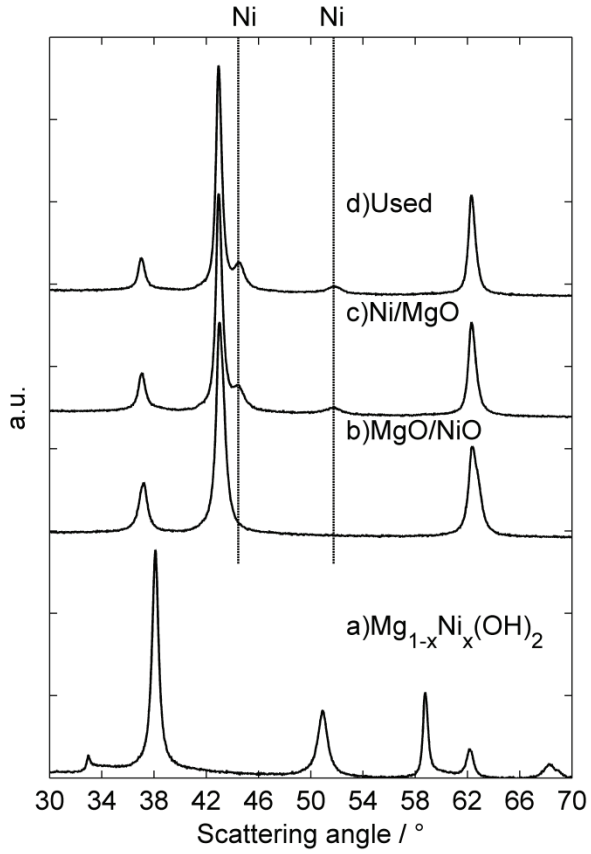

Figure 7-3: Transformation of the XRD pattern during the preparation of catalyst Ni17-MgO (Ni11-MgO appears analogously). During the impregnation, mixed granular magnesium/nickel hydroxide (a) is formed, which is decomposed to the mixed oxide (b). Reduction of the mixed oxide in hydrogen atmosphere leads to the formation of the active catalyst (c), a Ni/MgO solid solution with NaCl structure. The diffraction pattern is unchanged after >20 hours of methanation, as evidenced in diffraction pattern (d). Labels are shown above the corresponding diffraction pattern, and the characteristic cubic nickel reflections at 44.6 and 51.8 ° are marked with solid lines.

Figure 7-2 shows the TEM bright field image and the corresponding elemental maps of magnesium and nickel. Magnesium and nickel are mostly equally distributed within the solid catalyst mass, which is in good accordance with the XRD measurement, supporting the presumed formation of a Ni-MgO solid solution. The logarithmic differential Hg intrusion versus pore diameter plot (Figure 7-4) reveals a uniform pore size distribution for both catalysts with a maximum at approximately 60 nm. The pore structure does not change after >20 hours of methanation. Increase of nickel loading leads to a minor decrease of the specific surface area. The specific surface area of catalyst Ni11-MgO was calculated to amount to 67 m^2g^{-1} compared to a value of 55 m^2g^{-1} for catalyst Ni17-MgO. After > 20 hours of methanation these specific surface areas decrease slightly to 58 m^2g^{-1} for Ni11-MgO and 53 m^2g^{-1} for Ni17-MgO.

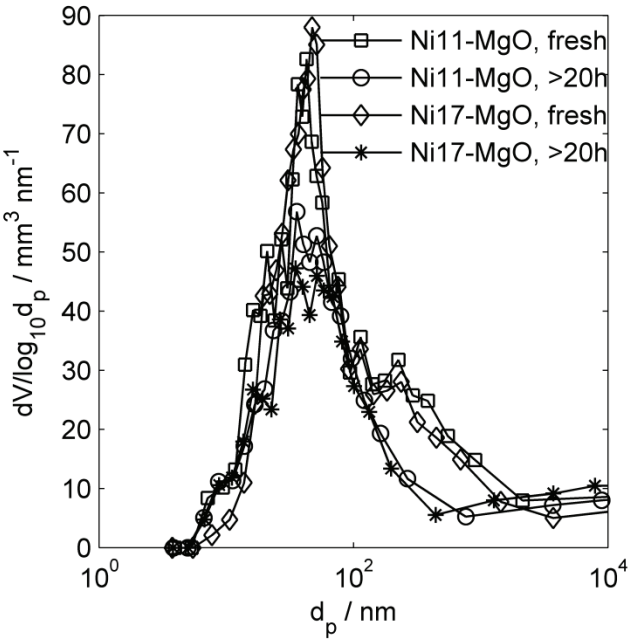

Figure 7-4: Differential mercury intrusion versus $\log_{10}$ of pore diameter d_P determined by porosimetry for the freshly reduced catalysts and for the catalysts after > 20 hours of methanation.

7.3.2 Catalyst performance

7.3.2.1 Scanning experiments: controlled increase of the temperature at the end of the catalyst bed

After an initial heating phase of 25-30 minutes, a proximate linear increase of temperature with time (= temperature gradient) could be established at the measurement positions above (T5), at the end (T4), and after (T3) the catalyst bed, as well as in the center of the heating zone (HT2) surrounding the catalyst bed. This gradient was achieved by adjusting the heater power to the desired gradient (average of 1.9 °C min^{-1} at T4) within a time interval of 5 minutes. At first, the heater power was set to 25 % for the top and central heating zone to establish the initial heating phase. After the initial heating phase it was reduced to 18 %, and increased again stepwise for the top heating zone (see Fig. 5b and 6b). Methanation of CO_2 (Eq. 1) and CO (Eq. 2) are highly exothermic reactions. Between 110 and 600 °C and ambient pressure the standard enthalpy of reaction $\Delta H°_{R,CO2}$ for gas-phase CO_2 methanation (see Eq. 14) and $\Delta H°_{R,CO}$ for CO methanation (see Eq. 15) can be approximated with a second order polynomial (data was fitted to calculations with HSC Chemistry 8.0.6, $R^2 > 0.999$).

$$\Delta H^{o}_{R,CO2} = 0.00002 * T^2 - 0.0528 * T - 163.43 \text{ kJ mol}^{-1} \quad (14)$$

$$\Delta H^{o}_{R,CO} = 0.00003 * T^2 - 0.0476 * T - 204.75 \text{ kJ mol}^{-1} \quad (15)$$

The generation of heat due to the exothermal reactions 1 and 2 could not be suppressed for the controlled temperature increase at the end of the catalyst bed. Therefore, the output value of the central heating zone (which surrounds the catalyst bed) had to be decreased at high reaction

rates (see black line in Figure 7-5b and Figure 7-6b). Consequently, the temperature distribution in flow direction of the reactor tube is not linear. At a low conversion rate, the temperature at the outside of the reactor HT2 is the highest in the system, and T3, T4, and T5 are in a comparable range. At a higher conversion rate, T4 becomes the highest temperature in the system.

As the dry gas composition is monitored online at a time interval of 5 seconds, it is possible to calculate CO_2 conversion and CH_4 selectivity during the heat-up of the reactor (Figure 7-5a and Figure 7-6a). Therefore, an insight into the progress of conversion with temperature can be provided with only one experiment for each catalyst. For validation purposes, conversion and selectivity determined in scanning experiments (red and black line in Figure 7-5a and Figure 7-6a) can be compared to the steady state experiments (marked with x in Figure 7-5a and Figure 7-6a), which are discussed in detail in section 7.3.2.2. The conversion determined in scanning experiments is in good agreement with the conversion determined in steady state experiments. Conversion determined in scanning experiments is slightly shifted to higher temperatures due to the lag in detection time (the product gas has to be transported from the end of the catalyst bed to the online gas analyzer through the tubing system and the condenser vessel). The selectivity determined in scanning experiments is in good agreement at elevated conversion. Nevertheless, selectivity determined in scanning experiments is overestimated to a certain extent compared to the selectivity determined in steady-state experiments for low conversion. Both catalysts show a rapid increase of conversion with temperature to a maximum value and slight decrease at temperatures above the maximum value (see Figure 7-5a and Figure 7-6a). A conversion of 10 % is reached at 241 °C (T4) for Ni17-MgO compared to 266 °C (T4) for Ni11-MgO. The maximum conversion of 75 % is reached at 356 °C (T4) for Ni11-MgO compared to a maximum conversion of 86 % at 360 °C (T4) for Ni17-MgO. Thus, nickel loading does improve conversion under isothermal conditions. Additionally, the selectivity is improved by increased nickel loading (see Figure 7-5a and Figure 7-6a).

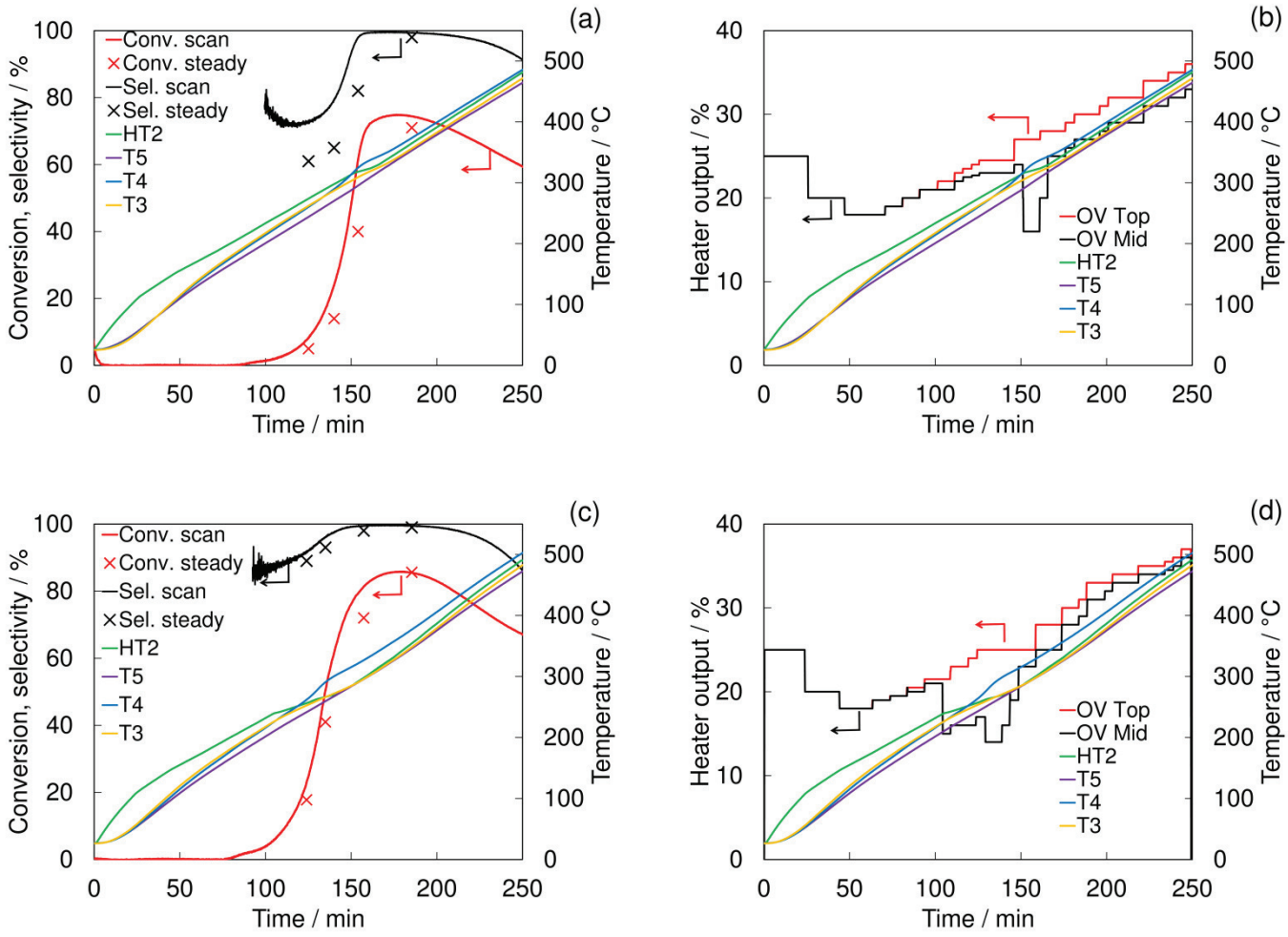

Figure 7-5: CO_2 conversion (conv. scan) and CH_4 selectivity (sel. scan) for Ni11-MgO (a) and Ni17-MgO (c) during controlled increase of temperature T4 measured at the end of the catalyst bed. Conversion and selectivity determined in steady state experiments are marked with x. The heater output has to be adapted to the exothermal reaction conditions to establish a proximate linear temperature increase within the reactor setup and depends on the conversion rate (b: Ni11-MgO, d: Ni17-MgO).

7.3.2.2 Steady state operation

The influence of feed flow rate and nickel loading on CO_2 conversion and CH_4 selectivity was investigated under steady state conditions for at least 30 minutes. The criterion to assign this 'steady state condition' was that the standard deviation of T4 must be within ±0.8 % of the mean value of T4 and within ± 1.5 % for T5, T3, and HT2. The standard deviation of the dry product gas composition must also be within ± 1.5 %. The lower the WHSV (see Eq. 16), the longer is the contact time between gas phase and catalyst bed.

$$\mathrm{WHSV} = \frac{\mathrm{F_{CO2}}}{\mathrm{m_{cat}}} \qquad (16)$$

The influence of feed flow, temperature at the end of the catalyst bed (T4), and nickel loading on conversion and selectivity can be seen in Figure 7-6 and Figure 7-7. At isothermal operation conditions a decrease of the feed flow rate leads to an increase of conversion and selectivity. An increase of temperature under constant feed flow rate yields an increased conversion and

selectivity up to levels near thermodynamic equilibrium at 325-375 ° for Ni17-MgO and at 375 °C for Ni11-MgO, indicating that the investigated operation range is in the range of reaction rate control. This finding is in agreement with the results of the scanning experiments presented in section 7.3.2.1. For otherwise constant operation conditions an increase of nickel loading leads to an increase of conversion and selectivity, whereas at 375 °C both catalysts yield comparable results. CH_4 selectivity above 99 % is attainable with increased nickel loading and/or increased temperature and/or decreased WHSV. However, under non-ideal conditions, carbon monoxide is formed, resulting in a decrease of selectivity. This leads to the assumption, that carbon dioxide methanation on the catalyst described in this work proceeds via reverse water-gas-shift (Eq. 17) followed by carbon monoxide methanation (Eq. 2). This assumption is in agreement with the results of our earlier work, were it was demonstrated that MgO is an active reverse water-gas-shift catalyst [32].

$$CO_2 + H_2 \rightarrow CO + H_2O \qquad (17)$$

Figure 7-8 shows that T4 (temperature at end of catalyst bed) is always the highest temperature under steady state operation conditions. Furthermore, the target temperature could be reached and kept within ±0.8 % independent of nickel loading, conversion, and inlet flow. The temperatures T3, T5, HT2, however, show a different trend for Ni11-MgO compared to Ni17-MgO. The highest conversion under constant inlet flow conditions was achieved at 325 °C for Ni17-MgO and at 375 °C for Ni11-MgO. If at this temperature the inlet flow is decreased, conversion increases. Together with this increase of conversion, the temperature span is broadened for Ni11-MgO. In the case of Ni17-MgO the opposite span is observed at 260, 290, and 325 °C.

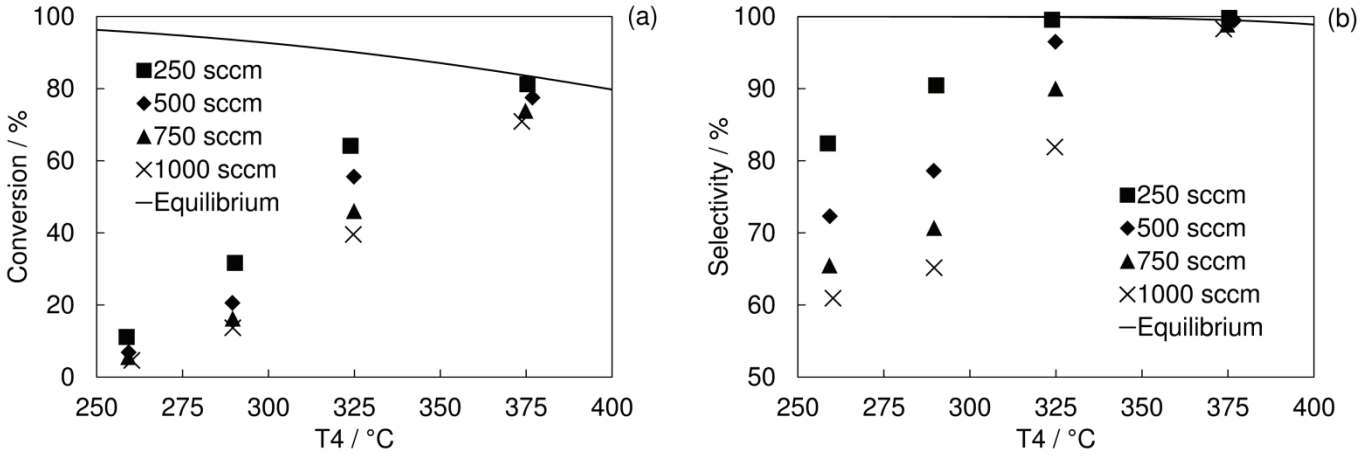

Figure 7-6: Steady state operation of catalyst Ni11-MgO (sccm … $cm^3_{STP}min^{-1}$).

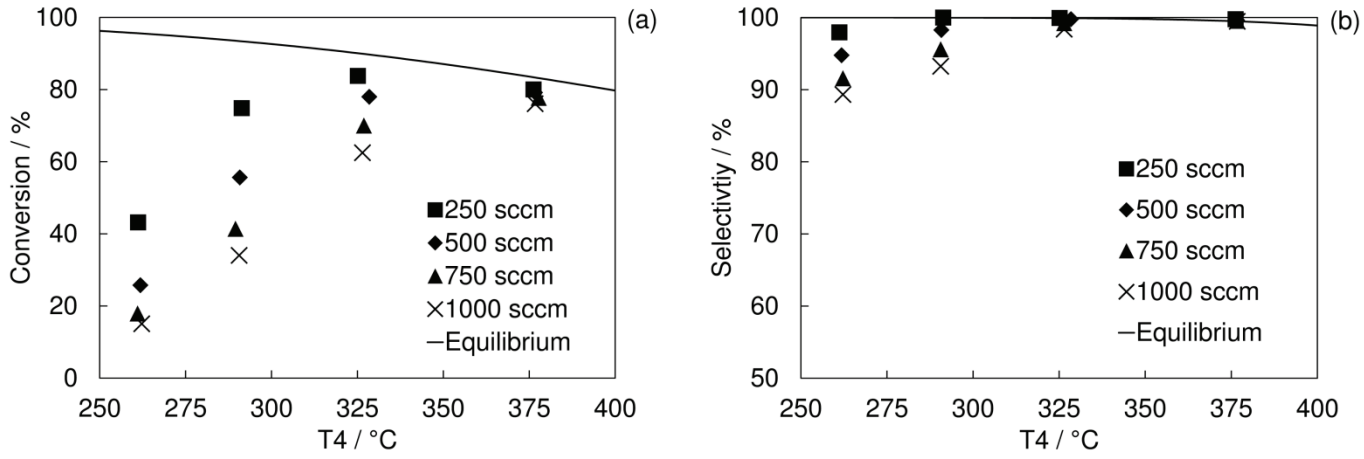

Figure 7-7: Steady state operation of catalyst Ni17-MgO (sccm … $cm^3_{STP}min^{-1}$).

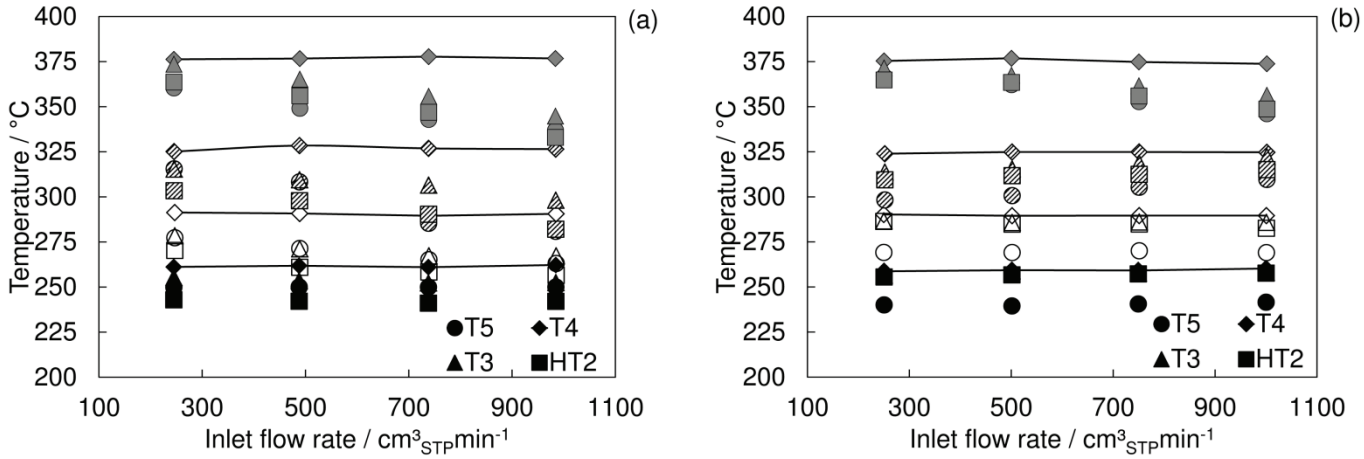

Figure 7-8: Temperature distribution in the reactor setup for Ni17-MgO (a) and Ni11-MgO (b). Full symbol = target temperature at T4 = 260 °C, empty symbol: target temperature at T4 = 290 °C; hatched symbol: target temperature at T4 = 325 °C; gray symbol: target temperature at T4 = 375 °C.

An increase of the feed flow rate leads to an increase of temperature distribution for all target temperatures. The order of the temperature distribution is different for Ni11-MgO (Figure 7-8b) compared to Ni17-MgO (Figure 7-8a). For Ni17-MgO the order T4 > T3 > T5 ~ HT2 stays true, compared to T4 > T3 ~ HT2 > T5 for Ni11-MgO for all inlet flow rates and target temperatures 260-325 °C. One possibility for this difference could lie in a slight change of experimental procedure. When the target temperature was reached, the inlet flow was increased stepwise from 250 to 1000 $cm^3_{STD}min^{-1}$ for Ni17-MgO but decreased stepwise from 1000 to 250 $cm^3_{STD}min^{-1}$ for Ni11-MgO. The difference in procedure did not influence the conversion and selectivity, as determined for each operation point. Operation point $O(F,T_{tar})$, in this context, describes one specific combination of feed flow rate F and target temperature T_{tar}. This was checked by replicating specific operation points after stepwise variation of the inlet flow rate. It simply points out, that, if one target temperature is selected, the other temperatures in the system are not determined likewise. For the target temperature of 375 °C, however, both

catalyst not only revealed a similar conversion and selectivity, but also the order of temperature span (T4 > T3 > T5 > HT2) was the same.

The liquid product of all steady state experiments was condensed at 0 °C and collected. The TOC-value was below 100 ppm for all experiments, thus no other liquid bulk products than water were formed according to Eq. 1, 2 and 17.

7.3.2.3 Reaction kinetics

The applicability of a quasi-isothermal ideal plug flow packed bed reactor for the methanation with catalyst Ni17-MgO is assumed. Due to the high methane selectivity above 90 %, carbon monoxide formation is neglected and the kinetic evaluation is based on carbon dioxide methanation according to Eq. 1. The rate of carbon dioxide conversion $-r_{CO2}$ can thus be calculated as the derivative of the relative conversion X_{CO2} with respect to the ratio of catalyst mass m_{cat} and carbon dioxide inlet flow rate F_{CO2} (Eq. 18). During steady-state operation the catalyst mass was constant (m_{cat}=12.09 g), whereas the inlet flow rate was varied at four set points (F_{CO2}=1.1, 2.2, 3.3, 4.4 * 10^{-3} $mol_{CO2}min^{-1}$). Steady-state operation was performed at four different temperatures measured at the end of the catalyst bed (T4=260, 290, 325, 375 °C). Therefore, 16 experimental datasets were available for kinetic computations.

$$-r_{CO2} = \frac{dX_{CO2}}{d\left(\frac{m_{cat}}{F_{CO2}}\right)} \tag{18}$$

Eq. 19 was applied to fit the increase of conversion with the decrease of inlet flow rate of CO_2 at each of the four temperature levels. The coefficient of determination was above 0.998 in all cases. As a consequence, the reaction rate was calculated from the analytical solution of the derivative depicted in Eq. 20.

$$X_{CO2} \cong a * \left(1 - \exp\left(-b * \frac{m_{cat}}{F_{CO2}}\right)\right) + c * \left(1 - \exp\left(-d * \frac{m_{cat}}{F_{CO2}}\right)\right) \tag{19}$$

$$-r_{CO2} = \frac{dX_{CO2}}{d\left(\frac{m_{cat}}{F_{CO2}}\right)} \cong a * b * \exp\left(-b * \frac{m_{cat}}{F_{CO2}}\right) + c * d * \exp\left(-d * \frac{m_{cat}}{F_{CO2}}\right) \tag{20}$$

An elementary power law (Eq. 21), three different models of simplified Langmuir-Hinshelwood type (Eq. 22a-22c), and an approach that takes the equilibrium of forward and backward reaction (Eq. 23) into account were tested for their ability to predict the reaction rate.

$$\text{PL: } -r_{CO2} = k_1 * c_{CO2}^{n_{CO2}} * c_{H2}^{n_{H2}} \tag{21}$$

$$\text{LH1: } -r_{CO2} = \frac{k_1 * c_{CO2}^{n_{CO2}}}{1 + K_1 * c_{CO2}^{n_{CO2}}} \tag{22a}$$

$$\text{LH2: } -r_{CO2} = \frac{k_1 * c_{CO2}^{n_{CO2}} * c_{H2}^{n_{H2}}}{1 + K_1 * c_{CO2}^{n_{CO2}}} \tag{22b}$$

$$\text{LH3:}\ -r_{CO2} = \frac{k_1 * c_{CO2}^{n_{CO2}} * c_{H2}^{n_{H2}}}{1 + K_1 * c_{H2}^{n_{H2}}} \tag{22c}$$

$$\text{EqR:}\ -r_{CO2} = k_1 * c_{CO2}^{n_{CO2}} * c_{H2}^{n_{H2}} - k_2 * c_{CH4}^{n_{CH4}} * c_{H2O}^{n_{H2O}} \tag{23}$$

The concentration of water c_{H2O} in the humid product gas was calculated from the dry product gas composition and Eq. 1. The gas phase concentrations c_i were applied as molar quantities per cubic meter of product gas under process conditions applying the ideal gas law. The rate constants were assumed to follow the Arrhenius law (Eq. 24), adsorption constants were treated as van't Hoff type (Eq. 25).

$$k_i = A_i * \exp\left(-\frac{E_{a,i}}{RT}\right) \tag{24}$$

$$K_i = B_i * \exp\left(-\frac{H_{ads,i}}{RT}\right) \tag{25}$$

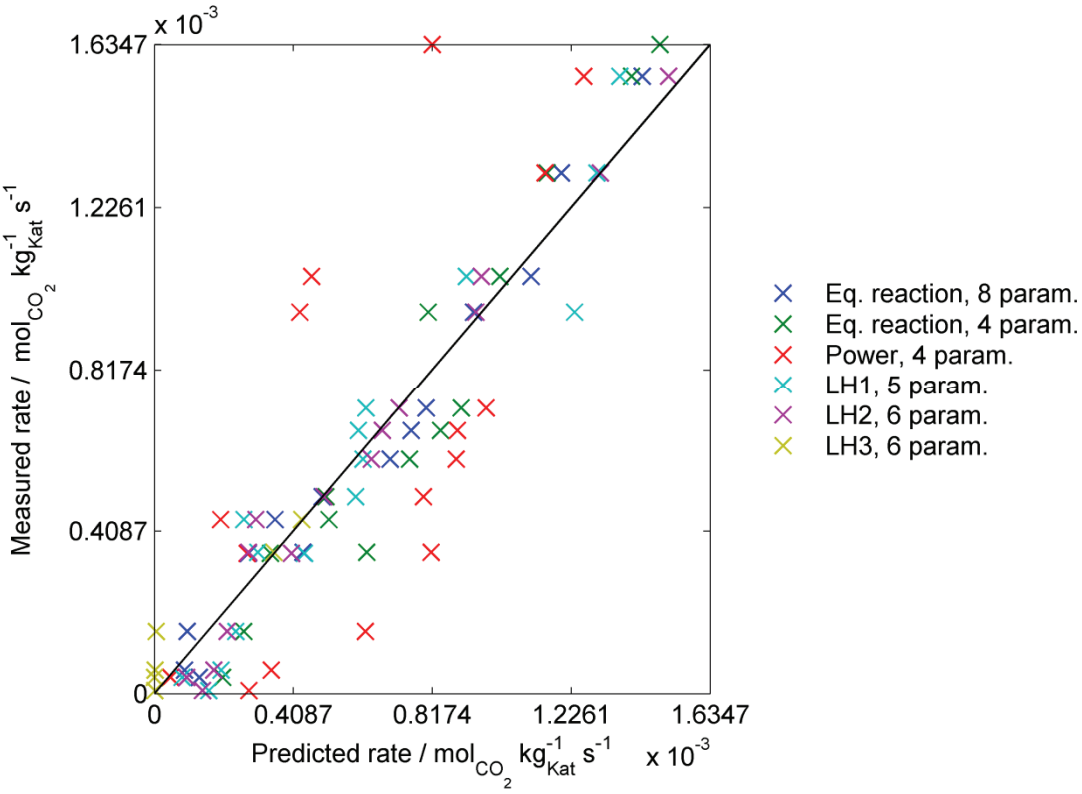

Figure 7-9: Parity plot for the rate laws tested. Eq. reaction, 8 param.: Equilibrium reaction (Eq. 23), rate constants and reaction order were computed; Eq. reaction, 4 param.: Equilibrium (Eq. 23), rate constants were computed; Power: Power law (Eq. 21); LH1: Langmuir-Hinshelwood type approach (Eq. 22a); LH2: Langmuir-Hinshelwood type approach (Eq. 22b); LH3: Langmuir-Hinshelwood type approach (Eq. 22c)

Table 7-2: Regression results for pre-exponential factors A_i and B_i, activation Energy $E_{a,i}$, adsorption enthalpy $H_{ads,i}$, and reaction order n_i together with the coefficient of determination R^2.

	1 PL[1]	2 LH[2]	3 LH[3]	4 LH[4]	5 EqR[5]	6 EqR[5]	7 EqR[5]	8 EqR[5]	9 EqR[5]	10 EqR[5]	10 EqR[5]	12 EqR[6]
R^2	0.427	0.941	0.980	0.943	0.908	0.897	0.905	0.908	0.889	0.896	0.896	0.977
A_1, $m^3\ kg_{cat}^{-1}s^{-1}$	$2.6*10^{-5}$	$2.4*10^{-4}$	$2.4*10^{-6}$	$2.6*10^{-6}$	507	987	219	$1.4*10^{3}$	296	134	134	$1.0*10^{5}$
$E_{a,1}$, kJ mol^{-1}	15.1	0.7	-23.6	3.0	70.8	73.9	64.4	75.6	71.6	62.2	62.2	82.1
A_2, $m^3\ kg_{cat}^{-1}s^{-1}$	-	-	-	-	$5.4*10^{7}$	$2.5*10^{8}$	$3.8*10^{5}$	$5.2*10^{8}$	$3.0*10^{15}$	$1.9*10^{5}$	$1.3*10^{5}$	$6.4*10^{3}$
$E_{a,2}$, kJ mol^{-1}	-	-	-	-	158.2	153.9	111.6	151.5	236.9	112.2	112.2	82.6
B_1, $m^3\ kg_{cat}^{-1}s^{-1}$	-	$3.3*10^{-8}$	$1.7*10^{-10}$	$7.7*10^{-11}$	-	-	-	-	-	-	-	-
H_{ads}, kJ mol^{-1}	-	-71.7	-109	-80.7	-	-	-	-	-	-	-	-
n_{CO2}	-4.0	5.0	5.3	0.9	1	1	0.5	1	0.5	0.5	0.5	0.9
n_{H2}	4.5	-	-0.9	4.0	0.5	0.5	0.5	0.5	1	0.5	0.5	-0.5
n_{CH4}	-	-	-	-	0.5	0.5	0.5	0.5	0.5	1	0.5	0.4
n_{H2O}	-	-	-	-	2	1	0.5	0.5	0.5	0.5	1	0.7

1: Power law (Eq. 21)
2: Langmuir-Hinshelwood type approach (Eq. 22a)
3: Langmuir-Hinshelwood type approach (Eq. 22b)
4: Langmuir-Hinshelwood type approach (Eq. 22c)
5: Equilibrium reaction (Eq. 23), A_i and $E_{a,i}$ calculated from regression, reaction order as fixed input value
6: Eq. reaction (Eq. 23), A_i, $E_{a,i}$, and reaction order calculated from regression

The parameters of the rate laws (Eq. 21-23) were estimated with Matlab R2012b, using the built-in NonLinearModel.fit least-squares method. The reaction rate calculated with Eq. 20 was used as the response variable (= measured rate) and the concentrations of CO_2, H_2, CH_4, and H_2O as the predictors. Figure 7-9 shows that the power law cannot predict the measured rate appropriately, whereas all other rate laws (Eq. 22-23) yield a reasonable conformity of measured and predicted rate (see Table 7-2 for coefficients of determination R^2). Each of the three Langmuir-Hinshelwood type approaches (Eq. 22a-c) yields a coefficient of determination above 0.942 (Table 7-2, column 2-4). The combination of numeric values of the model parameters A_i, $E_{a,i}$, B_i, H_{ads}, n_i is, however, outside a physically meaningful range for all three approaches. The best result in terms of acceptable coefficient of determination together with meaningful numeric values of the model parameters was achieved with the rate law that takes the equilibrium of forward and backward reaction into account (Eq. 23). When both, reaction orders and rate constant parameters, were computed from nonlinear regression, the coefficient of determination equals 0.977 and the activation energy of forward and backward reaction are in the same range of approximately 82 kJ mol^{-1} (Table 7-2, column 12) This value for the activation energy is comparable to values published for Ni/Al_2O_3 [35,36]. Results for the reaction kinetics of catalytic CO_2 methanation using Ni/MgO catalysts have not been published to our knowledge. The reaction orders for CO_2, CH_4, and H_2O are approximately 1, 0.5, and 2/3. The reaction order for H_2, however, equals -0.5. This could be interpreted as an opposing effect of hydrogen on the run of reaction or limitations in hydrogen adsorption, as applied in Langmuir-Hinshelwood approaches. Further investigations on this effect would need experimental data at increased pressure and different inlet flow compositions. If the reaction orders of CO_2, H_2, CH_4, and H_2O are not computed via nonlinear regression but are used as fixed positive input parameters, the coefficient of determination for the rate law depicted in Eq. 23 is around 0.90. Depending on the combination of reaction orders, the activation energy of the forward reaction varies between 62 and 75 kJ mol^{-1}, whereas the activation energy of the backward reaction varies between 112 and 237 kJ mol^{-1}. The activation energy of the backward reaction is thus two- to threefold the activation energy of the forward reaction. Most rate laws published for various Ni-based methanation catalysts (see e.g. ref. [35] for a compilation) are of Langmuir-Hinshelwood type. As the experiments in this study were performed at ambient pressure, effects of adsorption and desorption on the reaction kinetics seem to be negligible compared to the effect of the reaction equilibrium. Nevertheless, a fundamental appraisal of the most appropriate rate law together with its mechanistic interpretation has to be based on a multitude of the experimental data points available. However, a first insight is provided in this study.

7.3.2.4 Catalyst stability

Catalytic CO_2 methanation in PtG applications needs to be performed with robust catalysts. Therefore, after performing the experiments described in sections 7.3.2.1 and 7.3.2.2, catalyst Ni17-MgO was tested for its operation and down time stability for steady state operation at 330 °C and 1000 $cm^3_{STP}min^{-1}$ feed flow rate. This stability test consisted of operation for nine days,

whereas methanation was performed on three days. Between methanation periods, the catalyst was preserved in nitrogen at ambient temperature.

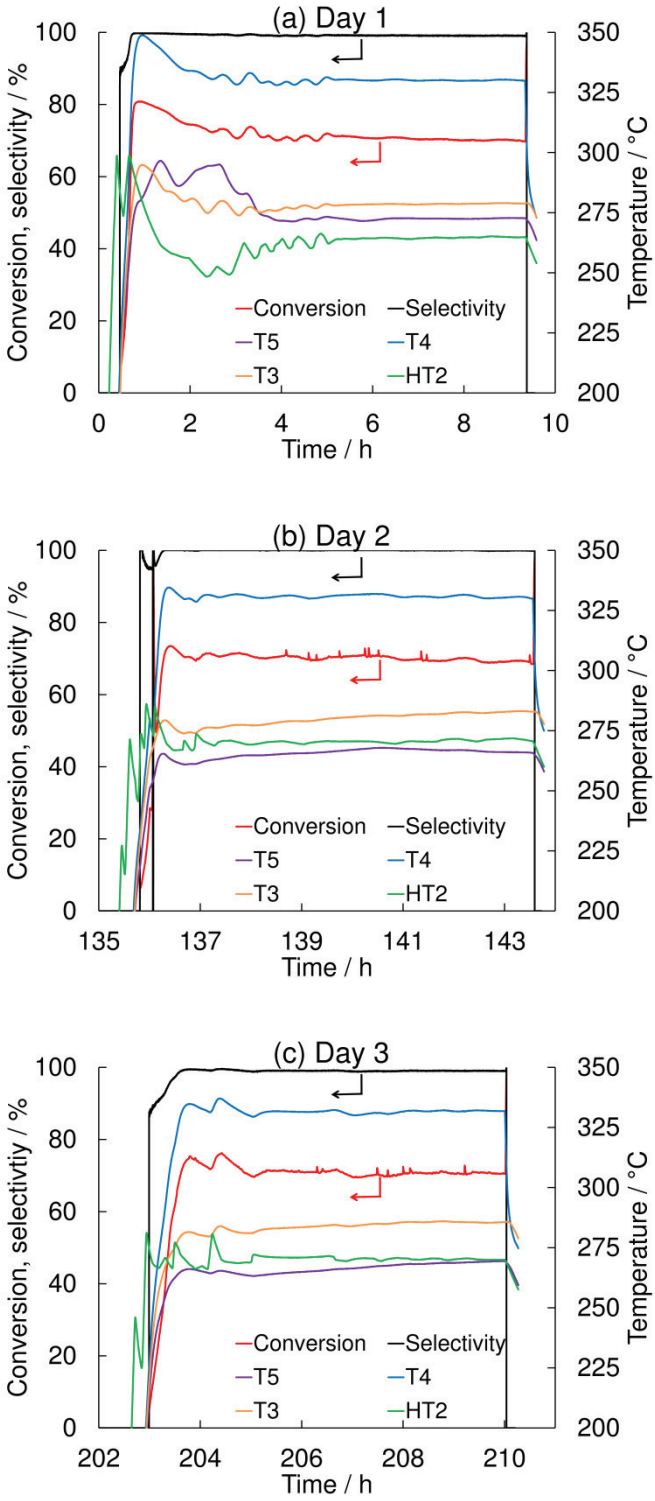

Figure 7-10: CO_2 conversion and CH_4 selectivity of Ni17-MgO during stability test of 210 hours. Between operation days, the catalyst was stored under nitrogen inside the reactor tube.

Table 7-3: Time of steady state operation (t_{steady}) and storage time of catalyst inside the reactor tube (t_{store}) during stability test of Ni17-MgO. When temperature T4 at the end of the catalyst bed reached steady state, CO_2 conversion (X_{CO2}), and CH_4 selectivity (S_{CH4}) remained constant during methanation periods.

	t_{steady} / h	t_{store} / h	T4 / °C	X_{CO2} / %	S_{CH4} / %
Day 1	6.5	135	330 ± 1	70 ± 1	99.1 ± 0.1
Day 2	6.5	46	331 ± 1	70 ± 1	99.9 ± 0.1
Day 3	5.2	0	331 ± 1	70 ± 1	99.0 ± 0.1

On the first day (Figure 7-10a), the system was slightly overheated and the heater output had to be reduced to reach a steady state after approximately 4 hours operation time. During steady state methanation the conversion was at 70 ± 1 % on all operation days and selectivity was beyond 99 % (see Table 7-3). The temperature span, however, was different on day 2 and 3 compared to day 1. During steady state operation of day 1, T3 was higher than T5 and HT2. On Day 2 and 3 HT2 was slightly above T5. As observed in the steady state experiments described in section 7.3.2.2, this deviation of temperature span between operation days did not affect conversion and selectivity, as T4 was kept constant at 331 ± 1 °C.

7.4 Conclusions

Wet impregnation, followed by calcination in air and reduction in hydrogen leads to the formation of a stable and active Ni/MgO methanation catalyst. XRD and EFTEM confirm the formation of a Ni/MgO solid solution with NaCl type structure. A bench scale tubular reactor setup with online gas analysis was used that allowed for the exact control of the temperature at the end of the catalyst bed (T4). An experimental procedure referred to as 'scanning experiment' was presented that includes the constant increase of T4 with time, so that a first insight into the dependency of CO_2 conversion and CH_4 selectivity on catalyst temperature can be provided within a single experiment. Increase of nickel loading from 11 to 17 %wt. leads to a pronounced increase of catalytic activity under otherwise constant operation conditions. The results from scanning experiments are in good agreement with results from steady state operation experiments. During steady state operation, an increase of the WHSV leads to a decrease of selectivity and conversion, whereas an increase of catalyst temperature from 260 to 325 °C leads to conversion and selectivity near thermodynamic equilibrium. The temperature above and below the catalyst bed, as well as the outer wall temperature deviate from T4, depending on the catalyst, feed flow rate, and heating procedure. Therefore, it was proven that it is crucial in catalyst studies of exothermic reactions to exactly state the temperature measurement position referred to in temperature vs. conversion plots and preferably place the thermocouple for measurement of the 'catalyst temperature' at the supposedly highest temperature position. At 260 °C and 275 °C carbon monoxide was formed as a by-product. The higher the contact time between catalyst and gas flow (= decrease of WHSV), the lower was the CO concentration. Hence, CO_2 methanation on the Ni/MgO catalyst used in this work is proposed to proceed in a sequential reaction scheme of reverse water-gas-shift followed by CO methanation. 16 experimental steady-state data points were evaluated to provide a first insight into the reaction

kinetics of CO_2 methanation. The results of the nonlinear regression revealed that a rate law that includes the equilibrium of reactants and products describes the kinetics satisfyingly. Finally, constant conversion of 70 % at a feed flow rate of 1000 $cm^3_{STP}min^{-1}$ and feed composition of H_2:CO_2:N_2=4:1:5 and a selectivity of >99 % at 330 °C was demonstrated for shut on/shut off operation over a total period of 210 h, with steady-state methanation performed during 18 hours.

Acknowledgments

The project 'Reduzierende Kalzinierung' is funded by the Austrian 'Klima- und Energiefond' in the framework of the program 'ENERGY MISSION AUSTRIA'. The authors wish to thank Dr. H. Schmid (voestalpine Stahl GmbH, Austria) and Dr. A. Stadtschnitzer (VA Erzberg GmbH, Austria) for their valuable collaboration in the course of the project 'Reduzierende Kalzinierung'. The authors gratefully acknowledge the support from the NAWI Graz program. Thanks are also due to G. Kaufmann for his support in the performance of the experiments.

References

[1] K. Ghaib, K. Nitz, F.-Z. Ben-Fares, Katalytische Methanisierung von Kohlenstoffdioxid, Chemie Ing. Tech. 88 (2016) 1435–1443. doi:10.1002/cite.201600066.

[2] S. Rönsch, J. Schneider, S. Matthischke, M. Schlüter, M. Götz, J. Lefebvre, et al., Review on methanation - From fundamentals to current projects, Fuel. 166 (2016) 276–296. doi:10.1016/j.fuel.2015.10.111.

[3] X. Su, J. Xu, B. Liang, H. Duan, B. Hou, Y. Huang, Catalytic carbon dioxide hydrogenation to methane: A review of recent studies, J. Energy Chem. 25 (2016) 553–565. doi:10.1016/j.jechem.2016.03.009.

[4] M.A.A. Aziz, A.A. Jalil, S. Triwahyono, A. Ahmad, CO2 methanation over heterogeneous catalysts: recent progress and future prospects, Green Chem. 17 (2015) 2647–2663. doi:10.1039/C5GC00119F.

[5] M. Bailera, P. Lisbona, L.M. Romeo, S. Espatolero, Power to Gas projects review: Lab, pilot and demo plants for storing renewable energy and CO2, Renew. Sustain. Energy Rev. 69 (2017) 292–312. doi:10.1016/j.rser.2016.11.130.

[6] M. Götz, J. Lefebvre, F. Mörs, A. McDaniel Koch, F. Graf, S. Bajohr, et al., Renewable Power-to-Gas: A technological and economic review, Renew. Energy. 85 (2016) 1371–1390. doi:10.1016/j.renene.2015.07.066.

[7] M. Lehner, R. Tichler, H. Steinmüller, M. Koppe, Power-to-Gas: Technology and Business Models, (2014) 93. doi:10.1007/978-3-319-03995-4.

[8] M. Sterner, Bioenergy and renewable power methane in integrated 100% renewable energy systems, Universität Kassel, 2009.

[9] P. Sabatier, S.J. Baptiste, New methane synthesis, C. R. Hebd. Seances Acad. Sci. 134 (1902) 514–516.

[10] J. Kopyscinski, T.J. Schildhauer, S.M. a. Biollaz, Production of synthetic natural gas (SNG) from coal and dry biomass – A technology review from 1950 to 2009, Fuel. 89 (2010) 1763–1783. doi:10.1016/j.fuel.2010.01.027.

[11] K. Porter, D. Volman, Flame ionization detection of carbon monoxide for gas chromatographic analysis, Anal. Chem. (1962) 748–749. doi: 10.1021/ac60187a009.

[12] J. Gao, Q. Liu, F. Gu, B. Liu, Z. Zhong, F. Su, Recent advances in methanation catalysts for the production of synthetic natural gas, RSC Adv. 5 (2015) 22759–22776. doi:10.1039/C4RA16114A.

[13] W. Wang, S. Wang, X. Ma, J. Gong, Recent advances in catalytic hydrogenation of carbon dioxide., Chem. Soc. Rev. 40 (2011) 3703–27. doi:10.1039/c1cs15008a.

[14] G.A. Mills, F.W. Steffgen, Catalytic methanation, Catal. Rev. 8 (1973) 159–210. doi:10.1080/01614947408071860.

[15] V. Barbarossa, C. Bassano, P. Deiana, G. Vanga, CO2 conversion to CH4, in: M. De Falco, G. Iaquaniello, G. Centi (Eds.), CO2 A valuab. source carbon, Springer, London, 2013: pp. 123–145. doi:10.1007/978-1-4471-5119-7.

[16] V.R. Choudhary, a. S. Mamman, Energy efficient conversion of methane to syngas over NiO–MgO solid solution, Appl. Energy. 66 (2000) 161–175. doi:10.1016/S0306-2619(99)00039-2.

[17] N. De Miguel, J. Manzanedo, P.L. Arias, Active and stable Ni-MgO catalyst coated on a metal monolith for methane steam reforming under low steam-to-carbon ratios, Chem. Eng. Technol. 35 (2012) 2195–2203. doi:10.1002/ceat.201200259.

[18] F. Frusteri, S. Freni, V. Chiodo, L. Spadaro, O. Di Blasi, G. Bonura, et al., Steam reforming of bio-ethanol on alkali-doped Ni/MgO catalysts: Hydrogen production for MC fuel cell, Appl. Catal. A Gen. 270 (2004) 1–7. doi:10.1016/j.apcata.2004.03.052.

[19] A.M. Gadalla, M.E. Sommer, Synthesis and characterization of catalysts in the system Al2O3-MgO-NiO-Ni for methane reforming with CO2, J. Am. Soc. Ceram. Soc. 72 (1989) 683–687. doi:10.1111/j.1151-2916.1989.tb06197.

[20] M. Jafarbegloo, A. Tarlani, A.W. Mesbah, J. Muzart, S. Sahebdelfar, NiO-MgO solid solution prepared by sol-gel method as precursor for Ni/MgO methane dry reforming catalyst: effect of calcination temperature on catalytic performance, Catal. Letters. 146 (2016) 238–248. doi:10.1007/s10562-015-1638-9.

[21] Y.H. Wang, H.M. Liu, B.Q. Xu, Durable Ni/MgO catalysts for CO2 reforming of methane: Activity and metal-support interaction, J. Mol. Catal. A Chem. 299 (2009) 44–52. doi:10.1016/j.molcata.2008.09.025.

[22] A.J. Vizcaíno, P. Arena, G. Baronetti, A. Carrero, J.A. Calles, M.A. Laborde, et al., Ethanol steam reforming on Ni/Al2O3 catalysts: Effect of Mg addition, Int. J. Hydrogen Energy. 33 (2008) 3489–3492. doi:10.1016/j.ijhydene.2007.12.012.

[23] Y.H. Hu, E. Ruckenstein, Binary MgO-based solid solution catalysts for methane conversion to snygas, Catal. Rev. 44 (2002) 423–453. doi:10.1081/CR-120005742.

[24] Y.H. Hu, Solid-solution catalysts for CO2 reforming of methane, Catal. Today. 148 (2009) 206–211. doi:10.1016/j.cattod.2009.07.076.

[25] M.T. Fan, J.D. Lin, H.B. Zhang, D.W. Liao, In situ growth of carbon nanotubes on Ni/MgO: a facile preparation of efficient catalysts for the production of synthetic natural gas from syngas, Chem. Commun. 51 (2015) 15720–15723. doi:10.1039/C5CC04728E.

[26] S. Tada, T. Shimizu, H. Kameyama, T. Haneda, R. Kikuchi, Ni/CeO2 catalysts with high CO2 methanation activity and high CH4 selectivity at low temperatures, Int. J. Hydrogen Energy. 37 (2012) 5527–5531. doi:10.1016/j.ijhydene.2011.12.122.

[27] Y. Yan, Y. Dai, H. He, Y. Yu, Y. Yang, A novel W-doped Ni-Mg mixed oxide catalyst for CO2 methanation, Appl. Catal. B Environ. 196 (2016) 108–116. doi:10.1016/j.apcatb.2016.05.016.

[28] T. Nakayama, N. Ichikuni, S. Sato, F. Nozaki, Ni/Mgo catalyst prepared using citric acid for hydrogenation of carbon dioxide, Appl. Catal. A Gen. 158 (1997) 185–199. doi:10.1016/S0926-860X(96)00399-7.

[29] Y. Li, G. Lu, J. Ma, Highly active and stable nano NiO–MgO catalyst encapsulated by silica with a core–shell structure for CO2 methanation, RSC Adv. 4 (2014) 17420. doi:10.1039/c3ra46569a.

[30] N. Takezawa, H. Terunuma, M. Shimokawabe, H. Kobayashib, Methanation of carbon dioxide: preparation of Ni/MgO catalysts and their performance, Appl. Catal. 23 (1986) 291–298. doi:10.1016/S0166-9834(00)81299-3.

[31] H.M. Rootare, C.F. Prenzlow, Surface areas from mercury porosimeter measurements, J. Phys. Chem. 71 (1967) 2733–2736. doi:10.1021/j100867a057.

[32] G. Baldauf-Sommerbauer, S. Lux, W. Aniser, M. Siebenhofer, Reductive calcination of mineral magnesite: hydrogenation of carbon dioxide without catalysts, Chem. Eng. Technol. 39 (2016) 2035–2041. doi:10.1002/ceat.201600094.

[33] H.E. Swanson, E. Tatge, Standard X-ray diffraction powder patterns, Natl. Bur. Stand. Circ. 539 (1953) 1–95.

[34] Y.D. Kondrashev, Y.A. Omel'chenko, X-ray diffraction examination of some oxide and sulfide systems, Russ. J. Inorg. Chem. 9 (1964) 512–516.

[35] F. Koschany, D. Schlereth, O. Hinrichsen, On the kinetics of the methanation of carbon dioxide on coprecipitated NiAl(O)x, Appl. Catal. B Environ. 181 (2016) 504–516. doi:10.1016/j.apcatb.2015.07.026.

[36] J. Yang, J. Mcgregor, A.J. Sederman, J.S. Dennis, Kinetic studies of CO2 methanation over a Ni/γ-Al2O3 catalyst using a batch reactor, Chem. Eng. Sci. 141 (2016) 28–45. doi:10.1016/j.ces.2015.10.026.

8 Findings and future directions

8.1 Findings

Several novel options for the mitigation of CO_2 emissions during the beneficiation of mineral metal carbonates were investigated. The focus was set on carbonates with industrially relevant applications: the Mg-Mn siderite phase of a mineral from the Erzberg (Eisenerz, Austria), magnesite/dolomite (Breitenau, Austria), and magnesite (Turkey). Siderite is used as a raw material for iron production, whereas magnesite is used i.a. as the raw material for refractory production.

During calcination in nitrogen, Mg-Mn siderite is converted into Mg-Mn wuestite and Mg-Mn magnetite (Eq. 1). The stability of wuestite at room temperature arises from partial substitution of iron by magnesium and manganese in the crystal lattice. Compared to state-of-the-art calcination in air (= roasting), a product with a higher iron loading is formed: FeO (77.7 %wt. Fe) and Fe_3O_4 (72.4 %wt. Fe) compared to Fe_2O_3 (69.9 %wt. Fe). Consequently, less reducing agent is needed for the production of iron. For coke as the reducing agent in the blast furnace process, this directly leads to a considerable decrease in CO_2 emissions. The reaction kinetics of the calcination of Mg-Mn siderite in purified form (SEP) and as present in the original mineral (ICM) was investigated with two computational methods – an isoconversional method and multi-variate nonlinear regression (MVNR). Both computational methods yield comparable results, while MVNR proofed to be more robust. The Prout-Tompkins model Bna [1] with α as the relative conversion, reaction order n, and model parameter m, describes the calcination of siderite in nitrogen best. The N_2-calcination kinetics of Mg-Mn siderite in purified form can be described with Eq. 2, whereas Eq. 3 is used to describe the calcination kinetics in N_2 atmosphere of Mg-Mn siderite as present in the original mineral. The presence of accompanying carbonates in the original mineral lead to an increase of the pre-exponential factor, activation energy, and reaction order.

$$FeCO_3 \rightarrow (1-x)FeO + \frac{x}{3}Fe_3O_4 + \left(1-\frac{x}{3}\right)CO_2 + \frac{x}{3}CO \qquad x = 0-1 \tag{1}$$

$$\frac{d\alpha}{dt}(\text{SEP, Eq. 1}) = 3.16 * 10^{12} * \exp\left(\frac{-210}{R_{gas}T}\right) * \alpha^{0.32}(1-\alpha)^{1.26} \tag{2}$$

$$\frac{d\alpha}{dt}(\text{ICM, Eq. 1}) = 1.58 * 10^{19} * \exp\left(\frac{-310}{R_{gas}T}\right) * \alpha^{0.25}(1-\alpha)^{1.93} \tag{3}$$

As an alternative to the two-step process of calcination of iron carbonate and reduction of iron oxides in a separate step, direct reduction of the purified Mg-Mn siderite phase with hydrogen was investigated. Direct reduction would lead to a 60 % decrease of CO_2 emissions compared to the state-of-the-art process. Formation of iron from iron carbonate during reduction with hydrogen (Eq. 4) is proposed to proceed in a temperature controlled nucleation and diffusional

growth mechanism. This proposal is based on the finding, that the two-dimensional Avrami-Erofeev model A2 [2] describes the kinetics best (Eq. 5). Kinetics parameters were determined by MVNR of linear heating rate thermogravimetry data.

$$FeCO_3 + H_2 \rightarrow Fe + H_2O + CO_2 \tag{4}$$

$$\frac{d\alpha}{dt}(\text{SEP, Eq. 4}) = 7.41 * 10^9 * \exp\left(\frac{-165}{R_{gas}T}\right) * 2 * (1-\alpha)[-\ln(1-\alpha)]^{1/2} \tag{5}$$

Due to its chemical nature, the decomposition of 1 mole of metal carbonate MCO_3 is always coupled to the emission of 1 mole of CO_2. To omit these inevitable CO_2 emissions, a procedure that couples CO_2 emission and utilization via CO_2 hydrogenation termed reductive calcination (Eq. 6) was introduced. A thermodynamic analysis revealed that during the reductive calcination of magnesium carbonate and iron carbonate, methane and carbon monoxide are the accessible products besides carbon dioxide. This finding was confirmed in many experiments.

$$(a+b)MCO_3 + \left[(a+b)\left(\frac{c}{2}+d\right)+b\right]H_2 \rightarrow$$

$$a\,MO + b\,M + (a+b)CH_cO_{2-d} + [b + d(a+b)]H_2O \tag{6}$$

The reductive calcination of Mg-Mn siderite was investigated in steady-state, quasi-isothermal experiments on a tubular reactor setup. A study based on design of experiments revealed that methane yield can be distinctly raised by increased reaction pressure and low reaction temperature. An increase of residence time and hydrogen concentration in the reactor feed gas revealed to have a minor positive effect on methane yield. A method to calculate the time-dependent conversion of metal carbonates from the online gas analysis of tubular reactor experiments was developed. With this method at hand, it was possible to derive a lump kinetics approach for the formation of the Mg-Mn iron oxides, methane, carbon monoxide, and carbon dioxide from 5-10 mm Mg-Mn siderite for steady-state, quasi-isothermal conditions in the temperature range 375-415 °C at both ambient pressure and 8 barg. At ambient pressure, a contracting volume model R3 [2], whereas at 8 barg, a zero order model F0 [2] predicted the dataset best. As a consequence, the relative conversion of 5-10 mm Mg-Mn siderite $X_{Sid\text{-}Ox}$ can be described with Eq. 7 for ambient pressure and the temperature span 375-415 °C. Eq. 8 has to be applied at 8 barg and 375-415 °C. Methane and carbon monoxide yield Y_i were modelled with a power approach that could be linearized with the parameters $s_{a,i}$ and $d_{a,i}$ in the temperature (T) region investigated (Eq. 9).

$$\frac{dX_{Sid-Ox}}{dt}(0\text{ barg}) = 1.88 * 10^5 * \exp\left(\frac{-129}{R_{gas}T}\right) * 3 * (1-X_{Sid-Ox})^{2/3} \tag{7}$$

$$\frac{dX_{Sid-Ox}}{dt}(8\text{ barg}) = 1.37 * 10^7 * \exp\left(\frac{-138}{R_{gas}T}\right) \tag{8}$$

$$Y_i(T) = \left[s_{a,i} * T[K] + d_{a,i}\right] * X_{Sid-Ox}^{\left[s_{b,i} * T[K] + d_{b,i}\right]} \tag{9}$$

The model equations represented in Eq. 7-9 were applied to evaluate a first design of a counter current, isothermal tube bundle reactor. A case study assuming a throughput of 1 Mt year^{-1} of iron carbonate mineral from the Erzberg revealed that the reactor height is increased by a factor of 4, when the reaction temperature is decreased from 415 to 375 °C. This substantial decrease in reactor size is, however, counteracted by a decrease of methane yield from 37 to 7 % at ambient pressure and 71 to 42 % at 8 barg.

Reductive calcination of mineral magnesite and magnesite/dolomite (1:1 mol:mol) was investigated in steady-state, quasi-isothermal tubular reactor experiments. It was shown that by varying temperature and pressure mineral magnesite (98 %wt. $MgCO_3$) can be converted into magnesium oxide and a mixture of CH_4, CO, and CO_2 without external catalysts. If dolomite accompanies magnesite in a 1:1 equimolar mixture, the reaction temperature for magnesite decomposition has to be increased. Carbon monoxide is produced in higher quantities whereas methane is produced in traces only, compared to pure magnesite. Additionally, it was shown that magnesium oxide produced from mineral magnesite is a highly active catalyst for the reverse water-gas-shift reaction.

The investigations on the reductive calcination of mineral iron and magnesium carbonate revealed that it is possible to partially convert a metal carbonate into methane and carbon monoxide. An increase of methane yield can be reached if reductive calcination is coupled to a gas valorization unit with a highly active heterogeneous catalyst like Ni/MgO. A study on the activity of Ni/MgO prepared by wet impregnation was performed. Ni/MgO with a loading of 17 %wt. Ni is not only highly active with conversion and selectivity near thermodynamic equilibrium at moderate temperatures as low as 325 °C, but was also proven to be stable during shut on/shut off operation over several days.

8.2 Future directions

As lined out in chapter 4, the mechanism of iron formation from Mg-Mn siderite during reductive calcination in hydrogen is yet not quite clear. For the development of the lump kinetics model (Eq. 7-9), only the formation of iron oxides was assumed. The XRD analysis, however, revealed that cohenite Fe_3C was formed as a by-product. Cohenite formation is an indication for iron formation via an alternative reaction path (see Figure 4-24). Inclusion of Fe_3C formation and an extension of the kinetics model to predict the composition of the solid product (Fe, FeO, Fe_3O_4, Fe_3C) would be a fruitful field for future investigations.

Selective production of neither carbon monoxide nor methane was observed during reductive calcination of mineral iron and magnesium carbonate as carbon dioxide was always present in the product gas. The gaseous product of single-stage reductive calcination (Figure 8-1) is thus a stream containing a mixture of CO_2, CO, CH_4, H_2O, H_2 (if used in excess), and possibly inert gases. An upgrade of this product gas in a second stage – dual-stage reductive calcination (Figure 8-2) – may be beneficial, depending on the application. For hydrogen storage via chemical conversion

into methane, for instance, a high methane yield is desirable. Thus the second stage would include a reactor including a methanation catalyst (e.g. Ni/MgO, as outlined in this thesis). Alternatively, if reductive calcination is run under conditions that favor carbon monoxide formation, the second stage of reductive calcination could include any process based on syngas conversion, e.g. Fischer-Tropsch or methanol synthesis. Process development and analysis of alternative design options for dual-stage reductive calcination would be an interesting field for prospective research.

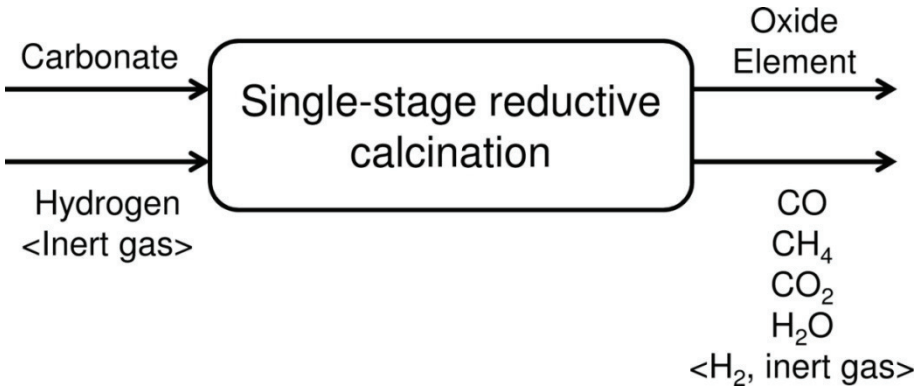

Figure 8-1: Process sketch of single stage reductive calcination.

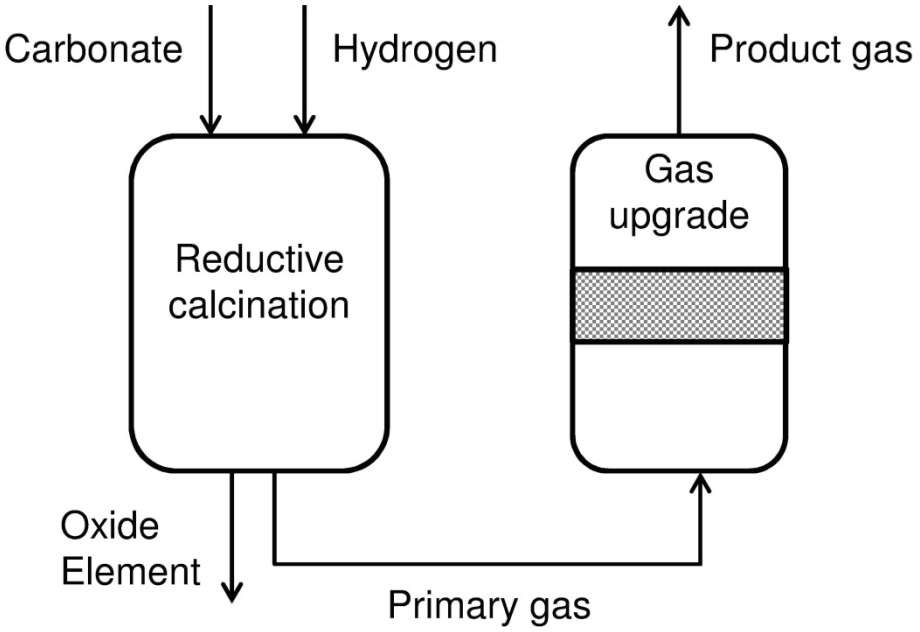

Figure 8-2: Process sketch of dual stage reductive calcination.

References

[1] M.E. Brown, The Prout-Tompkins rate equation in solid-state kinetics, Thermochim. Acta. 300 (1997) 93–106. doi:10.1016/S0040-6031(96)03119-X.

[2] A. Khawam, D.R. Flanagan, Solid-state kinetic models: Basics and mathematical fundamentals, J. Phys. Chem. B. 110 (2006) 17315–17328.

9 Appendix

9.1 List of publications

9.1.1 Peer-reviewed papers

G. Baldauf-Sommerbauer, S. Lux, J. Wagner, M. Siebenhofer, Determination of the kinetic triplet by an isoconversional and a regression method applied to the decomposition of mineral iron carbonate in nitrogen, Thermochim. Acta. 649 (2017) 1–12. doi:10.1016/j.tca.2017.01.001.

G. Baldauf-Sommerbauer, S. Lux, W. Aniser, M. Siebenhofer, Synthesis of carbon monoxide from hydrogen and magnesite/dolomite, Chemie Ing. Tech. 89 (2017) 172–179. doi:10.1002/cite.201600078.

G. Baldauf-Sommerbauer, S. Lux, M. Siebenhofer, Sustainable iron production from mineral iron carbonate and hydrogen, Green Chem. 18 (2016) 6255–6265. doi:10.1039/c6gc02160c.

G. Baldauf-Sommerbauer, S. Lux, W. Aniser, M. Siebenhofer, Reductive calcination of mineral magnesite: hydrogenation of carbon dioxide without catalysts, Chem. Eng. Technol. 39 (2016) 2035–2041. doi:10.1002/ceat.201600094.

9.1.2 Submitted papers

G. Baldauf-Sommerbauer, S. Lux, W. Aniser, B. Bitschnau, I. Letofsky-Papst, M. Siebenhofer, Steady state and controlled heating rate methanation of CO2 on Ni/MgO in a bench scale fixed bed tubular reactor.

9.1.3 Conference talks

Presenters are marked with an asterisk (*).

G. Baldauf-Sommerbauer*, S. Lux, M. Siebenhofer, Direct reduction of iron carbonate with hydrogen, in: Jahrestreffen Reaktionstechnik 2017, Würzburg, Germany.

G. Baldauf-Sommerbauer, S. Lux, M. Siebenhofer*, Hydrogen storage and carbon dioxide valorization through reductive calcination of mineral carbonates, in: AIChE Annual Meeting 2016, San Francisco, USA.

G. Baldauf-Sommerbauer, S. Lux, M. Siebenhofer*, Methanation of carbon dioxide with a nickel/magnesium oxide catalyst, in: AIChE Annual Meeting 2016, San Francisco, USA.

G. Baldauf-Sommerbauer, S. Lux, M. Siebenhofer*, Renewable hydrogen storage for energy applications using mineral carbonates, in: 19th Symposium on Separation Science and Technology for Energy Applications 2016, Gatlinburg, USA.

G. Baldauf-Sommerbauer, S. Lux, M. Siebenhofer*, Wasserstoffspeicherung, CO_2-Verwertung und Prozessoptimierung durch die reduzierende Kalzinierung mineralischer Rohstoffe, in: ProcessNet-Jahrestagung 2016, Aachen, Germany.

G. Baldauf-Sommerbauer*, S. Lux, M. Siebenhofer, Reductive Calcination - A means of Carbon Dioxide Utilisation in Minerals Processing, in: 14th International Conference on Carbon Dioxide Utilisation 2016, Sheffield, United Kingdom.

G. Baldauf-Sommerbauer*, S. Lux, M. Siebenhofer, Reductive Calcination: Process Integration in Mineral Processing, in: AIChE Annual Meeting 2015, Salt Lake City, USA.

G. Baldauf-Sommerbauer*, S. Lux, M. Siebenhofer, Methane from Carbon Dioxide: Industrial Implementation and Technical and Economic Benefits, in: European Symposium on Chemical Reaction Engineering 2015, Fürstenfeldbruck, Germany.

9.1.4 Conference proceedings

G. Baldauf-Sommerbauer, S. Lux, M. Siebenhofer, Wasserstoffspeicherung, CO_2-Verwertung und Prozessoptimierung durch die reduzierende Kalzinierung mineralischer Rohstoffe, in: Chemie Ing. Tech., Wiley-VCH Verlag GmbH & Co. KGaA, Deutschland, 2016: p. 1378. doi:10.1002/cite.201650115.

G. Baldauf-Sommerbauer, S. Lux, W. Aniser, M. Siebenhofer, Die Herstellung von Synthesegas aus Wasserstoff und Magnesit/Dolomit, in: U. Hirn (Ed.), Conf. Proc. 12th Minisymp. Verfahrenstechnik, Verlag der Technischen Universität Graz, 2016: pp. 83–86. doi:10.3217/978-3-85125-456-3.

G. Baldauf-Sommerbauer, S. Lux, M. Siebenhofer, Hydrogenation of carbon dioxide with Fe/Ni-catalysts, in: AIChE Annu. Meet. 2015 Proc., 2015. ISBN 978-0-8169-1094-6.

G. Baldauf-Sommerbauer, S. Lux, M. Siebenhofer, Reductive Calcination: Process Integration in Mineral Processing, in: AIChE Annu. Meet. 2015 Proc., 2015. ISBN 978-0-8169-1094-6.

G. Sommerbauer, S. Lux, H. Schmid, A. Kogelbauer, A. Stadtschnitzer, M. Siebenhofer, Methanisierung von Kohlendioxid und Kohlenmonoxid, in: Conf. Proc. 11th Minisymp. Verfahrenstechnik, BOKU Wien, 2015: pp. 219-222. ISBN 978-3-200-04069-4.

9.1.5 Poster contributions

G. Baldauf-Sommerbauer, S. Lux, M. Siebenhofer, Catalytic methanation of carbon dioxide with Ni/MgO, in: Jahrestreffen Reaktionstechnik 2017, Würzburg, Germany.

G. Baldauf-Sommerbauer, S. Lux, M. Siebenhofer, Reductive Calcination - A means of Carbon Dioxide Utilisation in Minerals Processing, in: 14th International Conference on Carbon Dioxide Utilisation 2016, Sheffield, United Kingdom.

G. Baldauf-Sommerbauer, S. Lux, M. Siebenhofer, Die Kalzinierungskinetik eisenkarbonathaltiger Erze in reduzierender Atmosphäre, in: Jahrestreffen Reaktionstechnik 2016, Würzburg, Germany.

G. Baldauf-Sommerbauer, S. Lux, W. Aniser, M. Siebenhofer, Die Herstellung von Synthesegas aus Wasserstoff und Magnesit/Dolomit, in: 12th Minisymp. Verfahrenstechnik 2016, Graz, Austria.

G. Baldauf-Sommerbauer, S. Lux, D. Kong, M. Siebenhofer, Hydrogenation of carbon dioxide with Fe/Ni-catalysts, in: AIChE Annual Meeting 2015, Salt Lake City, USA.

G. Sommerbauer, S. Lux, H. Schmid, A. Kogelbauer, A. Stadtschnitzer, M. Siebenhofer, Methanisierung von Kohlendioxid und Kohlenmonoxid, in: 11th Minisymp. Verfahrenstechnik 2015, Vienna, Austria.

9.2 Supervised and co-supervised thesis

A. J. Kathrein, Die katalytische Methanisierung von Kohlendioxid: Stand der Forschung, Katalysatorsynthese und Katalysatorscreening, *Bachelor's Thesis*, Graz University of Technology, Graz, 2015.

W. Aniser, Die reduzierende Kalzinierung von magnesithaltigen Erzen, *Bachelor's Thesis*, Graz University of Technology, Graz, 2015.

G. Kaufmann, Charakterisierung von Ni/MgO mit einer Ni-Beladung von 16 Gew.% zur katalytischen CO_2 Methanisierung, *Bachelor's Thesis*, Graz University of Technology, Graz, 2016.

J. Jäger, Determination of the oxidation and reduction kinetics of Erzber-Feinerz by isothermal thermogravimetric analysis at 600-700 °C, *Bachelor's Thesis*, Graz University of Technology, in progress.

B. Ottitsch, Wärme- und Stoffbilanzierung der reduzierenden Kalzinierung mit anschließender Methanisierung, *Project report (Kontruktionsübung)*, Graz University of Technology, Graz, 2015.

P. Krenn, Planung eines Rohrbündelreaktors zur reduzierenden Kalzinierung von mineralischem Eisenkarbonat, *Project report (Kontruktionsübung)*, Graz University of Technology, Graz, 2017.

A. J. Kathrein, Experimentelle reduzierende Kalzinierung eines mineralischen Eisenkarbonats der Kornklassen 0,5-1 mm und 5-10 mm bei 500 bis 530 °C, *Project report (Konstruktionsübung)*, in progress.

D. Kong, Catalytic Properties of Supported Iron/Nickel Catalysts, *Project report* submitted for partial fulfilment for MEng in Chemical Engineering at the University of Strathclyde, 2015.

B. Ottitsch, Die reduzierende Kalzinierung ausgewählter Kornklassen eines eisenkarbonathaltigen Erzes, *Master's Thesis*, Graz University of Technology, Graz, 2016.

A. Loder, Untersuchung zur katalytischen Umsetzung von Wasserstoff und Kohlendioxid mit kalziniertem Eisenkarbonat, *Master's Thesis*, Graz University of Technology, Graz, 2017.

P. Krenn, Eisenherstellung aus Eisenkarbonat – vom Stand der Technik zur Zukunftstechnologie, *Master's Thesis*, Graz University of Technology, in progress.

9.3 List of figures

9.4 List of tables